PRECISION ENGINEERING CENTER

2003 ANNUAL REPORT
VOLUME XXI
March 2004

Sponsors:

3M Corporation
Biomachines
Eastman Kodak Company
Los Alamos National Laboratory
National Science Foundation
Precitech Precision, Inc.
Sandia National Laboratory
Vistakon, Johnson & Johnson Vision Care Inc.

Faculty:

Thomas Dow, Editor
Greg Buckner
Jeffrey Eischen
Paul Ro
Phillip Russell
Ronald Scattergood
David Youden

Graduate Students:

Brett Brocato
Nathan Buescher
Stuart Clayton
Karalyn Folkert
Karl Freitag
David Hood
Patrick Morrissey
Nobuhiko Negishi
Witoon Panusittikorn
Travis Randall
Tao Wu
Yanbo Yin

Undergraduate Students:

Ryan Huth
Ryan Staton
Anthony Wong

Staff:

Lara Bodenhamer
Kenneth Garrard
Alexander Sohn
Laura Underhill

TABLE OF CONTENTS

SUMMARY

The goals of the Precision Engineering Center are: 1) to improve the understanding and capability of precision metrology, actuation, manufacturing and assembly processes; and 2) to train a new generation of engineers and scientists with the background and experience to transfer this new knowledge to industry. Because the problems related to precision engineering originate from a variety of sources, significant progress can only be achieved by applying a multidisciplinary approach; one in which the faculty, students, staff and sponsors work together to identify important research issues and find the optimum solutions. Such an environment has been created and nurtured at the PEC for over 21 years; the new technology that has been developed and the 90 graduates attest to the quality of the results.

The 2003 Annual Report summarizes the progress over the past year by the faculty, students and staff in the Precision Engineering Center. During the past year, this group included 7 faculty, 11 graduate students, 3 undergraduate students, 2 full-time technical staff members and 2 administrative staff members. Representing two different Departments from the College of Engineering, this diverse group of scientists and engineers provides a wealth of experience to address precision engineering problems. The format of this Annual Report separates the research effort into individual projects, however, this should not obscure the significant interaction that occurs among the faculty, staff and students. Weekly seminars by the students and faculty provide information exchange and feedback as well as practice in technical presentations. Teamwork and group interactions are a hallmark of research at the PEC and this contributes to both the quality of the research as well as the education of the graduates.

The summaries of individual projects that follow are arranged in the same order as the body of the report, that is the four broad categories of 1) metrology, 2) actuation, 3) control and 4) fabrication.

1) METROLOGY

The emphasis of the metrology projects has been to develop new techniques that can be used to predict surface shape as well as measure important parameters such as tool force.

Design and Fabrication of High-Current Density Electrical Connections

The fabrication of pulse power experiments at Los Alamos National Labs requires assembly of a combination of shrink fit, press fit, and bolted compression joints that are used to carry large electrical currents. These joints are also called on to support some mechanical stresses. As a result, the integrity of these joints is critical to the success of the experiments. The primary issues are: mechanics of the interference fits, physical description of the contact surfaces between the components and joint void description. To investigate these issues, finite element simulations have been carried out. The focus of this report is on the current generation liner glide plane system, which represents a significant departure from previous designs and reported results.

Effect of Phase Transformation on Scribing Behavior of Single Crystal Silicon

With the appropriate conditions, a diamond tool can produce ductile scribes on single crystal silicon due to a brittle-to-ductile transformation of the material beneath the scribe. This anomalous plastic flow has been attributed to a high-pressure phase transformation from diamond cubic to a metallic ß-tin phase. The residual stresses within the scribe create a bending distortion in a flat wafer sample. The deflection was measured using optical interferometery and correlated to a model of the bend effect due to the residual stresses. SEM and AFM characterization is used to aid characterization of the material removal. Raman spectroscopy was also used to study the nature of the material within the scribe region and to indicate whether the hypothesized transformation has occurred. The effects of tool geometry and loading, as well crystallographic orientation and direction of the wafer were studied.

Metrology Artifact Design

In the past, Oak Ridge Y-12 has used rotary contour gages to measure machined parts. The increased use of Coordinate Measuring Machines (CMMs) has warranted a need for a reference standard to compare previous measurements using rotary contour gages with current measurements using CMMs. After considering various types of artifact standards, a ring gauge was chosen for further development. A swept sine wave with ± 2.5 µm amplitude was inscribed on the ID of the ring gauge. The wave feature will facilitate the determination of the affect that small anomalies on a surface have on a measurement. The machining of the swept sine wave was completed in an open control loop. Initial measurements of the completed artifact were done at the PEC. Further evaluation is in progress at Oak Ridge Y-12.

Ultraform 2D

A polar profilometer, Ultraform 2D, has been built in a cooperative venture by Precitech and the PEC under a technology transfer license agreement. The design is based on the Polaris machine that was developed at the PEC in 2000. Ultraform incorporates numerous improvements in packaging, axis design and control software to produce a commercial measuring machine. Both the measurement volume and resolution have been increased compared to the Polaris design and controller level support for improved operating procedures has been incorporated. In particular, a means of following an arbitrary surface using the LVDT probe for axis feedback has been developed. Updating the user interface software to take advantage of these new hardware features and implementation of improved probe waviness compensation algorithms are in progress.

2) ACTUATION

Real-time control is a necessary technique to improve the precision — accuracy and repeatability — of a fabrication or measurement process. The metrology activities discussed above are intended to develop tools or devices to measure shape, force or properties. Equally important are improved actuators with the ability to create the motion necessary to correct errors.

Development of High-Speed, Low Amplitude Fast Tool Servo

Fast tool servos are used to create minute surface features on a cutting surface. Servos have been previously developed at the PEC. These designs as well as other actuation methods are explained. Increasing the operation frequency of a fast tool servo leads to an increase in production efficiency. The goal of this project is to create a device capable of operating at 10,000 Hz while producing a 5 _m stroke. The technical challenges, including actuator type, frequency limit, structural design, cooling and reliability, are explained and addressed in detail. Different actuation methods for the servo are explored, and a comparison is given. A preliminary design utilizing piezoelectric actuation and a lightweight ceramic tool holder is presented. Progression through associated calculations are used to show the feasibility of the design, and a plan for future work is explained.

3) FABRICATION

High-speed milling, plastic replication and a new technique for diamond turning have been the focus of the fabrication process research over the past year.

Force Feedback Control of Tool Deflection in Miniature Ball End Milling

Previous research at the PEC focused on open-loop compensation of machining errors associated with tool deflection in miniature ball end milling. These methods utilized tool force models to predict deflections and pre-compensate tool paths off-line to improve the dimensional tolerance and accuracy in finished parts. Real-time force feedback has the potential to further improve the accuracy of the machined profiles. Two specific force feedback approaches are discussed: cutting depth prediction based on a cutting force model and tool deflection prediction using a model of tool stiffness. Real-time control algorithms incorporating both methods were implemented and evaluated on a high-speed air-bearing spindle mounted on a 3-axis diamond turning machine. Results indicate that profile errors can be reduced up to 80% (to ± 2 μm) when compared to non-compensated cases.

2D Force-Feedback Tool Deflection using Instrumented Tool Spindle

The primary objective of this research is to improve dimensional tolerances and reduce total manufacturing time in precision milling operations through the implementation of force-feedback machining. Previous techniques utilized the machine tool axes to compensate these deflections but a better approach is to build the compensation into the spindle to create a "rigid" tool. The new 2D design utilizes a pair of 3-axis load cells that support the spindle and measure the magnitude and direction of the steady-state tool forces. This fixture is in turn supported on two piezoelectric actuators. These are located in a structure that can position the center-line of the spindle to compensate for the bending of the tool in two orthogonal directions. The 2D design has been designed, fabricated and calibrated. Initial testing of the prototype is underway.

Capabilities of Micro-Machining

The goal of this research is to reduce feature size and improve tolerances using micro-scale machining. This section reports on a literature search of current machining techniques that have been used to produce sub-millimeter features, the applications of these techniques and the features that can be produced. While many MEMS (Micro-Electro-Mechanical-Systems) devices are fabricated using the silicon etching techniques developed for the microelectronics industry, micro-machining is an attractive alternative because of its low start-up cost relative to other capital-intensive technologies, applicability to a wide range of materials, high flexibility of workpiece shape and aspect ratio, and low cost for prototype manufacturing. The search uncovered papers in the areas of proof of capability, companion processes, process analysis, and the applications of more general micromachining technologies.

Fixturing and Alignment of Free-Form Optics for Diamond Turning

The fabrication of free-form optics presents unique challenges not only to the diamond turning process but also to the process by which the workpiece is located with respect to the machine axes. While rotationally symmetric parts only require alignment in three directions, free-form optics require alignment in up to six directions. Distinct from alignment in an optical system, fixture alignment for diamond turning requires a separate set of techniques to accommodate the forces encountered in machining. General fixturing principles, alignment techniques and the application to a NASA optic are discussed. While the techniques discussed focus on diamond turning, many of the considerations apply to other fabrication techniques as well.

Elliptical Vibration Assisted Diamond Turning

Over the past 3 years, a project to develop an Elliptical Vibration Assisted Machining (EVAM) system was funded by Kodak. The goal was to create a device that could be used to study the influence of the process variables on this unique material removal process; specifically the shape of the elliptical tool motion, the magnitude of the forces, tool wear and surface finish. Two different prototypes (called the UltraMill) were created; leading to a high-speed version using piezoelectric actuators with a light-weight, hollow ceramic tool holder that can operate at over 4000 Hz. Features of this high-speed version include a closed loop temperature control system and a light-weight tool holder with a glued-in diamond tool. The performance of the UltraMill was impressive and test cuts were made on plastic, aluminum and silicon carbide. The surface finish was nearly as good as diamond turning if the speed of the workpiece was low with respect to the oscillation speed of the elliptical motion. The peak cutting forces were reduced by 50%. The UltraMill can produce optical quality surfaces and the tool wear is less than conventional diamond turning for difficult to machine materials such as steel and ceramics.

4) CONTROL

Control of a precision fabrication processes involves both the characterization of the electromechanical system and the selection of hardware and software to implement the control

algorithm. As a consequence, studies of each of these aspects are important research topics for the PEC.

Error Compensation using Inverse Actuator Dynamics

The use of fast tool servos (FTS) to create non-rotationally symmetric optical surfaces is growing. However, the amplitude and phase response of this dynamic system can result in form errors on the machined part. The motivation for this work is to implement open-loop modifications of the input signal to the Variform fast tool servo to correct for its dynamics. An algorithm using signal deconvolution was developed to generate the appropriate input commands that produce the desired response. Deconvolution is a mathematical procedure that can produce a modified input to reverse the effects of attenuation and phase if the impulse response of the dynamic system is known. Since this modified command is not calculated from the position feedback, there is no delay in the response. The result is dramatically improved following error especially for high frequency motion. An off-axis spherical surface feature has been selected for machining tests of these algorithms. The spherical profile is easily measured interferometrically and the machining parameters can be adjusted to study a wide range of frequencies and amplitudes in the FTS command signal.

1 FABRICATION, DISTORTION, AND METROLOGY OF SHRINK FIT ELECTRICAL CONNECTIONS

Patrick D. Morrissey
Graduate Student
Jeffrey W. Eischen
Associate Professor
Department of Mechanical and Aerospace Engineering

The fabrication of pulse power experiments at Los Alamos National Labs requires assembly of a combination of shrink fit, press fit, and bolted compression joints that are used to carry large electrical currents. These joints are also called on to support some mechanical stresses. As a result, the integrity of these joints is critical to the success of the mission. The primary issues at hand include the following: mechanics of the interference fits, physical description of the contact surfaces between the liner and glide planes, joint void description. To investigate these issues, finite element simulations have been carried out. The focus of this report is on the current generation liner glide plane system, which represents a significant departure from previously designs and associated reported results.

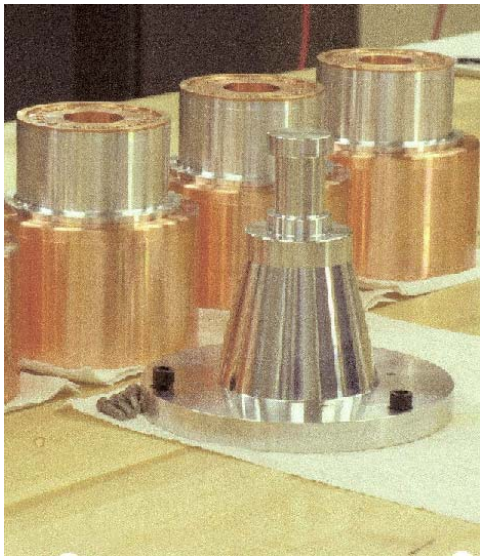

1.1 INTRODUCTION

After running several pulsed-power experiments using the ATLAS design described in previous reports, problems were encountered and thus design changes were needed. There were minor complications with the axial alignment of components during the shrink fit assembly, but more important were the problems associated with axial stability during the experiments themselves. The ATLAS Generation I shrink fit geometry lacked support for various components (namely the liner and glide planes) in the axial direction. This often resulted in slippage during the high-energy experiments, sometimes completely separating electrical connections. There was a need for a more robust geometry, and thus ATLAS Generation II was developed.

The concept behind ATLAS Generation II are identical to the design of Generation I. Large current pulses (> 10MA) are passed through the liner, resulting in a radial implosion. The liner implodes at speeds on the order of 10-20km/s, contacting a target contained within the liner. Major differences in this design include the following: the use of a mechanical press fit rather than a thermal shrink fit for liner/glide plane assembly, modified liner dimensions and overall geometry, and a new mechanism through which current flows from the liner. A cross section of the original design (Phase I) of ATLAS Generation II is shown in Figures 1 and 2.

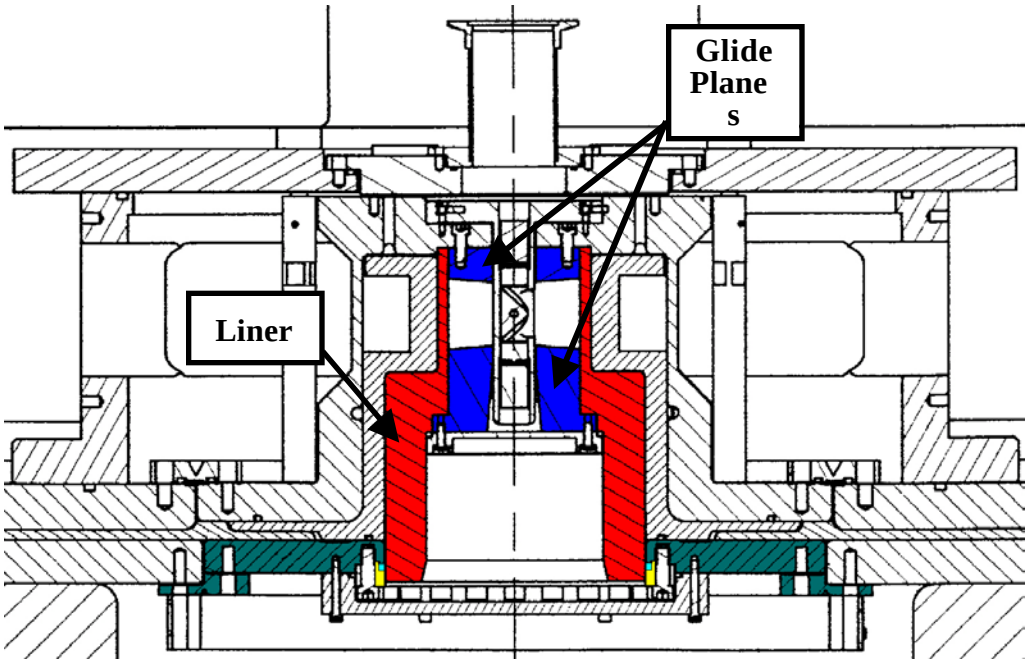

Figure 1. Cross section drawing of ATLAS Generation II (Phase I)

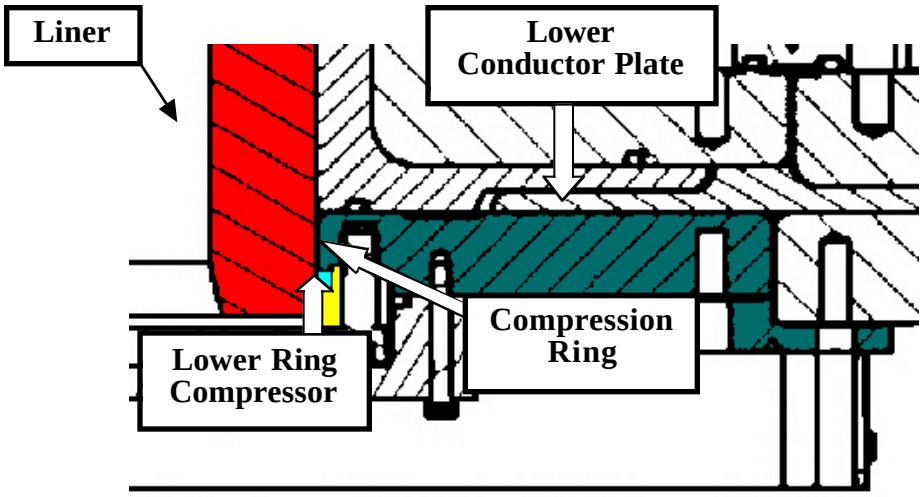

Figure 2. Zoomed view of ATLAS Generation II (Phase I)

One of the major differences of this design is the liner shape. The geometry is no longer a cylinder and lacks the "bump" features on each liner end. The liner dimensions, namely thickness, are easily adjustable during fabrication to meet performance demands determined by experimental parameters (current magnitude, sinusoidal rise-times, etc). Secondly, the upper glide plane is brought into contact with the liner via a mechanical press fit rather than a thermal shrink fit, as in ATLAS Generation I. Finally, the compression ring acts as the new mechanism to transfer current from the liner to the return conductor plates, where the current circuit is completed. The ATLAS Generation I design used the lower glide plane as the current exit route from the liner. Here, the compression ring is slipped over the end of the liner with 0.254mm (0.010in) of radial clearance. This clearance is compensated for by a sharp tooth on the conductor plate, which distorts the compression ring from the top, thus forcing contact with the liner. The integrity of this interface is vital to the success of the experiments, and therefore the design of the compression ring and its surrounding components (i.e., the liner, ring compressor, and lower conduction plate) are critical. For directional control of current flow, LANL places a high strength insulation tape around the liner OD in areas of close proximity to the lower conduction plate to ensure that the current flows *only* to the compression ring immediately after exiting the liner.

1.2 FINITE ELEMENT ANALYSIS AND RESULTS

Once again the system was modeled with LS-DYNA using axisymmetric elements. The parts surrounding the compression ring were slightly altered by LANL to overcome problems with the experiments, mainly unwanted distortion of other components. One such modification was placement of the tooth on the lower ring compressor that distorts the compression ring from the bottom rather than from the top as described earlier. The geometry of the upper glide plane and liner remained the same through this design transition. The LS-DYNA model of the most recent component geometry is seen in Figure 3.

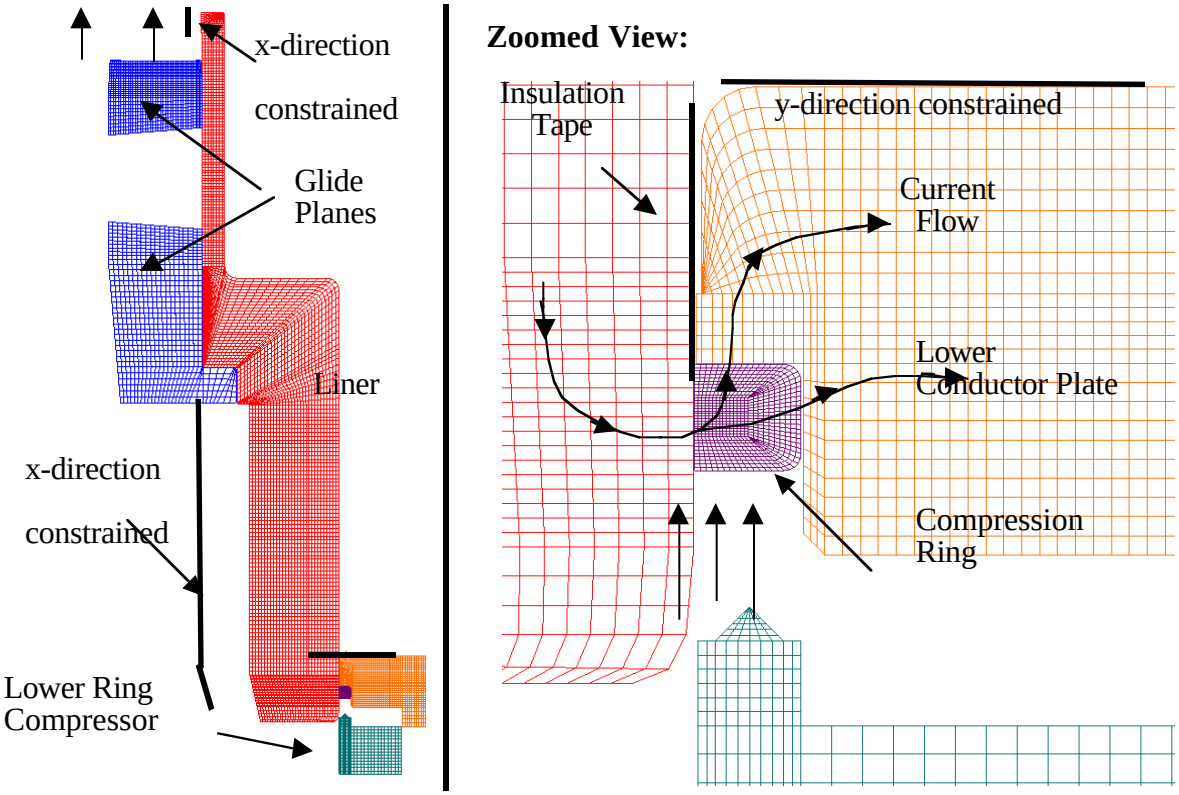

Figure 3. ATLAS Generation II finite element mesh (final design iteration)

The glide planes are composed of copper, the liner and compression ring are 1100 aluminum, the lower conductor plate is 6061 aluminum, and the lower ring compressor is composed of 304 stainless steel.

The six components noted in Figures 1 and 2 are the ones of greatest interest for analysis, and the number of elements used for each of these components is listed in Table 1

Table 1. Number of elements used in the ATLAS Generation II model

Component	# of Elements
Liner	5,002
Small Glide Plane	1,179
Lower Conductor Plate	1,155
Compression Ring	775
Large Glide Plane	774
Lower Ring Compressor	471
Total Elements	*9,356*

1.2.1 RESULTS-UPPER GLIDE PLANE/LINER INTERACTION

During the assembly process, a ring of bolts executes the small glide plane's upward motion and torque specifications are used to indicate the final axial position of the glide plane. A geometric interference created by a radially tapered liner ensures contact with this upper glide plane, which is essential for proper current flow from the glide plane into the liner. To simulate the glide plane's upward motion, a displacement was imposed on a node corresponding to the location of the bolt centerline. An additional, equivalent displacement was imposed on the top node located at the inner radius of this glide plane to prevent detrimental rotation in the FEA model. The locations of these displacement vectors are shown in Figure 3, and the magnitude of these displacements was such that the final axial position of the glide plane mimicked that of the actual assembly. A plot of the radial stress contour for this region can be seen in Figure 4. Note the highly localized stress concentration, which coincides with the relatively small region of radial interference between the two components. Also note the equilibrium of the stress distribution between the two components near this interface.

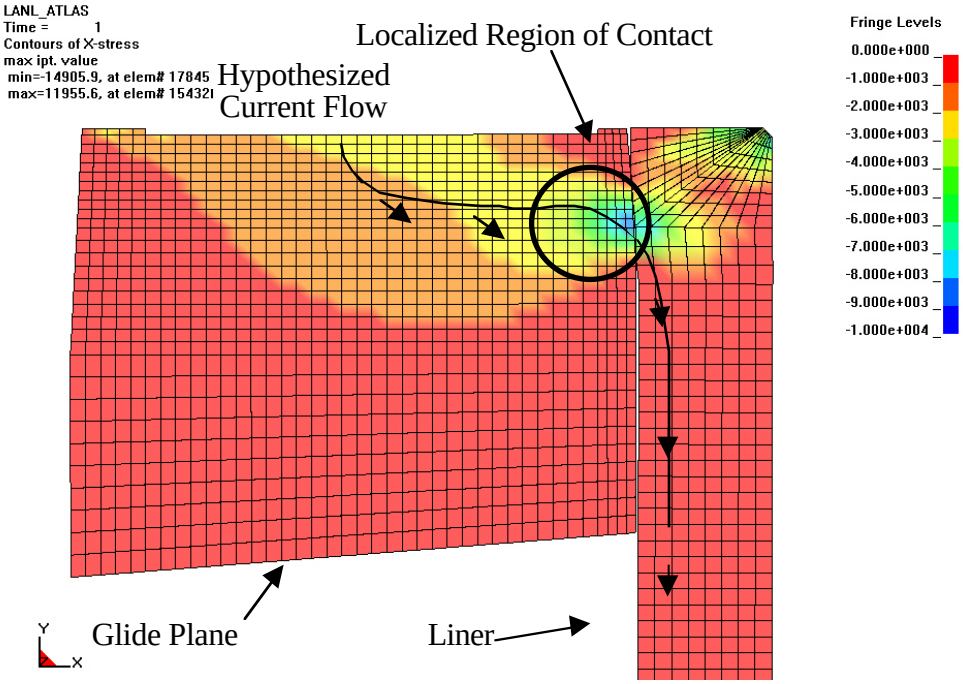

Figure 4. Radial stress (x-stress) of liner/glide plane interface for ATLAS Generation II

The maximum radial stress is approximately 9,500psi. The hoop stresses have similar distribution. This suggests a maximum hoop stress of approximately 7,700psi. Therefore, some localized yielding occurs in the 1100 aluminum liner, but not in the mating glide plane.

1.2.2 RESULTS-COMPRESSION RING/LINER INTERACTION

During these pulsed-power experiments, the current flows from the top glide plane to the liner, and exits the liner via the compression ring. The integrity of the contact between the compression ring and the liner is contingent on the action of the lower ring compressor. A sharp tooth located on the ring compressor acts as a mechanism to distort the compression ring, thus forcing contact with the adjacent liner. A contour plot of the radial stress is shown in Figure 5. The stress distribution and magnitude in the radial direction were used to gauge the contact integrity of the compression ring's y-faces (interfaces ① and ②), whereas the axial stress distribution and magnitude were used to gauge contact of the ring's x-face (interface ③).

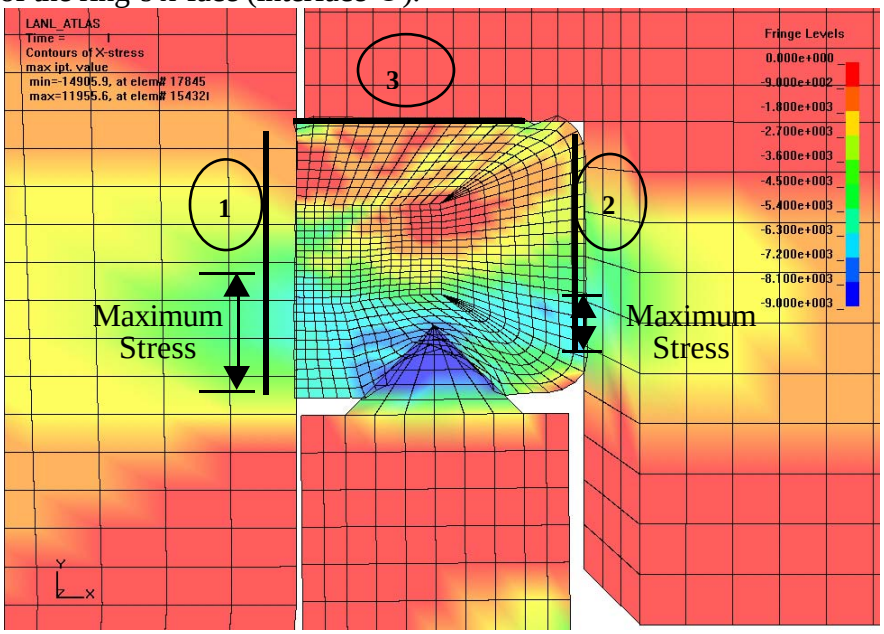

Figure 5. Radial stress (x-stress) in the compression ring for ATLAS Generation II

The stress level in the y-faces of the compression ring is a maximum at the regions near the tooth of the ring compressor. Moving in the positive y-direction along these same faces yields smaller radial stresses. Such a trend suggests a tapered compression ring, which indeed coincides with the shape of the ring compressor's tooth. It is clear that the tooth directly affects the stress levels along each interface, and therefore alternative shapes for this feature were investigated. Since current flows through each of these three interfaces as illustrated in Figure 4, it is important to maximize the level of contact in these regions. By altering the shape of this tooth and investigating the average stress x-stress along interface ① and ②, and the average y-stress along interface ③, it can be determined which geometry changes should be made. This investigation could be used to possibly enhance the effectiveness of these pulsed-power experiments.

Three new geometries of the lower ring compressor were modeled for the purpose of investigating which models, if any, improved contact on the three pertinent interfaces of the compression ring.

These geometries included a sharper, narrower tooth (Redesign #1); a tooth with a flat top surface (Redesign #2); and a shorter, wider tooth (Redesign #3). They are shown in Figure 6.

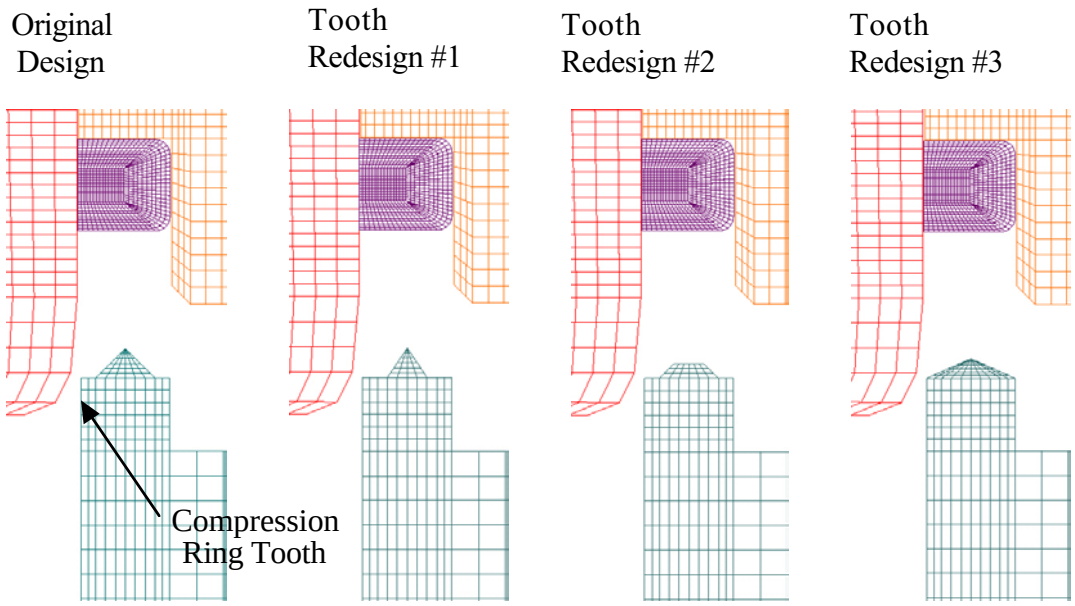

Figure 6. Design changes suggested for the ring compressor's tooth geometry

The average normal stress values along each interface was determined for comparison. Average radial stress (x-stress) was calculated for the inner and outer vertical faces of the compression ring, and average axial stress (y-stress) was calculated for the top, horizontal surface. A larger average stress over a given interface would suggest enhanced contact with the mating component on that particular surface. Stresses of the different designs in comparison to values obtained from the original geometry are summarized in Table 2.

Table 2. Average stress magnitudes of compression ring elements on each interface

	Radial Stress (inner)	**Radial Stress (outer)**	**Axial Stress (top)**
Original Design	-3300 psi	-2850 psi	-4500 psi
Redesign #1	-3500 psi	-3000 psi	-4050 psi
Redesign #2	-2900 psi	-2700 psi	-4150 psi
Redesign #3	-2050 psi	-1850 psi	-4250 psi

Whereas the average stress magnitude is quantifiable, it is difficult to quantify the actual level of contact for each interface. The stress levels between each design do not considerably fluctuate, but they do indeed vary. This suggests that the tooth geometry does affect the compression ring interfaces to some extent. Determining which interface integrities are of utmost importance would be vital to determining which redesign, if any, should be implemented in ATLAS Generation II.

Regardless, finite element analysis provides the opportunity to further explore alternative geometric designs without the concerns associated with actual testing.

1.2.3 COMPOSITE LINERS

Composite liners, i.e. liners composed of two dissimilar materials, have been proposed for use in certain experiments. These liners consist of inner and outer thin-walled cylinders that are press fit together, though cooling is sometimes used to assist the assembly process. The motivation behind the use of composite liners comes from the machining process. Problems can arise when machining thin-walled cylinders, with vibration often encountered during the final tool passes. The current fabrication process for composite liners is such that the inner cylinder wall thickness is much greater during the initial assembly process than the required final dimension, which may also be true for the outer cylinder. The proposed configuration contains an outer cylinder composed of 1100 aluminum with an inner cylinder composed of copper, tantalum, stainless steel, or 6061 aluminum (Figure 7). For assembly, a nominal slip fit exists between the mating cylinders over most of their length. The OD of the inner cylinder is machined oversize at one end in order to form a tight joint. This is also the case with the ID of the outer cylinder on the opposite end. Upon completion of this initial machining process, the two components are slipped together using a minimal press force over the final few millimeters of insertion. The ID of the inner component and the OD of the outer component can then be machined with fewer complications, as the press fit joint carries much of the torque induced by the machining process. The final liner product can then be assembled with the glide planes via a shrink fit, as previously described in this thesis.

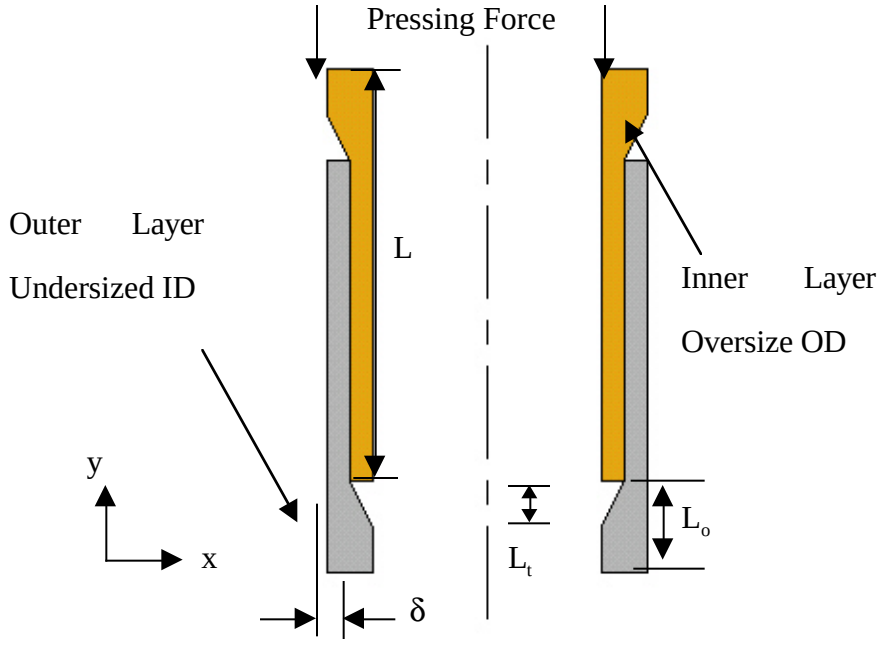

Figure 7. Schematic of a composite liner, shown in configuration just prior to lockup

There were several questions that arose when considering the use of composite liners. Such concerns included: the shape of the transition region and its effect on the contact interface between the two mating components, tradeoffs between press fits and thermal shrink fits, and prevention of yielding with the use of desirable geometric dimensions.

Composite Liner Geometry Effects

There are three main parameters that can be varied in geometry of the composite liners: the overall length of the transition region L_o, the length of the taper within the transition region L_t, and the radial interference δ that is created by this taper. Each of these parameters was expected to affect the results of interest, and the geometric representations can be seen in Figure 7. To investigate the effects of these varying parameters, LS-DYNA was utilized once again. Axisymmetric models were composed of 8 elements through the thickness of each mating cylinder, thus providing 16 elements through the thickness of the assembled composite liner. Copper and 1100 aluminum were used as the materials for the inner and outer components, respectively. The nodes along the horizontal boundary at the bottom end of the outer cylinder were constrained in the y-direction, allowing for radial displacement only. The nodes along the horizontal boundary at the top of the inner cylinder were subjected to nodal displacements specified in the negative y-direction, which mimicked the pressing action. The displacement occurred over the entire simulation using 100 implicit time steps, and the magnitude of the displacement was such that the cylinder ends were perfectly aligned at the conclusion of the simulation. The moving inner cylinder was also able to deflect in the radial direction, as it was not constrained in any way. Thermal cooling was initially *not* used. It was decided that cooling would only be used if problems arose during the simulation due to excessive interference or sudden surface directional changes that were too extreme to model (i.e., a very short taper length).

The assembled length L was a constant 51.445mm (2.0254in), similar to the ATLAS Generation I liner length. The inner component had a constant ID of 97.409mm and the outer component had an OD of 100.000mm. The thickness of each component was equal to a constant 0.645mm in the slip fit sections. The overall length of the transition shape L_o was established at ~7.5mm and also remained constant. Prior to this analysis, very few guidelines for the dimensional range for each of the varied parameters were provided; hence 0.0008in (20.32μm) was chosen as the baseline interference value δ. This value closely matched the interference value of ~15μm for the liner/glide plane interface in the ATLAS Generation I design. The design analysis began by first altering the taper length. For the selected interference value, five models of varying taper length were generated. A schematic of this shape variation is shown in Figure 8.

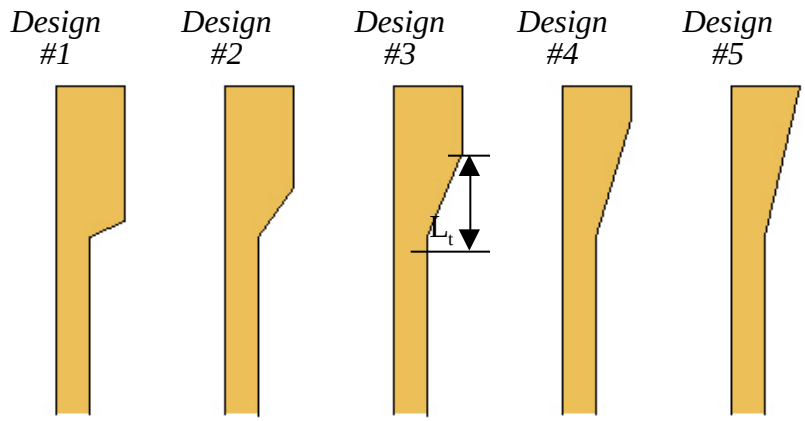

Figure 8. Schematic of a composite cylinder transition shape variation

Radial Gap Analysis

The interfaces of each of the assembled composite liner designs were first investigated. Gaps between the mating components were deemed undesirable, as they would obviously limit contact and therefore lower the integrity of the press fit. To do this, final x- and y-coordinate locations of the nodes along the interface (along the inner cylinder OD and the outer cylinder ID) were plotted for the final time step in the simulation, which represented the state of completed assembly. Plots for three of these designs are shown in Figure 9.

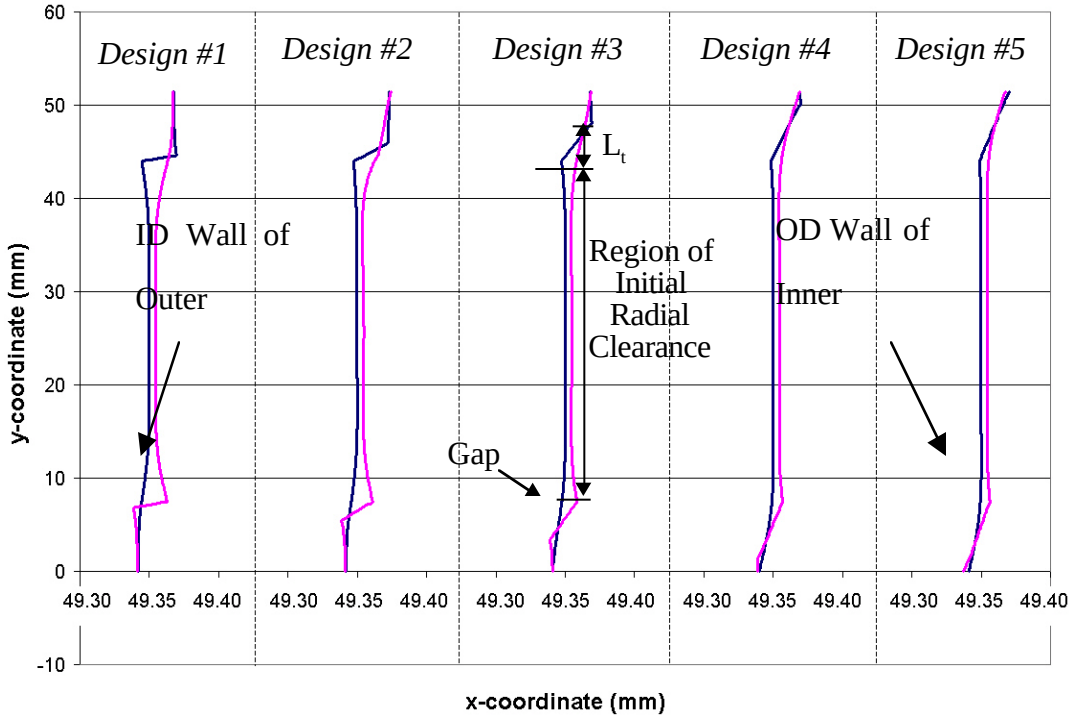

Figure 9. Nodal coordinate locations after composite liner assembly for nodes falling along press fit interface (δ = 0.0008in, 20.32μm)

Similar to an actual composite liner, the LS-DYNA model included an initial radial clearance (5μm) between the inner and outer cylinder walls. This clearance existed in the region between the transition shapes located at either end, which is somewhat evident in the plots in Figure 9. It is clear from these plots that with a shorter taper length L_t comes a larger gap. To quantify this, the maximum radial distance between the inner and outer components was determined. This maximum separation was consistently located at the point where the radial taper begins, when moving from the cylinder's mid-length position towards the free end. These gap sizes are summarized in Table 3.

Table 3. Maximum radial separation between inner and outer cylinders in a composite liner (δ = 0.0008in, 20.32μm)

	Design Number				
	#1	**#2**	**#3**	**#4**	**#5**
Gap Size	20.1μm	15.0μm	12.5μm	7.6μm	5.0μm

The results are indeed intuitively sound. A more gradual taper allows for the mating cylinders to remain in contact over a greater percentage of the overall length, thus reducing the gap size. Such a reduction in gap provides a stronger composite liner that can carry more torque induced by the final machining of both components.

1.3 CONCLUSIONS

Finite element analysis of the Atlas Generation II liner/glide plane system has been carried out successfully. The focus of the analysis was on the stress distribution in the vicinity of the upper glide plane/liner joint and on the stress and deformation distribution in the vicinity of the compression ring/liner joint. Results were also generated to gain an understanding of the response of a proposed composite liner.

2 CHARACTERIZING SCRIBING BEHAVIOR ON SINGLE CRYSTAL SILICON AND THE EFFECT OF HIGH PRESSURE PHASE TRANSFORMATION

Travis Randall
Graduate Student
Dr. Ron Scattergood
Professor
Materials Science and Engineering

With the appropriate conditions, a diamond tip can produce scribes on single crystal silicon that are ductile in nature due to a brittle-to-ductile transformation of the material beneath the scribe. This anomalous plastic flow has been attributed to a high-pressure phase transformation from diamond cubic (dc) to a metallic β-tin phase. The residual stresses within the scribe traces that result from the elastic-plastic constraint of the displaced material create a bending distortion in a flat-plate geometry wafer sample. The deflection is measured and extracted using optical interferometery techniques and will be correlated to the residual stresses created using a bend effect model developed for previous scribing research. SEM and AFM characterization is used to aid understanding of the material removal. Raman will be used to study the nature of the material within the scribe region and will indicate whether the hypothesized transformation has occurred. The effects of tool geometry and loading, as well crystallographic orientation and direction of the wafer are tested.

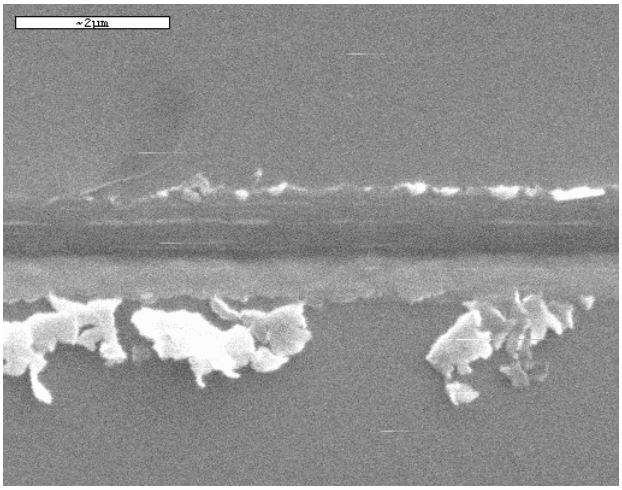

2.1 INTRODUCTION

This investigation is part an NSF-sponsored research program aimed at characterizing the effects of high-pressure phase transformations of silicon, germanium, and silicon nitride during manufacturing processes such as slicing, grinding, or diamond turning. Silicon, a normally brittle material, is subject to subsurface fracture damage associated with material removal processes that reduces part quality and lifetime. Extensive research has shown that under the intense pressure of diamond indenters and other tool tips, silicon will undergo a phase transformation from its brittle diamond cubic (dc) phase to a metallic β-tin phase and exhibit plastic flow. [1] It can certainly be argued that exploitation of this atypical plastic behavior could be used to improve machinability of this material. It is hoped that better understanding of the mechanics of the transformation can be used to improve the manufacturing processes to produce devices at lower cost and higher quality.

The scope of this investigation is the study of the stresses generated within scribe grooves of single crystal silicon to better understand the nature of material removal during machining. Scribing tests act to model the grinding and polishing process by replicating the material deformation behavior of an individual grinding or polishing particle. Residual stresses are the result of the elastic-plastic constraint of the deformed and displaced material. As the material is released from load it acts to push on the elastic half-space of the surrounding material. If the scribes are placed on one face of a thin plate of Si, the difference in stress states on the opposing faces creates a bending distortion. This bending distortion can be used to corroborate the residual stress model that has tensile dipole forces to predict the bend effect. [2]

During the investigation, scribing data was obtained for various directions on (100) and (111) crystallographic planes of silicon. The effects of loading and tip geometry are also considered. Scribes are studied with scanning electron microscopy to determine the nature of material removal within the scribe trace and to observe the fracture behavior/plastic deformation in relation to crystallography. Atomic Force Microscopy allows for depth of cut measurements as well as reinforces SEM study. Raman spectroscopy will be used to identify differences in structure between the untouched silicon and that within the scribe. It is hoped that either crystalline or amorphous phases of silicon that are indicative of β-tin phase transformation can be identified within the transformation zone. What is not known however is the role of high pressure phase transformation (HPPT) in the generation of residual stress.

2.2 DETAILS OF THE PROJECT

The initial stages of this investigation entail collecting bend data as well as Raman measurements for (100) and (111) crystallographic orientations of silicon. Scribing along the <100> and <110> will be studied for the (100) orientation. <110> and <112> directions will be studied for the

(111) orientation. Various loads with in the ductile range and extending into the fracture region are tested for two different geometries of tip interaction with the surface.

2.2.1 EXPERIMENTAL SETUP

Scribing

A Zwick micro hardness tester is fitted with a Dynatex diamond tip (Figure 1(a)) in a custom holder as pictured in Figure 1(b.) To produce a scribe, the sample is translated under the diamond tip such that either the cutting edge or table is oriented in the scribe direction, depending on the desired tip geometry. The samples are held firmly in place between two metal slides mounted to a custom stage. This motorized stage is used to create translation at a constant rate of 0.250 mm per second. Samples are scribed at various loads ranging from 20-250 mN. Multiple, evenly spaced (50-100 μm) scribes are placed on the surface to generate measurable deflection (the effects of multiple scribes are additive to the bend) and to produce a more statistically significant measurement than that of a single scribe.

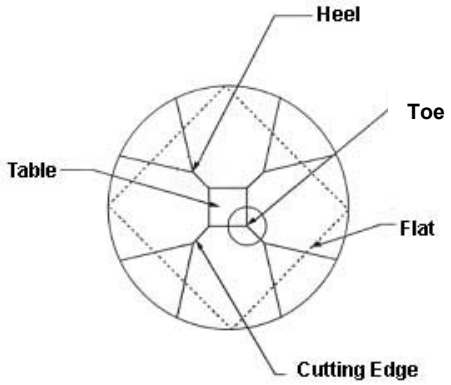

Figure 1(a.) Dynatex Tip [2]

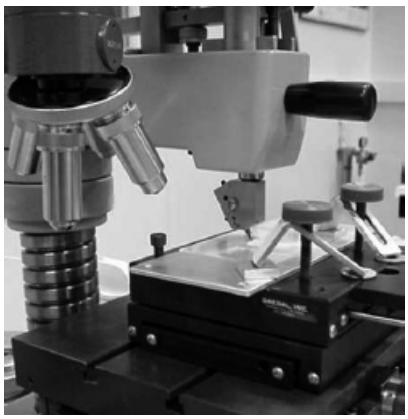

Figure 1(b.) Picture of scribing setup [2]

A tool holder was designed to hold the cutting edge of the diamond tip at an angle of 3.3 degrees from the sample surface as shown in Figure 2(a.) Figure 2(b.) is an SEM image of the area enclosed in the circle in Figure 2(a.) The tip orientation allows for two different geometric interactions with the surface depending on which way the stage is translated. Translating in one direction creates a ploughing action of the table into the surface, which is nominally termed "blunt" cutting. Translating in the opposite direction creates a slicing action of the cutting edge, which is nominally termed "sharp" cutting. The two different geometric interactions create vastly different responses in the material.

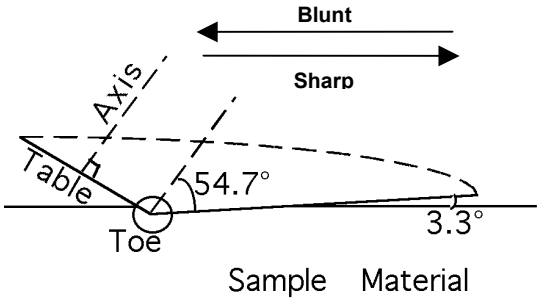

Figure 2(a.) Geometry of tip to sample surface [2]

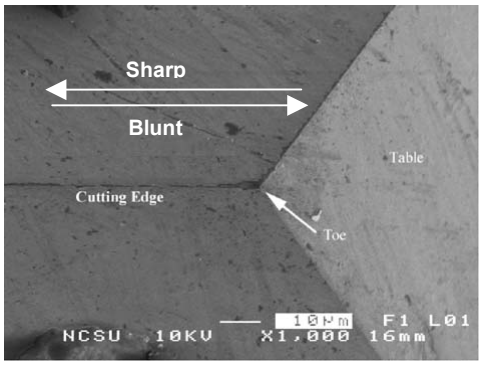

Figure 2(b.) SEM of area encircled in Fig. 1a

Interferometric Analysis

Topographic data is collected for an as-received 1cm x 2cm x 525 μm Si sample using a Zygo GPI Laser interferometer pictured in Figure 3. The sample is measured again using the interferometer after scribing.

Figure 3. Image of Zygo GPI Laser interferometer

MetroPro, the software suite used to analyze the interferometer data, allows the user to subtract the data collected before scribing from that collected after scribing. The resulting profile created is the net bending effect. The data collected from the Zygo is then converted with a utility to an ASCII format. The Y and Z data for an X approximated as the center of the long axis is then used to create a plot of the bend profile. Microsoft Excel is used to graph these values. The generated plot is then used to approximate the angle of deflection from the initial state. The deflection angle data is then correlated to the residual stresses created by scribing using a bend effect model.

Characterization

Raman Spectroscopy Characterization of the scribe/indent region was accomplished with Micro-Raman spectroscopy done at room temperature using an ISA U-1000 scanning monochromator. Raman excitation was done with the 514.5 nm line of an Argon-ion laser, with a spot size of approximately 3 to 4 μm in diameter. An Olympus BH-2 optical microscope produced laser focus. Raman spectra were taken in the 200-600 cm^{-1} range, which contains the characteristic peaks normally associated with crystalline, amorphous, and various metastable crystalline phases seen in other research. A spectral resolution of ≈ 4 cm^{-1} was utilized, and the laser power was ≈ 5 mW.

Scanning Electron Microscopy SEM was carried out using a Hitachi S-3200N is a Scanning Electron Microscope operating at 20 keV at varied working distances. The Everhart-Thornley detector was used for topographic imaging of the scribes. Digital image capture was done using NIH Image collection.

Atomic Force Microscopy AFM was done with a VISTA-100 Scanning Probe Microscope. A low stiffness cantilever was used to perform contact mode measurements of the sample surface. Image studio 3.0 was used to capture images as well as interpret data.

2.2.2 ANALYTICAL APPROACH

Measurement of Bend Deflection

A 3-D oblique plot as shown in Figure 4 as generated by MetroPro represents the bend profile. The data is then converted to a line plot format with a conversion utility. An X is selected that is estimated to be the center of the long axis. The Y and Z data for that X is used to generate a 2-D profile in which the flat portions of the profile can be fit to lines and the angle of the deflection from the flat position can be calculated. Figure 5 illustrates an example of a 2-D bend profile generated with fitted lines.

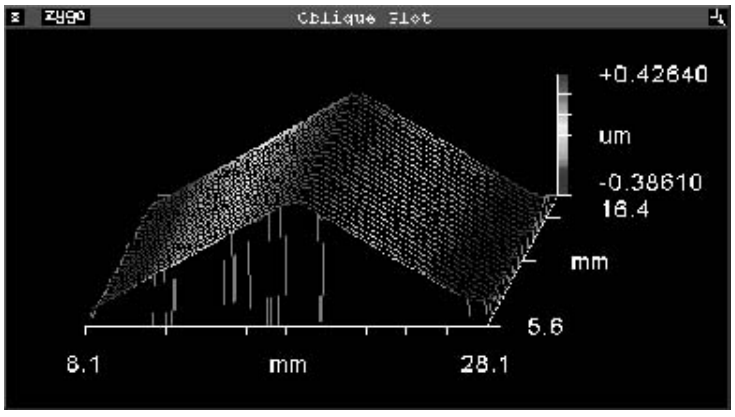

Figure 4. Oblique plot of bend angle effect generated in Metropro.

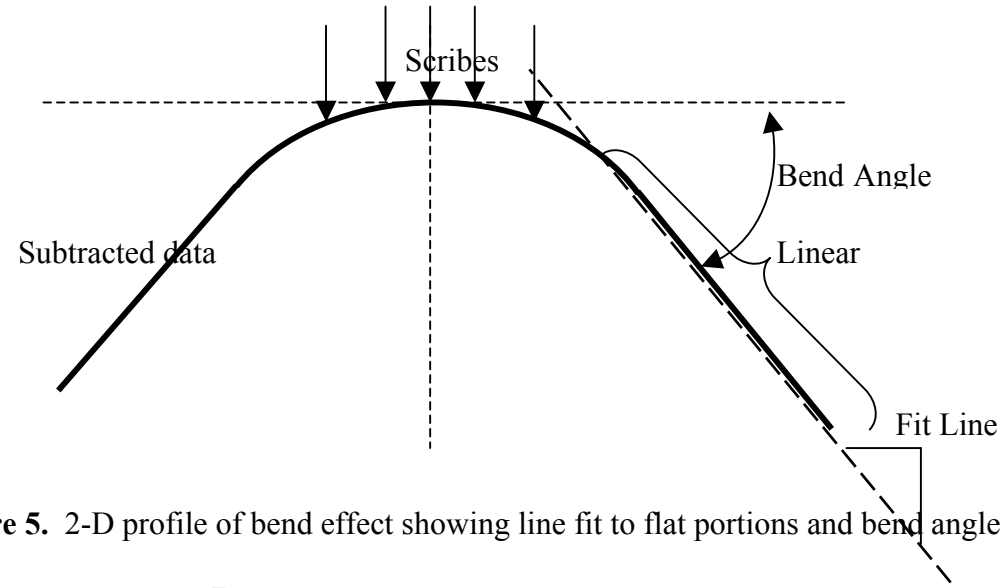

Figure 5. 2-D profile of bend effect showing line fit to flat portions and bend angle [2].

2.2.3 EXPERIMENTAL RESULTS

Scribing Behavior

Tip Geometry Effects Figures 6 a, b and c show SEM images of the three general material responses seen due to scribing with the Dynatex tip. Figures 6a and 6 are of ductile cuts generating no debris and debris, respectively. Figure 6c displays the third response, fracture. It is important at this point to distinguish between a purely ductile and the combination of ductile /elastic fracture as a response to scribing. Each sample was viewed under an optical microscope to make an initial observation on material removal processes. If no chipping is present along the scribe traces, it is reasoned that the material removal is mostly by plastic mechanisms. If chipping is apparent, it is reasoned that the material removal is influenced by elastic fracture mechanisms, and that the plastically deformed material will be removed in the process.

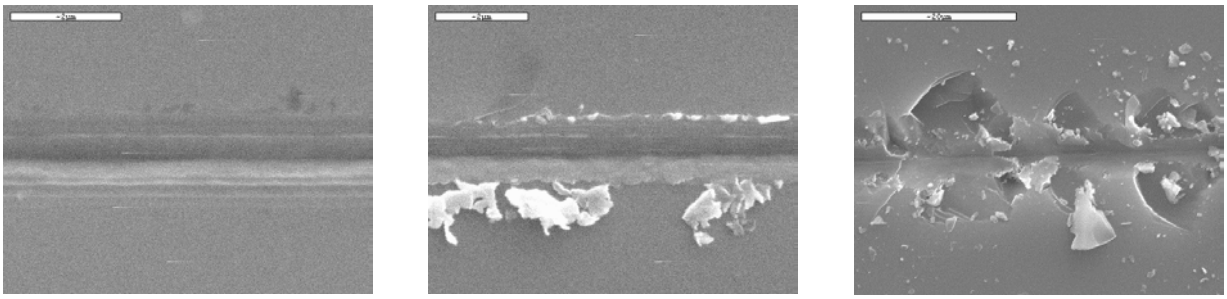

a. Ductile (no debris)
Sharp (ductile regime)

b. Ductile (plastic debris)
Blunt (ductile regime)

c. Fracture
Either (above fracture threshold)

Figure 6. General material responses to scribing with Dynatex Tip

Ductile responses shown in Figure 6(a.) and (b.) were seen when scribing **within the ductile regime** for a particular direction. The "ductile-no debris" response seen in Figure 6(a.) was created by translating the stage to cause the sharp geometry interaction while translation in the blunt geometry direction would elicit the "ductile-plastic debris" response in Figure 6(b.). Figure 6(c.) is a generic fracture response (fracture pattern depends on geometry and crystallographic orientation and will not be discussed) created by either geometry when scribing above a particular direction's fracture threshold.

AFM imaging afforded a look at the profile of a scribe to determine shape and depth of cut. Figures 7(a.) and (b.) show profiles within the ductile regime of blunt and sharp scribes, respectively, made on a (100) wafer, scribing in the [100] direction. Additionally, as the load applied to the tip increased, the depth of cut also increased until the fracture threshold was achieved.

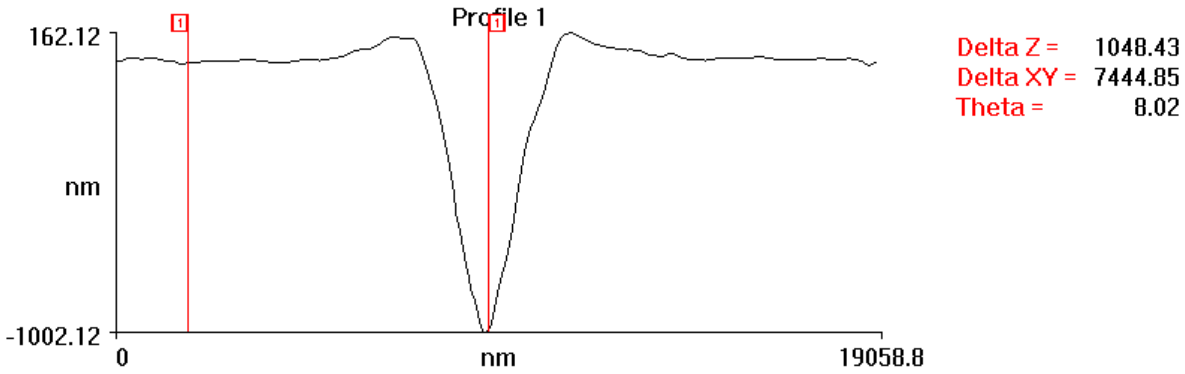

Figure 7(a.) AFM profile of blunt scribe on (100) in [100] direction in ductile regime.

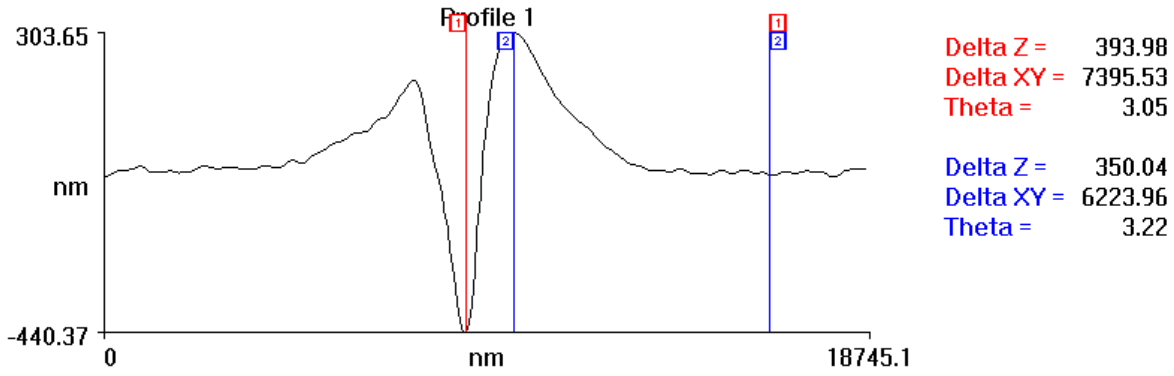

Figure 7(b.) AFM profile of sharp scribe on (100) in [100] direction in ductile regime.

Within the ductile regime for a particular direction, cuts made with the blunt interaction created scribes that where deeper than those made with the sharp interaction. This was true for all cutting

directions tested within the ductile regime. The difference in the depth of cut could be due to two things. First, the area of contact of the tool in the material is much smaller for the blunt interaction than it is for the sharp interaction. This creates a larger pressure for a given normal load, resulting in a deeper penetration of the tool into the material. Secondly, it is thought that within this regime, blunt cutting tends to remove more of the plastically created material resulting in a greater depth of cut as well as the presence of debris. The absence of debris and shallower depths of cut during sharp cutting indicates little removal of the plastic material, but rather a displacement of that material into the surrounding elastic matrix. The sharp interaction also seemed to create larger pile-ups on the edges of the scribe, as well.

Crystallographic Orientation/Scribing Direction Effects For ease of explanation, it is important at this point to distinguish between a good cutting direction and a poor cutting direction. A good cutting direction for a given tip geometry is that which creates ductile cutting with no fracture through a range of loads that is larger than the other possible directions. In other words, a good cutting direction will exhibit a larger fracture threshold than a bad cutting direction. On the other hand, a poor cutting direction will create fracture at a relatively low loads rather than a ductile response.

At low loading, for each cutting direction tested a given tip geometry will elicit a ductile response. As load is slowly increased a threshold will occur and fracture will initiate. (Threshold occurs at a much lower load with a freshly sharpened tip.) The initiation point is dependent on cutting direction and either tip will produce a different response.

For example, given a (100) Si wafer, scribing with the blunt geometry interaction would create good cutting in the [100] direction, and bad cutting in the [011] direction. Oppositely, scribing with the sharp geometry interaction would reverse the response making [011] a better cutting direction than [100].

A similar effect was noted in a (111) wafer; the blunt geometric interaction gave the opposite cutting behavior than that of the sharp. Tables 1 and 2 summarize the general cutting behavior as a function of direction and tip geometry on (100) and (111), respectively.

Table 1. Cutting behavior for (100) wafer

	Blunt	Sharp
[100]	Good	Poor
[011]	Poor	Good

Table 2. Cutting behavior for (111) wafter

	Blunt	Sharp
[1-10]	Good	Poor
[-1-12]	Poor	Good
[11-2]	Poor	Good

The good/bad behavior for blunt cutting seems to match up well with directional dependencies seen in diamond turning work [3,4]. Figures 8(a.) and (b.) are schematics of (100) and (111) wafer faces, respectively. As the wafer was turned using conditions close to the fracture

threshold for the poor direction, a cross pattern on the face could be seen (pitting creates cloudiness on the reflective surface, while ductile regions are reflective.) The white regions are those where purely ductile cutting was achieved (good cutting direction) and the dark regions indicate areas of pitting fracture (poor cutting direction.) The directional dependency seems to sync up with the blunt cutting and be opposite of the sharp cutting.

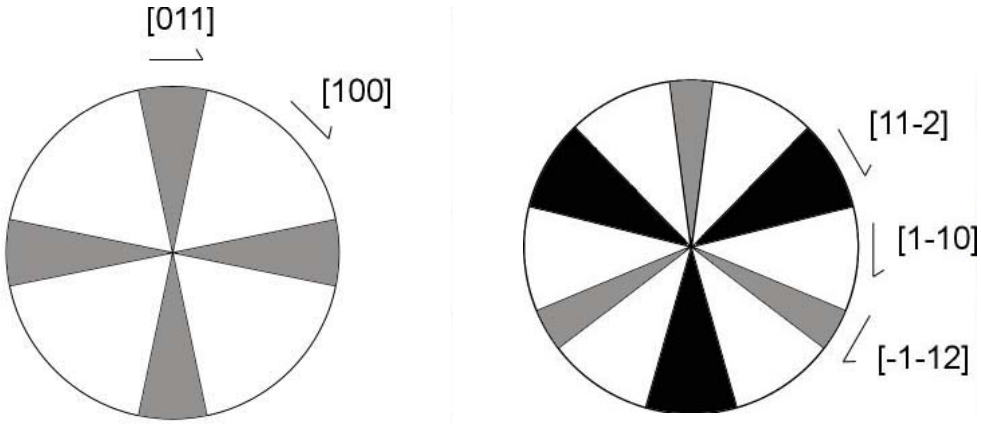

Figure 8(a.) and (b.) Diagram of (100) and (111), respectively, diamond turned wafer. The white regions indicate areas of ductile cutting while the gray and black regions indicate areas of mild and extreme pitting, respectively.

Residual Stress Generation

As a scribe is created within the ductile regime the plastic material is either removed (debris) or displaced into the surrounding elastic material. The plastically displaced material, whether driven by the β-tin metallic phase or not, is pushed by the tip into the surrounding elastic material. This creates residual stress, which generates the deflection in the sample geometry. This stress is due to the elastic-plastic constraint associated with the deformed material that is displaced from the scribe region. Figure 9 depicts the expansion of the constrained plastic zone, creating the resulting distortion of a flat wafer due to the difference in stress states between the two wafer faces. [2]

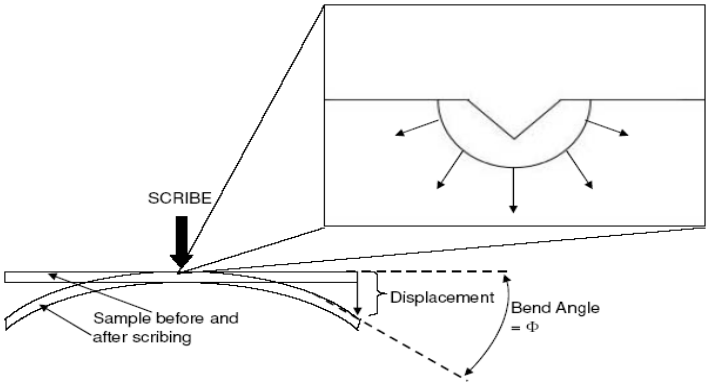

Figure 9. Illustration of expansion of constrained plastic zone and resulting deflection.

Figures 10 and 11 show deflection data and the corresponding optical micrographs of scribes made at various loads for the [1-10] and [-1-12] directions, respectively, on a (111) wafer. Both blunt and sharp geometries were tested. The two general cases of behavior seen for all the directions tested can be seen in the two directions presented in Figures 10 and 11. The first case (Figure 10) exhibited what was termed good cutting with the blunt geometry and poor cutting with the sharp geometry, as seen in scribing in the [1-10] direction. The second case (Figure 11) exhibited the opposite behavior in which the blunt geometry created poor cutting while the sharp direction created good cutting, as seen in scribing in the [-1-12] direction.

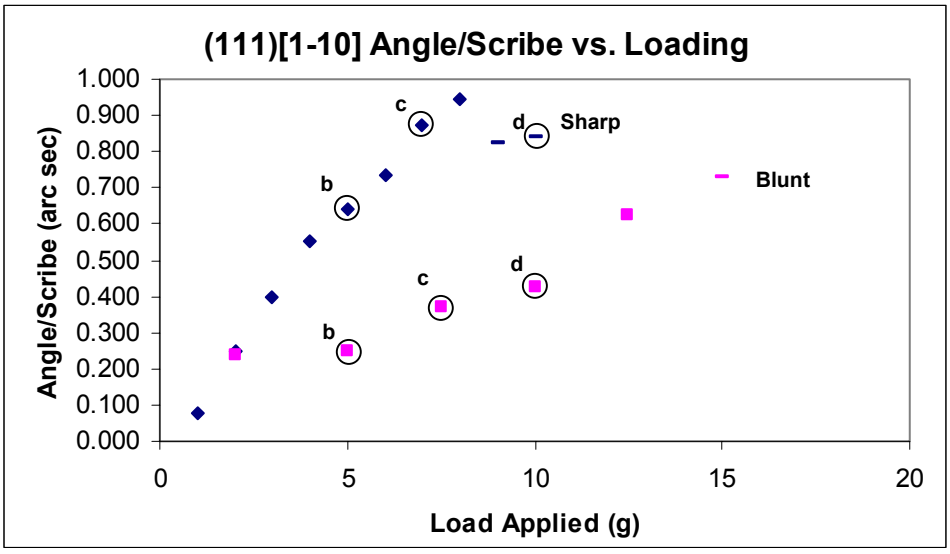

a. Angle/Scribe vs. Load Applied

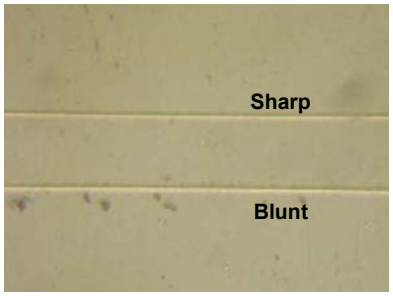

b. Sharp- Ductile
Blunt-Ductile

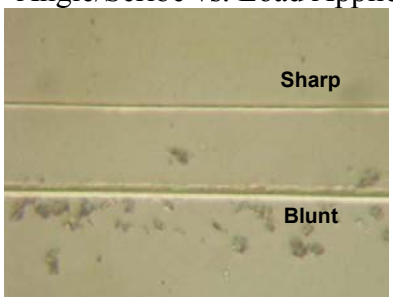

c. Sharp- Ductile
Blunt- Ductile

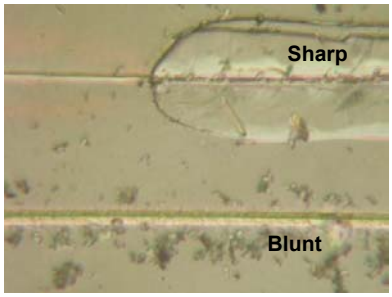

d. Sharp-Fracture
Blunt-Ductile

Figure 10. (a) Deflection vs. Load for (111)[1-10]. Sharp and Blunt cutting geometries are indicated on the graph. (b-d.) Optical micrographs corresponding to those circled and lettered on the graph.

Figure 10a is a plot of the angle/scribe vs. load applied for scribes cut in [1-10] on (111). A higher angle/scribe indicates the presence of higher residual stress within the scribe region. (The bend effect model has not been used to quantify the value yet.) Until a fracture threshold point is reached, cuts appeared to remain purely ductile (as indicated by a diamond or box.) Dashed lines on the plot indicate the presence of fracture under optical microscopy. Both sharp and

blunt geometries are indicated on the graph. The letters on each plot (b,c and d) correspond to the micrographs in figures 10(b.), (c.), and (d.), where a comparison is made of the two geometries. For this direction, sharp cutting produced good ductile cuts until a load of 9 grams was applied. Within the ductile region, the bend/angle increased linearly with load applied. This indicates that increasing the load applied increased the amount of residual stress within the scribe trace. At the onset of fracture, the behavior deviated from linear, and the bend/angle dropped considerably. Because fracture alleviates some of the residual stress accumulated in the scribe region, the deflection amount decreases. Blunt cutting produced good ductile cuts, with the onset of small amounts of fracture at 15 g applied load. The debris seen in each of the micrographs was created by blunt cutting only, and appeared ductile in nature.

The residual stress as indicated by the angle/scribe is considerably lower for blunt cutting than it is for sharp in the range tested. This is perhaps due to the amount of plastic material constrained within the scribe region. Observations of the presence/absence of debris and depth of cut measurements may be indications of this. The observations support the idea that for blunt cutting, the plastic material is predominantly removed, creating less residual stress than seen in sharp cutting, where the material is thought to be displaced into and constrained by the elastic material, creating large residual stresses. Similar behavior was noted for [100] cutting on a (100) wafer but will not be presented here.

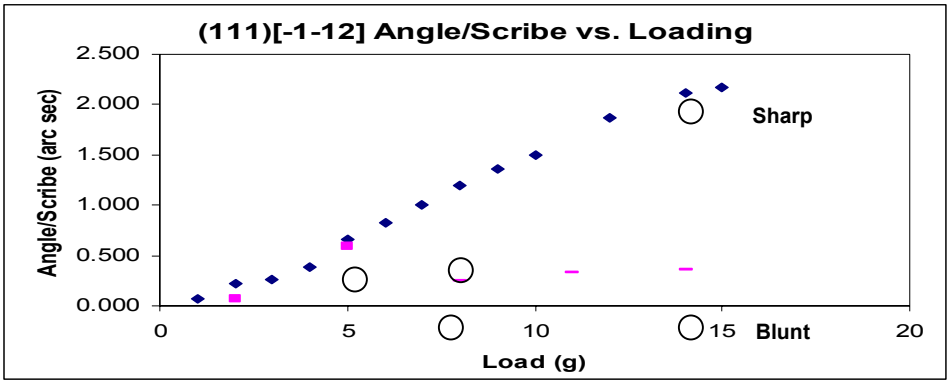

a. Angle/Scribe vs. Load Applied

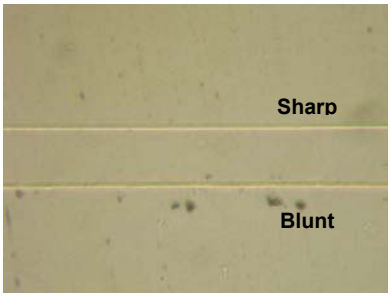

b. Sharp- Ductile
Blunt-Ductile

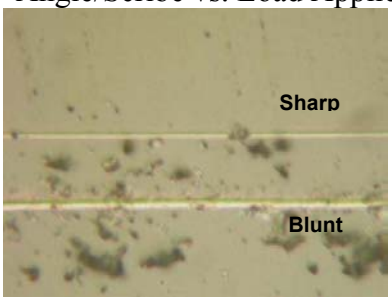

c. Sharp- Ductile
Blunt- Fracture

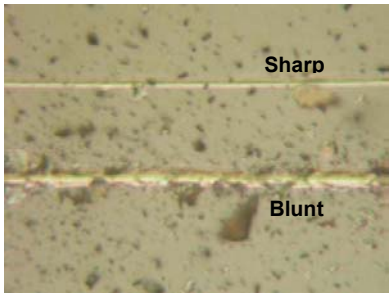

d. Sharp- Ductile
Blunt- Fracture

Figure 11. (a) Deflection vs. Load for (111)[-1-12]. Sharp and Blunt cutting geometries are indicated on the graph. (b-d.) Optical micrographs corresponding to those circled and lettered on the graph.

Figure 11(a.) is a plot of the angle/scribe vs. load applied for scribes cut in [-1-12] on (111) . The letters on each plot (b,c and d) correspond to the micrographs in figures 11(b.), (c.), and (d.), where a comparison is made of the two geometries. For this direction, sharp cutting produced good ductile cuts through the load range tested (onset occurred around 20 g applied load). Again, within the ductile region, the bend/angle increased linearly with load applied. This indicates that increasing the load applied increased the amount of residual stress within the scribe trace. Blunt cutting produced ductile cuts at low loads, but rapidly saw the onset of heavy fracture damage at loads above 5 grams. The debris seen in each of the micrographs was created by blunt cutting only, and appeared as fracture chips, rather than plastic in nature. The residual stress as indicated by the angle/scribe is considerably lower for blunt cutting than it is for sharp in the range tested. Fracture alleviates the residual stress induced by the scribing operation, producing relatively no deflection in the sample. For sharp cutting the plastically generated material is displaced and constrained, leaving residual stress as indicated by the deflection generated [11-2] cutting on (111) wafers and [110] cutting on (100) wafers saw the same behavior, but will not be presented here.

Raman Measurements of Scribe Regions and Debris

Raman was performed on scribes with both geometries, displaying no apparent sign of peaks corresponding to the phases commonly seen after scratching tests. It is unknown to the authors why this has occurred. It could be possible that the phase transformation may not be occurring with the Dynatex tip due to the nature of the geometry tip and that the plastic displacement is by some other mechanism, for example, dislocations. The detection proficiency of the Raman unit may be responsible as well. The transformation zones are thought to be very small (on the order of a few hundred nanometers.) If the penetration depth of the laser is much greater than that of the depth transformation zone, or if the laser spot size is large compared to the scribe width, the Raman spectra for the transformation product may not be detected. It is reasonable to make this conclusion, because at the very least, the nature of the material seen around in and around the scribe regions appears plastically generated. It is assumed that such material would be amorphous in nature, if not by a HPPT, then by extreme dislocation generation and motion by shear. Because no amorphization has been shown, it may be reasonable to assume that the Raman system cannot detect this small region. Sufficient data is not yet available to draw a conclusion for scribing experiments. Raman performed on debris created has not drawn any conclusions. Problems occur with sample heating that could be misinterpreted as the presence of nanocrystalline domains within and amorphous matrix.

2.3 CONCLUSIONS

2.3.1 SCRIBING BEHAVIOR

Scribing behavior as a dependency of load applied, cutting direction, and tool geometry was investigated. Both the (100) and (111) wafers exhibited ductile material generation for a range of loads on the order of a few grams. It was found that certain directions were less prone to fracture damage depending on the tool geometry. There were three types of material responses including ductile with material displacement, ductile with material removal, and fracture. Cutting into the surface with a sharp edge (sharp cutting) produced scribes in which the plastic material was condensed into the surface resulting in smaller depths of cuts and no apparent debris generation. The ploughing action of a flat triangular face (blunt cutting) in which plastically generated material was removed and left on the surface as debris produced a larger depth of cut. Both geometric interactions could create fracture depending on the cutting direction and the load applied. Cutting directions that exhibited ductile cutting through a large range of loads (good cutting) given a particular geometry would see the opposite response from the other geometry.

Additionally, the blunt geometry displayed the same crystallographic dependencies as previous diamond turning work. Cutting directions shown to be the most easily fractured directions (poor cutting) in diamond turning matched those created by the blunt geometry.

2.3.2 RESIDUAL STRESS GENERATION

Stress generation was related to the amount of distortion measured in a small section of wafer. Larger residual stress equates to a greater degree of bend. For scribes created in the ductile regime, deflection appeared to be a linear function of the load applied. This could imply that the constrained plastic zone may increase in size, or become denser with increased loading. Sharp cutting, which is thought to displace the plastic material in the surrounding matrix, generated higher residual stresses than that of blunt cutting, where the material is predominantly removed. This is thought to occur as the majority of the plastically generated material becomes constrained within the elastic matrix, generating greater stress. If the material is mostly removed by the operation, the remaining material is under less residual stress. The onset of fracture also decreased the amount of residual stress within the region as indicated by a drop in the bend angle.

2.3.3 RAMAN MEASUREMENT

Raman analysis has proven difficult for both the scribe region and debris analysis. There has been a lack of sufficient data that can attribute the plastic behavior to a high-pressure phase

transformation. At this point the authors will not comment on the mechanism for the anomalous plastic flow seen in the scribing experiments

2.4 FUTURE WORK

Stress Modeling At the current time stress modeling for directional dependencies of machining behavior as well as the bend effect model for quantification of residual stress is being undertaken. The models have not been developed extensively and will

Bend Effect Model A model shown in previous work [2] to accurately reflect the bend effect generated by the line- force dipoles created from a scribe will be used to characterize residual stress in the single crystal silicon. A line-force dipole, shown in Figure 12, will be used to model the elastic-plastic deformation zone along a scribe path. The dipole forces act outward from the scribe trace since the plastically deformed material region forces the surrounding elastic material outward after unloading. The line-force dipole model was extended from a model created by Yoffe [5] in which orthogonal dipole forces acting on an elastic half space describe residual forces left by indentation. The line-force dipole model is derived by the superposition of the dipole "blister" fields proposed by Yoffe. Standard elasticity solutions [6] are used to obtain the line-force dipole stresses for a limiting case of infinitesimal dipole spacing. By applying the line-force dipole stresses to a beam bending problem the stresses will be then be approximated as a function of loading and bend angle from prediction curves created in previous work.[2] The parameter derived from the bend effect model, force dipole strength is a direct measure of the magnitude of the residual stresses produced by scribing.

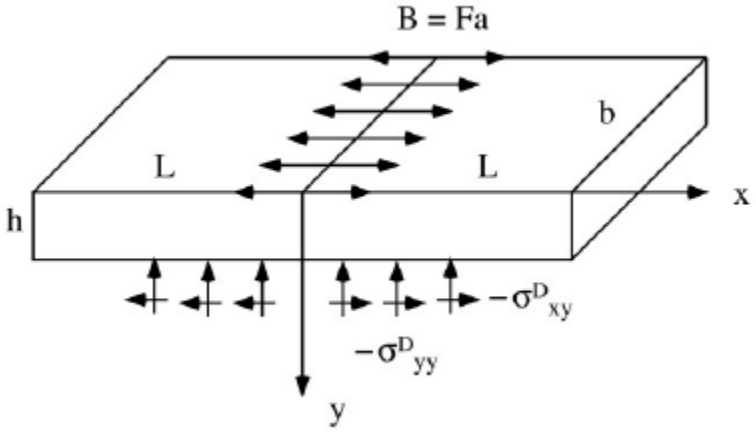

Figure 12. Line-force dipole model.

Crystallographic Dependency Models Models used in previous work [4] to explain the crystallographic dependency on the appearance of fracture during diamond turning are being modified to include explanation for the tip dependency demonstrated in this investigation. The original model predicts directions of easiest fracture using a point force which resolves tensile

stress on planes of high cleavage creating fracture. The current model will be adjusted for a different stress field which can better account for the tips geometry. Other crystallographic planes of easiest fracture are also being considered. Figure 13 shows a preliminary result of the modeling.

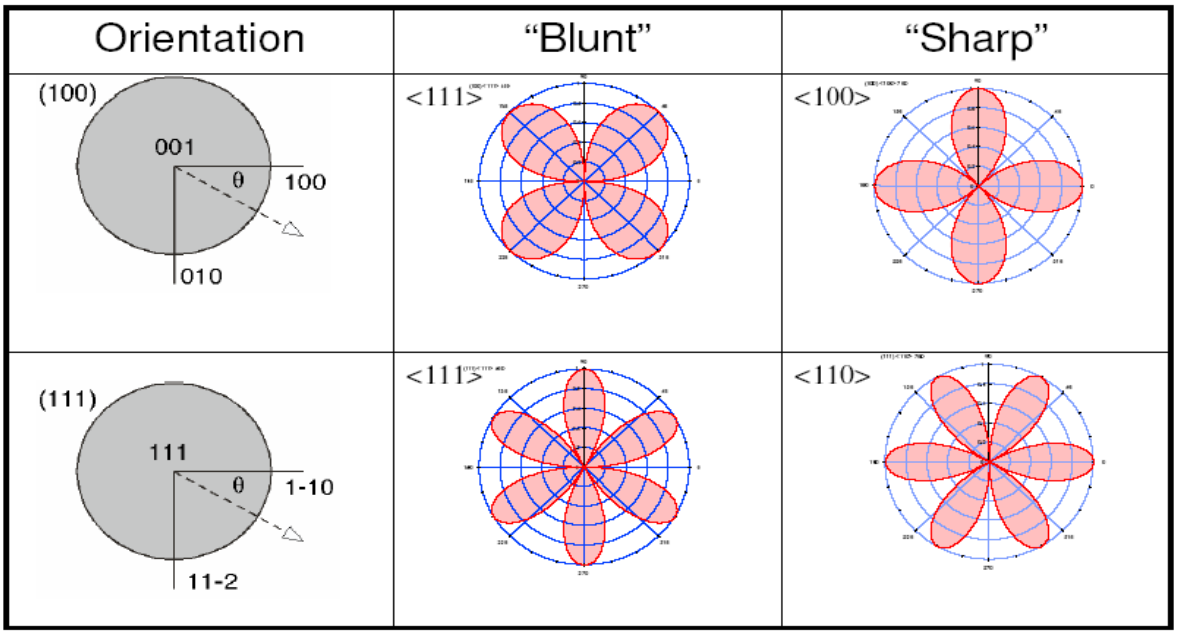

Figure 13. Stress modeling of scribing operation used to show directions of easiest fracture for blunt and sharp cutting.

The shade lobes in Figure 13 indicate directions of easiest fracture for both blunt and sharp cutting on both (100) and (111) wafers. The model is still in experimentation, but initially it is thought to match the behavior seen. The authors will not elaborate on the model or its validity as it is still preliminary modeling.

Diamond Turning Diamond Turning operations are currently under way to confirm past results of machining behavior as well as allow for Raman analysis of turned surfaces and debris. Dependencies on crystallographic orientation and cutting direction will be explored. Parameters found to be important such as tool rake angle and feed rate are being explored.

Scribing with DTM Axes Scribing will also be performed under penetration depth-controlled conditions using the DTM axes. Force measurements may also be taken to better understand the magnitude of forces creating the ductile behavior.

REFERENCES

1. Austin, B., M.S. Thesis, *Scribing of Brittle Materials*, North Carolina State University, 2000.
2. Blake, P., PhD Thesis, *Ductile-Regime Diamond Turning of Germanium and Silicon*, North Carolina State University, 1998.

3. Blackley, W.S. and R.O. Scattergood. “Crystal Orientation Dependence of Machining Damage- A Stress Model.” J. Amer. Cer. Soc. 73 [10] (1990) 3113
4. Domnich, V. and Y. Gogotsi. “Phase Transformations In Silicon Under Contact Loading”, Rev.Adv.Mater.Sci. 3 (2002) 1-36
5. Johnson, K. L., “Contact Mechanics”, Cambridge Univ. Press, p.17 (1985).
6. Yoffe, E. H., “ Elastic Stress Fields Caused by Indenting Brittle Materials”, Phil. Mag. A, vol. 46, no. 4, 617 (1982).

3 METROLOGY ARTIFACT DESIGN

Karalyn Folkert
Graduate Student
Dr. Thomas A. Dow
Professor
Department of Mechanical and Aerospace Engineering

The objective of this project is to develop a transfer standard to relate previous measurements using rotary contour gages with current measurements using CMMs. In the past, artifacts have been developed for numerous applications. These range from a gauge block to an optical artifact. In this case, a ring gauge was chosen for the first fabrication. This ring gauge also included a swept sine wave feature on the inner surface of the ring. The completed artifact was measured before being given to Y-12 for evaluation.

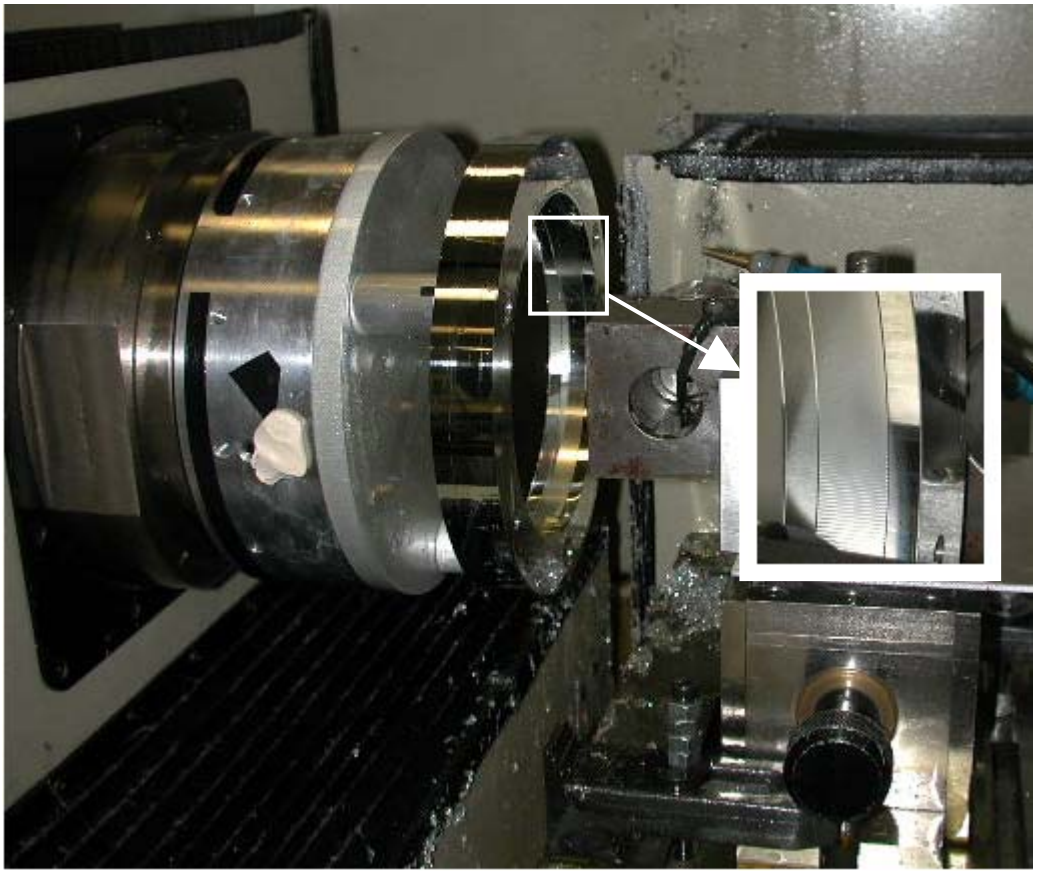

3.1 INTRODUCTION

The Y-12 National Security Complex (Y-12) relies on its ability to manufacture precision work pieces to develop parts for other government agencies or private companies. To quantify the shape of a part, it has to be dimensionally inspected. In the past, Y-12 has used rotary contour gages to measure parts. More recently, they have been switching to Coordinate Measuring Machines (CMMs). However, Y-12 does not have a transfer standard to relate the previous measurements using the rotary contour gages to the current measurements using a CMM.

A rotary contour gage consists of a rotary table and an LVDT on a tilting stage. The part, such as a hemishell, is placed on the table where it is inspected by the LVDT probe that can move in the Y and Z directions. The inspection of the part is accomplished in one of two ways. One approach is to place the probe at a particular location on the part and then rotate the table to make the latitude measurement. The other method keeps the table stationary while moving the probe to make a longitudinal measurement. Some machines may have dual opposing probes that are able to measure the ID, OD and thickness at the same time.

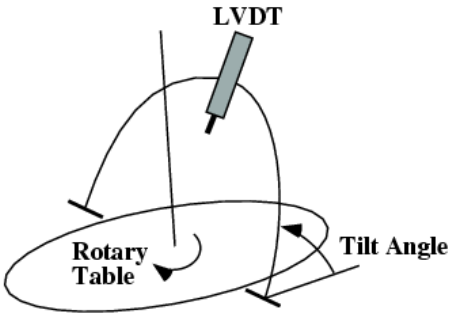

Figure 1. Rotary contour gage.

A CMM is a much more versatile machine. It consists of three carriages that are mutually orthogonal. Each machine can have a different configuration. In Figure 2, the three axes are able to move while the table remains fixed. Displacement transducers are fixed along each linear axis of the CMM. This allows a spatial reference point on the probe to be used to determine the displacement along a coordinate path in the working volume of the CMM.

Figure 2. Moving bridge CMM at NCSU.

Another aspect of a CMM is its use of a probe. In Figure 2, the probe is attached to the end of the z-axis carriage. As the carriages move and the probe contacts the surface of a workpiece, the probe takes a coordinate measurement reading at the point of contact. The probe is an integral part of the CMM but increases the inherent error of the CMM.

3.1.1 PROBES

A probe can be classified into one of two categories: contact and non-contact. Within the contact group, there are touch-trigger probes and scanning probes. Occasionally, a probe may exhibit both capabilities.

Touch-Trigger Probes

A touch-trigger probe examines the surface of a part by contacting a point on the surface, where it takes a reading, and then moves out to engage another point to inspect on the workpiece. The axes on the CMM can be moved manually or programmed to touch the surface in a pre-determined pattern. The armature of the probe consists of three arms that rest on three sets of two balls or cylinders located 120° apart [2]. The stylus of the probe deflects when it comes into contact with the workpiece and causes one or two of the arms to lift out of its neutral position. The electronic interface notices the change and triggers the CMM to take a reading [2]. After a number of readings, the CMM can relate the measurement data to basic geometric shapes [3].

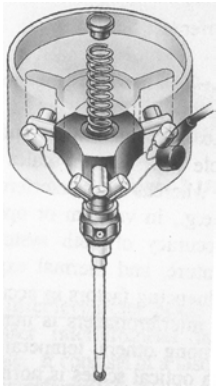

Figure 3. Touch trigger probe [1].

The accuracy of the touch-trigger probe depends on the inherent errors of the probe. Pre-travel variations are the main source of its error. A pre-travel variation is defined as the "distance traveled by a probe between the actual touching of a surface and the trigger event [4]." Lobing errors are an example of a variation. The kinematic arrangement of the arms permits different probing forces to produce a signal, depending on the direction of approach [2,4]. A map of the displacement of the lobing errors can be seen in Figure 4. Lobing errors are dependent on the reference plane and the orientation and length of the stylus [2].

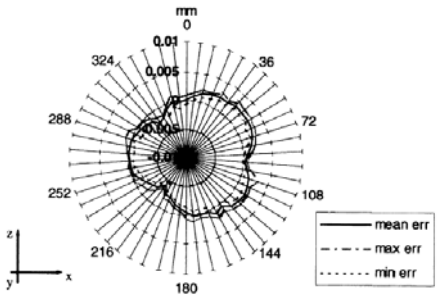

Figure 4. Example of lobing in the X-Z plane [2].

Scanning Probes

A scanning probe remains in constant contact with the workpiece as the measurement is performed [3]. There are two types of continuous analog scanning probes. They are proportional displacement and nulling [5]. The photodiodes of a proportional displacement probe (shown in Figure 5) are electrically connected in a differential mode to sense the movement of LEDs to determine the deflection of the probe [6]. The nulling probe instructs the machine to reset itself to zero after each reading to ensure that it takes a new reading when it finds an error [5].

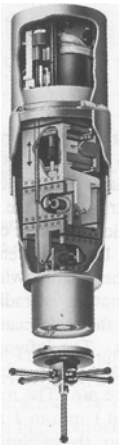

Figure 5. Proportional displacement probe [1].

During a scanning measurement, the CMM maintains a constant gauging force through feedback control and detects the deflection of the probe. The accuracy of the measurement depends on the linearity of the probe as it responds to changes in the surface [3]. The increased amount of measurement readings as compared to the touch-trigger probe also improves the quality of the measurement. There are two methods for using the probe to obtain measurements. The probe can provide feedback to the CMM to maintain a constant displacement on the workpiece, which requires no prior knowledge of the shape of the surface, or if the shape was known, the probe could operate independent of CMM controls to re-trace the fabrication tool path and make a faster measurement through open-loop control [5].

3.2 ESTABLISHED ARTIFACTS

Throughout the years, there have been a number of artifacts [7-15] developed to evaluate the performance of a coordinate measuring machine and/or to assist in its calibration. The artifacts may be used for a specific application or for a more generalized purpose. Artifacts may also be classified by the methods in which they are used to assess the accuracy of a CMM. Those methods include kinematic reference standard technique, the parametric calibration technique, and the transfer standard technique [12].

3.2.1 GAUGE BLOCK

One of the most straightforward methods to test CMMs is by use of a gauge block. A gauge block is a piece of metal of calibrated length. It is measured in various orientations and positions on the working volume of the CMM. A variety of gauge blocks can be used as length transfer standards [7].

3.2.2 RING GAUGE

A ring gauge is a circular artifact with calibrated diameter and circularity. It should be measured in at least two positions in space along with various stylus configurations. Two of the positions in space may be in the horizontal or vertical orientations. To accurately calibrate a CMM, it is suggested that 30 points be probed or scanned. The probed data is compared with the calibration data of the ring gauge. The lobing error is based on the geometry data comparison, and then machine errors are determined from the error pattern of circular error in the gauge [7].

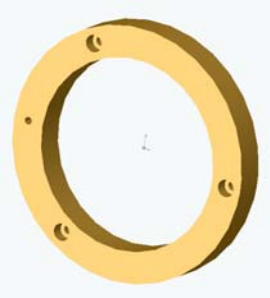

Figure 6. Ring gauge.

3.2.3 BALL BAR

A ball bar consists of a rigid bar with a sphere at each end. Multiple types of ball bars exist today. They can be free-standing or have fixed magnetic sockets. The length from the centers of each sphere remains constant. The free-standing ball bar is placed on a gauge stand in a number of orientations in the working volume of the CMM. Each ball is probed and the difference in the length measurement between ball centers is compared to the calibrated distance. The magnetic ball bar includes a magnetic socket fixed to the CMM table while the other magnetic socket takes the place of the probe. The ball bar is kinematically supported in the sockets. The CMM can be moved to different positions to take the length measurements. The machine errors are determined using this technique without finding the probe errors [7].

Figure 7. Ball bars [8].

3.2.4 Hole Bar

The hole bar is another artifact. It is approximately 540 mm in length with an I-beam cross section. As seen in Figure 8, the bar includes 11 holes along the length. These holes have a diameter of 13 mm with a uniform distance between any two hole centers of 50 mm. The artifact can be used to determine the 21 parametric errors of the CMM. The artifact is oriented and mounted in 17 different positions to evaluate the performance. The location of the hole centers are used in the transfer method in the validation of the CMM [9].

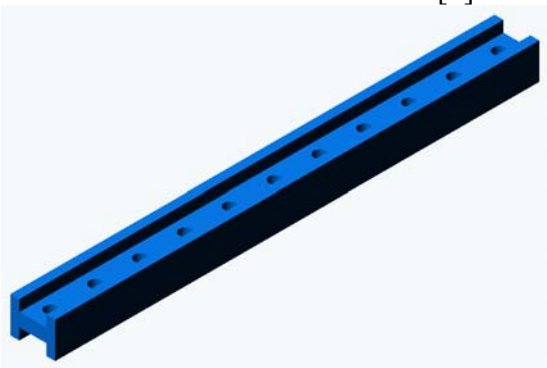

Figure 8. Hole bar.

A variation in the basic hole bar involves mounting spheres in the center of each hole to transform the hole bar from a two-dimensional artifact to one that is three-dimensional. The Geostep™ 10, Figure 9, has a length of 850 mm, a width of 101.6 mm, and a thickness of 38.1 mm. The ten, 19 mm diameter spheres are mounted along the centerline of the beam. Center to center distance between the spheres is approximately 85 mm. The center-to-center dimensions are varied to separate the systematic errors from the step standard. The three-dimensionality of the spheres negates the possibility of alignment or cosine errors of the artifact or positioning on the CMM because the origin of a sphere is characterized by its radius as an infinitely small value in three-dimensional space [10]. The spheres are treated as single points rather than 3D objects.

Figure 9. Geostep™ 10 hole bar [10].

3.2.5 BALL PLATE AND HOLE PLATE

The ball plate is comprised of a square plate with ceramic or stainless steel spheres arranged in space. The balls may be resting on the surface of the plate [12] or positioned at various heights. Four points on each sphere need to be probed to determine the center of the ball. If bending of the plate occurs, due to thermal expansion or other external forces, the center dimension is susceptible to change [11]. The ball plate is predominantly used for day-to-day verification of CMM parametric errors.

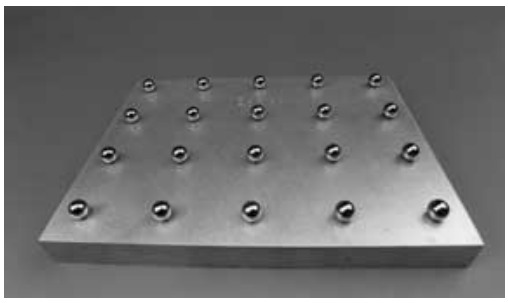

Figure 10. Ball plate [12].

The hole plate is very similar to the ball plate. Instead of balls configured in space, precision-machined holes are configured on the plate at qualified distances. Each hole has three points probed to determine the center. Bending of the plate does not have much effect on the center dimensions because bending would occur along the same plane as the centers. The hole plate is used for the parametric error calibration of a CMM [11].

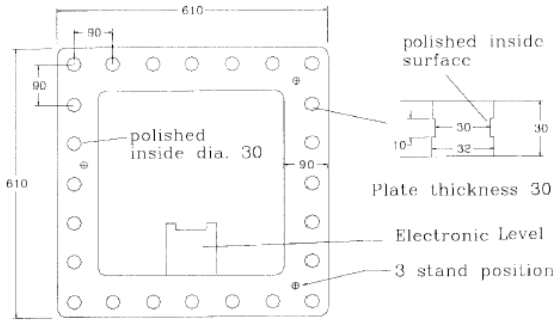

Figure 11. Ceramic hole plate [11].

3.2.6 SPACE FRAME

The modular space frame includes a triangular plate along with three magnetic ball links attached to a sphere at the apex. The links are made of carbon reinforced plastic for its low coefficient of expansion and high stiffness-to-weight ratio [7,13]. It is important that the spheres resist corrosion and be accurate in shape and size. With the space frame, it is only necessary to calibrate the magnetic ball links and the plate before use with a CMM [13]. The main function of the space frame is to indicate error tendencies of the machine and where adjustments are needed without representing a large amount of detail of machine errors [7]. To accommodate different CMMs, the space frame should be moved and measured to characterize more of the working volume.

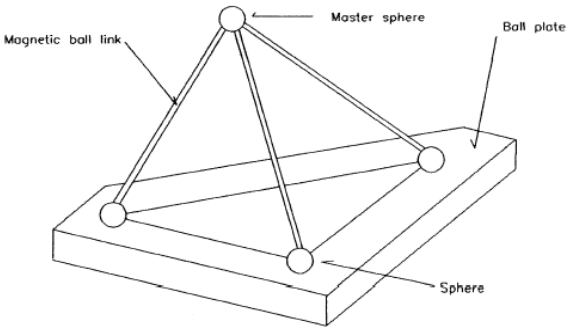

Figure 12. Modular space frame [13].

3.2.7 MODULAR FREEFORM GAUGE

The modular freeform gauge is intended for the task-specific measurement of complex parts such as turbine blades. This artifact models a freeform object with regular geometric shapes. For a turbine blade, two cylinders of different diameters are chosen. Each shape can be calibrated separately to reduce the calibration uncertainty. For measurement, the calibrated shapes are placed on the CMM, and their relative positions are determined. The assembly is modeled in CAD with the relative position points. The experimental uncertainty can be established and used with the calibration data to ascertain the uncertainty of the freeform measurement. This artifact is not useful with objects that have varying shapes and concave surfaces [14].

(a) (b)

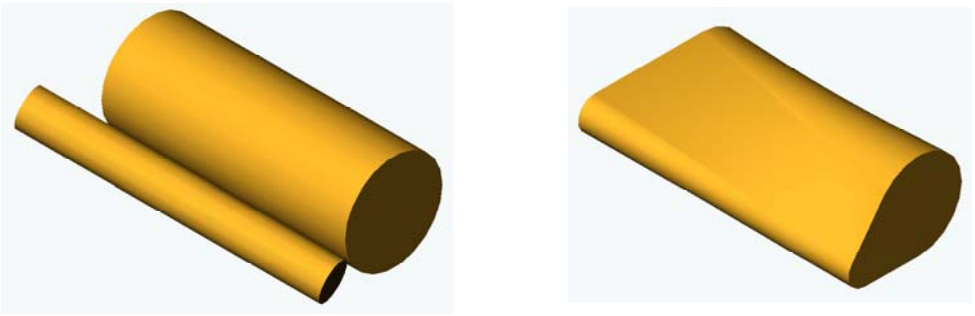

Figure 13. (a) Regular geometric shapes to simulate (b) a freeform object such as a turbine blade.

3.2.8 OPTICAL ARTIFACT

Some CMMs have the ability to measure an object with a mechanical or an optical probe. An artifact to take advantage of the optical capability has been developed. The design is based on a hole or ball plate. It consists of 25 elements mounted in equally spaced holes on a steel plate. Each element is a thin steel disc with a hole through the center. The surface of each disc is specially prepared to obtain a scratch-free face. Inside each hole, the disc rests on a ground surface and is clamped down. The plate can be measured on both horizontal surfaces and the CMM geometry can be established [15].

3.3 RING GAUGE

The initial artifact manufactured was a ring gauge. One of the important features of the gauge is a swept sine wave on the inside diameter (ID) of the ring. A swept sine wave is a sine wave that continuously varies its frequency. In this case, the wave begins at a low frequency and progresses to a higher frequency in the first 90 degrees. At this juncture, the wave is "flipped" to line up with the last wave and then the frequency decreases to the starting frequency as it reaches

180 degrees. From 180 to 360 degrees, the wave is a mirror image of the first 180 degrees. Figure 14 below illustrates these characteristics.

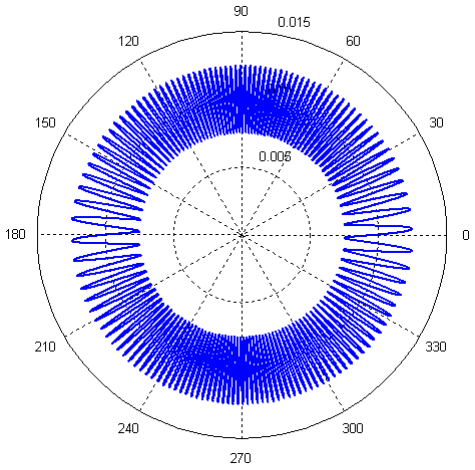

Figure 14. Swept sine wave on the ID of the ring.

The purpose of the swept sine wave is to simulate the effect of small features on a part to be measured. Depending on the radius of a probe, the ability to detect small features varies. If a small-radius probe was used to measure a part with small anomalies, the question arises whether the overall measurement would be significantly influenced. The different frequency of each wave creates a range of values to be evaluated. The ring gauge includes a reference cylinder groove on the outside diameter (OD) and on the inside diameter (ID). The swept sine wave is inscribed into the ID groove.

3.3.1 INITIAL PREPARATION

The disk, spacers, and ring were machined from 60GI T6 Aluminum. The disk and spacers were necessary for mounting the ring gauge on the Rank Pneumo ASG25001 diamond turning machine (ASG). The vacuum chuck on the ASG cannot secure a hollow cylinder like the ring gauge. The solid disk was manufactured for this purpose while the spacers allowed for clearance for the cutting tool and fast tool servo. Each face had to be diamond turned to obtain a better surface finish and to improve the flatness of the surface profile. First, the three spacers were bolted to the aluminum disk. The disk was placed on the chuck of the ASG and held by a vacuum of approximately 20 in. Hg. The ring was attached to the spacers by bolts with spherical washers between the bore and the bolt. The spherical washers were used to keep the ring from warping on the spacers under the screws. With the spherical washer, the screw allows for all three moments while restricting the three translational directions. Figure 15 demonstrates the assembly of the disk, spacers, and ring gauge.

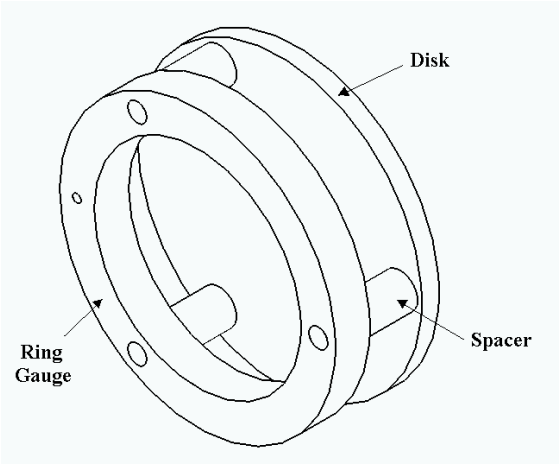

Figure 15. Assembly of fabrication.

It is important that the ring is centered with respect to the spacers. An electronic encoder probe was placed on the ID of the ring was used to take readings. As the vacuum chuck was rotated by hand, the indicator needle moved left and right to indicate where the "high" and "low" spots on the ring occurred. The bolts on the ring were loosened. By slightly tapping the ring, the center was adjusted to within ± 2 μm.

After the ring had been centered, the ID, OD, and top of the ring could be turned. The first step was to "touch-off" on the ring. The z-axis on the ASG had to be zeroed so that a specific depth of cut could be selected. The x-axis was set off approximately 10 mm to the right of the ring. Because the width of each face was 1" (25.4 mm), the computer could be programmed to have the x-axis traverse across the width. Due to the approximate origin of the x-axis, the ASG was programmed to travel 50 mm. The spindle speed was 500 RPM. A feed rate of 20 mm/min was used to obtain a theoretical PV roughness of approximately 10 nm using a cubic Baron nitride tool. The depth of cut on the top face was 40 μm. It took four passes to achieve a flat surface. During the operation, oil was used on the tool as a coolant.

The bottom of the ring also had to be turned. The ring was flipped over and bolted down. The ring was centered again before it was turned. The depth of cut was set to 40 μm and three passes were necessary. After machining, it was clear that a small portion of the top of the bolts were trimmed off. To protect the diamond tool later, the tops of the bolts were ground. The OD of the ring was turned in the same fashion except that the x-axis was used to touch off while the z-axis was set off the part. The OD needed three passes with a 40 μm depth of cut to obtain a flat surface. However, during the operation, the chips collected on the tool and may have contributed to some scratching on the surface. The setup to turn the ID of the ring was somewhat complicated. The z-axis was set slightly off the edge of the face. The tool would traverse from the inside to the outside so that the clearance between the tool holder and the disk would not become a problem. Once more, the depth of cut was 40 μm, and it took two passes to obtain a flat surface.

The ring gauge includes a hole through its thickness that will serve as a theta reference during the measurement process. The perpendicularity of the hole was checked using an electronic indicator. Beginning at the edge of the hole and proceeding to the opposite edge, the values ranged from –2 μm to 12 μm or approximately 0.03 degrees. It was determined that this error was not significant enough to warrant improvements on the hole.

3.3.2 NATURAL FREQUENCY ANALYSIS

Ring Analysis

To select the operating conditions to machine the artifact, a finite element analysis was completed on the ring gauge in SolidWorks. The first natural frequency would occur around 1500 Hz. Figure 16 represents the mode shape at this frequency. It simulates how the ring would deform.

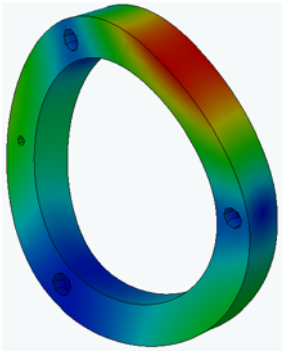

Figure 16. First natural frequency mode shape.

One of the requirements of the swept sine wave was that it had to range from 80 waves per inch to 4 waves per inch. It was possible to meet this requirement and stay below the ring's natural frequency if the ring was spun at less than 50 RPM.

FTS Analysis

The natural frequency of the Fast Tool Servo (FTS) was another consideration. The piezoelectric stacks of the FTS are excited by the signal from a high voltage amplifier. The frequency and voltage signal affect the movement of the tool on the FTS. Any unexpected vibration of the tool would change the amplitude of the wave. Therefore, it is important to know the natural frequency of the FTS. The Stanford Network Signal Analyzer was used to generate a swept sine wave. The output from the Stanford was sent to dSPACE. dSPACE is a piece of hardware connected to a computer that facilitates the input and output of a Simulink control model. In dSPACE, the wave was offset to make it entirely positive. The servo cannot handle a negative signal. The modified signal entered the high voltage amplifier where the signal was

multiplied by 10 before it could reach the fast tool servo. The Stanford then captured the output of the servo. The swept sine wave began at 1 Hz and increased to 7000 Hz. The range of the signal could be decreased to focus on some of the irregularities. It was observed that an irregularity occurred close to 600 Hz. The fabrication of the wave onto the ID now would have to occur below 600 Hz.

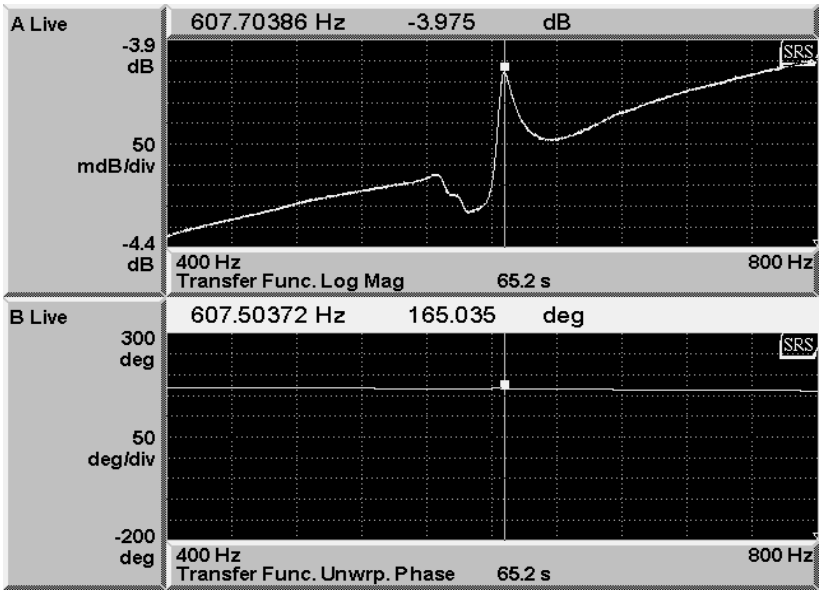

Figure 17. Transfer function and phase angle of FTS between 400 and 800 Hz.

3.3.3 FTS CONTROL

The capacitance (cap) gage on the FTS is used to measure the displacement of the tool as it is moved by the piezoelectric stacks. The control of the fabrication was to be open loop. This being the case, the cap gage was not needed to monitor the displacement. However, it was needed to verify the output of the FTS as commanded by the controller that was used for the fabrication prior to fabrication. Before it could be used for verification, it had to be calibrated. The Federal gage was calibrated using the laser interferometer on the ASG before it was used to calibrate the cap gage.

There is a rotary encoder mounted onto the ASG that keeps track of the number of rotations of the spindle. In effect, it measures the rotational speed. The encoder output can be monitored through the program ControlDesk that displays the Matlab/Simulink model. The pin connectors were re-wired to create the correct configuration before being inserted into the dSPACE board.

Simulink was used to develop control of the movement of the FTS. One of the key elements to the Simulink program was the look-up table, Figure 18. A Matlab program generated the points of the swept sine wave. Inputs to the program included amplitude, starting frequency, ending frequency, length, and number of data points. The length was equivalent to a quarter of the

circumference. The number of data points was limited to the number of counts of the encoder. Each point from the look-up table is referenced by a single point on the encoder. The function box, the box labeled Fcn in Figure 18, linearly corrects for the displacement of the FTS when a specific voltage is present. Finally, the signal was sent to the FTS. Figure 18 represents the Simulink model.

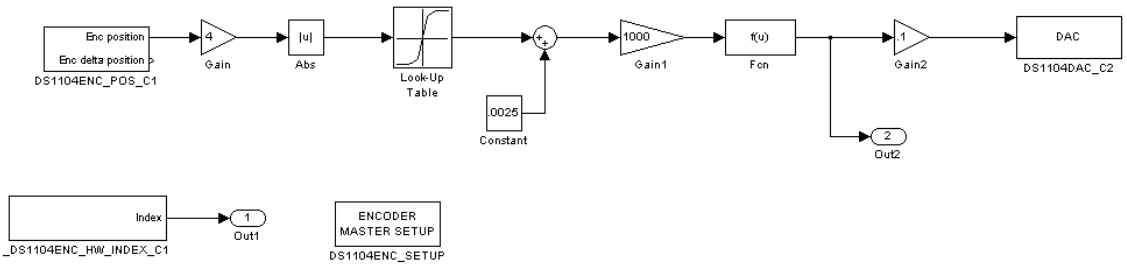

Figure 18. Simulink model of FTS control.

3.3.4 FABRICATION

Before the swept sine wave could be cut into the ID of the ring, the ID, OD, top, and bottom of the ring had to be turned with a diamond tool. This was completed in much the same fashion as was done with the CBN tool. The ring gauge was centered within 4 μm. Each bolt had a 100 in-lb torque applied to it. The surface finish improved with a 2.1 mm/min feed rate and a 200 RPM spindle speed in the clockwise direction. A total of 22 μm was taken off each face. On the OD, a 30 μm, off-center groove was added to act as another reference surface. The groove was cut with the same feed rate and speed as each face. Figure 19 displays a cross section of the ring gauge with grooves.

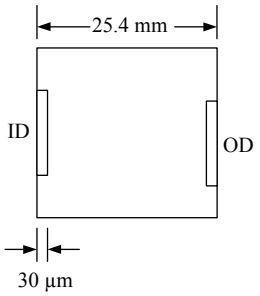

Figure 19. Ring cross section.

The ID was faced off with the FTS. Figure 20 illustrates the following setup description. The servo was attached to a mounting block and placed on the micro height adjuster. A thin piece of aluminum was inserted between the mounting block and the height adjuster. Minor adjustments were made with the micro height adjuster to achieve a height of 6 inches as defined by two gauge blocks. The height adjustment was necessary for vertical centering of the tool. The ID was finished at a feed rate of 8.4 mm/min and a spindle speed of 200 RPM. Another groove was cut into the ID with the same feed rate and spindle speed; it was also 30 μm. Finally, the swept sine wave was cut into the groove on the ID. The feed rate was 0.84 mm/min with a spindle speed of 20 RPM.

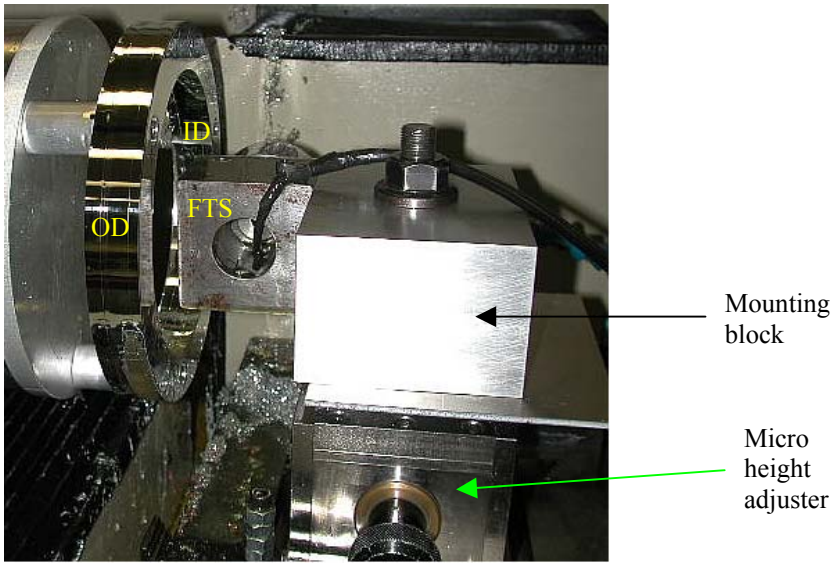

Figure 20. Setup with FTS and ring gauge.

3.3.5 MEASUREMENT OF THE ARTIFACT FEATURES

After the swept sine wave was cut into the surface, it was measured using an LVDT. The LVDT was calibrated using the ASG and an oscilloscope. The probe tip radius was determined using the Zeiss microscope. It is approximately 1 mm, which is significantly larger than the radius of curvature of the smallest wave. The measurement demonstrated a decrease in amplitude from the ± 2.5 μm goal. Figure 21 displays the measurement.

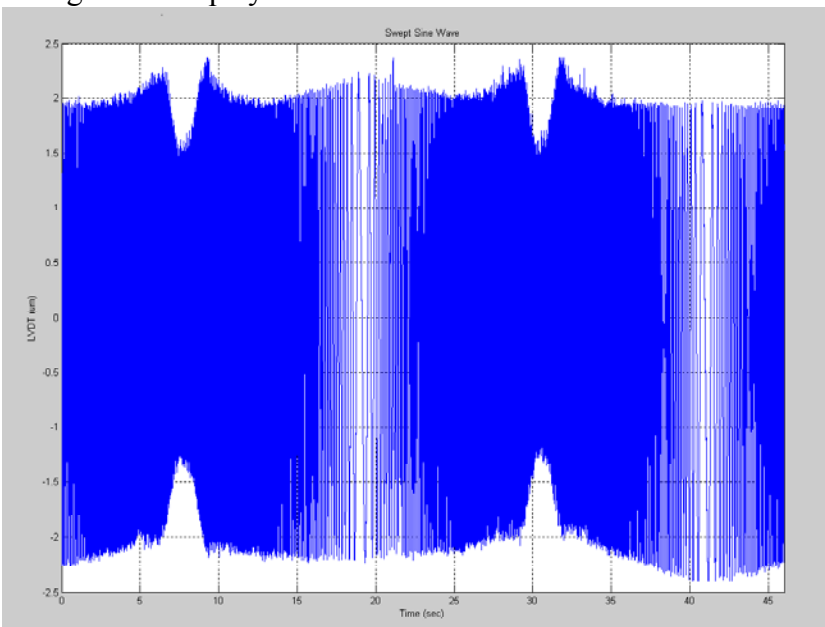

Figure 21. LVDT measurement of swept sine wave.

The figure indicates "dips" in the LVDT measurement. This may be attributed to the high frequency of the waves. The natural frequency of the LVDT may have been exceeded which is

disallowing the electronics to take a correct reading. The minimum constant rotational speed of the ASG is too fast for the LVDT measurement.

Distortion of the Ring

The profile of the surface around the bolt holes was observed before and after the bolts were loosened. The PV values for the surface while the bolts were still torqued were 380 nm, 712 nm, and 858 nm. Figure 22 shows the surface/wavefront map at one bolt location.

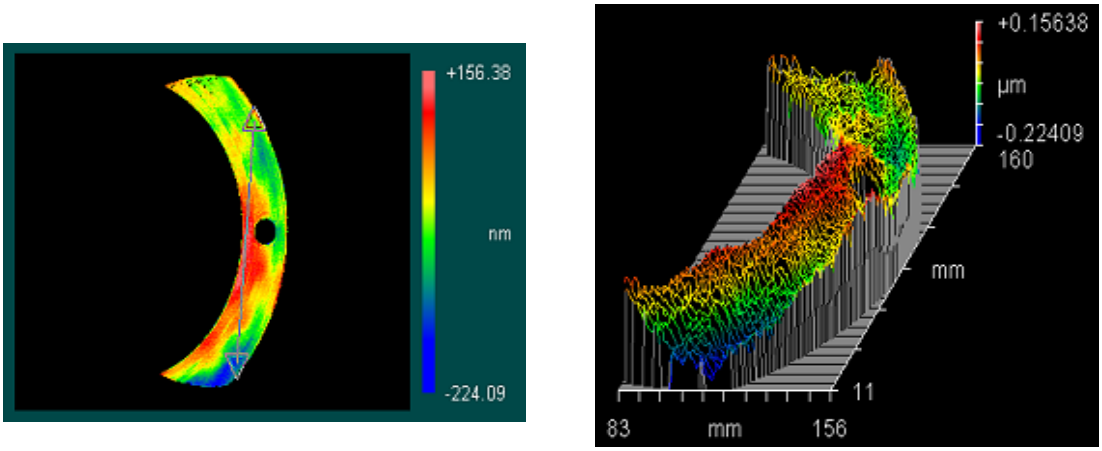

Figure 22. Surface profile of ring gauge with bolts in place.

When the bolts were untorqued and taken out, the difference in PV values was almost a factor of 10. Those values were 3.3 µm, 4.4 µm, and 4.7 µm. The high amount of torque on the bolts was arbitrarily chosen which may have caused a distortion on the surface. This can be seen in Figure 23.

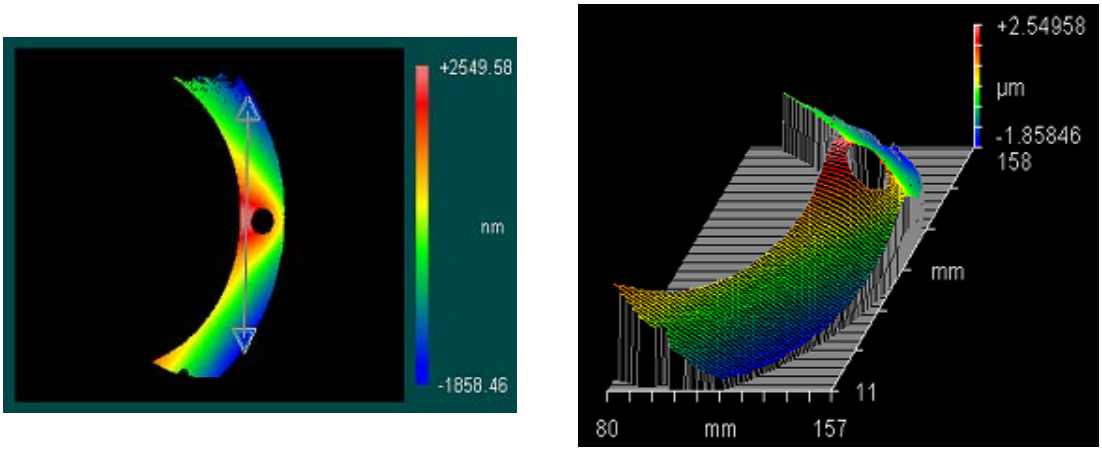

Figure 23. Surface profile of ring gauge with bolts removed.

3.4 FUTURE CONSIDERATIONS

The evaluation of the ring gauge by Y-12 will be the basis for the decision of another artifact. A second artifact will be designed and fabricated. However, the artifact may be an improvement on the first model or be a completely new design. The ability to mount the artifact in a variety of orientations on the CMM is another consideration. The final artifact will include an instruction manual on how it should be used and how to evaluate the performance of the CMM based on the calibration of the artifact.

REFERENCES

1. Bosch, J. A. (ed.) *Coordinate Measuring Machines and Systems*. New York: Marcel Dekker, Inc. 1995.
2. Chan, F. M. M., Davis, E. J., King, T. G., Stout, K. J., *Some performance characteristics of a multi-axis touch trigger probe*. Meas. Sci. Technol., 1997, 8 (8), p. 837-48.
3. Destefani, J. D., *CMMs make contact*. Manufacturing Engineering, 2001, 127 (3), p. 100-5.
4. Cauchick-Miguel, P. A., King, T. G., *Factors which influence CMM touch trigger probe performance*. Int. J. Mach. Tools Manufact., 1998, 38 (4), p. 363-74.
5. Marino, E. A., *Three-Dimensional Measurement Probe*. Master's Thesis, NC State University, 1999.
6. EMD Sceptre System Proportional Displacement Probe Data Sheet, http://www.emdsceptre.com/pdprobe.htm.
7. Cauchick-Miguel, P., King, T., Davis, J., *CMM verification: a survey*. Measurement, 1996, 17 (1), p. 1-16.
8. Bal-tec Adjustable Ball Bars Data Sheet, http://www.precisionballs.com/CMM/CMM-10Page1.htm.
9. Lim, C. K., Burdekin, M., *Rapid volumetric calibration of coordinate measuring machines using a hole bar artefact*. Proc. Instn Mech. Engrs, Part B, Journal of Engineering Manufacture, 2002, 216 (B8), p. 1083-93.
10. Bal-tec The Geostep 3400-10 Data Sheet, http://www.precisionballs.com/CMM/CMM-26Page1.htm.
11. Lee, E. S., Burdekin, M., *A hole-plate artifact design for the volumetric error calibration of CMM*. Int. J. Adv. Manuf. Technol., 2001, 17 (7), p. 508-515.
12. Bal-tec The 1216 Ball Plate Data Sheet, http://www.precisionballs.com/CMM/CMM-28.htm.
13. Silva, J. B. A., Burdekin, M., *A modular space frame for assessing the performance of co-ordinate measuring machines (CMMs)*. Precision Engineering, 2002, 26 (1), p. 37-48.
14. Savio, E., De Chiffre, L., *An artefact for traceable freeform measurements on coordinate measuring machines*. Precision Engineering, 2002, 26 (1), p. 58-68.

15. Hansen, H. N., De Chiffre, L., *A combined optical and mechanical reference artefact for coordinate measuring machines*. CIRP Ann Manuf Technol, 1997, 46 (1), p. 467-8.

4 ULTRAFORM 2D

Alex Sohn
Ken Garrard
Precision Engineering Center Staff
Thomas A. Dow
Professor
Department of Mechanical and Aerospace Engineering

A polar profilometer, Ultraform 2D, has been built by Precitech and the Precision Engineering Center under a technology transfer license agreement. The design is based on the Polaris machine that was developed at the PEC in 2000. Ultraform incorporates numerous improvements in packaging, axis design and the control software to produce a commercially viable machine. Both the measurement volume and resolution have been increased and controller level support for improved operating procedures has been incorporated into Ultraform. In particular, a means of following an arbitrary surface using the LVDT probe as an auxiliary axis feedback has been developed. Updating the user interface software to take advantage of these new hardware features and implementation of improved probe waviness compensation algorithms are the principal tasks remaining.

4.1 INTRODUCTION

Profilometers for form and roughness measurements have traditionally been based on Cartesian geometry. Large aspect ratio parts present significant challenges for commercially available measurement systems. Optical profilometers are limited to a few degrees of slope by the ratio of fringe spacing to camera resolution. Mechanical profilometers are usually limited by the clearance angle of the tip and the non-perpendicular loading direction of the probe – both of which often limit the measurable slopes to less than 45°. Certain industries, in particular those making high aspect-ratio optics, require the measurement of geometries more polar than Cartesian in nature. A polar profilometer, *Polaris*, was designed and built in 2000 at the Precision Engineering Center to address this need [1, 2]. The device is capable of measuring figure as well as roughness on hemispheres and aspheres both concave and convex inside a circular measurement field 50 mm in diameter. This design can be used to measure surfaces with a resolution of 20 nm and an overall accuracy of 200 nm.

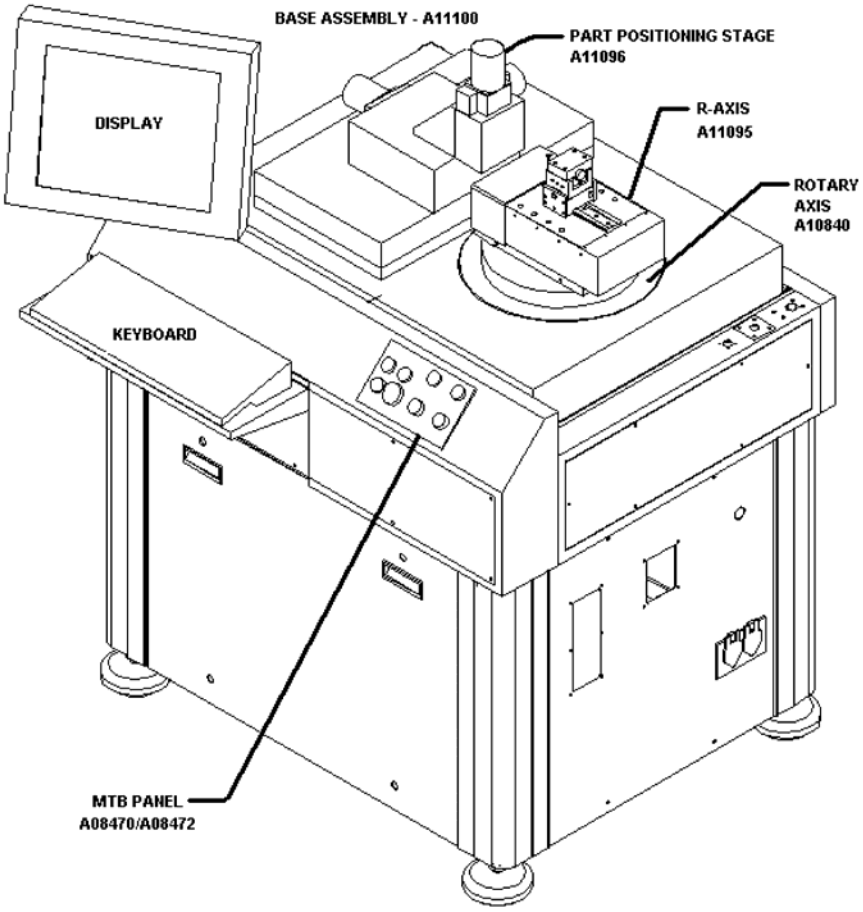

Figure 1. Ultraform 2D.

Ultraform 2D, shown in Figure 1, is a commercial prototype of the polar profilometer *Polaris*. As a joint project with Precitech Precision, Ultraform 2D maintains the layout and concept of Polaris while changing certain components to make the instrument commercially viable. The most significant change is an increase in both R-axis travel and measurement range. The travel of the Ultraform R-axis has increased to 70 mm. With the addition of a manually adjustable LVDT gauge mount the overall measurement field has been increased to a diameter of 100 mm.

4.2 CHANGES FOR COMMERCIALIZATION

4.2.1 HARDWARE CHANGES

Several changes were made to the hardware to either improve performance, reduce cost or both. Some components were not suited to a production machine whereas others that were purchased from other vendors could be produced by Precitech. A summary of the components of each machine are shown in Table 1.

Table 1. Hardware comparison of Ultraform 2D and *Polaris*.

MAJOR COMPONENT COMPARISON		
Component	***Polaris***	***Ultraform***
Vibration Isolation	Fabreeka Precision Aire	Fabreeka Precision Aire
Machine base	Rock of Ages	Rock of Ages
Three-axis part positioner	NEAT Stepper	NEAT Stepper
Part mounting plate	Bolt Grid	Vacuum Chuck
Rotary Air Bearing	Precitech RT 200/270	Precitech RT 200/270
Rotary encoder	Heidenhain	Renishaw
Linear Air Bearing Slide	Dover	Precitech Custom
LVDT Support	Fixed	Adjustable
Air-Bearing LVDT	Lion/Colorado Precision	Precitech
Rotary Stage Motor	Aerotech Brushless, Frameless	Hathaway Brushless, Frameless
Linear Motor	Trilogy	MTS
Controller Cabinet	ElectroRack/Desk Type	Precitech Custom/In machine base
Linear scale	Heidenhain	Sony
PC	IBM NetVista	Panel PC
Motion Controller	Delta-Tau UMAC	Delta-Tau UMAC

The Fabreeka vibration isolation system performed flawlessly and exceeded all performance expectations on *Polaris*. This system was retained based on this experience, reasonable cost and

the importance of the isolation system. Similarly, the granite slab to provide mass for effective damping and a stable platform for the machine continues to be sourced from Rock of Ages.

The three-axis part positioner remains the same for both machines with the exception of a longer travel (100 mm) in the X and Z directions to accommodate the longer travel of the R-axis. The Y-axis still has a range of 50 mm. All three positioning axes are driven by microstepping motors to give an overall position resolution of 0.5 μm. The part mount on the positioner has been changed from the grid of bolt holes used on *Polaris* to a vacuum chuck for Ultraform.

The rotary stage (θ-axis) has been modified. While the Precitech air bearing table remains the same, the rotary encoder and the motor are somewhat different. The Renishaw rotary encoder has increased the rotary axis resolution to 0.02 arcsec from the previous 1.8 arcsec Heidenhain encoder, mainly due to a tenfold increase in interpolation. The Hathaway rotary axis drive motor is of the same type as the previous Aerotech model, with a three-fold reduction in torque from 11.7 N-m peak to 3.8 N-m peak. It was selected primarily to save space and reduce cost. Since the θ-axis does not need to accelerate or decelerate rapidly, this reduction in torque should have little impact on the operation of Ultraform.

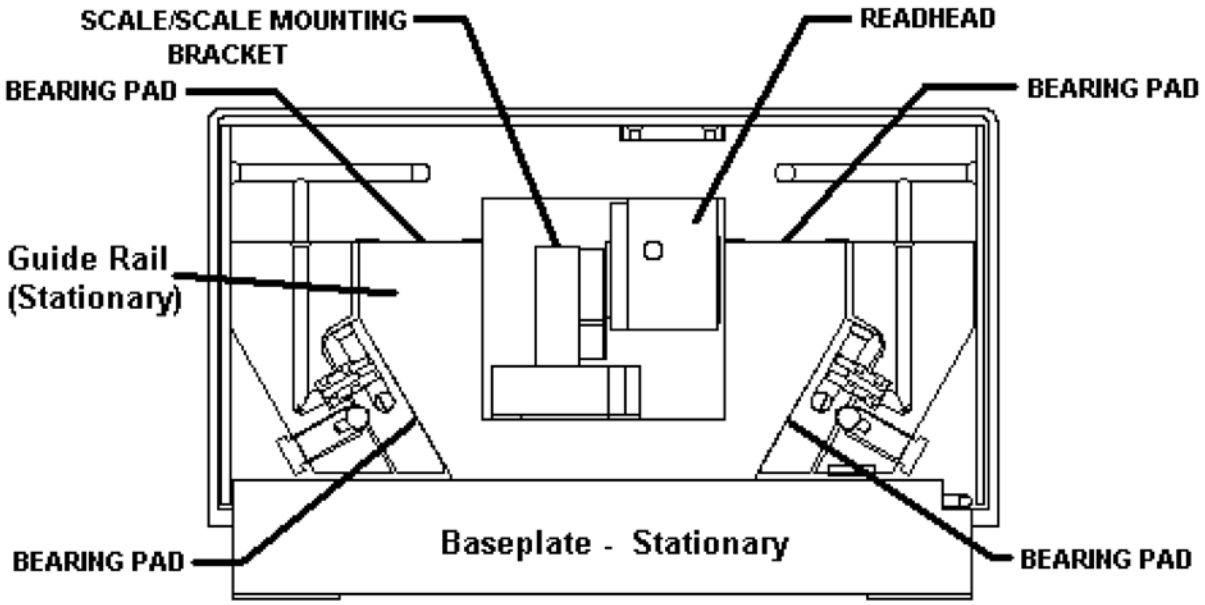

Figure 2. Cross section of linear air bearing slide. Note the dovetail shape and center mounted linear scale. The linear motor resides immediately behind the scale.

The linear (R) axis has changed significantly. *Polaris* used a Dover box-slide of anodized aluminum with encoder and motor on either side outboard of the slide. Precitech has designed a new dovetail slide with 70 mm of travel that is based on the aluminum dovetail slides used in some of the Optoform diamond turning machines. Shown in section in Figure 2, the slide is

constructed of stainless steel and accommodates both the linear motor and encoder in the center of the dovetail. This eliminates Abbé offset in the tangential direction which was present on the Dover slide and contributed to yaw errors. The motor on Ultraform is an MTS model with 43 N peak force as opposed to *Polaris's* Trilogy model with 133.5 N peak force. Due to space constraints, the coil size was reduced along with the force. The Heidenhain Diadur linear scale with 20 nm resolution has been changed to a Sony scale, also with 10 nm resolution.

A new mount has been constructed for the air-bearing LVDT gauge. Adjusting the position of the gauge for probe centering on *Polaris* required tapping the monolithic mount. Ultraform has a fully adjustable base as shown in Figure 3. A differential thread screw allows fine adjustments of the LVDT's tangential position. Additionally, the bottom of the mount is dovetailed to allow the LVDT to be positioned manually in the axial or R-direction, increasing the coverage area for measurements to a diameter of 100 mm.

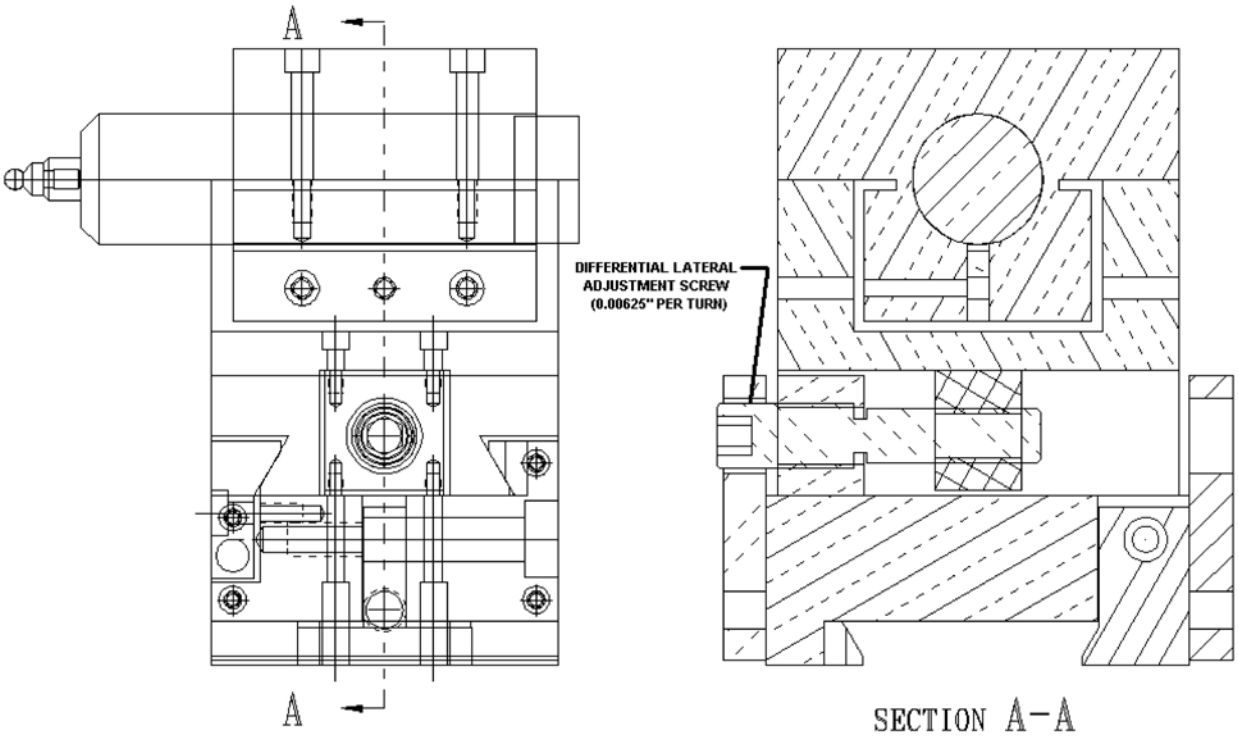

Figure 3. The LVDT holder is now adjustable with a horizontal differential screw that is perpendicular to the LVDT axis. The mount also slides on a dovetail on top of the R-axis to allow a larger measurement envelope.

The control system has been changed by placing all components on a single machine base. *Polaris* had a separate desk, which contained the control components, provided workspace and the host PC. In place of the desk, Ultraform uses a panel PC mounted on a stalk on the side of

the machine. The Delta Tau UMAC motion controller is the same as on *Polaris*. While the controller hardware has not changed, software changes are significant.

4.2.2 SOFTWARE MIGRATION

Migration of the *Polaris* software to the Ultraform platform requires significant modifications to the code at three different levels. At the lowest level is the Delta Tau firmware and the data structures that configure it to control the hardware. Included in this category is the 512K x 24-bit data acquisition buffer. The next level includes the software PLCs and motion programs that implement the operational functions required to setup, perform axes calibration and measure a specimen. The top level is the User Interface (UI) software that executes on a PC host computer connected to the UMAC controller via USB. With the exception of the handwheel jogger, the mounting of a specimen on the 3-axis part positioner and the power on/off, emergency-stop and emergency-stop reset switches, all user interactions with the machine are through the UI program. Communication among the software components is through global access to the UMAC's internal variables and the acquisition buffer. The division of operational tasks among the UI, control PLCs and motion programs is the principal update required of the prototype software.

Performance Improvements

Crowning and Calibration Several operational tasks in the Polaris need to be improved. The auto-crowning and calibration procedures can occur faster if the process of nulling the probe against a part is performed by a triggered jog procedure (PLC or motion program) on the UMAC instead of by incremental jog and test loops on the host PC. Probe nulling is performed by moving the Z axis during crowing, the R axis during calibration and both R and Z when initiating a measurement.

Triggered Moves To move a specimen into contact with the LVDT probe, two triggered move commands been implemented in the jog PLC. One moves the R axis (for calibration operations and measurement setup) and the other moves the Z axis (for horizontal and vertical crowning). Currently these operations are performed by the UI as a sequence of discrete UMAC commands: *move*, *wait for motion to complete* and *check LVDT position and status*. The sequence is repeated until the LVDT signal is sufficiently close to zero. Finding the part with the probe can be time consuming as the R or Z axis commanded motion cannot exceed the range of the LVDT. Thus, many iterations are required if the part and probe are not jogged close to one another by the operator before starting these automatic motion command sequences. Replacing this, rather tedious technique with triggered moves represents a significant time savings for the operator. Zeroing the LVDT now requires approximately 10 seconds at a typical stand-off distance of 5 mm. In the worst case, less than one minute is required when the probe is as far away from the

measurement artifact as possible. The process is repeatable to about 100 nm when moving the R axis and 300 nm when moving the Z axis.

Data Acquisition The time to uploading data after completion of a measurement can be reduced by utilizing the PMAC library routines for transfer of binary data. Presently the data is "dumped" to the host PC in ASCII format and converted to a numeric format for analysis. The conversion process is insignificant, but transferring the data as characters requires about twice the USB bandwidth. Also, the USB channel incurs significant setup overhead for each communication cycle relative to its ultimate per byte transfer rate. Thus a large data transfer buffer is desirable.

Data Analysis Two types of least-squares curve fitting are implemented by the UI software: linear (slope and intercept) and circular (radius and center coordinates). Both are performed on the data after it is converted to Cartesian coordinates. This transformation of the data leads to uncertainty in both the independent variable (the abscissa or X axis) and the dependent variable (the ordinate or Z axis). In addition, the required least-squares assumptions of independence and Gaussian error distributions are violated as a result of the transformation. The technique used for the circular fit is known to be very susceptible to round-off errors and to fail completely in some trivial, degenerate cases (e.g., when the data forms a vertical, straight line). The preferred algorithm for general linear least-squares is known as the Singular Value Decomposition (SVD). Either the SVD or a general purpose non-linear algorithm (e.g., Levenberg-Marquardt) will be used for all curve fitting. It may also be possible to implement the fitting routines with the polar coordinate data to avoid problems associated with the transformation.

Control

The machine control software is logically divided into two categories: PLCs and motion programs. Essential functions such as emergency stop, jogging and homing are controlled by the PLCs. Motion programs are used for activities that require both synchronized motion along a prescribed path and data acquisition. The final (ρ, τ) calibration step, θ calibration and part measurement are done with motion programs. The calibration motion programs are stored in the UMAC's non-volatile program memory. Coarse (ρ, τ) calibration and X,Y crowning were performed by the UI issuing jog commands directly to the UMAC and waiting for motion to complete. These functions will be improved with saved motion programs to simplify the UI interactions with the control system. Improved performance is also expected.

LVDT Following Mode For *Polaris*, a new part measurement motion program that drives the R and θ axes along a nominal part profile was generated by the UI software and downloaded to the UMAC for each measurement setup. For Ultraform, a more generic measurement mode will be implemented that does not require a nominal probe trajectory. Techniques for using the LVDT

signal as a secondary feedback for the R axis motion control are being investigated. This will eliminate the need for generating nominal part profile motion programs and measurement offsets and permit the measurement of surfaces of unknown cross-section. It may still be desirable for the user to specify whether the part is concave or convex at its apex although this information may be available from the crowning procedure. During measurement of an unknown surface, the θ axis will be commanded to rotate slowly through a prescribed arc length while the controller maintains a null LVDT feedback signal by moving the R axis in response to displacements of the probe. Four approaches for implementing LVDT following mode have been identified.

1. **Periodic modification of the commanded position for the R axis.** A test was performed with the prototype instrument using a simple motion program. In this test, the R motor was defined as the W axis in a coordinate system and commanded to follow an appropriately scaled LVDT feedback signal. Rotary table motion via incremental jog commands were generated by the handwheel jog PLC. The trade-off between delay timing and motion velocity was found to be critical as the R axis has a high bandwidth (~50 Hz) relative to the LVDT and can "bounce" the probe. The resulting instability is a major obstacle to measuring parts with large local slopes.

2. **Dual feedback.** That is, the controller uses a linear combination of the LVDT signal and the R axis encoder signal as the control feedback for the R axis. The UMAC firmware allows for both position and velocity feedback as well as master-slave following modes. A typical example is the slaving of an axis to a manually operated handwheel or a spindle.

3. **LVDT-only feedback for the R axis.** A significant problem occurs if the probe looses contact with the surface during measurement. Switching between the two feedback signals is also problematic.

4. **The inverse kinematics** facility of the UMAC provides a means of "getting inside the loop" with respect to trajectory command generation. Although similar to the dual feedback technique, the inverse kinematic PLC is executed on every servo cycle (currently 440 μsec). The constant timing simplifies the task of implementing a low pass filter to avoid problems associated with the low bandwidth, directionally dependent response the LVDT air bearing.

With all four techniques, two issues must be resolved. First, rapid corrective motions of the R axis must be filtered or the air bearing LVDT will loose contact with the surface; second, the transition into and out of following mode must be smooth.

User Interface

The user interface is a Windows application written in C and C++ using the Borland C++ Builder integrated development environment. The Delta Tau PComm32 library provides functions to communicate with the UMAC controller and the Iocomp Plot Pack and Instrument Pack component libraries provide 2D plotting facilities and instrumentation display capabilities (e.g., analog gauges, LEDs, progress bars, etc.).

Data Files Three types of files are created and maintained by the UI:

1. **The Preferences file** (Polaris.ini) is a binary format file containing the user selectable preferences accessed via the **Preferences** menu and the results of the most recent calibration.
2. **Part data description files** (*.pdm) are the result of processing a G-code file to create a motion path for the UMAC axes to follow. These files will no longer be needed after the LVDT following mode is implemented.
3. **Measurement data files** (*.mdm) are the saved ASCII data acquired by the controller during a measurement scan. They consist of six columns of numbers preceded by a single header line containing column labels. The columns labels are: **Index**, **X**, **Z**, **R**, **Theta** and **Rho**. Index is simply a sequence number for the each data row, X and Z are the data points expressed in Cartesian coordinates and R, Theta and Rho are the positions of the moving axes at each data collection interval. X, Z and R are in units of millimeters, Theta is in degrees and Rho is in micrometers. The data is saved after compensation for LVDT linearity, R axis pitch, (ρ, τ) offsets and probe radius are performed. The X,Z Cartesian transformation is relative to $(X_0,Z_0)= (0,0)$. Improvements in the measurement file format are needed. In addition to column labels the header should contain the data and time of the measurement, the calibration information used to compensate the data, the LVDT range setting, the data acquisition rate and the spatial filtering parameters used to calculate surface normals.

Code Modules The most significant UI code change needed for the migration from *Polaris* to Ultraform is the separation of the command and control functions from the data analysis and plotting functions. *Polaris* UI software also contains numerous interaction sequences with the UMAC PLCs and motion programs. Simplification of these interactions by directing all communication activities through a single module will facilitate debugging, code maintenance and the possible future migration to different controller hardware. From experience with the *Polaris* prototype, it is also apparent that the mechanisms employed for data allocation and thread management (ie, multi-tasking) are not robust. The separation of code modules into functional groups and redesign of these features will reduce the occurrence of errors and speed execution of code.

4.3 TESTING

Preliminary measurements have been made to characterize error motions of Ultraform 2D. Straightness measurements of the linear (R) axis revealed horizontal straightness of 160 nm and vertical straightness of 100 nm over the axis travel of 70 mm. Compensation will be performed for the horizontal straightness to achieve overall measurement accuracy of 100 nm. R-axis pitch, of particular concern due to the large Abbé offset between the linear encoder and the LVDT gauge, was measured to be 0.4 arcsec on Ultraform. This is a significant improvement over the 1 arcsec value obtained for *Polaris*. It does, however, still produce an error of 230 nm over the axis range. As with *Polaris*, this error will be compensated in software. Finally, the θ-axis roundness was found to vary by as much as 180 nm over the measurement range. This error will also be mapped and compensated.

4.4 PROBE WAVINESS COMPENSATION

Of significant concern for achieving an overall accuracy of 100 nm with Ultraform is the waviness of the probe tip. Typical carbide or ruby probe tips are available with a grade 5 roundness (±5 μin or ±127 nm). This represents an appreciable error, which must be accounted for in each measurement. To eliminate this error, a calibration technique will be used. Each time a probe tip is placed on the machine, a flat will be measured near the θ-axis center of rotation. For a perfectly aligned probe tip with no waviness, there will be no deflection of the LVDT during the measurement. Any displacement will be a combination of misalignment and tip waviness. Since these errors manifest themselves in the same way on the measurement as the calibration (they are distinguishable only by their degree of symmetry), they need not be separated, only mapped and removed from measurement data.

The process of waviness compensation requires that, first, the waviness of the probe tip be evaluated and, second, the result be applied to every subsequent measurement. The unique geometry associated with a polar measuring system allows a certain degree of self calibration. This feature of the profilometer was exploited in *Polaris* to align the instrument's measuring probe with the rotary axis, thus establishing a true polar coordinate system. Two orthogonal alignment errors are identified: radial offset (ρ_0), and tangential offset (τ_0). Radial offset has a straightforward effect on a measurement in that it merely needs to be added to the measured radial position R in order to obtain the correct position.

$$R' = R + \rho_0 \tag{1}$$

The impact on a measurement of the tangential offset is a bit more involved, since it influences both R and θ. The corrected radial position is given by Equation (2).

$$R'' = (R'^2 + \tau_0^2)^{1/2} \tag{2}$$

While the corrected angular position is given by Equation (3).

$$\theta' = \theta + \tan^{-1}\left(\frac{\tau_0}{R'}\right) \tag{3}$$

Waviness (w), on the other hand, is a function of the probe contact angle (γ), which is itself a function of R and θ'. As shown in Figure 4, radial offset error (ρ_0), tangential offset error (τ_0) and waviness error ($w(\gamma)$) are all present in any measurement.

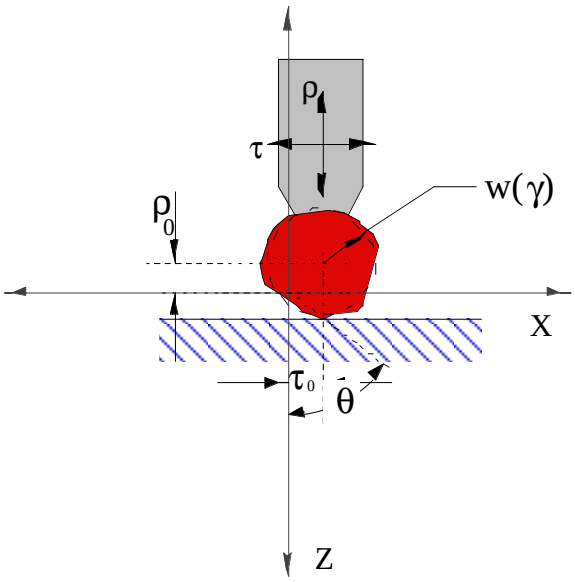

Figure 4. Probe error is a combination of radial offset error (ρ_0), tangential offset error (τ_0) and waviness error ($w(\gamma)$).

4.4.1 WAVINESS EVALUATION

Evaluating the waviness of a given probe tip is inexorably linked to evaluation of probe misalignment. Probe misalignment can be considered as a special case of waviness with a high degree of symmetry. Unfortunately, this does not alleviate the need to find the relative position of the probe tip with respect to the axis of rotation of the rotary stage. A method for evaluating probe tip alignment has been developed that uses a flat surface as a reference standard.

For a probe tip with a radius of r, the probe position will be –r for all positions of θ if the center of the tip is positioned with its center at $\rho = 0$. One means of achieving this is by placing a flat plate ($\lambda/20$) at –r as shown in Figure 5. If the probe is truly centered, the probe output will give only the probe waviness as the rotary axis is traversed through the angular extent of the probe tip.

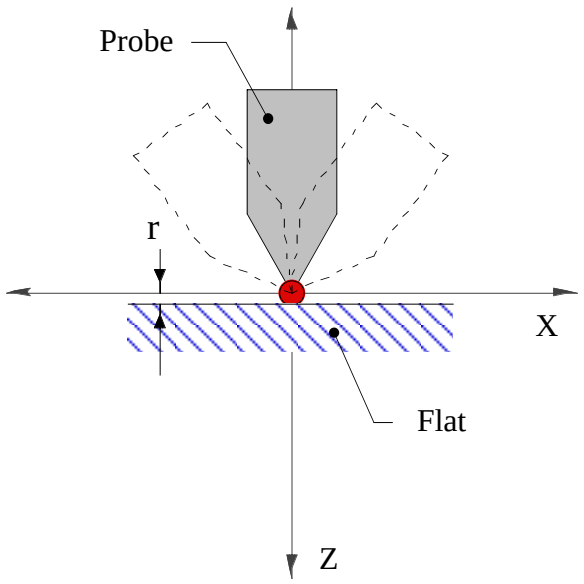

Figure 5. When the probe tip's center is aligned with the machine origin, rotation of the θ axis will yield only waviness data.

However, if there is an offset in either the ρ or τ directions, the probe output will change in a characteristic way for each direction that is a linear combination of all these errors. As shown in Figure 6, for an offset of ρ_0 in the ρ direction, the output of the LVDT will change as a function of the rotary axis position, θ. Equation (4) describes the LVDT response as a function of probe offset and rotation angle.

$$\rho = \rho_0\left(\frac{1}{\cos\theta} - 1\right) \tag{4}$$

After a calibration measurement is performed and ρ_0 is found, the *R* axis zero position can be offset in the control software. In addition to ρ offsets, there can be an offset in the τ direction. This offset produces a different response when measured using the flat method.

The response of the LVDT to a τ offset is a function of θ as shown in Figure 7 can be written as Equation (5).

$$\rho = \tau_0 \tan\theta \tag{5}$$

This characteristic output can be used to detect and correct the offset – this time in the τ direction.

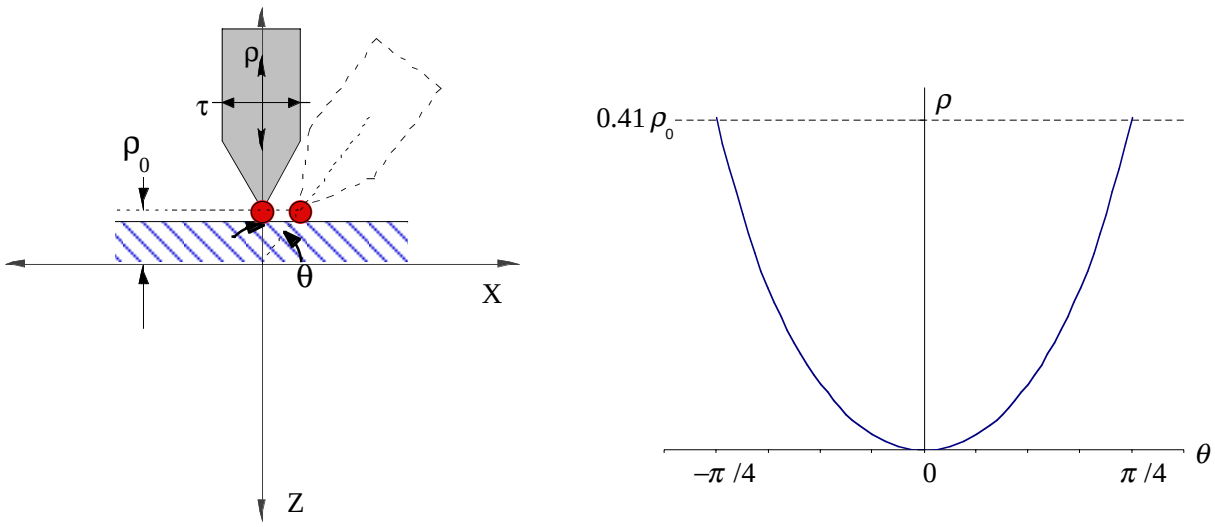

Figure 6. Schematic and plot of LVDT deflection due to an offset of ρ_0 in the ρ direction. The probe response as a function of θ can be used to determine the offset and adjust the machine.

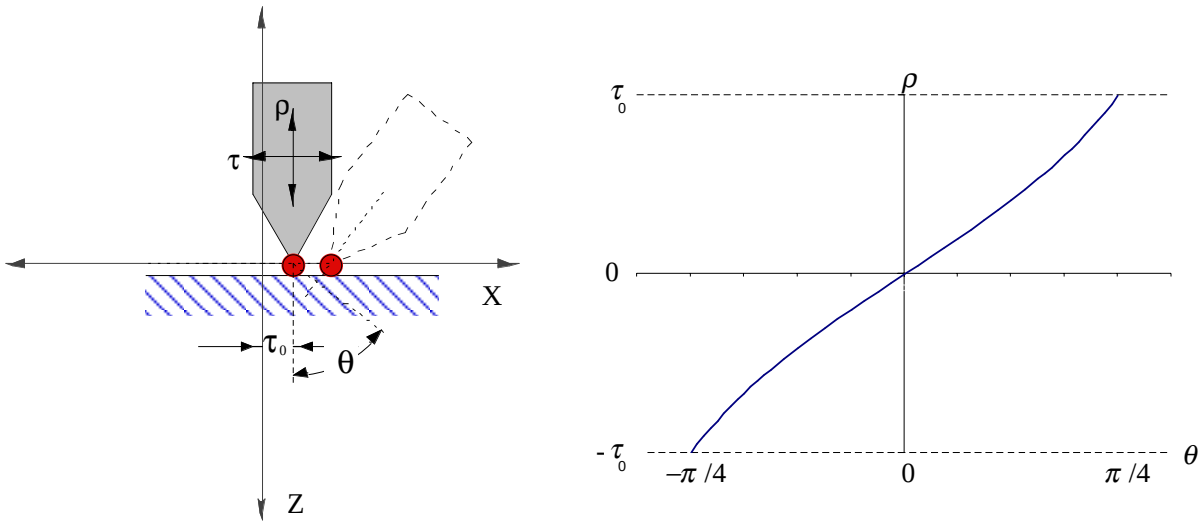

Figure 7. Schematic and plot of LVDT deflection with an offset of τ_0 in the τ direction.

The actual alignment procedure is slightly more complex. A combination of offsets will produce an output of the probe according to the sum of Equations (4) and (5) as shown in Equation (6).

$$\rho = \rho_0\left(\frac{1}{\cos\theta} - 1\right) + \tau_0 \tan\theta \tag{6}$$

Least squares can be used to find the values of ρ_0 and τ_0 that are maximum likelihood estimators for the data from a calibration measurement. The residual error can be considered the waviness of the probe since, for a flat, $\theta = \gamma$.

The disadvantage of this method is that, for large amounts of waviness, the determination of ρ_0 and τ_0 via a curve fit can be affected, increasing uncertainty in the location of the rotary axis center. Fortunately, by limiting the magnitude of the waviness to ±125 nm, the influence on the fit is minimized.

4.4.2 Error Correction

Once the tip waviness and probe alignment errors are known, data from subsequent measurements can be corrected in software. None of the errors are of sufficient magnitude to require real-time alteration of probe position during a measurement. Gauge misalignment and nonlinearity are easily corrected by applying their compensation formulas sequentially. Once the misalignment errors have been compensated using Equations (1-3), the procedure for probe radius and waviness correction is similar to that of modifying a tool path prior to a machining process. An important difference for a metrology instrument is that for each point in the data file the direction cosines of the correction vector must be estimated from the data itself.

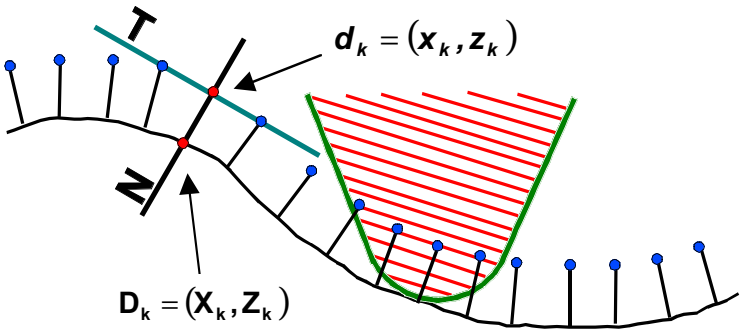

Figure 8. As the probe tip traverses the surface, the contact angle changes. This contact angle can be determined from the slopes of the interpolated line segments between data points.

Figure 8 illustrates the procedure for estimating a sequence of surface data points, $\mathbf{D_k}$, from probe center locations, $\boldsymbol{d_k}$. In its most basic form, the probe radius correction and waviness compensation is numerical and requires a minimum of three data points. The first step is to estimate the surface normal vector at each probe center location. The normal vector (**N**) at a point, $\boldsymbol{d_k}$, cannot be calculated directly, but it can be estimated as a perpendicular to the line segment (**T**) through $\boldsymbol{d_k}$ that connects $\boldsymbol{d_{k-1}}$ and $\boldsymbol{d_{k+1}}$. The slope of **T**, m_k is given by Equation (7).

$$m_k = \frac{z_{k+1} - z_{k-1}}{x_{k+1} - x_{k-1}} \tag{7}$$

The inverse of this point slope is the slope of the normal vector, **N**. By substituting m_k and d_k into the point-slope form of the normal line given in Equation (8), the location of the corresponding surface point, $\mathbf{D_k}$, can be found.

$$Z_k - z_k = m_k\left(X_k - x_k\right) \tag{8}$$

Considering waviness as a polar variation in probe radius, a combined correction for probe radius and waviness is found using Equations (9) and (10) to find the components of $\mathbf{D_k}$, namely X_k and Z_k.

$$X_k = x_k + r(\gamma)\cdot\frac{m_k}{\sqrt{m_k{}^2+1}} \tag{9}$$

$$Z_k = z_k + r(\gamma)\cdot\frac{-1}{\sqrt{m_k{}^2+1}} \tag{10}$$

The function $r(\gamma)$ is the probe radius as a function of contact angle or the sum of the nominal probe radius r and the waviness $w(\gamma)$.

$$r(\gamma) = r + w(\gamma) \tag{11}$$

The contact angle γ is a function of the local slope m_k and the probe angular position, θ'.

$$\gamma = \theta' - \tan^{-1}\left(-\frac{1}{m_k}\right) \tag{12}$$

The special cases of zero or infinite slope are easily detected before applying Equation (12) and compensated by adding $r(\gamma)$ to $\boldsymbol{x_k}$ if the slope is zero or $\boldsymbol{z_k}$ if the slope is infinite.

For smooth surfaces with slowly varying slopes this process is relatively straightforward and effective. However for high aspect surfaces, care must be taken to design a filtering process that removes the effects of noise without obscuring the presence and location of important surface features. The effect of probe waviness on measured data is a convolution of the probe and the actual surface. Although implemented iteratively as a filtering process, the extraction of corrected surface data from measured data is equivalent to spatial deconvolution. As such, the techniques developed for scanned probe microscopy are relevant to our implementation [3].

4.5 CONCLUSION

The commercial prototype of Ultraform 2D is expected to be completed by June 2004. The principal tasks that have not been completed are: implementation of LVDT following, enhancement of the user interface to accommodate controller level code changes and probe waviness compensation. Production versions will follow and the control system may be ported to the QNX-based UPX controller platform by Precitech. The prototype will returned to the PEC and used as a development platform for the Ultraform 3D, for full 3D profilometry.

REFERENCES

1. Sohn, A., K.P. Garrard and T.A. Dow, The Polar Profilometer *Polaris*. Proceedings of the American Society for Precision Engineering Sixteenth Annual Meeting, **v. 25**, pp. 28-31 (2001).
2. Sohn, A. and K.P. Garrard, The Polar Profilometer *Polaris.* 2001 Precision Engineering Center Annual Report, **v. 19**, pp. 1-15 (2002).
3. Villarrubia, J.S., Algorithms for Scanned Probe Microscope Image Simulation, Surface Reconstruction, and Tip Estimation. Journal of Research of the national Institute of Standards and Technology, v. 102, n. 4, pp. 425-454 (1997).

5 DEVELOPMENT OF HIGH-SPEED, LOW AMPLITUDE FAST TOOL SERVO

Nathan Buescher
Graduate Student
Thomas A. Dow
Professor
Mechanical Engineering Department

An overview of the development of a high-speed fast tool servo is presented. The technical challenges of the project are enumerated and addressed. A comparison of drive techniques is included and a preliminary decision is made. Finally, calculations are used to show the feasibility of the project, and future work to be completed is explained.

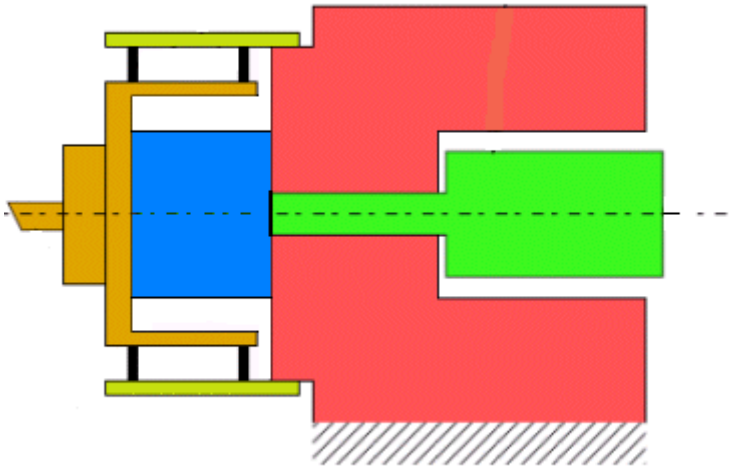

5.1 INTRODUCTION & BACKGROUND

Machining surface features onto a part has always been a need of the manufacturing industry. These features may be used to obtain a desired optical property, texture or design. Often, these features are very small, even on the order of micrometers, and must be machined onto a very large surface. That is where a fast tool servo can be used. This tool, when used in conjunction with a diamond turning machine, will produce minute features on a work surface. The higher the frequency of the fast tool servo, that is, the faster it can "get to the next feature," the more productive and efficient the entire cutting process can be.

The objective of this project is to design and build a high-speed fast tool servo to create features on a surface during a diamond turning operation. These features are to be created at frequency of 10 KHz or greater and be at least 5 μm peak-to-valley.

The PEC has built a number of piezoelectrically driven fast tool servos over the past 20 years. The first device was part of a diamond turning machine designed and built in the Center, the second was a long range actuator (100 μm range) for Oak Ridge National Labs and the third was a low-amplitude system built for Los Alamos National labs used to generate harmonic or random features (10 μm P-V) on sub-millimeter diameter targets for laser Inertial Confinement Fusion experiments. Each of these designs was based on a common theme: a cylindrical high-voltage piezoelectric element preloaded by a diaphragm, a capacitance gage for position feedback and a tool holder for a standard diamond tool. These actuators were integrated into a digital controller with closed-loop feedback from the capacitance gage to reduce the hysteresis in the actuator and improve the fidelity of the machine features.

Specifically there were three PEC projects that have a direct bearing on the proposed FTS*TURBO*: the first is the fast tool servo, the second is the actuator built for the elliptical vibration assisted machining and the third is the ultrasonic actuator motor. Each of these will be described below.

5.1.1 FAST TOOL SERVOS

When the PEC began operation in 1983, one area of emphasis was feedback control of the repeatable errors in a precision machining operation. The first technique pursued was the use of a fast tool servo to correct for spindle errors. To that end, a machine tool called the PAUL (Parallel Axis Ultra-precision Lathe) was built. This machine used a pair of vertical axis, airbearing pindles: one holding the workpiece and the second holding the tool with on a swing arm that could pass over the workpiece. This geometry produced a compact yet rigid design. Integral with this machine was a Fast Tool Servo (FTS) powered by a piezoelectric actuator. This servo was built into the arm to change the depth of cut. A photograph and a cross-section of the actuator are shown in Figure 1. This FTS has a range of motion of 20 μm and a first natural frequency on the

order of 8 KHz. The closed loop bandwidth - the maximum speed for controlled motion – is approximately 2 KHz. The size of the unit is about 100 mm long and 50 mm high. The cutaway shows the piezoelectric actuator (a hollow cylinder with an OD of 25 mm, ID of 13 mm and a length of 18 mm) that moves the tool holder and the cylindrical diaphragms that guide the tool holder in a linear motion. A capacitance gage is inserted through the center of the piezoelectric element to sense the position of the tool. This position measurement is used as feedback in the digital controller to reduce the error due to hysteresis and other disturbances. This servo has been in continuous operation since it was built in 1988.

A second FTS with a similar design was built for Los Alamos National Labs (LANL) in 1996. The actuator length was shorter (12.7 mm) and the system had a slightly higher natural frequency of 9500 Hz. This actuator has been used at LANL to fabricate sine wave features on 0.5 mm diameter aluminum targets that are used in Inertial Confinement Fusion experiments at Lawrence Livermore Labs and the University of Rochester. The goal was to produce 1 µm P-V sine waves with less than 10 nm form error. The FTS was able to achieve the goals but the maximum operating frequency was on the order of 1000 Hz.

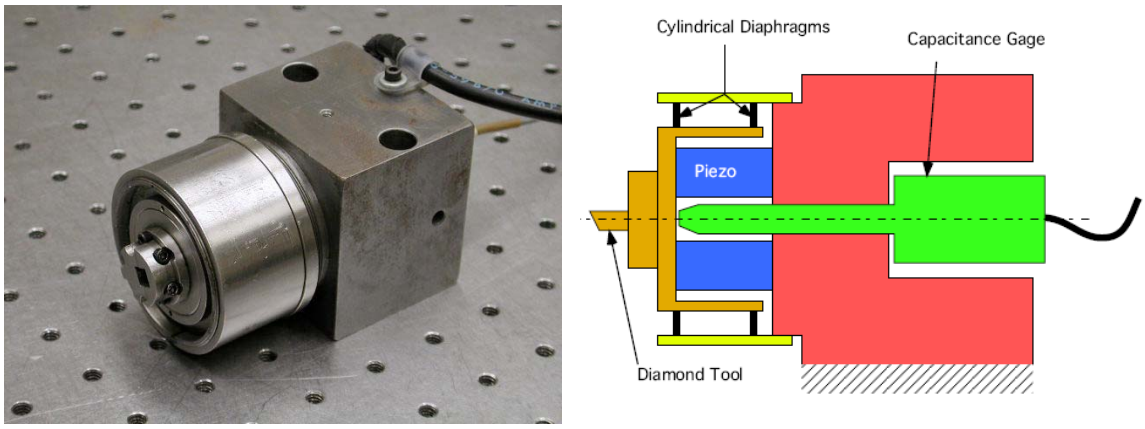

a) Photo of the Fast Tool Servo b) Cross section of the actuator

Figure 1. Fast tool servo used at the PEC

5.1.2 ELLIPTICAL VIBRATION ASSISTED MACHINING (*EVAM*)

A new technique for precision machining of ferrous and ceramic components is to add vibration to the tool motion to change the chip geometry and bring the tool tip out of contact with the part. For *EVAM*, the motion of the tool cutting edge is a combination of the elliptical motion of the actuator and the linear motion of the workpiece. The goal of the recent work at the PEC was to understand the effects of the size and frequency of this elliptical tool motion. To create a

versatile actuator, the structure was designed to operate below its first natural frequency so that the shape and magnitude of the motion could be easily changed.

Two generations of piezoelectric tool holders were built at the PEC to study the *EVAM* process. They are both shown in Figure 2. The first (shown in the background) used long, cylindrical actuators to create elliptical motion of a standard diamond tool. The maximum operating frequency of this system was less than 500 Hz. Significant experience was gained with this design that led to the second-generation system shown in the foreground. This new design has a hollow alumina tool holder that combines lightweight with high-stiffness and includes a fluid cooling system to allow continuous high-speed operation. The Generation II device can displace the tool in an elliptical or circular path with a maximum stroke of the major and minor axes of 60 µm and 10 µm respectively for frequencies up to 5,000 Hz or the equivalent of 300,000 rpm for a single flute flycutter.

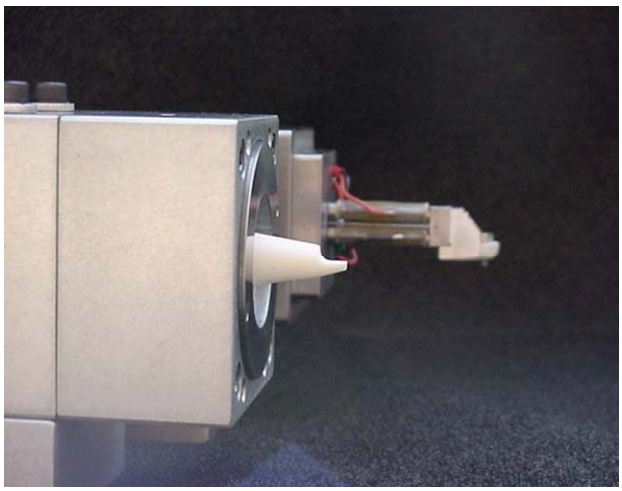

Figure 2. Photograph of UltraMill Generation II (foreground) and Generation I (background)

The hollow ceramic tool holder with a glued-in diamond tool was a key technology for increasing the natural frequency of the system. The total mass of the tool holder is on the order of 3 grams compared to 200 grams for the FTS described in Figure 1. The tool is 1x1x5 mm in size and is glued into a groove in the ceramic holder using epoxy. To remove the diamond for resharpening the holder is heated to soften the glue. This is a technique that is used often and will be an important part of the new FTS*TURBO* design.

5.1.3 ULTRASONIC PIEZOELECTRIC ACTUATOR

To achieve the high speed needed for the proposed FTS*TURBO* design, different actuator designs need to be considered. One example is the high-speed piezoelectric actuator that was developed

as a compact drive system for linear or rotary motion. Several designs were evaluated and the best is shown in Figure 3.

This actuator utilizes longitudinal and bending motions of a piezoelectric material, each driven by a sine wave of the same frequency to move the slideway. The longitudinal vibration mode changes the load on the surface and the bending mode moves the tip along the direction of motion of the slide. The direction of motion coincides with the bending displacement at the high normal load and a change in the phase of the bending displacement will reverse the direction. The tip of the device displaces about 1 μm in an elliptical path at one of the system's resonant frequencies at 50 KHz. By changing the phase of the tangential and longitudinal vibrations, the shape of the path can be changed.

This design indicates the potential of piezoelectric designs to operate at high frequency. A photograph of the ultrasonic actuator is shown in Figure 4. This picture calls attention to the way that the actuator is attached to the support structure. For a machining configuration, two changes are necessary. First, a diamond tool must be attached to the end of the actuator. The Ultramill described previously used a ceramic (Al_2O_3) holder into which the tool was glued. The actuator shown could also be configured in this manner. Second, the support structure must be more rigid than the design shown in Figure 4. One solution is to create supports on both sides of the actuator at the front node (see the mode shapes in Figure 3).

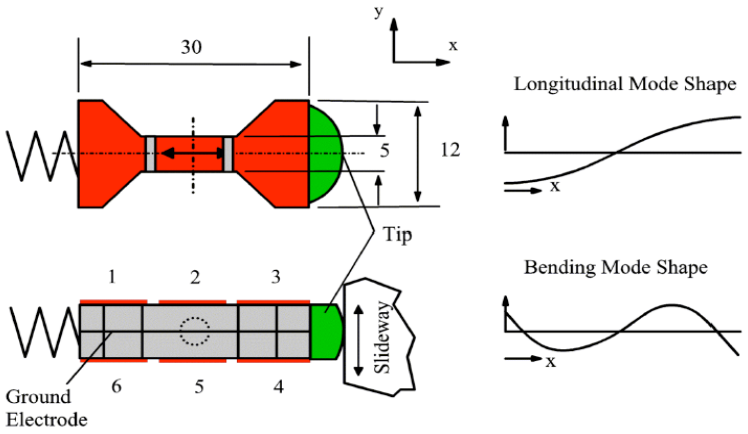

Figure 3. Ultrasonic piezoelectric actuator design. The numbers in the side view (a) indicate the size of the actuator in mm. This design has three active elements and the six electrodes are indicated in the top view (b). The graphs at right are the mode shapes at 50 Khz.

Figure 4. Photograph of ultrasonic actuator with flexures for loading against slideway.

The actuator shown in Figures 3 and 4 operates at a resonant frequency well above the first mode; and as a result, the motion cannot be controlled in real time. The goal was to design the shape of the actuator that will produce the mode of operation desired. However, this design emphasizes the experience of the PEC in producing high-speed piezoelectric actuators and the experience gained will be valuable in producing the desired system.

5.2 TECHNICAL CHALLENGES

The design of an actuator capable of 5 μm stroke with a closed-loop bandwidth of 10 KHz will be a challenging undertaking. The specific technical challenges to be addressed are described below. The solution to these challenges is the subject of the Plan of Work that follows.

5.2.1 ACTUATOR AND TOOL HOLDER DESIGN

A high-speed fast tool servo capable of producing a 5 μm stroke with a bandwidth of at least 10 KHz implies a natural frequency of five times that value and pushes the design envelope for weight and stiffness. To meet these performance specifications, the actuator must be carefully chosen. Different piezoelectric designs developed at the PEC were discussed in the last section. Piezoelectric elements are attractive for their small size but hysteresis can create heating problems that must be addressed. New piezoelectric materials with reduced hysteresis as well as temperature control schemes used in previous designs will be evaluated. Whatever the drive system, the moving mass must be kept as light as possible to retain a high natural frequency. System natural frequency and heat generation will be the main factors limiting the maximum operating frequency of the fast tool servo.

Other actuators that are being considered for FTS operations are both linear and rotary electric motors. Two different designs were described at the recent ASPE meeting [1,2]. To provide the required force and stiffness, these devices are relatively large, consume enough power to get hot and have not yet demonstrated the bandwidth required in this project. However, the advantages and disadvantages of such drive systems will be evaluated based on the published results.

5.2.2 POSITION FEEDBACK AND CONTROL

The motion of the tool will have gain and phase differences with respect to the commanded motion as a result of the electromechanical system that drives it and a controller must be used to ensure the accuracy of the cutting path. The control strategy can take two forms: open loop and closed loop. Closed loop control uses the known dynamics of the electromechanical system with feedback from the cap gage to modify the input signal to maximize rise time but reduce overshoot and steady state error. Open loop control can be used to modify the input signal to correct it for the effects of gain error and phase delay for multi-frequency signals. Panusittikorn, Dow and Garrard are working on a project [3] that should improve the fidelity of the surface features at speeds approaching the natural frequency of the actuator. The results of this work will be incorporated into the controller implementation.

The closed-loop controller for the servo uses the feedback from the capacitance gage to position the tool. This controller can reduce the effect of steady state errors due to signal gains or actuator nonlinearities as well as correct for external disturbances introduced to the actuator system. To design the control algorithm, a generalized block diagram must be created that includes the amplifier, actuator, cutting forces, structural dynamics and position feedback. The transfer function for this electromechanical system can be found with the help of the Stanford SR780 Signal Analyzer. The Signal Analyzer generates a sign wave with constant amplitude and varying frequency that is input to the actuator system. It then monitors the output from the cap gage and creates the transfer function (amplitude and phase as a function of frequency) between the input and output of the system. This relationship can then be used to find a control algorithm that will provide optimal response of the tool without undesirable overshoot.

The open loop controller uses the dynamics of the closed loop system to modify the input signal to compensate for different gains and phase lags at different frequencies. For example, if the desired trajectory has components at different frequencies, the electromechanical system will distort this trajectory and produce an error. By modifying the input to include these effects, the error can be reduced.

After design, the controller will be prototyped using the DSpace hardware and the Simulink software available at the PEC. The block diagram with all the control gains is constructed in Simulink and then downloaded to the DSpace CLP1104 processor board to control the system. The position sensor in the FTS sends its data to the DSpace board, which it turn uses it as feedback in the control loop. The DSpace board then outputs the proper voltage to the system, resulting in accurate and controlled tool movement. The CLP1104 can operate at 100 kHz, so the high frequencies of this application will not present any problem.

5.2.3 COOLING SYSTEM

An important natural characteristic of piezoelectric elements is hysteresis. Hysteresis is defined as a loss of energy as a result of reversing driving direction. At high frequencies, the piezo element is reversing quickly, causing much energy to be lost. This energy appears in the system as heat. Too much heat generation can damage the structure, thus making it necessary to use some type of cooling system. Cooling has been used often in high frequency applications, and the analysis involves the use of basic heat transfer relationships. However, it is possible that new reduced-hysteresis materials have eliminated the need for a cooling system. These new materials can operate at very high frequencies with relatively low heat generation. The total heat generation of the selected piezoelectric actuator will be calculated, and an according cooling system, if necessary, will be designed.

5.2.4 COMPONENT LIFE AND RELIABILITY

Piezoelectric actuators have been tested and have shown no loss of performance up to billions of cycles. However, no formula exists to calculate the lifetime of a piezoelectric element due to the many parameters that have a nonlinear influence on performance. These parameters include temperature, humidity, voltage, acceleration, load, operating frequency, and insulation materials. It is imperative that a suitable orientation of the actuator and an optimized set of working conditions are chosen to maximize its life.

5.3 DRIVE TECHNIQUE COMPARISON

One of the first decisions is to select the type of actuator to be used to drive the servo. Many aspects such as size, cost, heat generation, necessary control scheme and potential acceleration are evaluated. The following is a comparison of four different types of actuation: magnetostrictive, Lorentz force, variable reluctance (electromagnetic), and piezoelectric.

5.3.1 MAGNETOSTRICTIVE

Magnetostrictive materials expand when exposed to a magnetic field. Conversely, a strain in these materials will result in a changed magnetic field (also called the Villari effect). This property is caused by magnetic domains inside a material. When exposed to a magnetic field, the randomly oriented domains align, causing a strain in the material. Controlling the initial configuration of the domains through the fabrication processes using thermal annealing and cold working can optimize this effect. Some common magnetostrictive materials include iron, nickel, cobalt, and terfenol.

According to NASA [4], these materials can operate at higher temperatures and generally undergo higher strains with lower input voltages than piezoelectric materials. However, limited work has been done with magnetostrictive materials. Eda [5] developed a magnetostrictive actuator with a 2 μm stroke, although no frequency response was provided for this device. Liu [6] created a 50 μm stroke magnetostrictively actuated tool holder. This system had a natural frequency of 1.5 KHz, but no closed loop bandwidth was specified. Other problems associated with these materials are the fact that they are not easily integrated into a control system and also have a hysteresis effect (heat generation).

5.3.2 LORENTZ FORCE

Another possibility for diamond turning applications is a fast tool servo driven by a Lorentz force actuator (moving-magnet galvanometer). One application of this drive technique is a rotary servo. This type of servo is especially useful for machining spherical workpieces. The tool holder is placed on a rotational axis attached to the base structure. This enables the tool to access a spherical piece at its pole as well as its equator, as shown in the figure below.

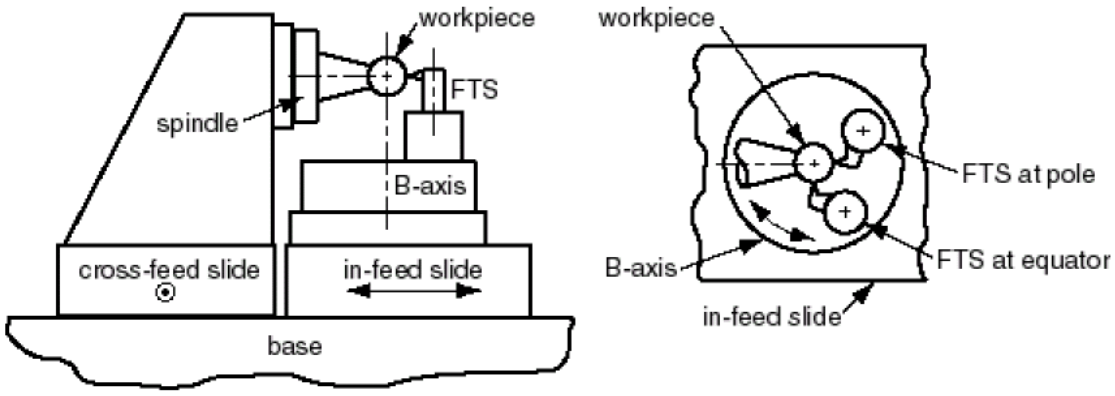

Figure 5. An example of a rotary fast tool servo set up for operation on a two-axis lathe. Side view (left). A top view (right) shows the servo's ability to engage the workpiece at its pole and equator by rotation about the B-axis.

A rotary servo offers other attractive qualities as well. The reaction forces created during the cutting process are significantly reduced when compared to a more traditional linear servo. A balanced rotary design can essentially eliminate linear reaction forces, leaving only torque forces. Also, it is claimed that rotary servos have higher achievable accelerations, lower cost,

and a more compact size than a linear FTS [7]. Finally, heat generation is not an issue for this type of drive technique.

Much literature exists on this type of actuation. Douglass [8] developed a linear slide fast tool servo. It was powered by a large voice coil motor. The stroke was 500 μm and it has a 100 Hz bandwidth. Greene and Shinstock also developed a linear voice coil based fast tool servo [9]. This FTS had a very large stroke of 6mm. However, the bandwidth was only 100 Hz. Due to the low bandwidth and low mass, the dynamic system of the system was so low that the design was not feasible for cutting applications. Todd and Cuttino [10] built a long range FTS with a stroke of 1 mm at 20 Hz . It was driven through a rotary motor through a steel ribbon. Ludwick and Trumper developed a rotary FTS with a bandwidth of 200 Hz, 50 G peak acceleration, and a stroke of 30 mm [11]. This servo was driven by a commercial brushless motor and had a resolution on the micrometer scale. Additionally, the use of a balanced rotary design cancelled reaction forces.

Although designs using Lorentz force actuators have had success in the past, there are some problems associated with this type of drive technique. The maximum achievable acceleration of the motor is severely limited by the heat generated and the magnetic flux density. The acceleration of this type of actuator falls below 100 G's in the literature. This value is considerably less than the necessary 1000 G's needed for operation at 10 KHz with a 5 μm stroke.

5.3.3 VARIABLE RELUCTANCE

Another design that has been introduced is that of a variable reluctance (electromagnetically driven) fast tool servo. This design is based around an armature that is push-pull driven by two high frequency solenoids. A high bandwidth linear power amplifier powers these solenoids. Attached to the armature is a very light moving mass and cutting tool, and position feedback is obtained with a capacitance gauge observing the back of the armature. A general schematic of the design is shown below.

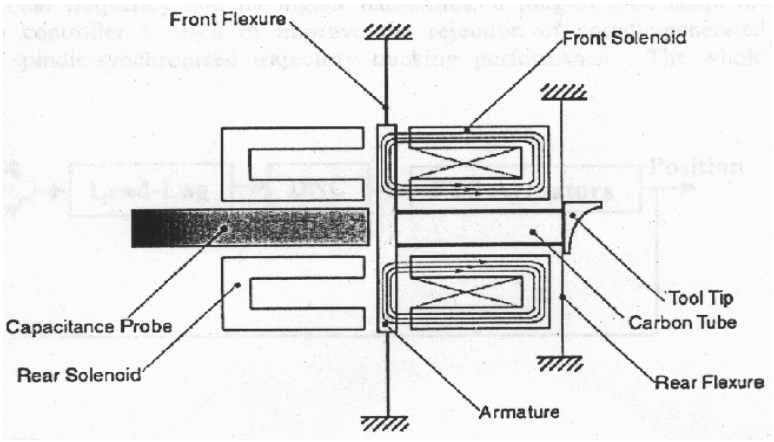

Figure 6. A schematic for an electromagnetically driven FTS

Not many researches have focused on variable reluctance actuators, most likely because of the inherent non-linearity in such a system. Gutierrez and Ro [12] developed a magnetically driven fast tool servo with a stroke of 800 μm and a bandwidth of 100 Hz. However, the control scheme used to improve the tracking performance had a negative effect on the resolution. Currently, Liu et al are developing a prototype with proposed specifications of a 50 μm stroke and 20 KHz bandwidth [2].

There is no doubt that very high accelerations are achievable with the use of electromagnetic actuators. Additionally, no problems with heat generation were described in the literature. However, because of the inherent nonlinearity of the actuating force (proportional to the current squared, inversely proportional to the air gap squared), the system is very hard to control. Another problem with this method is the induced Eddy currents by the high frequency magnetic field. These currents may reduce the force density, limiting the bandwidth. It is therefore necessary to use materials with low conductivity properties in this design.

5.3.4 PIEZOELECTRIC

Piezoelectric materials are those that deform when subjected to an applied voltage and, conversely, produce a voltage when subjected to a mechanical stress. In this way, piezoelectric materials are similar to the magnetostrictive materials described earlier. Because of their high stiffness and high achievable bandwidth and acceleration, most FTS's use piezoelectric actuators.

Much research has been done in this area. Patterson and Magrab designed a FTS with a 2.5 μm and 660 Hz bandwidth [13]. The natural frequency of this design was above 1 KHz. The basis of this servo was a moving cylindrical shell that held in line by two diaphragm flexures. Rasmussen and Tsao used a piezoelectrically actuated FTS for asymmetric turning purposes

[14][15]. The tool was driven with the help of a lever assembly and had a 50 μm stroke and 200 Hz bandwidth. Okazaki developed a fast tool servo with 15 μm stroke, 2.5 KHz bandwidth and 2 nm resolution [16]. A 19 mm long stacked ring piezoelectric actuator was used to achieve a primary resonant frequency of 10 KHz.

Piezoelectric actuators do have some undesirable qualities. One of these is the heat generated due to dielectric loss in the material, also known as hysteresis. Often, a cooling system must be implemented to account for this heat generation. Another problem with piezoelectric actuators is that expensive high-voltage amplifiers must be used to drive the system. However, new innovations in the piezoelectric industry include much smaller piezo stack sizes as well as low voltage/low heat generation materials. These discoveries are very promising for the possibility of creating a FTS with a much higher bandwidth than before.

5.4 PROPOSED DESIGN

Based on preliminary evaluation of the alternatives, it appears that a piezoelectric actuator will best fit this application. The very small sizes that are available (5 X 5 X 9 mm) as well as the development of the low voltage piezo stacks weighed heavily in this decision. This new type of actuator will lead to a compact design in which cooling will likely not be a major issue. Additionally, piezoelectric actuators can be controlled through fairly conventional methods, unlike an electromagnetically driven system. A general schematic of one possible design for a piezoelectrically actuated system is shown in the figure below.

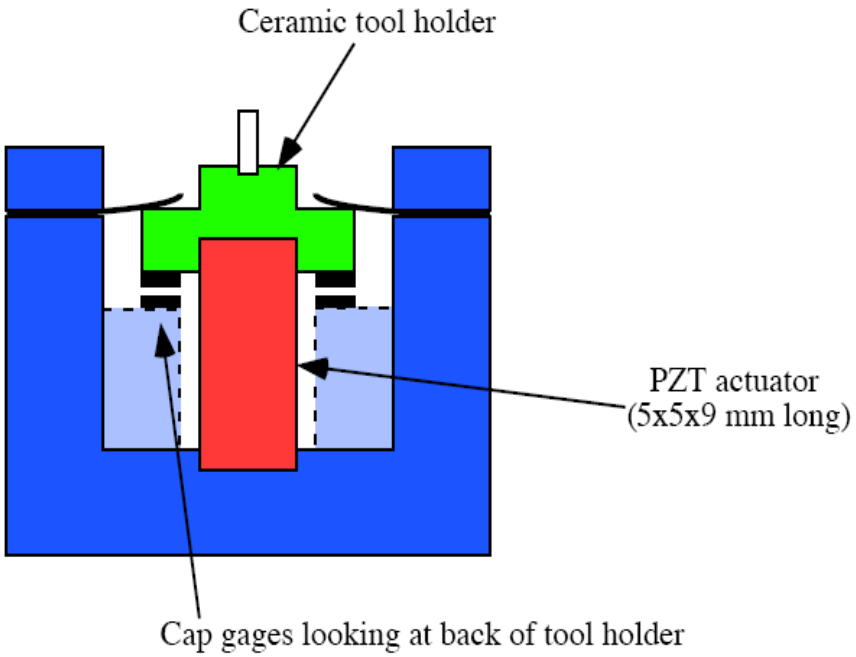

Figure 7. General schematic of a possible piezoelectric FTS

5.4.1 NATURAL FREQUENCY

For the servo to have a bandwidth of at least 10 KHz, it is imperative that the first natural frequency occurs at a much higher value. Through the use of published material properties and estimated values for certain components it is possible to predict the natural frequency of the system. These predictions are shown below for previous projects at the PEC in Table 1. Equation 1 (given below) may be used to obtain the theoretical natural frequency. (Values based on published values for PI-885.10 piezoelectric stack).

$$\omega_n = \frac{1}{2\pi}\sqrt{\frac{k}{m}} \tag{1}$$

$$\omega_n = natural\ \ frequency\ \ (Hz)$$

$$k = piezo\ \ stiffnes\ \ (N/m)$$

$$m = effective\ \ moving\ \ mass\ \ (kg)$$

Substituting values for upcoming project,

$$\omega_n = \frac{1}{2\pi}\sqrt{\frac{115e6\,N/m}{.003\,kg}}$$

$$\omega_n = 31\,KHz$$

Table 1. Properties of previous fast tool servos developed at the PEC.

	Moving Mass (g)	Stiffness (N/μm)	Theoretical Natural Frequency (KHz)	Experimental Natural Frequency (KHz)
FLATS	225	720	9	8
TARGIT	100	484	11	9.3
FTS_{turbo}	3	115	31	???

This value for the natural frequency of the FTS_{turbo} is considerably higher than the desired bandwidth and should be acceptable.

The phase lag associated with operation at 10 KHz for this system is given in Equation 2.

$$\phi = 2\tan^{-1}(\frac{f}{f_0})$$
$$\phi = \textit{phase angle} \ (\text{deg}) \qquad (2)$$
$$f = \textit{operating frequency} \ (Hz)$$
$$f_0 = \textit{resonant frequency} \ (Hz)$$

Substituting,

$$\phi = 2\tan^{-1}(\frac{10000}{31000})$$
$$\phi \approx 37°$$

Traditional control techniques should be able to compensate for this amount of phase lag.

5.4.2 PEAK FORCE

The maximum force created by the servo motion is an important calculation, as it will be used to determine the preload of the piezoelectric actuator. A preload is important because such actuators are not designed to act in tension. The maximum force (based on 10 KHz operation) is given in Equation 3.

$$F_{\max} = mA\omega^2$$
$$m = \textit{effective moving mass} \ (kg) \qquad (3)$$
$$A = \textit{amplitude of motion} \ (m)$$
$$\omega = \textit{frequency of operation} \ (Hz)$$

Substituting,

$$F_{\max} = (.003kg)(2.5e-6\,m)(2\pi * 10000Hz)$$
$$F_{\max} = 29.6\,N$$

This force will be multiplied by a safety factor but should not be so large as to be a problem.

5.4.3 HEAT GENERATION

It is also important to determine the heat generated by the piezo. If it produces too much heat, another alternative must be used. However, a cooling system may be developed to account for a modest amount of heating. This calculation is obtained through the use of Equation 4.

$$Q = K\frac{cV^2 f}{2}$$

$$K = proportion\ \ of\ power\ lost\ to\ heat \tag{4}$$

$$c = capaci\ \tan ce\ of\ piezo\ (F)$$

$$f = frequency\ \ of\ operation\ \ (Hz)$$

$$V = voltage\ \ (V)$$

Substituting,

$$Q = .25\frac{(0.6e-6F)(100V)^2(10000Hz)}{2}$$

$$Q = 7.5\ Watts$$

This is not a huge amount of heat generation. However, the very small size of the piezoelectric stack will mean a considerable rise in temperature. This temperature change is given by Equation 5.

$$\Delta T = \frac{Q}{mC}$$

$$m = mass\ \ (kg)$$

$$C = specific\ \ heat\ \ (\frac{J}{kg\cdot °C}) \tag{5}$$

$$Q = heat\,in\ system\,(Watts)$$

$$\Delta T = change\,in\,temperature\ (°C/\sec)$$

$$\Delta T = \frac{7.5Watts}{(.003kg)(430\frac{J}{kg\cdot °C})}$$

$$\Delta T = 5.8°C/\sec$$

The small surface area of the piezoelectric stack will make it difficult to remove the required amount of heat with room temperature air. A cool air convection system or some type of fluid cooling system will most likely have to be implemented to control the temperature of the system.

5.5 CONCLUSIONS

Research as well as basic calculations show that a piezoelectric actuator will indeed be suitable for this application. This type of material provides a high natural frequency without generating a very large amount of heat. While a foundation has been laid, much work remains to be done. Each challenge enumerated above must be carefully considered. Future work includes plans to design the housing and moving sections of the FTS, design and implement a control scheme, and create a cooling system, if necessary. The system will then be rigorously tested under a variety of different conditions to assess accuracy. Final adjustments will be made, and an in depth thesis will be written which describes all phases of the project in detail.

REFERENCES

1. Montesanti, R. and Trumper D, "High Bandwidth Short Stroke Rotary Fast Tool Servo", Proceedings 2003 ASPE Annual Meeting, Portland, OR.
2. Lu, X. and Trumper, D, "Electormagnetically Driven Fast Tool Servo", Proceedings 2003 ASPE Annual Meeting, Portland, OR.
3. Panusittikorn, W., Garrard, K. and Dow, T, "Surface Deconvolution for Diamond Turning", Proceedings 2003 ASPE Annual Meeting, Portland, OR.
4. NASA "You Decide" tutorial. http://virtualskies.arc.nasa.gov/research/youDecide/magnetoStrictive.html
5. H. Eda et al, "Ultra-precise machine tool equipped with a giant magnetostriction actuator – development of new materials and their application," in *CIRP annals*, Vol. 41, No. 1, pp. 421-424, 1992.
6. D. Liu et al, "Surface texture improvement in the turning process via application of a magnetostrictively actuated tool holder," in *ASME Journal of DSMC*, 120:193-199, 1998.
7. Trumper, David L. et al, "Calibration and Control of a Rotary Fast Tool Servo", Proceedings 1999 ASPE Annual Meeting.
8. S. S. Douglass, "A machining system for turning non-axis-symmetric surfaces," Ph.D. thesis, the University of Tennessee, Knoxville, 1983.
9. W. Greene, D. Shinstock, "Design of a linear voice coil actuator for fast tool servo applications," in Proceedings of ASPE 1995 annual meeting.
10. M. W. Todd, J. F. Cuttino, "Development of a long range, traction drive fast tool servo for diamond turning applications, " in Proceedings of ASPE 1997 annual meeting.
11. S. J. Ludwick, "A rotary fast tool servo for diamond turning of asymmetric optics," in *International Progress in Precision Engineering: Proceedings of 8th International Precision Engineering Seminar*, MIT PH.D. thesis, Cambridge, Massachusetts, 1999.
12. H. M. Gutierrez and P. I. Ro, "Parametric modeling and control of a long-range actuator using magnetic servo-levitation," in *IEEE Tran. on Magnetics*, Vol. 34, No. 5, 1998,

13. S. R. Patterson, E. B. Magrab, “The design and testing of a fast tool servo for diamond turning,” in *Precision Engineering*, Vol. 7, No. 3, pp 123-128, 1985.
14. J. D. Rasmussen et al, “A piezoelectric tool servo system for variable depth of cut machining,” in *Precision Machining: Technology and Machine Development and Improvement*, Volume PED-58, page 119-130, ASME 1992.
15. J. D. Rasmussen et al, “Dynamic variable depth of cut machining using piezoelectric actuators,” in *International Journal of Machine Tools and Manufacture*, 34(3): 379-392, 1994.
16. Yuichi Okazake, “Fast tool servo system and its application to three dimensional fine surface figures,” in Proceedings Of ASPE 1998 annual meeting.

6 FORCE FEEDBACK CONTROL OF TOOL DEFLECTION IN MINIATURE BALL END MILLING

David W. Hood
Graduate Student
Gregory D. Buckner, Thomas A. Dow
Department of Mechanical and Aerospace Engineering

This research demonstrates that force feedback can be used to predict tool deflection and compensate for deflection during the milling operation, reducing susceptibility to uncertainties in model parameters and workpiece alignment. Two specific force feedback approaches are presented here: cutting depth prediction (based on a non-dynamic cutting force model) and tool deflection prediction (using a non-dynamic model of tool stiffness). Real-time control algorithms incorporating both methods were implemented and evaluated on a high-speed air-bearing spindle. A non-dynamic tool force model developed previously at the Precision Engineering Center used measured forces to predict depth of cut. A separate tool stiffness model was developed to predict tool deflections (axial and radial) based on measured forces. Experiments involving machined grooves in hard steel workpieces, including simple slotting cuts and three-dimensional finishing operations, were conducted at various tool tilt angles to evaluate the effectiveness of force feedback control. Results indicate that profile errors can be reduced up to 80% compared to non-compensated cases. These results confirm that real-time force feedback control can significantly improve the dimensional tolerance and accuracy of injection molds created using miniature ball end mills.

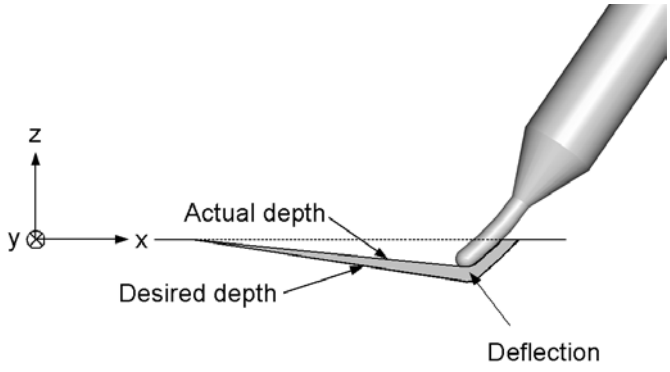

6.1 INTRODUCTION

Injection molding is an important manufacturing process for optical and mechanical components. The hard steel dies used in this process play a direct role in the quality of molded parts. Traditionally, fabricating these dies involved rough milling followed by heat treatment, grinding, and polishing to the desired shape. Recently, high-speed machining of heat-treated steel (hardness > 55 R_c) has become a viable approach for reducing fabrication times while retaining the necessary shape control. However, as feature sizes drop below 1 mm with dimensional tolerances on the order of 10 μm, tool deflection can create significant errors in the shape of mold surfaces. Deflections associated with miniature ball end tools can exceed 30 μm, rendering finished dies out of tolerance.

To date, most of the research associated with milling tool deflection compensation has involved open-loop techniques that use non-dynamic models of the cutting process to modify the desired tool path prior to cutting [3, 4, 5, 6, 7]. Research conducted at NCSU's Precision Engineering Center (PEC) resulted in open-loop correction techniques for tool deflection of miniature ball end mills [2]. This effort used a non-dynamic tool force model developed for diamond turning and modified it for ball end milling. These modeled cutting forces were used to predict tool deflections for specified machining conditions, and to modify the tool path before cutting. The specified tool path, together with a CAD model of the workpiece surface, were used to determine the depth of cut, feed rate, and normal cutting force vector. This information was then used to predict the magnitude and direction of cutting forces and tool deflections, which were used to modify the tool path off-line (prior to cutting). Form errors were reduced from 50 μm to less than 10 μm with accurate knowledge of the cutting conditions and parameters.

Despite the promising results obtained from off-line tool deflection prediction and open-loop compensation, these methods rely on accurate models of the cutting process and cannot adapt to changes in model parameters, disturbances in the cutting process, or uncertainties associated with workpiece alignment. Thus, open-loop compensation results are only as accurate as the assumed model parameters and workpiece characteristics. For example, a worn tool may have wearland and radius dimensions different than expected or the workpiece may be inaccurately positioned, resulting in cutting depths that are larger or smaller than expected. Critical model parameters such as tool wearland, workpiece material properties, and instantaneous spindle speed are difficult to estimate, and may change dramatically during milling.

This report demonstrates that force feedback can be used to predict tool deflection and compensate for deflection during the milling operation, reducing susceptibility to uncertainties in model parameters and workpiece alignment. Two specific force feedback approaches are presented here: cutting depth prediction (based on a non-dynamic cutting force model) and tool deflection prediction (based on a non-dynamic model of tool stiffness). Real-time control

algorithms incorporating both methods were implemented and evaluated on a high-speed air bearing spindle. A non-dynamic tool force model developed previously at the PEC used measured forces to predict depth of cut. A separate tool stiffness model was developed to predict tool deflections (axial and radial) based on measured forces. Experiments involving machined grooves in hard steel workpieces, including simple slotting cuts and three-dimensional finishing operations, were conducted at various tool tilt angles to evaluate the effectiveness of force feedback control. Results indicate that profile errors can be reduced up to 80% compared to non-compensated cases. These results confirm that real-time force feedback control can significantly improve the dimensional tolerance and accuracy of injection molds created using miniature ball end mills.

6.2 MODELING TOOL FORCES AND DEFLECTIONS

The tool force model developed by Clayton [12] can be used to calculate cutting and thrust forces during milling operations. Inputs to this model include material properties and friction at the rake and flank faces of the tool. Tool geometry and cutting conditions are used to find the cross-sectional area of the chip and the area of contact between the flank face of the tool and the workpiece. The model can be expressed:

$$F_c = \frac{35WA_C}{3}\left(\frac{\cot(\gamma)}{\sqrt{3}}+1\right)+\mu_f A_f\left(21.7W\sqrt{\frac{1505W}{E}}\right) \quad (1)$$

$$F_t = \frac{35\mu WA_C}{3}\left(\frac{\cot(\gamma)}{\sqrt{3}}+1\right)+A_f\left(21.7W\sqrt{\frac{1505W}{E}}\right) \quad (2)$$

where:

F_c = cutting force
F_t = thrust force
A_c* = cross-sectional area of the chip
A_f* = area of the tool flank face
μ_f = friction coefficient on the flank face
μ = friction coefficient on the rake face
W = volumetric work
ϕ = shear angle in the workpiece
E = Young's modulus of the workpiece
*

These forces rotate with the flank face of the milling tool, but can be readily converted to orthogonal forces (in the x, y, and z machine directions) for comparison to experimental measurements using the three-axis load cell.

*parameter is a function of depth, *d*, and feedrate

6.2.1 MEASURED TOOL FORCES

Preliminary cutting experiments were conducted on a Nanoform 600 Diamond Turning Machine (DTM) (Figure 1) to validate the tool force Equations (1) and (2). Cutting forces were measured using a Kistler three-axis piezoelectric load cell, shown in Figure 2. This load cell was mounted below the workpiece on the x-axis of the diamond turning machine, while the high-speed spindle was mounted on the y-axis slideway (Figure 1). Experimental results for an S-7 steel workpiece machined at a spindle speed of 10,000 rpm, a feed rate of 100 mm/min, a tool tilt of 25 degrees with respect to the z-axis, and a cutting depth of 100 µm, are presented in Figure 3.

Figure 1: Nanoform DTM machine and setup

Figure 2: Workpiece mounted on three-axis piezoelectric load cell

This plot compares modeled cutting forces with measured cutting forces for a single revolution of the tool. The z-component of force in Figure 3 is dominated by thrust force (2). The x and y force components are influenced more by cutting force (1), which rotates in the plane of the workpiece and changes from an x-direction force to a y-direction force every quarter rotation of the tool.

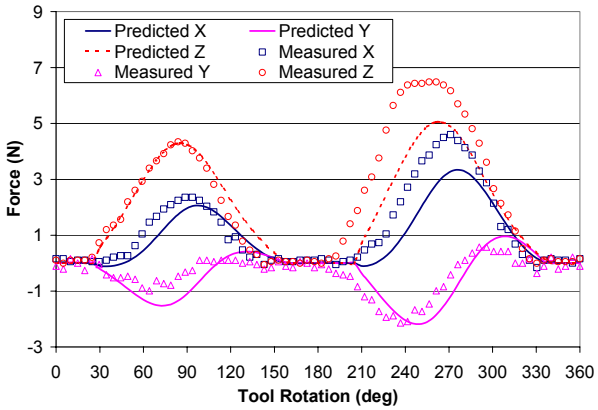

Figure 3: Measured and predicted orthogonal cutting forces: 25 degree tool tilt

6.2.2 TOOL STIFFNESS AND DEFLECTION

The long shank, ball end milling tools used in this research have a 4.0 mm shank with a 0.8 mm ball diameter end. When used to fabricate free-form surfaces, the tool can be loaded in the axial direction, the radial direction, or both. The tool stiffness is significantly lower in the radial direction (Table 1), therefore regions of a machined surface where the tool is loaded primarily in the radial direction will be subject to large tool deflections and form errors.

Table 1: Measured and computed stiffness values for long shank, ball end tools

Axial Stiffness (N/m)	1421000
Radial Stiffness (N/m)	98930
25 degree Tilt Stiffness - Calculated (N/m)	419565
25 degree Tilt Stiffness - Measured (N/m)	455120

For most of the experiments presented in this section, the tool was tilted at a 25 degree angle with respect to the z-axis to emphasize the effects of tool deflection. For arbitrary cutting conditions, the tool stiffness in the direction orthogonal to the workpiece (normal tool stiffness k_n) can be determined by the experimentally validated expression:

$$\frac{F_n}{\delta_n} = k_n = \frac{1}{\frac{\cos^2\phi}{k_a} + \frac{\sin^2\phi}{k_r}} \tag{3}$$

where:

δ_n = normal tool deflection
F_n = normal tool force
k_a = axial tool stiffness
k_r = radial tool stiffness
ϕ = tool tilt angle

6.3 CLOSED-LOOP COMPENSATION OF TOOL DEFLECTION

Real-time force feedback can be used to predict and compensate for tool deflection during milling operations, reducing susceptibility to uncertainties in the model parameters and workpiece alignment. Two specific force feedback approaches are presented here: cutting depth prediction (based on a non-dynamic cutting force model) and tool deflection prediction (using a non-dynamic model of tool stiffness). Figure 4 illustrates the effect that tool

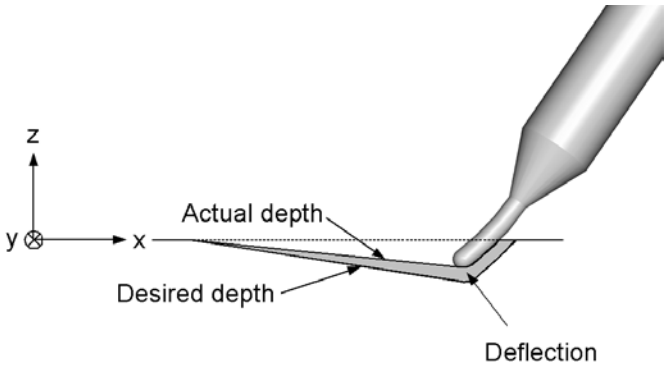

Figure 4: Tool deflection with desired and actual depth

deflection has on a groove profile. The tool tip is programmed to follow a desired path. However, due to deflection the tool tip, the tool actually creates a depth of cut less than desired (labeled "actual depth" in the figure). The shaded area in this figure represents material not removed due to tool deflection.

6.3.1 CUTTING DEPTH PREDICTION

Figure 5 shows a block diagram for the cutting depth prediction control algorithm. The concept behind this algorithm is straightforward: start with a desired tool path, measure real-time cutting force, use cutting conditions and a non-dynamic force model to predict the instantaneous depth of cut, and then calculate an error equal to desired depth minus predicted depth. Once this error is known a motion program either holds z-axis position (depth of cut), advances z-axis position, or reduces z-axis position. The error calculated by the PID control algorithm is:

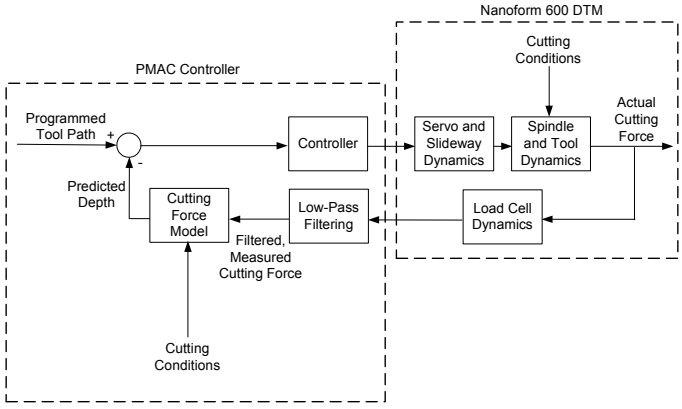

Figure 5: Diagram of predicted depth algorithm

$$\begin{aligned} error &= desired\ depth - predicted\ depth \\ \varepsilon &= x_d - \hat{x}(F,\psi) \end{aligned} \tag{4}$$

Using the validated cutting force model, cutting depth can accurately be predicted based on cutting conditions. This predicted cutting depth $\hat{x}(F,\psi)$ is a function of the cutting force model that includes 14 cutting parameters ψ. In this way the system can correct for errors associated with tool deflection and misalignment of the workpiece.

Advantages of Cutting Depth Prediction

- Precise alignment of the workpiece with respect to the axes of the machine is not necessary as this method uses only force feedback in the control algorithm without reference to machine axes
- The created profile is referenced to the workpiece surface; therefore precise knowledge of the workpiece surface before cutting is not necessary
- Cutting parameters required by the cutting force model (spindle speed, feed rate, material properties, etc.) are not difficult to determine

Disadvantages to Cutting Depth Prediction

- Wearland of the tool is difficult to measure and changes during machining
- Because it relies solely on force feedback to predict cutting depth, stability is a major concern for this control algorithm. During tool breaks and interruption of cuts, the instantaneous force goes to zero and thus the predicted depth of cut is zero. If the desired depth of cut is not zero, a large error exists in the control algorithm, resulting in large corrective federates and possible tool breakage and damage to the machine.
- Implementation and changes from encoder feedback to strictly force feedback is difficult because of the disadvantages listed above. To implement force feedback, both desired depth of cut and predicted depth of cut need to be approximately the same value, otherwise large errors can appear in the control algorithm.
- The algorithm is sensitive to drift and electrical noise in the load cell

6.3.2 TOOL DEFLECTION PREDICTION

A block diagram of the control algorithm predicting deflection using a model of tool stiffness is shown in Figure 6. The concept behind this algorithm is straightforward: start with a desired tool path, measure real-time cutting force, use the tool stiffness model and measured force to predict tool deflection, calculate an error equal to desired position minus DTM encoder position plus predicted deflection. Once this error has been calculated, PID control either holds position, moves further into the workpiece in the z-direction increasing the depth of cut, or moves out from the workpiece decreasing the depth of cut. With a validated stiffness model, deflection can accurately be predicted based on tool stiffness and a measured real time cutting force. In this way the system uses real-time force feedback to correct for errors associated with tool deflection and uses encoder feedback to maintain tool path stability. Error calculated by the PID control algorithm is:

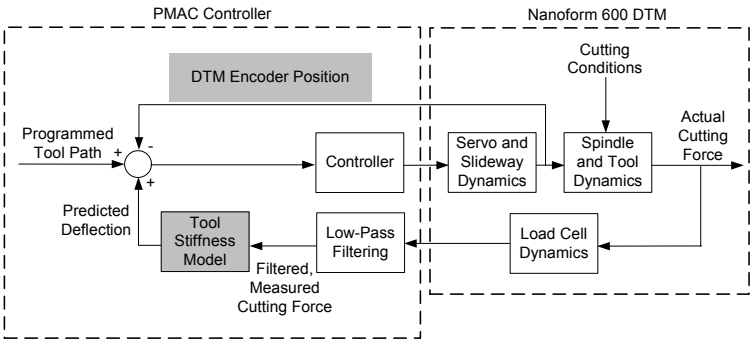

Figure 6: Diagram of predicted deflection algorithm

$$error = desired\ tool\ \ position - encoder\ axis\ \ position + predicted\ tool\ deflection$$
$$\varepsilon = x_d - x + \delta_n \tag{5}$$

Advantages to Deflection Prediction

- Wearland, spindle speed, feed rate, material properties, and depth are no longer required inputs to the cutting force model
- Deflection is dependent only on tool stiffness (which is a function tilt angle)
- Tool stiffness is easily calculated from measurements of axial and radial tool stiffness
- Encoder feedback ensures stable and reliable execution because it is a continuous, additional feedback mechanism. If cutting force goes to zero, the predicted deflection equals zero and the machine operates as if there was no force feedback in the control algorithm
- Load cell noise and drift are still critical to machining stability and accuracy, however, they affect predicted deflection only (which is typically of a smaller magnitude than DTM encoder position)

Disadvantages to Deflection Prediction

- Workpiece alignment with respect to the machine axes plays a direct result on the completed cut profile

6.4 EXPERIMENTAL IMPLEMENTATION

All experiments were conducted using a Nanoform 600 DTM with 3 orthogonal linear axes and a high-speed milling spindle (Figure 1). The spindle is a Westwind air bearing, turbine unit with a maximum speed of 60,000 rpm. The cutting tools are two-flute, long shank, ball end milling cutters with a diameter of 0.8 mm and a length of 4 mm. A Kistler three-axis piezoelectric load cell supports the workpiece, and is used to measure the tool forces in real-time. A Delta Tau Programmable Multi-Axis Controller (PMAC) system collects data from the load cell in real time, controls the DTM milling machine, computes the corrected slide command, and incorporates constant feedback for all three axes.

Originally, implementation of force feedback algorithms involved taking a desired profile and breaking it into a large number of incremental steps. Thus a cut might be broken down into thousands of increments each spanning tens of micrometers depending on the desired resolution and groove profile. Each increment was programmed as a separate line in a PMAC motion program. This approach, however, required relatively high federates and resulted in excessive accelerations that were prohibited by PMAC limits.

Real-time implementation of force feedback algorithms was accomplished using a custom motion program, written in machine g-code, which performed the following functions:

- read axis encoders
- calculate desired tool path
- calculate tracking error
- acquire force measurements
- filter force measurements
- calculate predicted cutting depth/tool deflection
- compensate for error in depth/deflection
- output control voltage to each axis servomotor

The PMAC was setup such that all three DTM axes were in a "dwell state", allowing the motion program to completely determine the voltage commands for each axis servo. Each of the three axes was controlled using custom digital proportional+integral+derivative (PID) algorithms. To ensure real-time execution, a dSPACE 1102 data acquisition (DAQ) system was used in conjunction with the PMAC. This system acquired the x, y, and z-component tool forces at a sampling rate of 10,000 Hz. It also filtered the force data, captured the maximum force, and calculated either the predicted cutting depth or predicted tool deflection. This prediction was then transferred as an analog signal to the PMAC for axis control. Figure 7 shows a functional diagram of the real-time signal processing performed on the dSPACE 1102 system.

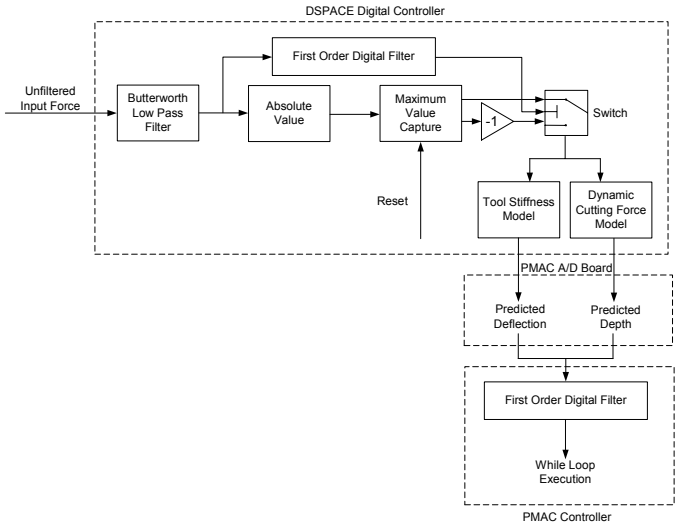

Figure 7: Diagram of dSPACE peak and hold algorithm

6.4.1 MAXIMUM FORCE IDENTIFICATION

The success of both force feedback approaches depended heavily on accurate, real-time identification of the maximum cutting force. This identification process was complicated, however, by the fact that cutting forces vary from a minimum value (which can be zero or even negative) to a maximum value at twice the rotational speed of the tool (Figure 8).

A "maximum force identification" algorithm was programmed using Simulink software and implemented on the dSPACE 1102 system. First, the cutting force data was filtered using a 5th order Butterworth low-pass filter with a 400 Hz cutoff frequency to eliminate noise above the spindle frequency (333 Hz). Next, a Simulink "maximum capture" function identified the peak force per spindle rotation. This maximum force was reset every two rotations of the tool based on a trigger pulse is acquired from the spindle. Figure 8 shows measured cutting force and maximum force identified using this algorithm from a typical cutting experiment (feedrate = 100 mm/min, spindle speed = 10,000 rpm, depth = 70 μm).

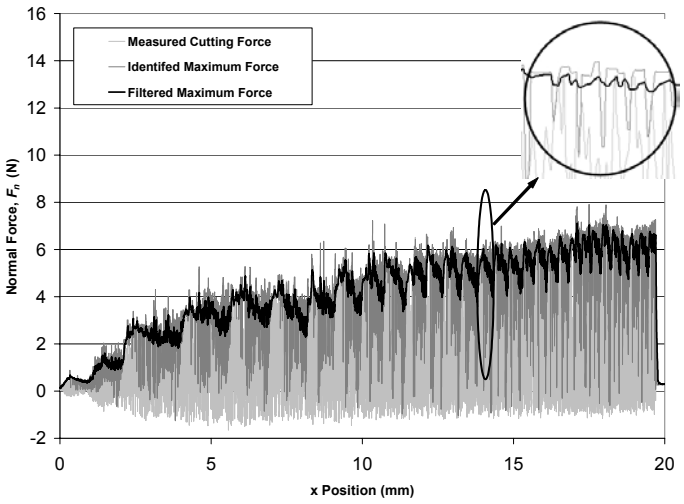

Figure 8: Experimental cutting force measurements and identified maximum force

Because the dSPACE system processed cutting data at 10,000 Hz, no fewer than 60 force measurements were acquired per rotation of the tool (30 per tooth). Sampling at this frequency improved the accuracy of the maximum force identification, and enabled effective implementation of the deflection compensation algorithms.

6.4.2 DEFLECTION COMPENSATION

Once the maximum cutting force was identified, the predicted cutting depth or predicted tool deflection was calculated (depending on which compensation algorithm was selected), and this value was transferred to the PMAC motion program as an analog signal. In the PMAC motion program, a first-order digital filter was implemented to filter the predicted cutting depth or tool deflection. Since the maximum force was reset every two rotations of the tool, step changes in this predicted value occurred from one revolution to the next. These step changes had destabilizing effects on the axes controllers, but the low-pass filter reduced abrupt variations and improved the robustness and performance of both compensation algorithms.

6.5 EXPERIMENTAL EVALUATIONS

To evaluate the effectiveness of the force feedback deflection compensation algorithms, extensive series of machining experiments were conducted on the Nanoform 600 DTM. Groove profiles were machined in S-7 tool steel samples (hardness > 55 R_c) mounted to the three-axis load cell (Figure 2). The workpiece was aligned with the axes of the Nanoform and cuts were

made along the x-axis (left to right) with the tool tilted at 25 degrees from the z-axis to emphasize the effects of tool deflection. The following sections detail these experimental evaluations.

6.5.1 LINEAR SLOTTING CUT EXPERIMENTS

Slotting cuts with linearly varying depth were made with and without compensation to evaluate the performance of real-time deflection compensation. Slots spanning 20 mm and 0-80 µm in depth were programmed, using a spindle speed of 10,000 rpm and a feed rate of 100 mm/min. This spindle speed was determined to be the minimum speed that provided adequate torque to make cuts in tool steel, and the feedrate was chosen to give a chip load of 5 µm/flute (which is on the order of the wearland of the tools and is acceptable machining conditions). The tool tilt angle, 25 degrees, was chosen to emphasize the effects of tool deflection.

Predicted Depth Compensation

Typical results for closed-loop compensation using predicted cutting depth and a non-dynamic cutting force model are shown in Figure 9, with the upper plot representing the uncompensated cutting profile, the middle plot representing the compensated profile, and the lower plot representing the desired profile. These profiles were measured using a Talysurf profilometer.

Profile errors were not significantly improved at the start of the groove, as both the compensated and uncompensated cases reveal similar errors (approximately 0-6 µm) for the first 8 mm of cutting. From this point forward, however, predicted depth compensation significantly reduced profile errors and produced more desirable results. Maximum error in the compensated groove is on the order of 8 µm (at a horizontal location of 8 mm), while maximum error (deflection) in the uncompensated groove reaches a maximum of 14 µm at a location of 18 mm. This equates to a 43% reduction in groove profile error.

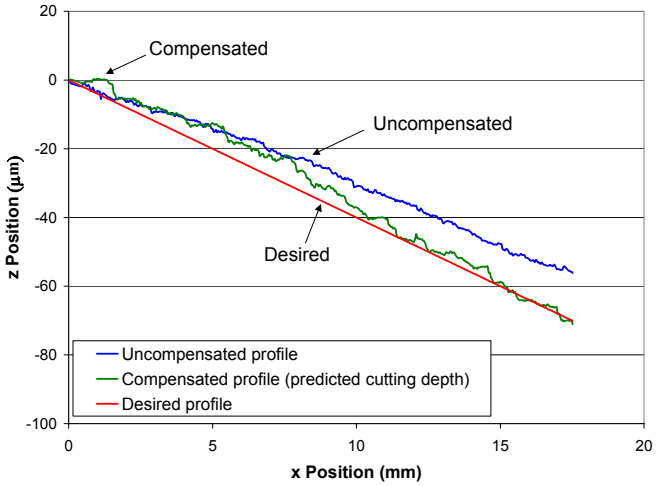

Figure 9: Experimental profile measurements: predicted depth compensation, linear slotting cut

There are several reasons for this lack of error reduction at the start of the groove. One involves implementation issues associated with the Nanoform 600 DTM. When transitioning from encoder feedback to force feedback, measurable

force needs to exist for cutting depth prediction to prevent a tool crash into the workpiece. Therefore, this method of compensation must be implemented after the tool begins to impart a force on the workpiece. A rotating tool is incremented toward the workpiece until a small force (on the order of 0.1 N) is measured. The axes are disabled and then the mode of machine operation is changed from encoder feedback to depth prediction compensation (force feedback). The axes are enabled, and the experiment begins. Initially, the desired cutting depth is zero. However, there is a measurable force, thus the predicted cutting depth is greater than zero. As a result, the control algorithm commands an initial move away from the workpiece, resulting in significant profile errors at the start of the groove.

Another source of error in the compensated profile involves the theoretical cutting depth vs. normal cutting force relationship, which has a very small slope at small cutting depths, making it difficult to measure forces at this operating condition due to their intermittent behavior. Thus, a small change in depth has a large effect on the force and limits this method's accuracy. As the depth increases, the forces become less intermittent (more consistent), resulting in more accurate predictions of cutting depth.

It should be noted that the results shown in Figure 9 represent the only acceptable results out of approximately 35 experiments conducted using this method of compensation. As a result, the second method of compensation using deflection was investigated to a much greater extent.

Predicted Deflection Compensation

Next, the predicted deflection compensation method (6) was compared to uncompensated machining. A typical set of results is shown in Figure 10, with the upper plot representing the uncompensated cutting profile, the middle plot representing the compensated profile, and the lower plot representing the desired profile.

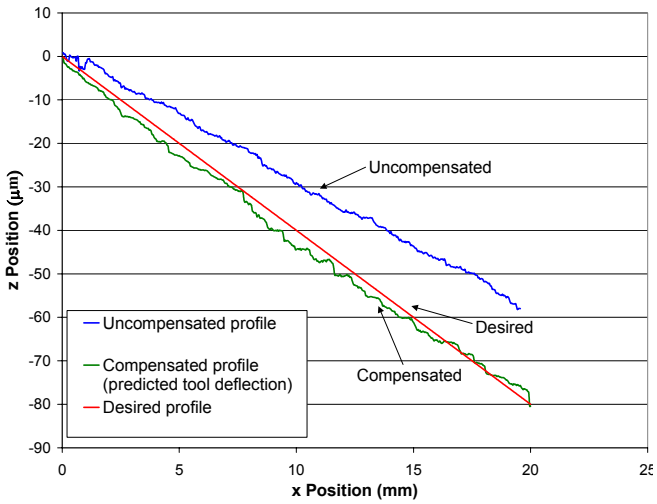

Figure 10: Experimental profile measurements: predicted deflection compensation, linear slot cut

Profile errors were significantly and consistently improved throughout the cutting experiment. Maximum profile errors with predicted deflection compensation are approximately 4 µm, compared to 21 µm with the uncompensated cut. This equates to an 80% reduction in groove profile error. In

contrast to the predicted depth compensation, errors are initially small and remain small throughout the experiment (between +4 µm and 0 µm), resulting in depth error at the end of the groove of -2 µm.

6.5.2 MODIFIED SINUSOIDAL SLOTTING CUT EXPERIMENTS

Slotting cuts with harmonically varying depth were also made with and without predicted deflection compensation to evaluate the performance of this approach. Trials were not conducted using predicted depth compensation due to problems with initial transients leading to tool breakage. Grooves spanning 20 mm with a two-period modified sinusoidal profile and peak depth of 80 µm were programmed, using a spindle speed of 10,000 rpm and a feed rate of 100 mm/min with the long tool. The resulting sine wave frequency was 1.05 Hz. As before, groove profiles were measured on the Talysurf profilometer.

A typical set of results is shown in Figure 11, with the upper plot representing the uncompensated cutting profile, the middle plot representing the compensated profile, and the lower plot representing the desired profile. Error in the groove profile is significantly improved throughout and the results show that this method of compensation reduced the form error from a maximum of 27 µm to 13 µm. This is a 52% reduction in error. It can be seen that groove profile error at the start as well as during the groove cut is bound between +14 µm and –1 µm.

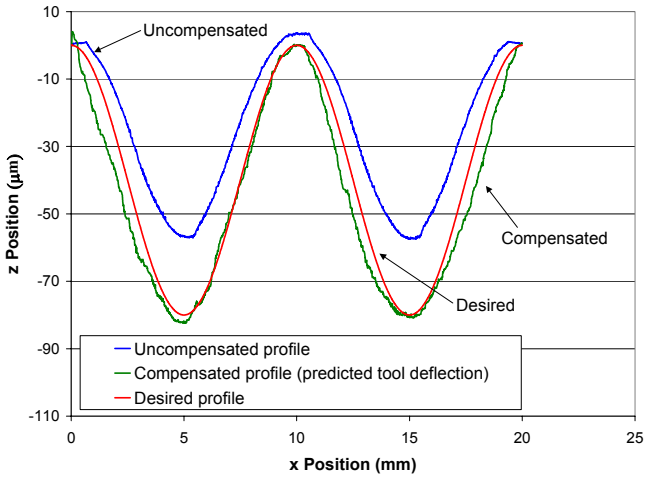

Figure 11: Experimental profile measurements: predicted deflection compensation, two period sinusoidal slotting cut

Profile errors in all experiments result from many different sources. Capturing the maximum cutting forces and filtering these forces both make significant impacts on the profile created. Also, there are significant transient responses in the DTM axes that create variations in the modified sine wave cuts. Another source of error involves interpretation of the data measured on the Talysurf profilometer. These and other error sources are discussed in greater detail in Section 6.5.5.

6.5.3 REPEATABILITY EXPERIMENTS

To evaluate the repeatability of the force feedback deflection compensation results of Figures 9-11, each of these cutting experiments was repeated with different tools. Closed-loop cutting tests were conducted with one tool, then repeated with a different tool on the same workpiece in a different location. The workpiece was not removed from the DTM fixture from one experiment to the next to eliminate misalignment errors.

Linear Slotting Cut Experiments

A typical set of repeatability results is shown in Figure 12, with the upper plot representing the compensated profile errors for Tool 1, and the lower plot representing the compensated profile errors for Tool 2. Although these results indicate excellent repeatability, profile errors associated with Tool 1 are less than those associated with Tool 2. These variations can be attributed to differences in the workpiece surface before cutting, as well as, differences in tool stiffness and flute wear from one tool to the next.

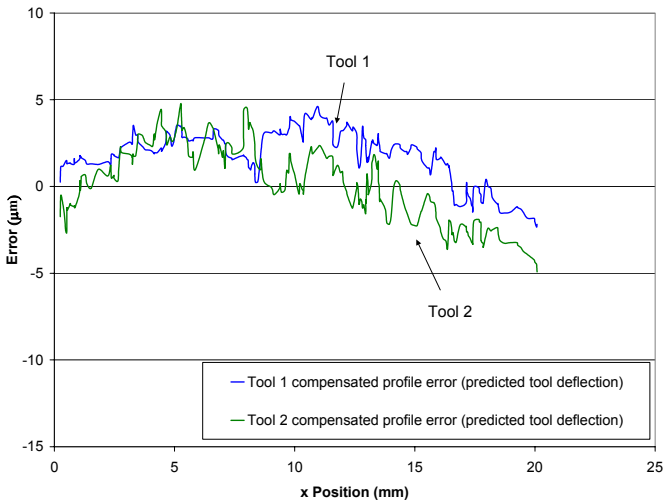

Figure 12: Experimental profile repeatability errors: predicted deflection compensation, linear slotting cut

As stated previously, the workpiece was not removed from the DTM fixture between cutting tests. However, "touching off" the surface of the part was necessary in each case, possibly introducing errors into the experiment. It is not likely that the precise surface location was found with the same accuracy each time, resulting in profile errors from one tool to the next that could not be determined from a Talysurf measurement only. This "touching off" the workpiece surface is a procedure where a rotating tool was incremented 1 µm in the z-direction toward the workpiece surface while measuring z-force on the load cell. Incremental movements were continued until a force of approximately 0.1 N was seen. At this point it was determined that the surface of the workpiece was found.

Two-Period Modified Sinusoidal Profile

Another typical set of results is shown in Figure 13, with the upper plot representing the compensated profile errors for Tool 1, and the lower plot representing the compensated profile errors for Tool 2. This experiment reveals that the correspondence between both experiments with the same compensation algorithm and cutting parameters is good. There is some error at the end of the groove profile for Tool 1 that is not seen for Tool 2. The reason for this is not clear however, as all parameters are the same and the part was not realigned between each experiment.

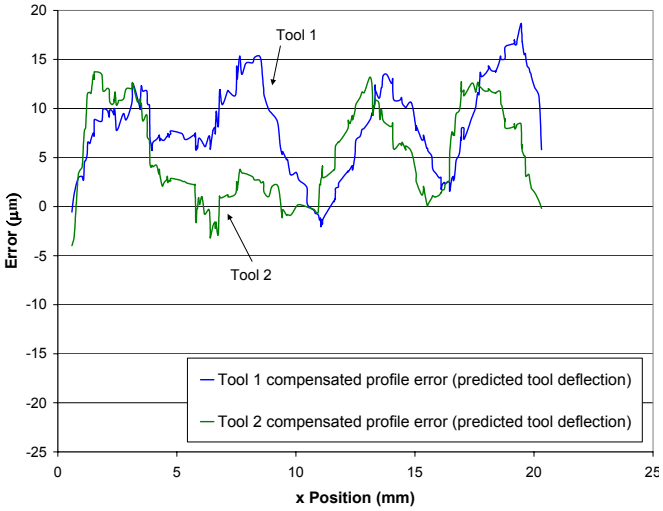

Figure 13: Experimental profile repeatability errors: predicted deflection compensation, two period sinusoidal slotting cut

6.5.4 Investigating Profile Errors in Small Groove Cutting Experiments

The causes of profile errors in the small groove experiments are difficult to determine exclusively from Talysurf measurements. To investigate the effects of controller inputs on groove profiles, cuts were made while the following variables and parameters were measured:

- unfiltered cutting force
- filtered cutting force
- identified maximum cutting force
- encoder position
- filtered tool deflection
- PID compensation errors
- workpiece surface before cutting

Groove profile measurements were made and compared statistically with these acquired measurements. To make these statistical comparisons, cross-correlation coefficients were computed between each gathered variable and the measured groove profiles.

Uncompensated Linear Slotting Cut: Cross-correlations

An uncompensated linear slotting cut was made as outlined in Section 6.5.1, and the variables highlighted on page 94 were acquired during cutting. For this uncompensated experiment, the correlations between cutting force to groove profile and controller variables to groove profile are easily separated, as encoder position is the only feedback variable (cutting force is measured but not used in the algorithm). Therefore, the effects of controller variables and cutting force on groove profile measurements should be apparent, as should the relationship between each. Figure 14 shows the filtered cutting force and maximum capture force for this uncompensated experiment. The resulting profile measurement is shown in Figure 15, where the maximum cutting force appears to be strongly correlated to this profile. Comparing Figure 14 to Figure 15 reveals similar irregularities at approximately 3 mm, 11 mm, and 20 mm. Thus it is expected that the maximum cutting force and groove profile should have a strong correlation.

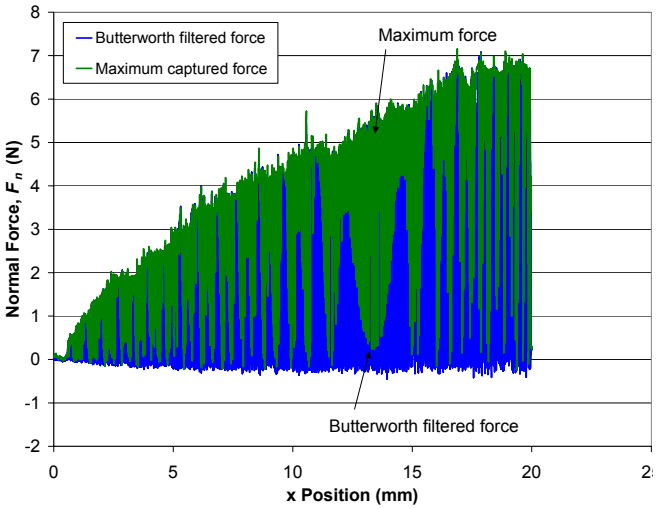

Figure 14: Experimental force measurements: filtered and captured maximum cutting force, uncompensated linear slotting cut

The workpiece surface profile before cutting is shown in Figure 16. This surface appears to have irregularities as well, and could possibly play an important role in the groove profile created. This figure reveals a significant variation in workpiece surface between 3 and 4 mm that appears to have an effect on cutting force. Therefore, is seems likely that cutting forces are dependent on workpiece surface profiles, and measured groove profiles are dependent on cutting forces. To validate these expectations, a cross-correlation analysis was performed on the acquired data, with results presented in Table 2.

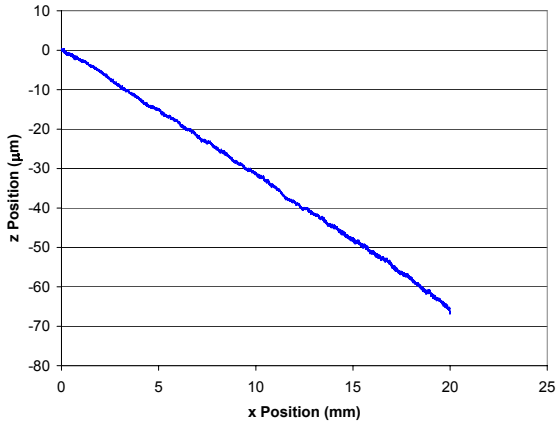

Figure 15: Experimental profile measurement: uncompensated linear slot cut

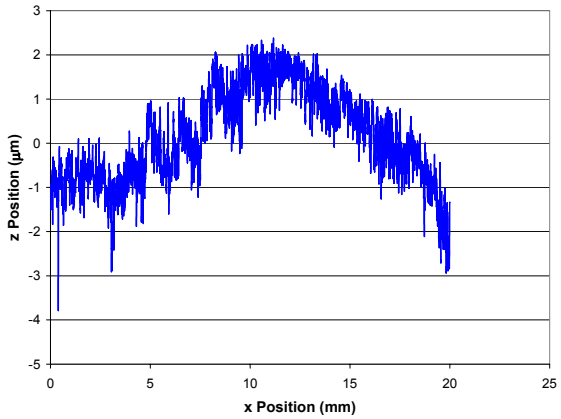

Figure 16: Experimental workpiece surface profile measurement before cutting

The variables with the strongest correlation coefficients are PMAC z-axis encoder position (-0.9989), PMAC filtered tool deflection (-0.9693), and dSPACE captured maximum force (-0.8634). The strong correlation between PMAC encoder position and groove profile is expected; it implies that the tool tip is following axes movement and creating the profile measured on the Talysurf. There is also a strong cross-correlation between PMAC tool deflection and dSPACE captured maximum force with measured groove profile, so it can be concluded that the maximum force during machining has a strong relationship with groove profile created.

Table 2: Cross-correlation coefficients for uncompensated linear slotting cut

Control Variable	Cross-correlation coefficient
Unfiltered cutting force (dSPACE)	-0.4808
Filtered cutting force (dSPACE)	-0.5134
Captured maximum force (dSPACE)	-0.8634
Filtered tool deflection (PMAC)	-0.9693
Z-axis encoder position (PMAC)	-0.9989
Proportional error (PMAC)	0.1881
Integral error (PMAC)	-0.2892
Derivative error (PMAC)	0.0612
Servo voltage (PMAC)	0.0499
Workpiece surface before cutting	-0.2097

Compensated Linear Slotting Cut: Cross-correlations

A linear slotting cut was then made using the deflection compensation algorithm and the same cutting conditions outlined in Section 6.5.1. The variables highlighted in Section 6.5.4 were again acquired during cutting. In this experiment, the correlations between cutting force to groove profile are related, as the control algorithm includes force feedback. Figure 17 shows the filtered cutting force and the capture maximum force for the compensated experiment. The resulting

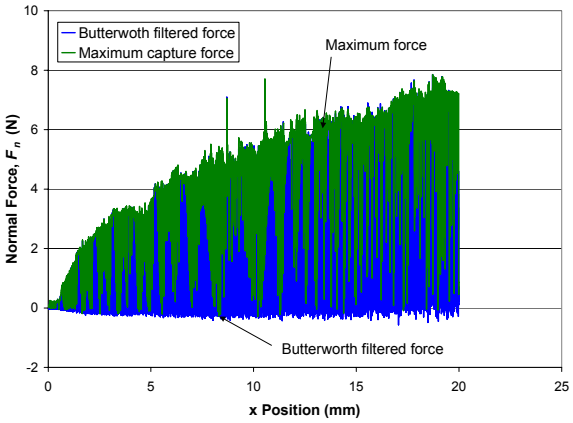

Figure 17: Experimental force measurements: Butterworth and maximum force capture, compensated linear slot cut

groove profile is shown in Figure 18. It can be seen that the maximum cutting force appears to be correlated to the groove profile. Comparing Figure 17 to Figure 18 at approximately 3 mm shows that both profiles have similar irregularities. A similar irregularity occurs at 11 mm and again near the end of the groove. Thus it is expected that the maximum cutting force and groove profile should have a strong correlation, and this is validated in the correlation coefficients presented below (Table 3).

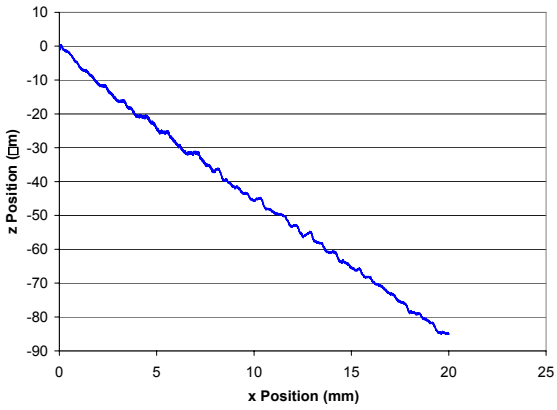

Figure 18: Experimental profile measurement: compensated linear slotting cut

The variables with the strongest correlation to groove profile are the same as in the uncompensated case: PMAC z-axis encoder position (-0.9989), PMAC filtered tool deflection (-0.9693), and dSPACE captured maximum force (-0.8634). The strong cross-correlation between encoder position and groove profile is expected, and implies that the tool tip is again following axes movements and creating variations in measured groove profiles.

Because of the high cross-correlation between PMAC tool deflection and dSPACE captured maximum force with groove profile, and the direct feedback of cutting force in the algorithm controlling the DTM axes, improvements to the peak force measurements during result in groove profiles with less error and reduced variance.

Table 3: Cross-correlation coefficients for compensated linear slotting cut

Control Variable	Cross-correlation coefficient
Unfiltered cutting force (dSPACE)	-0.4623
Filtered cutting force (dSPACE)	-0.4936
Captured maximum force (dSPACE)	-0.8569
Filtered tool deflection (PMAC)	-0.9707
Z-axis encoder position (PMAC)	-0.9989
Proportional error (PMAC)	0.183
Integral error (PMAC)	-0.3003
Derivative error (PMAC)	0.0415
Servo voltage (PMAC)	0.0235
Workpiece surface before cutting	-0.2299

6.5.5 Error Sources in Small Groove Cutting

The investigation of cross-correlation between different machining variables and resulting groove profiles for small groove experiments led to several important results. As discussed in the last section, dSPACE captured maximum force and PMAC filtered tool deflection have the strongest relationships with groove profile. This suggests that, for closed-loop machining, removing variations and inaccuracies in peak cutting force results in reduced tool deflection variations and therefore smoother and more accurate groove profiles. Other sources of profile error were identified in these experiments, however, and are addressed in the following sections.

Talysurf Profile Measurement Errors

One source of profile error involves Talysurf measurement processing and comparison to desired profiles. This error should not be confused with workpiece alignment error, which occur while taking Talysurf measurements. Instead it involves interpreting the measured profiles. Figure 19 shows three groove measurements made on the Talysurf.

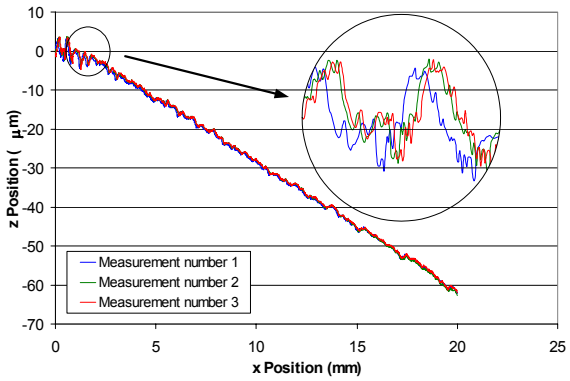

Figure 19: Repeatability measurements made on Talysurf

These three profile measurements were made on the same groove. For each measurement, the workpiece was removed from the Talysurf stage, repositioned and to the Talysurf axis. Figure 19 shows that measurements 2 and 3 are well aligned (left to right). However, measurement 1 is considerably shifted with respect to the other two. This alignment error is a result of data interpretation after making a Talysurf measurement, not the actual measurement

process. Misalignments in measured data are difficult to separate from error introduced through compensation technique.

This misalignment problem arises from the fact that it is difficult to determine exactly where a groove begins and ends. Thus, the proper relationship between desired groove profile and measured groove profile from Talysurf data is difficult to determine. Small variations in alignment of the measured groove profile with respect to the desired can result in drastically different measurements of the error. All such errors are interpreted as performance limitations of the compensation algorithm, when in fact they result from misalignment of the measured groove profile to desired profile.

Another source of error related to processing and interpreting Talysurf profile measurements involves workpiece tilt. Following each measurement, a linear regression is performed to remove "workpiece tilt" from data. This regression is performed separately for each experimental groove, thus points used from one groove to the next are different and could lead to differences in measurement. Figure 20 shows profile measurement data with (modified profile) and without (unmodified profile) workpiece tilt removed. Figure 20 shows that before removing workpiece tilt from the data, the unmodifed profile starts at –10 µm and ends at 10 µm. This effect results from the Talysurf stage or the workpiece surface being misaligned with the Talysurf probe tip axis. By removing this tilt from the data, the measurement can be compared to desired profile that starts at 0 µm deep and ends at 80 µm.

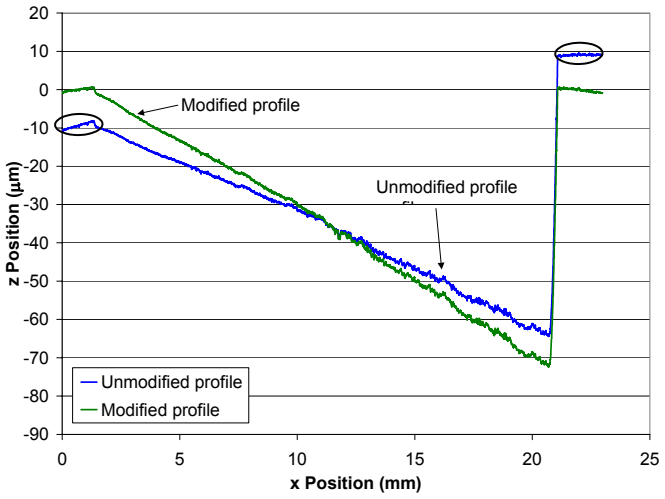

Figure 20: Removing workpiece tilt from Talysurf profile measurement data

The highlighted regions on the unmodified profile show the portions of the measurement used (by the linear regression) to remove workpiece tilt. Clearly the selection of reference points used in the regression process could lead to variations in the comparison to desired profiles.

Transient Response of the DTM Axes

The DTM axes used in the small groove experiments have inherent transient response characteristics that affect the machining performance. These transient responses would typically

be neglected in experiments with limited travel and federates. However, in experiments where the z-axis travel is on the order of 100 μm with feedrates of 100 mm/min, the z-axis transient response has an effect on groove profile created. Figure 21 shows the transient response of the z-axis (without cutting) tracking a linear groove profile. At the start of motion, the z-axis has a small transient characteristic, an undershoot, where the axis actually moves backwards and then along the correct path. This transient effect is more evident in the two-period modified sinudoidal profile.

Similar undershoots are evident at the start of the groove and upon changes in direction at approximately 3, 6, and 9 seconds. Ultimately, these undershoots appear as groove profile errors and due to the limited bandwidth of the DTM, they are difficult to remove. Each DTM axis weighs approximately 500 pounds, thus controlling transients requires very large actuation forces and torques. As stated previously, the DTM is a high-precision machine not designed for rapid changes in cutting direction. Although this machine performs well when moving in straight lines at constant velocities, it is expected to have transient response problems when making cuts requiring direction reversals (modified sine waves, etc.).

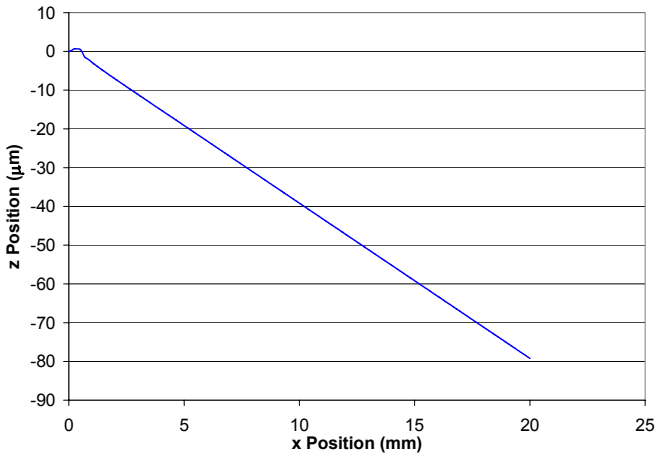

Figure 21: Transient response of z-axis to a linear groove profile (non-cutting)

6.5.6 LARGE GROOVE EXPERIMENTS

The experimental slotting cut results presented here indicate that the tool stiffness model (6) accurately predicts tool deflections, as every profile measurement created with predicted deflection compensation was within 20% of the desired profile.

These cutting experiments were conducted using a fixed tool tilt and varying depths of cut. However, the situation for most machining operations is more complicated and involves varying tilt angles as well as varying depths of cut. To verify that predicted deflection compensation is effective for more general machining, more comprehensive "large groove" experiments were conducted. The goal of these experiments was to create surfaces in which the cutting forces on the ball end mill vary in direction and magnitude during machining. These experiments also investigated the effects of forces that act in the plane of the workpiece surface.

These "large groove" experiments involved fabricating a 0.5 mm deep groove in a test specimen using a 3.0 mm ball end mill and enlarging the groove by 100 μm using a 0.8 mm ball end mill. Figure 22 is a schematic of the large groove experimental setup, where finishing cuts were made in the +y direction (bottom to top). The sweep angle (γ) was defined to be the angle between the vertical direction and the normal surface vector at the point of interest (as defined in Figure 23). The sweep angle range for these experiments was approximately ± 51°, and the desired

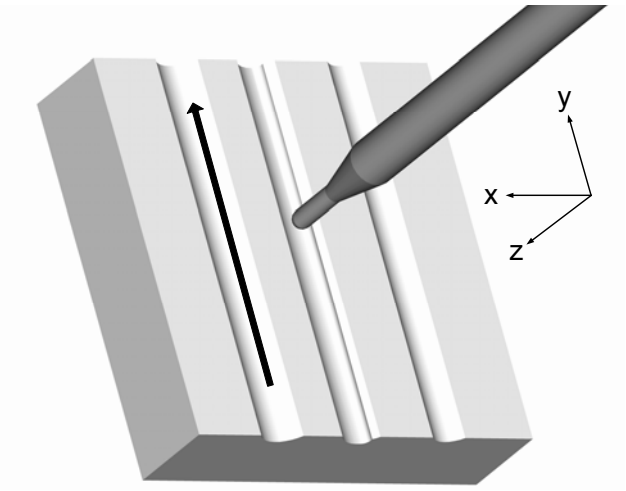

Figure 22: Large groove experimental setup

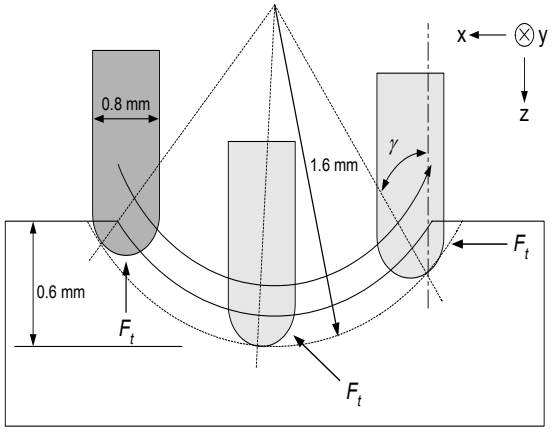

Figure 23: Cross sectional sketch of the tool path and thrust force for large groove experiment (where F_t = thrust force and γ = sweep angle)

depth of cut was 100 μm. The spindle speed was 10,000 rpm, the feedrate was 50 mm/min, and the cross feed was 25 μm/pass. The magnitude and direction of cutting forces during machining depended on the depth of cut as well as the sweep angle. The thrust force was assumed to start out primarily as an axial force and end primarily as a radial force. This change in tool force direction is illustrated in Figure 23, where the tool sweeps along the workpiece from left to right. This change in force direction has a dramatic effect on the deflection of the tool during machining due to the significant difference in axial and radial tool stiffness.

The air bearing spindle of the Nanoform 600 DTM has very limited torque at operating speeds below 60,000 rpm. However, the DTM's y-axis has a limited feedrate capability, requiring low spindle speeds to achieve proper chip removal per revolution. Proper chip removal is defined as

a feed per tool revolution on the order of the wearland. For these reasons, single-pass rough grooves were machined on a HAAS VF-1 CNC machine using a 3.0 mm ball end tool. Figure 24 shows the resulting groove profile error for a single rough pass groove from the desired radius of 1.5 mm.

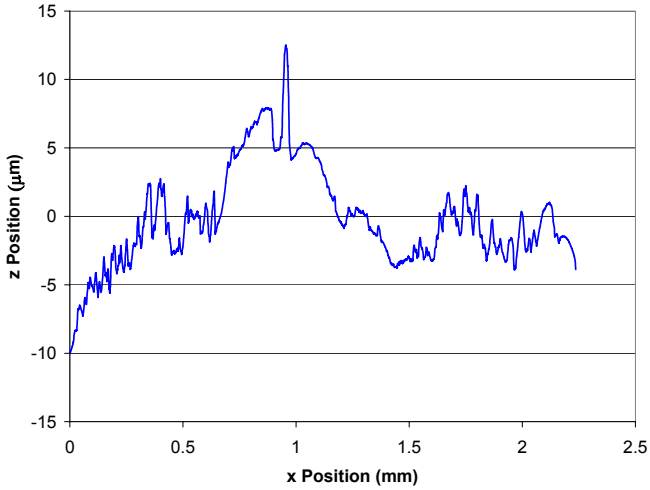

Figure 24: Rough pass large groove error from 1.5 mm radius

Subsequent finishing passes were performed on the Nanoform DTM using a 0.8 mm ball end tool, requiring accurate alignment of the workpiece with the x, y, and z axes. Finishing passes were made with and without compensation. Since the tool was oriented with the z-axis of the machine as shown in Figure 22 (zero tool tilt), deflection in the axial direction was assumed negligible to that in the radial direction. Hence compensation was implemented in the x-direction only. It was also assumed that the x-direction forces caused only radial deflections and the z-direction forces caused only axial deflections of the tool. Therefore, in the "large groove" experiments the tool path was altered in the x-direction, whereas in previous experiments the tool path was modified in the z-direction. Figure 25 shows profile measurements, made on a Talysurf profilometer, from an uncompensated cutting experiment.

For this cut, the tool entered the part at a sweep angle of -51° and moved through the workpiece. Cuts were made in 25 µm increments from left to right (Figure 23). The tool then exited the workpiece at a sweep angle of 51° (on the right side). The effects of tool flutes leaving the workpiece were evident when the sweep angle approaches 46° and tool deflections begin to decrease. The maximum profile errors in the uncompensated case range from 35 µm to –28 µm, giving a peak-to-valley error of 63 µm.

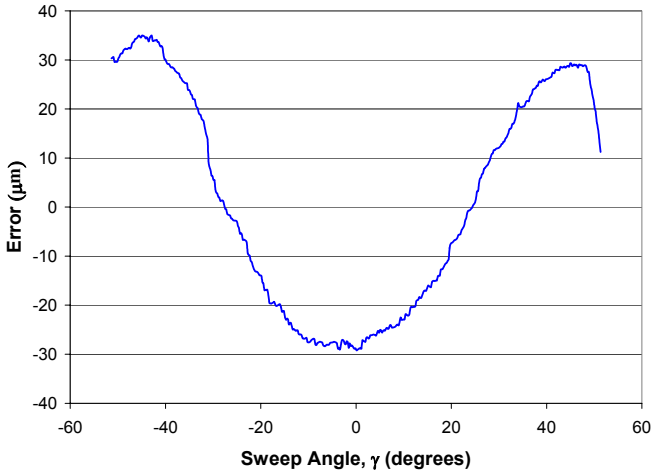

Figure 25: Experimental profile measurement: uncompensated large groove error from 1.6 mm radius

Results using predicted deflection compensation are presented in Figure 26. As before, the cutting parameters were a feedrate of 50 mm/min, 10,000 rpm spindle rotational speed, cross feed of 25 µm/pass, and a 0.1 mm

desired depth. Figure 26 shows the error from a best-fit radius of 1.6 mm for both the compensated and uncompensated profile.

Figure 26 reveals that the peak error is reduced from 63 µm in the uncompensated case to 18 µm using force feedback compensation, a 71% reduction. The 1.6 mm desired radius was achieved, producing an error plot that is neither convex nor concave. Peak-to-valley error

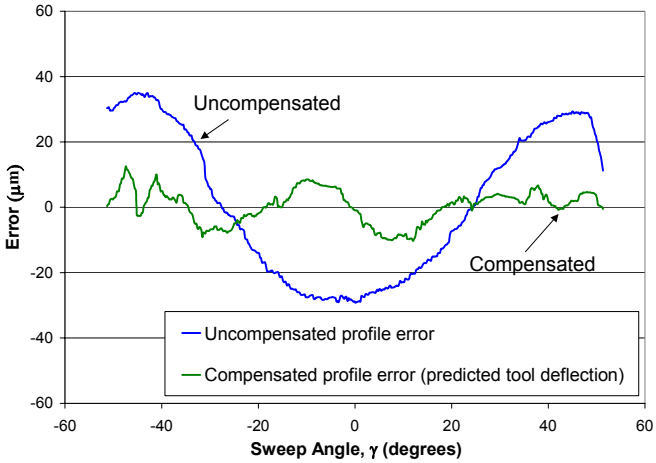

Figure 26: Experimental profile errors: predicted deflection compensation, large groove experiment

Table 4: Large groove experimental results: deflection compensation vs. uncompensated

experiment	best fit radius (mm)	P-V error (µm)
uncompensated	1.491	63
compensated: case 1	1.573	20
compensated: case 2	1.523	28

was reduced to 20 µm, a 68% reduction. Table 4 shows the peak-to-valley error comparison for the compensated and uncompensated cases. A "best fit radius" was determined for both cases, also shown in Table 4. Compensated groove profiles match the desired radius by 1.6%, while uncompensated profiles are 7% from the desired radius.

Repeatability of Predicted Deflection Compensation for Large Groove Experiments

Ten large grooves were fabricated on each workpiece using the HAAS machine. Thus once the part was aligned with the Nanoform, several different finishing cuts could be made without having to realign the workpiece. This made repeatability comparisons feasible without having to account for alignment issues. Two different error profile measurements using deflection compensation are presented in Figure 27.

Differences in profile errors can be attributed to having to "touch off" the tool for each experiment. It is unlikely that the touch off for all grooves was exactly the same, thus some errors were introduced. The accuracy of the Nanoform is considerably better than the HAAS machine, thus additional errors were introduced because grooves machined on the HAAS were not perfectly parallel. Nevertheless, these "large groove" experiments showed that force feedback compensation reduced overall error of the finished part. However, it is difficult to

differentiate between error introduced through the HAAS machine, misalignment of the part with respect to the Nanoform, and error from the compensation algorithm.

Another source of error was the limited bandwidth of the Nanoform, resulting in transient axes responses. When making cuts starting out of the part and moving into the part, a force and material is suddenly encountered, and transient response occurs leading to error.

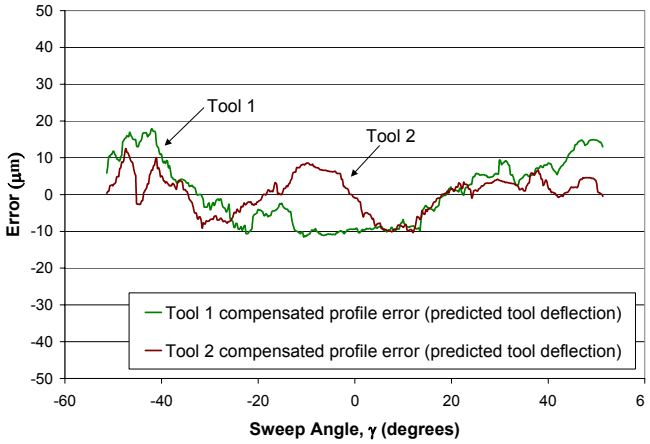

Figure 27: Experimental profile repeatability errors: predicted deflection compensation, large groove experiment

6.6 CONCLUSION

The forces generated during milling with a miniature ball end tool are relatively small (less than 10N) because of the limited size and strength of the tool edge. However, tool deflections can be a significant source of profile error because of low radial stiffness. Two force feedback approaches to tool deflection compensation are presented with advantages and disadvantages to each. The compensation algorithms presented here provide an avenue to reduce fabrication times and improve surface accuracy for hardened steel mold dies.

Predicting cutting depth using real-time cutting force measurements and a non-dynamic cutting force model can be used to compensate for errors arising from tool deflections and workpiece misalignment. Predicting tool deflection allows for compensation in profile error using force as well as machine encoder position feedback with good reliability. In this research, predicting deflection proved to be more robust and effective than predicting depth when implemented on the Nanoform DTM.

There are several reasons that predicting deflection yields better results than predicting depth in the compensation of profile errors. These include limited execution rate of the control algorithm, limited knowledge of actual cutting parameters, use of a multiplication factor in the depth prediction experiments, and use of laser feedback in the predicted deflection algorithm. When implemented on a DTM with higher bandwidth and faster execution rates, depth prediction may prove to be a viable approach to deflection compensation.

Reduction in error in small groove profiles over non-compensated groove profiles can be as great as 80% depending on the profile and method of compensation. The success of force feedback compensation depends heavily on the acquisition, processing, and filtering of cutting forces during machining. As shown in the cross-correlation analysis, maximum cutting force has a

strong relationship to the groove profile created. Therefore, smoother and more accurate maximum force measurements will result in smoother and more accurate groove profiles.

For the large groove experiments, reductions in profile error were not as significant as the small groove experiments. Several factors account for this difference: fabrication of the grooves on two different machines, alignment issues, touch off procedures, force measurement, and inherent complexity of the large groove experiments. Results show a groove was created with a best-fit radius differing by 27 μm from the desired radius in comparison with 109 μm for the uncompensated case. Peak to valley error from a radius of 1.6 mm was reduced from 63 μm to 20 μm when compared with a non-compensated cutting experiment.

Overall, force feedback control of miniature ball milling proved applicable in many situations for correcting errors in machined parts due to tool deflection. Significant reductions in profile error for large and small groove experiments were documented, with error reduction as high as 80%. The primary contribution of this research is a real-time feedback compensation algorithm that is capable of reducing form errors in workpieces machined using miniature ball end mills. In summary, the experimental results show that the force feedback control algorithms developed for this project were successful.

REFERENCES

1. Lechniak, Z., A. Werner, K. Skalski, K. Kedzior, "Methodology of off-line software compensation for errors in the machining process on the CNC machine tool," Journal of Materials Processing Technology, vol. 76, pp. 42-48, 1998.
2. Dow, T.A., E. Miller, A. Sohn and K. Garrard, "Compensation of Tool Forces in Small Diameter End Mills," ASPE Proceedings, vol. 20, pp. 546-550 and to be published in Precision Engineering in 2003.
3. Ikua, B.W., H. Tanaka, F. Obata, S. Sakamoto, "Prediction of cutting forces and machining error in ball end milling of curved surfaces – I theoretical analysis," Journal of the International Societies for Precision Engineering and Nanotechnology, vol. 25, pp. 266-273, 2001.
4. Liu, X.W., K. Cheng, D. Webb, and X.C. Luo, "Prediction of cutting force distribution and its influence on dimensional accuracy in peripheral milling", International Journal of Machine Tools and Manufacture, vol. 42, no. 7, pp. 791-800, 2002.
5. Tae, S.I., P. Depince, and J.Y. Hascoet, "Path compensation with respect to manufacturing tolerances", Proceedings of the 4th IFAC Workshop on Intelligent Manufacturing Systems 1997, Seoul, South Korea, July 1997.
6. Lim, E.M. and C.H. Menq, "Error compensation for sculptured surface productions by the application of control-surface strategy using predicted machining errors", ASME Journal of Manufacturing Science and Engineering, vol. 119, no. 3, pp. 402-409, 1997.

7. Suh, S.H., J.H. Cho, and J.Y. Hascoet, “Incorporation of tool deflection in tool path computation: simulation and analysis”, Journal of Manufacturing Systems, vol. 15, no. 3, pp. 190-199, 1996.
8. Watanabe, T., “Computerized numerical control to compensate for surface errors due to tool deflection in milling”, Systems and Control, vol. 27, no. 9, pp. 580-588, 1983.
9. Yang, M.Y. and C.G. Sim, “Reduction of machining errors by adjustment of feedrates in the ball-end milling process”, International Journal of Production Research, vol. 31, no. 3, pp. 665-689, 1993.
10. Masory, O., “Improving Contour Accuracy of NC/CNC Machine Tools using Real-time Cutting Force Measurements”, Recent Developments in Production Research. Collection of Refereed Papers Presented at the IXth International Conference on Production Research, Cincinnati, Ohio, 1987.
11. Ozaki, M., M. Tomizuka, C.K.H. Dharan, M. Won, and Y. Sheng, "Intelligent Control for Drilling of Carbon Fiber-Reinforced Laminates," North American Manufacturing Research Conference (NAMRCXXVII), Berkeley, California, pp. 69-74, 1999.
12. Clayton, S.H., “Force Modeling of Miniature Ball End Mills and Design of Closed-Loop Control Precision Actuation System”, Master Thesis, Department of Mechanical and Aerospace Engineering, North Carolina State University, Raleigh, NC, August 2003.
13. Franklin, G.F., J. David Powell, and A. Emami-Naeini, Feedback control of dynamic systems, 2nd ed., Addison-Wesley, Reading, MA, (1991).
14. Stockburger, D.W., Introductory Statistics: Concepts, Models, and Applications, www Version 1.0, Southwest Missouri State University, Springfield, MO, (1996).

7 FORCE FEEDBACK TOOL DELFECTION COMPENSATION OF MINIATURE BALL END MILLS

Karl Freitag
Graduate Student
Thomas Dow
Professor
Mechanical and Aerospace Engineering
Gregory Buckner
Assistant Professor
Mechanical and Aerospace Engineering
Ron Scattergood
Professor
Mechanical and Aerospace Engineering

The primary objective of this research is to improve dimensional tolerances and reduce total manufacturing time of precision milling operations through the implementation of force-feedback machining. Force-feedback machining consists of using real-time force measurement integrated with high bandwidth actuation to provide active error compensation of tool deflection. This research focuses on the development and implementation force-feedback machining using miniature (< 1 mm diameter) ball end mills.

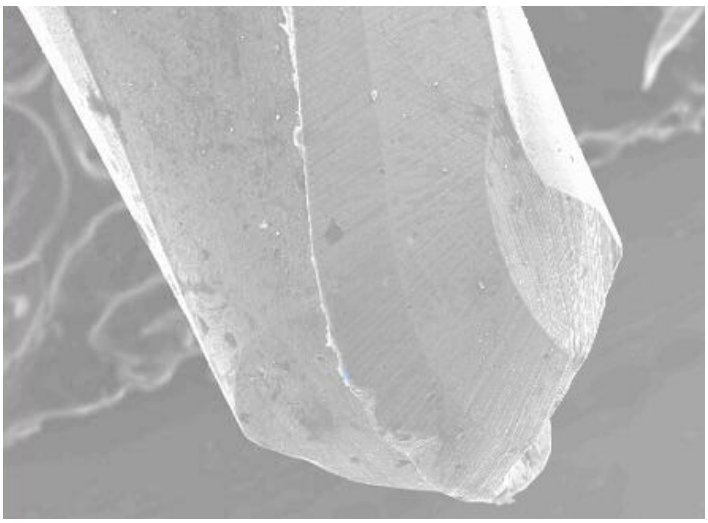

7.1 INTRODUCTION

One application of this research is in the fabrication of injection molding dies. These dies are machined from hard steels (Heat treated to ~ 60 Rockwell C) to provide durable, wear resistant dies. Figure 1 displays a photograph of lenses and gratings fabricated by the injection molding process. This process has the potential to yield high volumes while significantly reducing the cost of precision optical components.

Figure 1 Example of Optical Lens Fabricated from Injection Molding

Manufacture of these dies containing small features or precision surfaces require the use of tools with small radii. These tools (diameters < 1.0 mm) are termed miniature tools and are the primary focus of this research. To accommodate various applications and die geometries, these tools are available in several different shank lengths. Figure 2 is a photograph of the 0.8 mm diameter miniature ball end mills used in this research and an SEM image of the ball end tip.

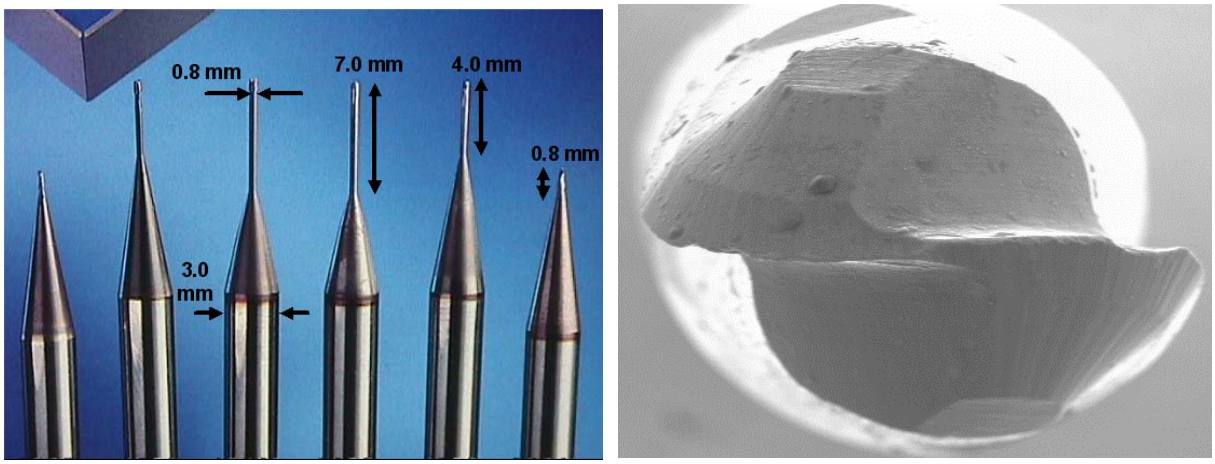

Figure 2 Miniature Ball End Mills (Left), SEM image of worn ball end (Right)

As seen from the photograph on the left, the thin geometry of these tools results in reduced tool stiffness, which becomes a significant factor when machining heat treated steels. Use of these long thin tools is often required to get into small features. These tools are made out from tungsten carbide with a titanium aluminum carbide coating. Although the tool material is very tough, deflections of these tools when used on heat treated steels can lead to undesirable errors in excess 50 μm with a 4.0mm shank tool. The primary goal of this research is to reduce these tool deflection errors to ± 2 μm, through the use of force-feedback machining.

7.1.1 PREVIOUS RESEARCH AT THE PEC

The Precision Engineering Center at North Carolina State University has conducted research in the modeling and prediction of cutting forces associated with milling processes. Previous research at NC State by Stuart Clayton [1] and David Hood [2] demonstrated that a piezoelectric actuated tool positioner resulted in significantly improved performance in comparison to the machine axes for compensation of tool deflection errors [3]. This improved performance was achieved through the higher bandwidth of the piezoelectric actuator and its significantly lower inertia.

Stuart Clayton designed and built a one-dimensional piezo actuated spindle using a work piece mounted load cell to measure cutting force [1]. This piezo actuated spindle is shown below in Figure 3.

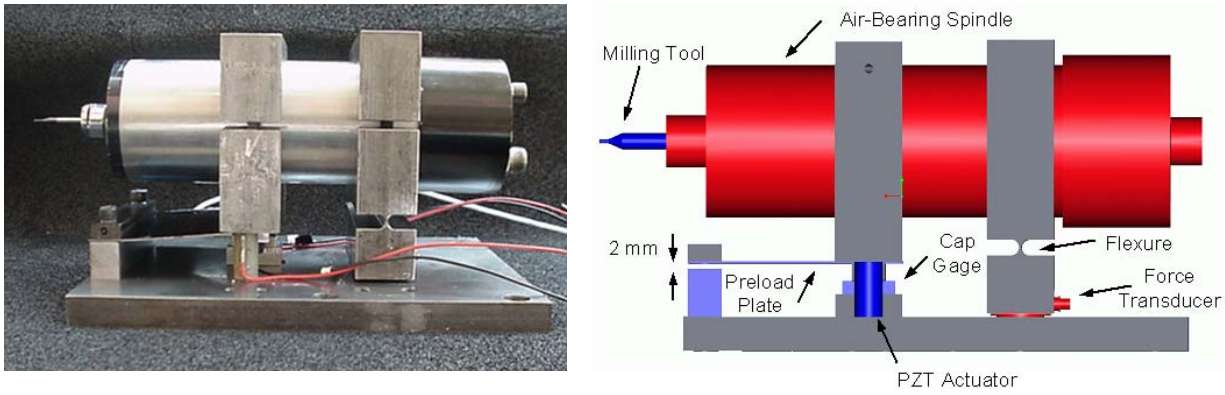

Figure 3 Piezo Actuated Spindle [1]

The piezoelectric actuated spindle showed promising results for the application of force feedback machining and its potential for reducing tool deflection error. Figure 4 displays the results achieved when comparing the closed loop control to the uncompensated cut machining a groove of increasing depth of cut.[1] In this figure it can be seen that as the depth of cut increases the uncompensated groove contains significant error. The closed loop compensation cut using force feedback significantly reduces this error and follows the desired path closely.

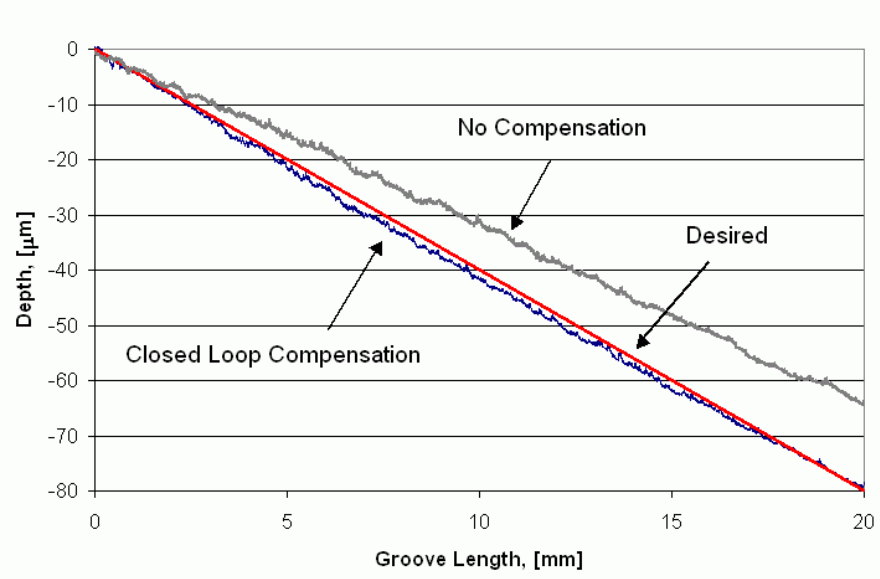

Figure 4 Closed Loop Error Compensation using Piezo Actuated Spindle [1]

The actuated spindle also contained a force transducer for measuring cutting forces on the spindle, but force measurements from the spindle were not as accurate as those obtained on the work piece. In order to improve the accuracy of cutting force measurements, the load cell needed to be repositioned to decouple it from the forces exerted by the actuator and to be able to remove the dynamic vibrations of the spindle.

7.2 CUTTING FORCE MEASUREMENT

7.2.1 EQUIPMENT - FORCE TRANSDUCER

A Kistler quartz three-axis force transducer (Model 9251) was used to measure the real-time cutting forces. This force transducer, shown in Figure 5, consists of three layers of piezo-electric elements which decompose the resultant force vector into its three (X,Y,Z) orthogonal components.

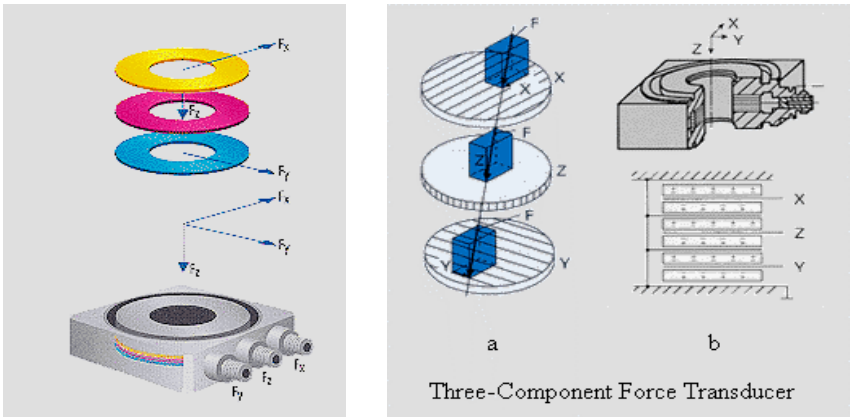

Figure 5 Three-axis Piezo-electric Force Transducer

7.2.2 EQUIPMENT - DATA ACQUISITION

The data acquisition of load cell measurements was performed using the dSPACE DS-1104 controller board with a CLP1104 connector panel shown in Figure 6.

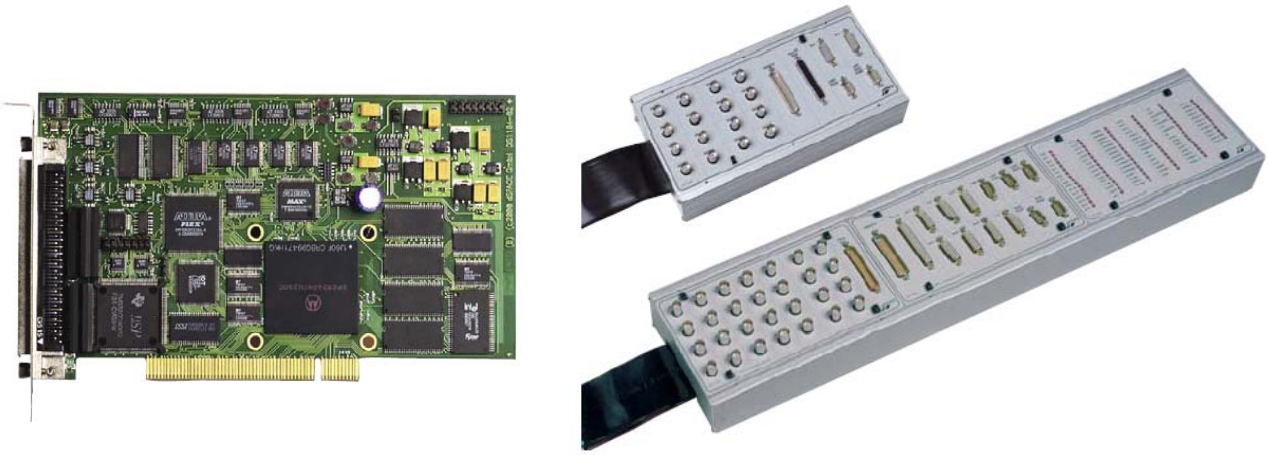

Figure 6 DS-1104 Controller Board (Left) and dSPACE CLP1104 Connector Panel (Right)

Figure 7 shows the capability of the Kistler force transducer and dSPACE data acquisition system to sample several data points of force measurement with one rotation of the tool at 10,000 RPM. The sample rate used to acquire force measurements on the dSPACE data acquisition board was 10 kHz.

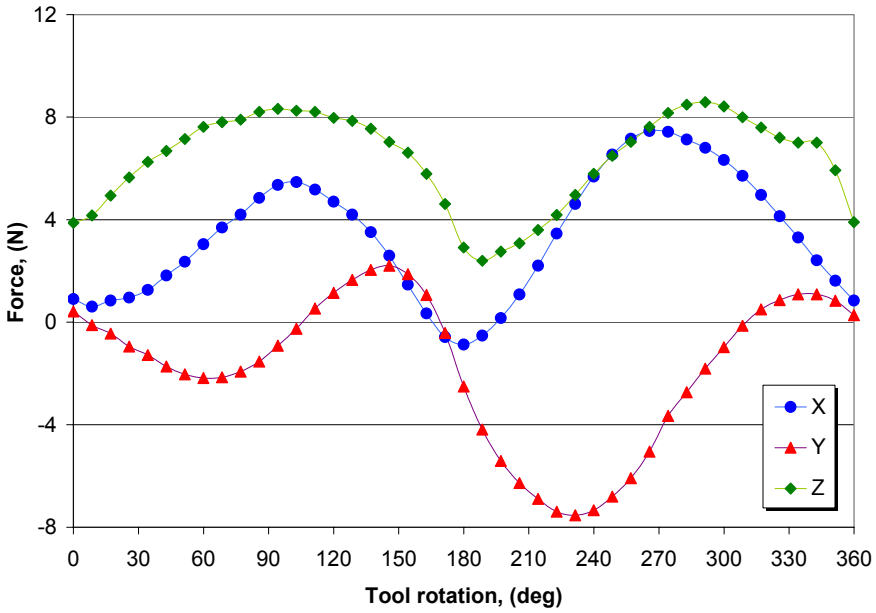

Figure 7 Sampled X, Y, and Z Cutting Forces at a spindle speed of 10,000 RPM

7.2.3 DUAL LOAD CELL SPINDLE

Measurement of the cutting forces from the spindle has several advantages over a workpiece based load cell. The primary advantage is that the mass and frequency response of the spindle assembly does not vary when cutting different work piece masses or geometries. This results in a consistent calibration of the dynamic cutting forces. The frequency response of the workpiece based force measurement is a function of the part geometry, modulus of elasticity and mass of the workpiece. To measure cutting forces from the spindle assembly, it is important that the load cells are not located inside the force loop between the actuator and ground. For this reason, the load cells are located directly beneath the spindle block and above the actuator as shown in Figure 8.

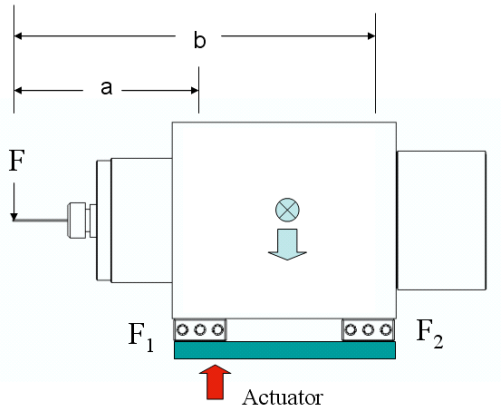

Figure 8 Force Measuring Spindle Design

Static Calibration of Dual Load Cell Spindle

In the force measuring spindle, two load cells are used and spaced equally about the center of gravity to minimize the effects of vibration. Using a model of a simply supported beam, the static equations can be derived to calculate the input force using the force measurements at the two load cell locations F_1 and F_2.

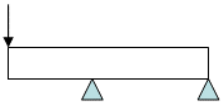

$$\sum M = 0$$

$$a \cdot F + (b-a) \cdot F_2 = 0$$

$$b \cdot F - (b-a) \cdot F_1 = 0$$

$$\Rightarrow \quad F = \frac{(F_1 - F_2)}{\left(\frac{b+a}{b-a}\right)} \tag{1}$$

Static Equations of Force Measuring Spindle

To test the model as a simply supported beam, the load cell spindle was calibrated by loading the tool tip in the X, Y and Z directions with fixed weights and recording the measured forces at the load cells. The coordinate directions are shown in Figure 9. From this data the resulting forces in each direction for a particular load could be calculated. Three equations were set up for the measured load in each direction as a function of the three X,Y, and Z forces (Equation 2).

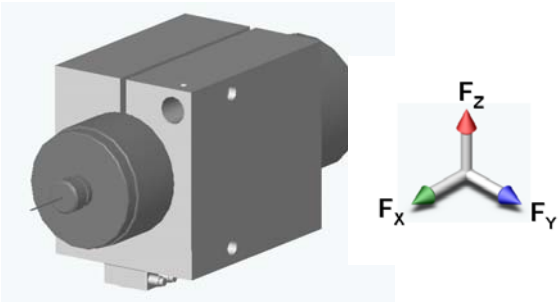

$$\begin{bmatrix} L_x \\ L_y \\ L_z \end{bmatrix} = \begin{bmatrix} a \cdot F_x & b \cdot F_y & c \cdot F_z \\ d \cdot F_x & e \cdot F_y & f \cdot F_z \\ g \cdot F_x & h \cdot F_y & i \cdot F_z \end{bmatrix} \tag{2}$$

Figure 9 Load Cell Coordinate System Loadcell Force Matrix

These values for the coefficients a,b,c…i are determined by loading the spindle in a single direction at a time. The results of these measurements are shown below.

$$A = \begin{bmatrix} a & b & c \\ d & e & f \\ g & h & i \end{bmatrix} = \begin{bmatrix} 0.8874 & 0 & 0 \\ 0 & 2.9904 & 0 \\ 1.3603 & 0.1625 & 3.2699 \end{bmatrix} \qquad F = \begin{bmatrix} F_x \\ F_y \\ F_z \end{bmatrix} \qquad B = \begin{bmatrix} L_{x1} + L_{x2} \\ L_{y1} - L_{y2} \\ L_{z1} - L_{z2} \end{bmatrix}$$

$$AF = B$$
$$F = A^{-1}B \tag{3}$$

Matrix Algebra solution for Input Forces (F)

Solving for F (input force), the matrix equation AX=B is solved by multiplying the inverse of the A matrix (Equation 3) which contains the coefficients obtained thru loading. The resulting static calibration equation is given by Equation 4.

$$\begin{bmatrix} F_x \\ F_y \\ F_z \end{bmatrix} = \begin{bmatrix} 1.127 & 0 & 0 \\ 0 & -.3344 & 0 \\ -.4688 & -.0166 & .3058 \end{bmatrix} \begin{bmatrix} (Lx_1 + Lx_2) \\ (Ly_1 - Ly_2) \\ (Lz_1 - Lz_2) \end{bmatrix} \tag{4}$$

Input Forces (Fx,Fy,Fz) in terms of the Load cell Measurements (Lx,Ly,Lz)

7.2.4 DYNAMIC RESPONSE OF SPINDLE

Although the spindle had been calibrated for static loads, the dynamic loading of the cutting process introduces additional gains which must be accounted for. To measure the frequency response of the system under cutting force conditions, the set-up in Figure 10 was constructed.

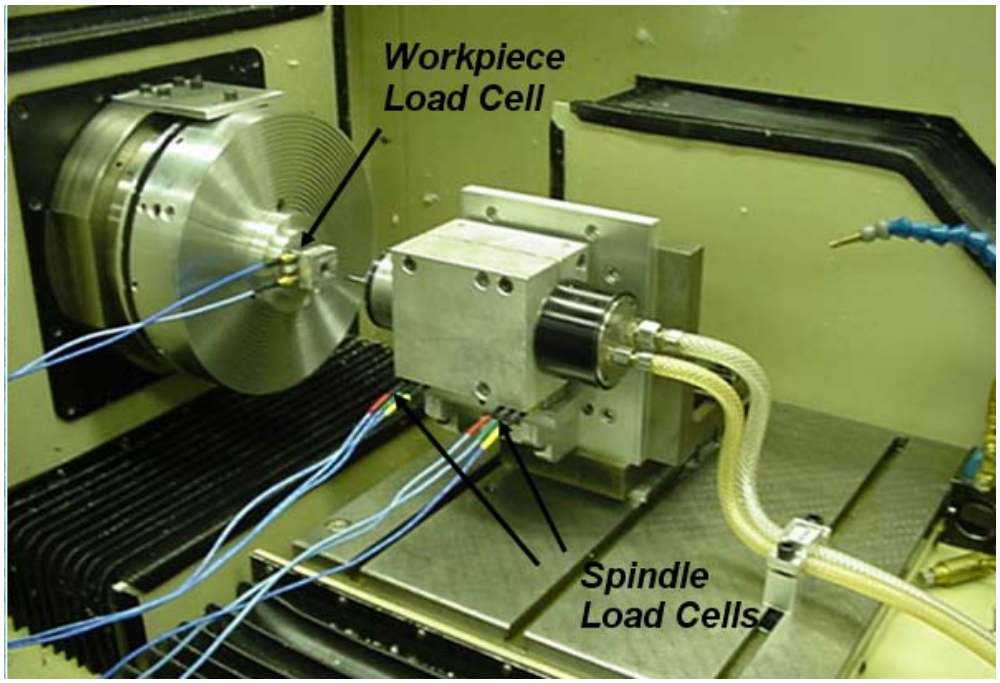

Figure 10 Load Cell Calibration Set-up on ASG Diamond Turning Machine

To measure the frequency response of the spindle assembly, the spindle speed was accelerated during the cut to increase the forcing frequency on the load cell. The measurements from all three load cells, two on the spindle assembly and one on the work piece were captured simultaneously for comparison.

The resulting force measurements displayed in Figure 11 illustrate the frequency response of the spindle. The force measured on spindle load cells goes thru a local maximum while the work piece load cell forces remain constant. In this data (Figure 11), the spindle speed was increased at a constant rate throughout the cut from 7500 – 10,000 RPM.

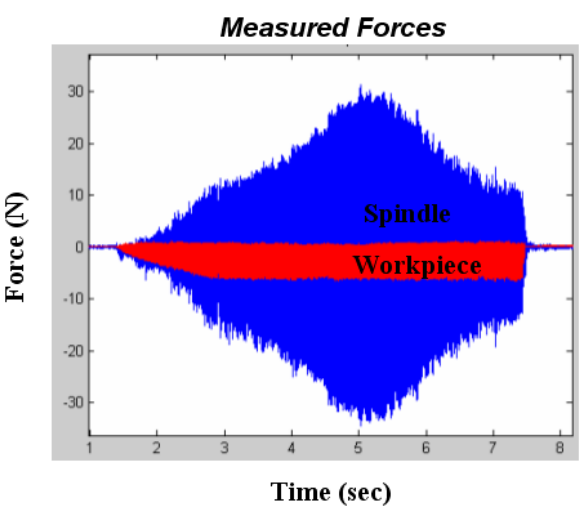

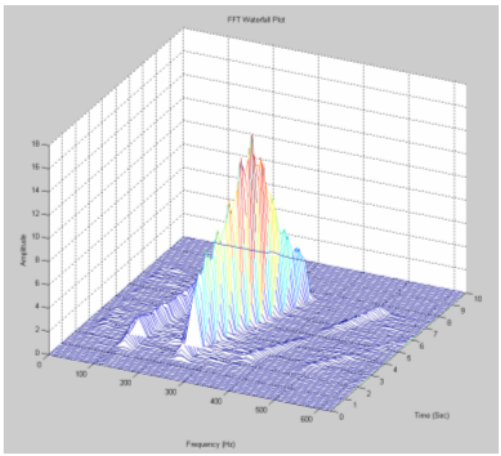

Figure 11(a) Spindle Force vs. Workpiece Force

Figure 11(b) Frequency Domain

As can be seen in both graphs, the magnitude of the cutting force measured on the spindle increased to a local maximum and then began to decrease as the spindle speed was continuously increased. This peak is shown if Figure 12 to be at a cutting frequency of 300 Hz or a spindle speed of 150 Hz. (2 Fluted Ball End Mill)

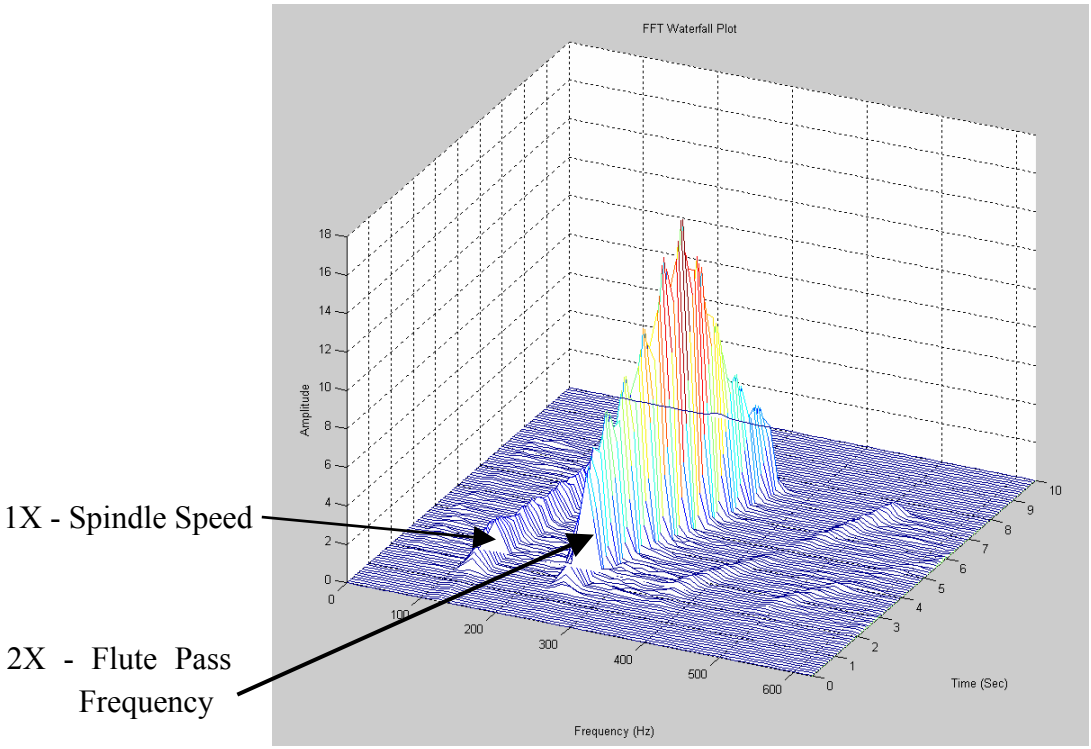

Figure 12 FFT Waterfall of Spindle Load Cell Measurement during cut

7.2.5 FORCE MEASUREMENT ALGORITHM

Using the results obtained by increasing spindle speed during cutting, the frequency response of the spindle assembly can be obtained in the X, Y and Z directions. From this data, a look-up table is generated in Simulink (Matlab) to cross reference the spindle speed (forcing frequency) with the appropriate dynamic magnification factor. The force measuring algorithm is shown in Figure 13.

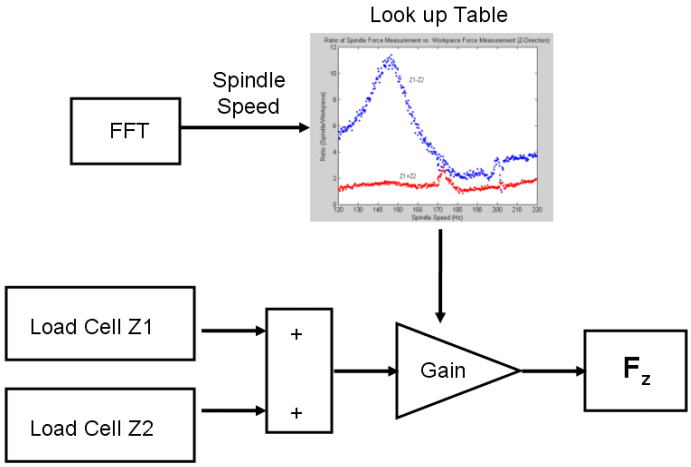

Figure 13 Force Measurement Block Diagram

The results of this force measurement technique very closely match the forces measured on the spindle to the forces measured on the work piece during a cut. Shown in Figure 14 is a comparison between the force measured on the work piece and the force measured on the spindle assembly as output from the force measurement algorithm above.

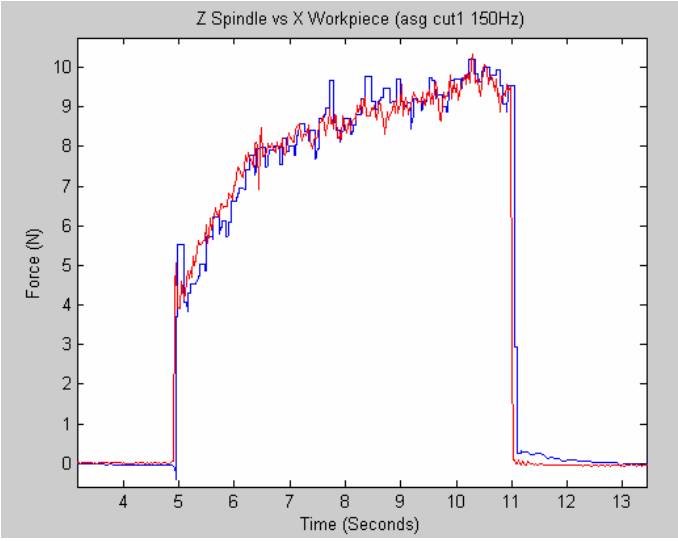

Figure 14 Comparison of the cutting forces measured on the work piece and spindle

7.3 ACTUATOR DESIGN

7.3.1 1-D ACTUATOR CONCEPT DESIGN

A design concept for a 1-D actuator is shown in Figure 15. The force measuring spindle is located above a piezoelectricly driven flexure plate. With the piezo location underneath the load cell, the reaction force during actuation does not pass through the load cells.

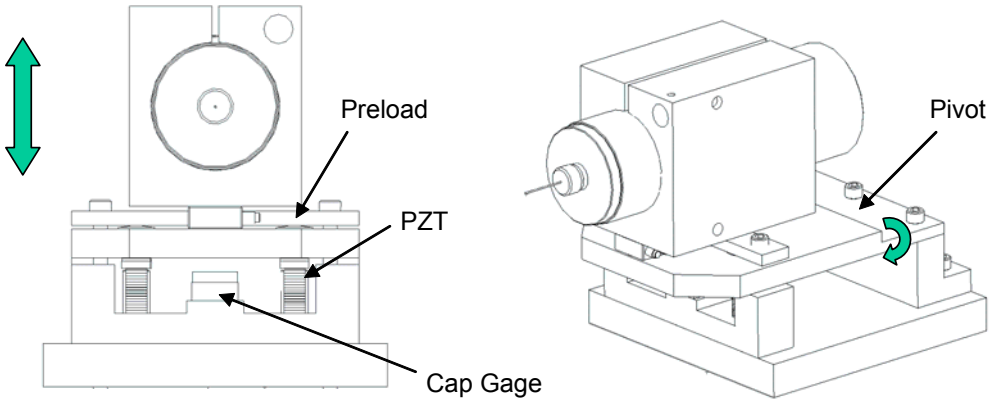

Figure 15 1-D Actuator Concept Design

Extension of the piezoelectric stacks results in vertical tool motion through deformation of the flexure plate as shown in Figure 16.

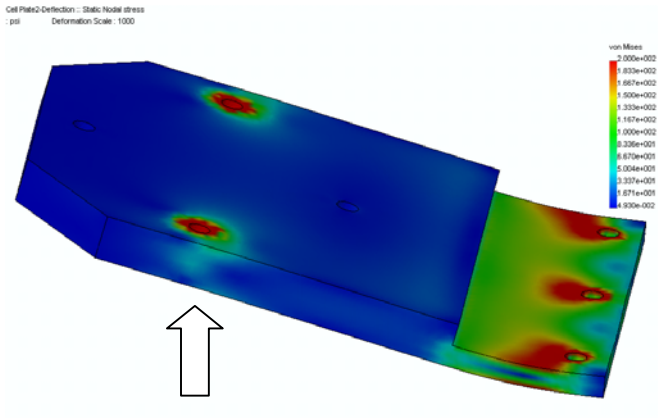

Figure 16 Deformation of Flexure Plate during Vertical Motion

7.3.2 2-D ACTUATOR CONCEPT DESIGN

A two dimensional actuator design concept was envisioned using the same flexure design but actuating the piezo stacks differentially as shown in Figure 17 creates horizontal motion in a method similar to the operation of the Ultramill used for elliptical vibration assisted machining (see section 10).

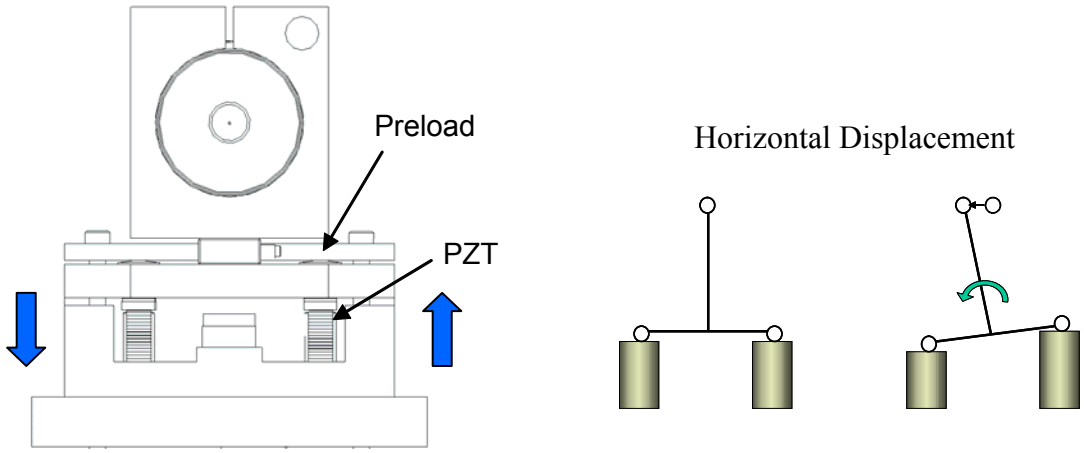

Figure 17 2-D Actuator Concept Design

Horizontal actuation of the tool tip is achieved by differential displacement of the two piezo actuators. This difference twists the guidance flexure and rotates the spindle support to produce horizontal displacement of the tool. The resulting deformation of the flexure plate can be seen in the finite element model in Figure 18.

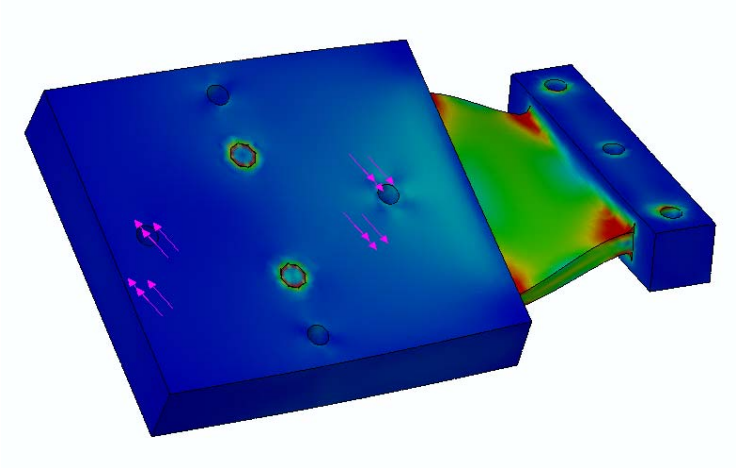

Figure 18 Finite Element Deformation of Flexure Plate

Displacement Loss – Parasitic Motion

Although this design could produce both horizontal and vertical motion of the tool, further analysis of the displacement revealed a significant loss in axial displacement during actuation of the tool. This undesired displacement or parasitic motion can be seen in the deformation model in Figure 19. As the flexure plate is deformed during vertical actuation, rotation about the flexure results in additional undesired motion. At full vertical displacement of the piezoelectric actuator (20μm), the tool undergoes an undesired axial displacement of 14μm in the direction of the arrow displayed in Figure 19.

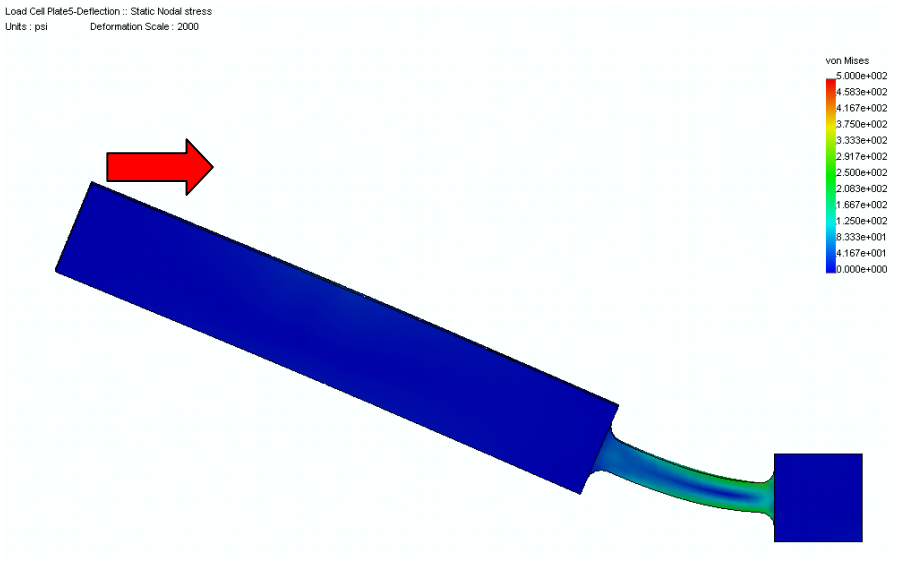

Figure 19 Displacement Loss during Actuation of Flexure

Two-Axis Flexure Design

To eliminate the parasitic axial motion of the tool, the vertical flexure must be located along the center line of the tool. With the vertical pivot point at the tool center, rotation about the pivot produces vertical motion for small displacements.

In order to produce horizontal motion, an offset between the horizontal pivot and the tool center must be present. Without this offset, rotation about the pivot would only rotate the tool about its center without producing any horizontal displacement.

The solution to this displacement dilemma was to create two flexure axes at the correct locations to produce the desired displacements. The resulting two-axis flexure design is illustrated in Figure 20. The dotted lines are the two flexure axes in this design.

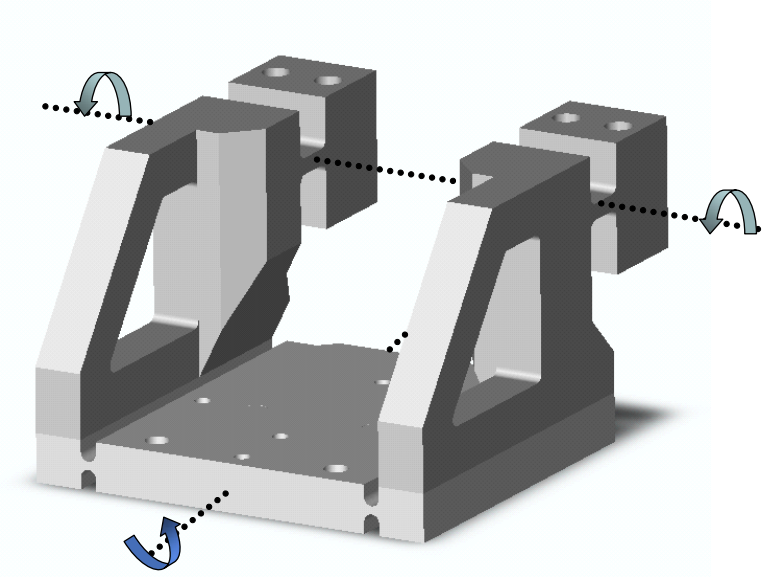

Figure 20 Two-Axis Flexure Design

7.3.3 FINITE ELEMENT ANALYSIS

Finite element analysis (model shown in Figure 21) was employed to predict the deformation and displacements of the flexure design. Through the use of two axes of rotation, the resulting motion of the tool tip was verified and the undesired motion was eliminated.

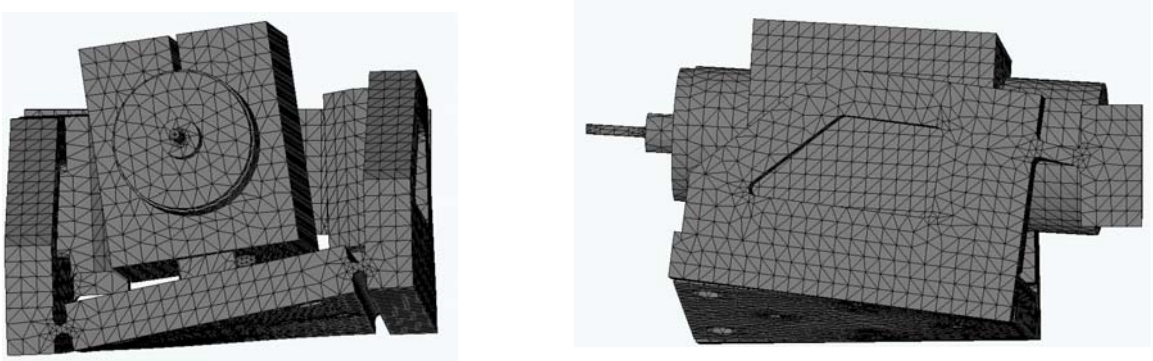

Figure 21 Finite Element Deformation of Two-Axis Flexure Design

7.3.4 DYNAMIC ANALYSIS

Finite Element Analysis was also employed to analyze the vibration modes of the structure and their natural frequencies. The lowest natural frequency of the total system was a rocking back and forth about the spindle's center support (Figure 22). This frequency was calculated to be 475 Hz and was too close to the cutting frequency of 330 Hz.

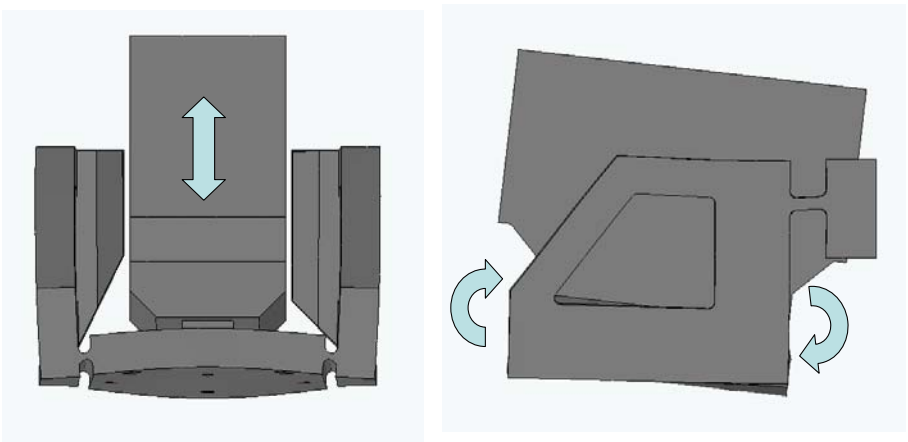

Figure 22 Lowest Mode Shape (475 Hz)

The mode shapes and associated frequencies of the support frame are illustrated in Figure 23. These resulting frequencies were acceptable and well above the tooth pass frequency of 330 Hz.

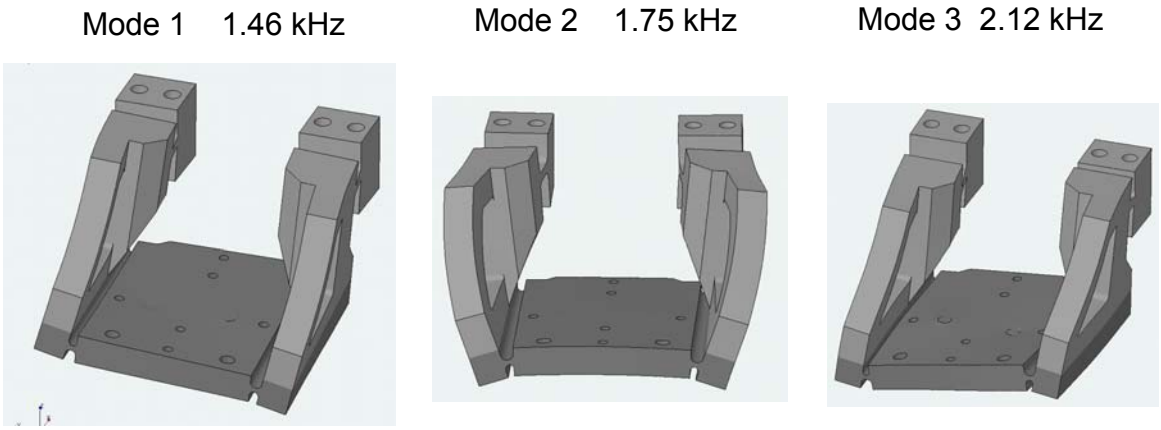

Figure 23 Mode Shapes of Spindle Support Frame

To increase the stiffness of the structure against the rocking motion illustrated in Figure 22, a rear nodal support was added to the structure (Figure 24). This nodal support has a high stiffness

in the vertical direction to create a node at this point while retaining a low stiffness in horizontal direction to not over constrain the flexure design.

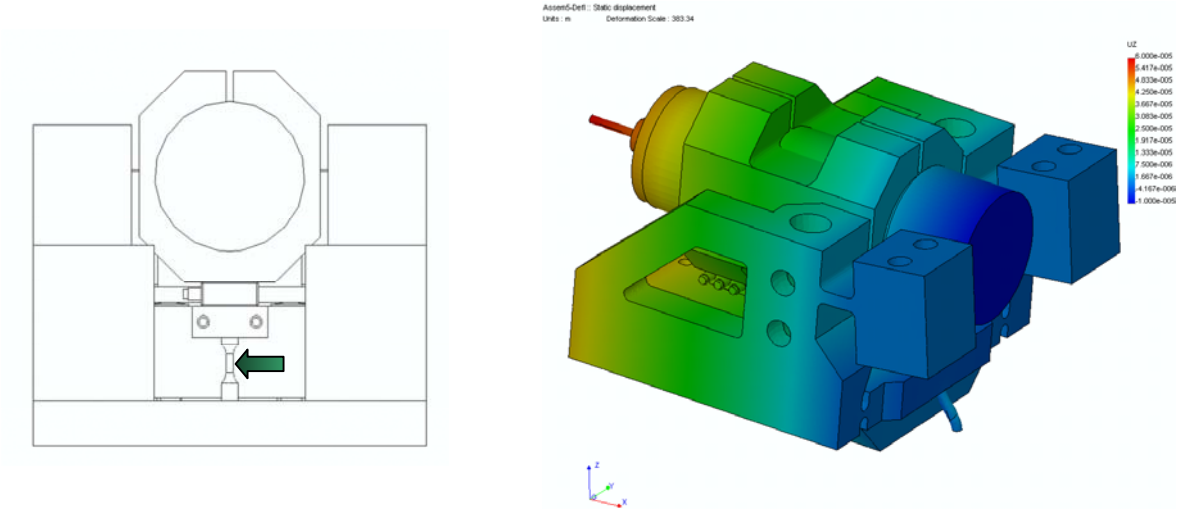

Figure 24 Rear Nodal Support

The addition of this nodal support increased the lowest natural frequency of the spindle assembly from 475 Hz to 600 Hz while maintaining the desired motion profiles without introducing any undesired displacements.

7.3.5 FINAL ASSEMBLY

The final two-axis spindle actuator design can be seen below in Figure 25.

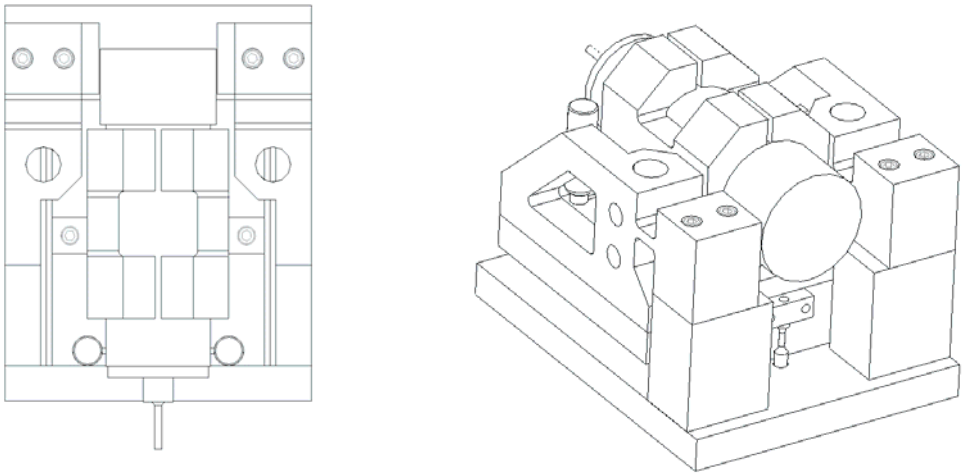

Figure 25 Two-Axis Force Measurement Spindle Actuator Design

7.4 CONTROLS

7.4.1 SYSTEM MODELING

The system was modeled as the composition of two-second order systems: one vertical spring mass damper system and one torsional spring mass damper system. (Figure 26)

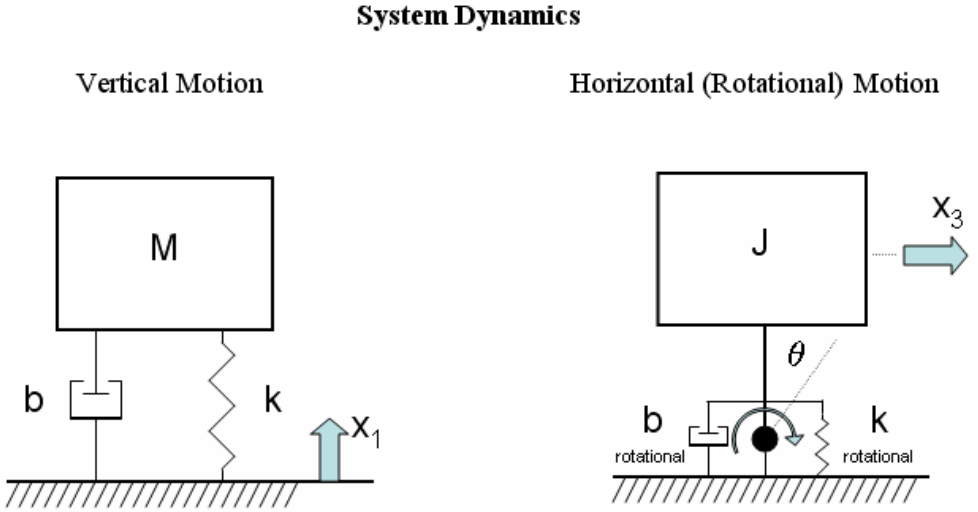

Figure 26 System Dynamics Model

Using the horizontal and vertical displacements (x_1 and x_3), the state dynamics equations can be derived as follows.

$$\sum F_v = 0$$

$$M\ddot{x}_1 + b_v\dot{x}_1 + k_v x_1 = 0$$

$$\ddot{x}_1 = \frac{-b_v}{M}\dot{x}_1 - \frac{k_v}{M}x_1$$

$$\sum T = 0$$

$$J\ddot{\theta} + b_r\dot{\theta} + k_r\theta = 0$$

$$\theta = \tan^{-1}\left(\frac{x_3}{d_{PZT}}\right) \cong \frac{x_3}{d_{PZT}} \quad \text{(small angles)}$$

$$\left(\frac{J}{d_{PZT}}\right)\ddot{x}_3 + \left(\frac{b_r}{d_{PZT}}\right)\ddot{x}_3 + \left(\frac{k_r}{d_{PZT}}\right)x_3 = 0 \qquad (5)$$

$$\ddot{x}_3 = \frac{-b_r}{J}\dot{x}_3 - \frac{k_r}{J}x_3 = 0$$

State Dynamics Equations

Defining state variables x_2 and x_4 as the time derivatives of displacements x_1 and x_3, the dynamics can be represented in matrix state space form (Equation 6).

$$\underline{\dot{x}} = \underline{\underline{A}}\,\underline{x} + \underline{\underline{B}}\,\underline{u} \qquad\qquad \underline{y} = \underline{\underline{C}}\,\underline{x} + \underline{\underline{D}}\,\underline{u} \tag{6}$$

State Differential Equation

In state space form, this system model is represented as:

$$\begin{bmatrix} \dot{x}_1 \\ \dot{x}_2 \\ \dot{x}_3 \\ \dot{x}_4 \end{bmatrix} = \begin{bmatrix} 0 & 1 & 0 & 0 \\ -\frac{k_v}{M} & -\frac{b_v}{M} & 0 & 0 \\ 0 & 0 & 0 & 1 \\ 0 & 0 & -\frac{k_r}{J} & -\frac{b_r}{J} \end{bmatrix} \cdot \begin{bmatrix} x_1 \\ x_2 \\ x_3 \\ x_4 \end{bmatrix} + \begin{bmatrix} 0 & 0 \\ -\frac{1}{M} & -\frac{1}{M} \\ 0 & 0 \\ \frac{sp}{2 \cdot J} & -\frac{sp}{2 \cdot J} \end{bmatrix} \cdot \begin{bmatrix} u_1 \\ u_2 \end{bmatrix}$$

$$\begin{bmatrix} y_1 \\ y_2 \end{bmatrix} = \begin{bmatrix} 0 & 0 & 1.6 & 0 \\ 2.3 & 0 & 0 & 0 \end{bmatrix} \cdot \begin{bmatrix} x_1 \\ x_2 \\ x_3 \\ x_4 \end{bmatrix} + \begin{bmatrix} 0 & 0 \\ 0 & 0 \end{bmatrix} \cdot \begin{bmatrix} u_1 \\ u_2 \end{bmatrix} \tag{7}$$

State Space Model

Where:

State Variables

x_1 = Displacement of (PZT Actuator 1 + PZT Actuator 2) / 2 (m)
x_2 = Velocity of x_1 (m/s)
x_3 = Displacement of PZT Actuator 1 – PZT Actuator 2 (m)
x_4 = Velocity of x_3 (m/s)
u_1 = Input Force of PZT 1 (N)
u_2 = Input Force of PZT 2 (N)
y_1 = Horizontal (X) Tool position (m)
y_2 = Vertical (Y) Tool position (m)

System Parameters

M = 6.7 Kg
k_v= 95 x 10^6 N/m
b_v= 0.1
J = 0.02 Kg m^2
k_r= 0.7 x 10^6 Nm/rad
b_r= 0.1
sp = 2” = 0.0508 m

7.4.2 OBSERVABILITY AND CONTROLLABILITY MATRICIES

From the state space matrix representation, the controllability and observability of the coupled two-input two-output system can be evaluated.

Controllability

Controllability Matrix

$$M_c = \begin{bmatrix} B & AB & A^2B & A^3B \end{bmatrix} \tag{8}$$

$$M_c = \begin{bmatrix} 0 & 0 & -0.149 & -0.149 & 0.0022 & 0.0022 & 2.12\times10^{6} & 2.12\times10^{6} \\ -0.149 & -0.149 & 0.0022 & 0.0022 & 2.12\times10^{6} & 2.12\times10^{6} & -63173 & -63173 \\ 0 & 0 & -1.27 & 1.27 & 6.35 & -6.35 & 4.445\times10^{7} & -4.445\times10^{7} \\ -1.27 & 1.27 & 6.35 & -6.35 & 4.445\times10^{7} & -4.445\times10^{7} & -4.445\times10^{8} & 4.445\times10^{8} \end{bmatrix}$$

Rank = 4, This system is fully Controllable.

Observability

Observability Matrix

$$M_o = \begin{bmatrix} C^T & (CA)^T & (CA^2)^T & (CA^3)^T \end{bmatrix} \tag{9}$$

$$M_o = \begin{bmatrix} 0 & 2.3 & 0 & 0 & 0 & -3.26\times10^{7} & 0 & 4.868\times10^{5} \\ 0 & 0 & 0 & 2.3 & 0 & -0.0343 & 0 & -3.26\times10^{7} \\ 1.6 & 0 & 0 & 0 & -5.6\times10^{7} & 0 & 2.8\times10^{8} & 0 \\ 0 & 0 & 1.6 & 0 & -8.0 & 0 & -5.6\times10^{7} & 0 \end{bmatrix}$$

Rank = 4, This system is fully Observable.

7.4.3 CLOSED LOOP CONTROL

Closed loop control of this system is incorporated using capacitance gages to provide position feedback for each piezoelectric actuator. Through the use of closed loop control, the effects of the hysteresis of the piezoelectric element can be controlled (Figure 27).

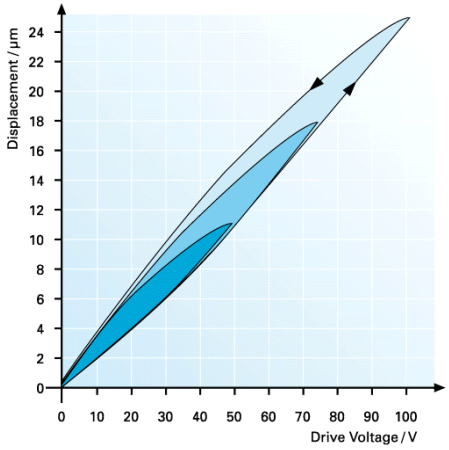

Figure 27 Hysteresis curve for an open loop piezo actuator for various peak voltages

Force Feedback Control Algorithm

The force feedback control algorithm reads the real time measured cutting force and multiplies it by the compliance of the tool to output tool deflection error. This error is sent to a PID controller to drive the piezoelectric actuator. A capacitance gage is used as closed loop feedback for the actuator motion. The force feedback loop for a single axis is shown below (Figure 28). For a two axis system, two of the force feedback loops will be implemented; one for each axis.

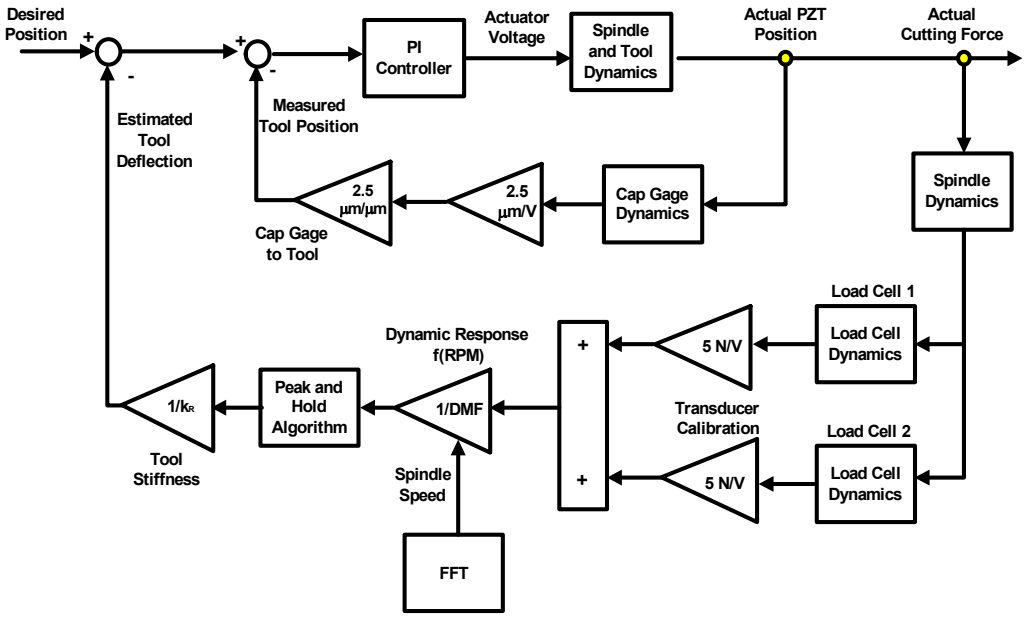

Figure 28 Force Feedback Control Block Diagram

The closed loop diagram for the MIMO two-input two-output controller utilizing coupled dynamics equations is as follows.

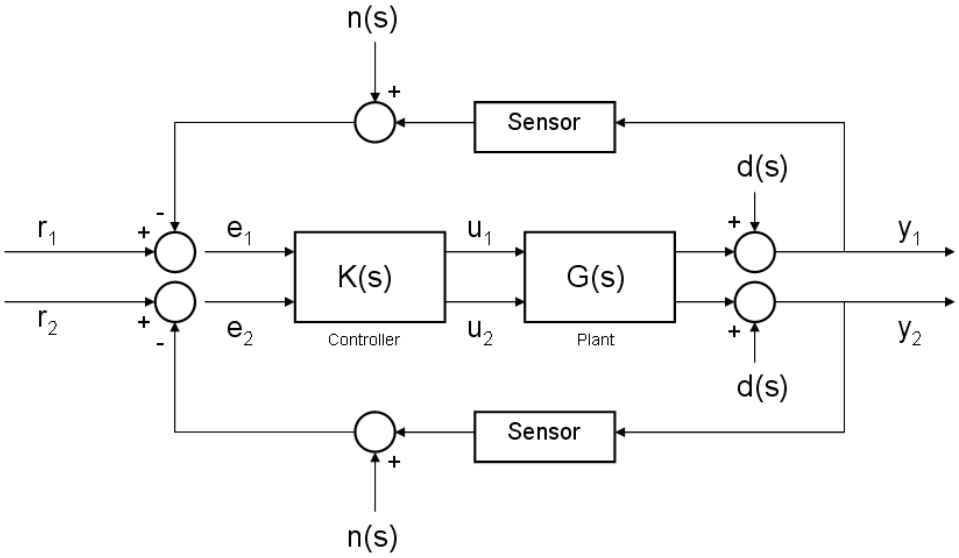

Figure 29 Closed Loop Block Diagram MIMO Controller

This multivariable control scheme accounts for the coupled dynamics of the system calculating the input voltage for each piezo based on both the horizontal and vertical dynamics. Work on this multivariable controller design is presently in process.

7.5 CONCLUSIONS AND FUTURE WORK

Cutting force measurement can be accurately obtained from the spindle assembly once the dynamic response and the spindle speed (forcing frequency) are known. This on-spindle force measurement technique can be used to supply a self contained force measurement and tool positioning system.

Design of the spindle actuator and flexure mechanisms has been completed and parts have been fabricated for the two axis spindle actuator. The next steps involved in this project are completion of the actuator assembly, calibration of the two axis motion profiles, and implementation of the two axis force feedback control algorithm.

REFERENCES

1. Clayton, S,. "Force Modeling and Deflection Compensation of Miniature Ball End Mills," MS Thesis, North Carolina State University, 2003.
2. Hood, D, "Force Feedback Control of Tool Deflection in Miniature Ball End Milling," MS Thesis, North Carolina State University, 2003.
3. Dow, T., Miller E., Garrard K., Sohn A., Wright, T. "Compensation of Tool Force in Small Diameter End Mills," ASPE Proceedings, Vol. 20, pp. 546-550, 199.
4. Miller, E., "Deflection Prediction and Error Correction of High Speed Miniature Milling Tools," MS Thesis, North Carolina State University, 2000.
5. Lobontiu, N., Compliant Mechanisms: Design of Flexure Hinges, CRC Press, 2003.
6. Drescher, J. D., "Tool Force Measurement in Diamond Turning," MS Thesis, North Carolina State University, 1989.
7. Drescher, J. D., "Tool Force, Tool Edge, and Surface Finish Relationships in Diamond Turning," Ph.D. Dissertation, North Carolina State University, 1992.
8. Arcona, C., "Tool Force, Chip Formation and Surface Finish in Diamond Turning," Ph.D. Dissertation, North Carolina State University, 1996.
9. Minor, P., "Tool Wear and Tool Forces in High Speed Machining of Aluminum," MS Thesis, North Carolina State University, 1998.
10. Karnovsky, I., Lebed, O., Formulas for Structural Dynamics, McGraw Hill, 2001.
11. Altintas, Y., Manufacturing Automation: Metal Cutting Mechanics, Machine Tool Vibrations, and CNC Design, Cambridge University Press, 2000.

8 CAPABILITIES OF MICRO-MACHINING

Brett Brocato
Graduate Student
Thomas Dow
Professor
Mechanical and Aerospace Engineering

The goal of this research is to improve feature size and tolerance using micro-scale machining. This section reports on a literature search of current techniques for producing sub-millimeter features and applications of these techniques. While many MEMS (MicroElectroMechanicalSystems) devices are fabricated using silicon etching techniques developed for the microelectronics industry, micro-machining is an attractive alternative because of its low start-up cost relative to other capital-intensive micromachining technologies, applicability to a wide range of materials, high flexibility of feature geometry and low cost for prototype manufacturing. The search uncovered papers in the areas of proof of capability, companion processes, process analysis, and the applications of more general micromachining technologies.

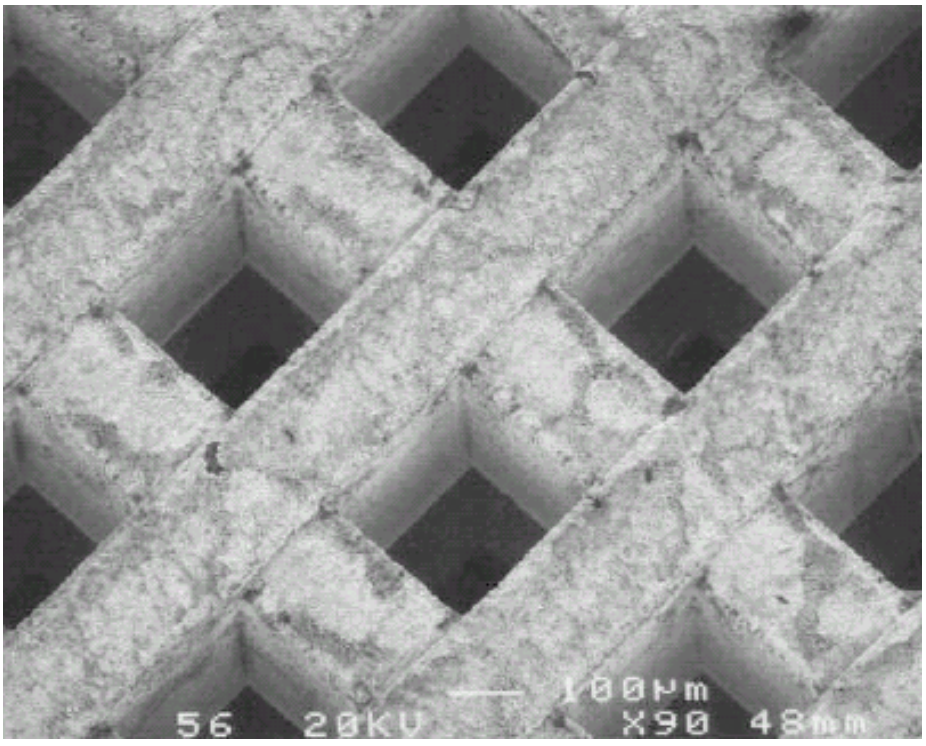

8.1 INTRODUCTION

Microelectromechanical systems (MEMS) offer designers the ability to create miniature mechanical oscillators, optical network components and biological labs on a chip. Although manufacturers are introducing a wide range of MEMS-based products, developers have found that guiding MEMS devices from the laboratory to the marketplace is a costly and time-consuming venture. For example, it is not unusual for a single MEMS prototyping run to take 3 months. The high cost of a MEMS fabrication facility forces companies to use existing foundries such as Sandia, MCNC or Berkeley with long lead times. The problem lies not with the MEMS devices themselves, but with the semiconductor-based manufacturing techniques employed to build them. Semiconductor wafer fabs excel at producing high-volume integrated circuits using standard CMOS processing, but many MEMS devices are manufactured in lower volumes with more complex structures such as moving three-dimensional micromirror arrays.

Table 1. Material and Feature Size Guidelines by Process Type [1]

Technology / Feature Geometry	**Min. Feature size** / Feature tolerance**	**Feature Positional Tolerance**	**Material Removal Rate**	**Materials**
Focused Ion Beam/ /2D & 3D	200 nm / 20 nm	100 nm	0.5 μm^3/sec	Any
Micro Milling or Turning /2D or 3D	25 μm / 2 μm	3 μm	10,400 μm^3/sec	Polymers, Al, Brass, Nickel, SS and Titanium
Excimer Laser /2D or 3D	6 μm / < 1 μm	< 1 μm	40,000 μm^3/sec	Polymers, Ceramics and some metals
Femto-Second Laser /2D or 3D	1 μm / <1μm	< 1 μm	13,000 μm^3/sec	Any
Micro-EDM(Sinker or Wire) /2D or 3D	25 μm /3 μm	3 μm	25x10^6 μm^3/sec	Conductive materials
LIGA /2D	< 1 μm / 20-500 nm	~ 300 nm across 75 mm	N/A	Copper, Nickel, Permalloy

**Feature size represents the width of a slot or a diameter of a hole

There are non-semiconductor processes for making MEMS devices that include focused ion beam machining, mechanical turning and milling, laser processing, electro-discharge machining

and LIGA. Each technique can be classified in terms of minimum feature size, position tolerance, maximum material removal rate and material compatibility [1] as shown in Table 1.

Focused Ion Beam (FIB) machining is a process in which the kinetic energy of accelerated ions is converted to thermal energy and used to vaporize very small amounts of material from a workpiece. It is a 3-D process with extremely high tolerances that can be used on any material. The main disadvantages are slow material removal rate (MRR) and high equipment costs. Excimer lasers and femto-second lasers have comparable removal rates to micro-machining. The achieved tolerances are superior to micro-machining. Excimer lasers have less material flexibility than micro-machining. Micro-Electro Discharge Machining (Micro-EDM) has an extremely high MRR and comparable accuracy to micro-machining, but only works on conductive materials.

The most common material-removal processes in macro manufacturing are turning and milling. The lower dimensional limits of these processes are being expanded by current research. Micro-machining is the process of chip removal by means of a spindle and an end mill in the diameter range of 200-μm or less. Part features are on the order of 25 μm. Carbide milling tools are commercially available in 100-μm size. Custom diamond tools as small as 22 μm have been created by researchers. Feature aspect ratios of 40:1 have been achieved on machined parts. Micro-machining has the advantage of greater material and geometry flexibility than that of lithography and most other micromachining processes.

Current micro-machining techniques using a high-speed spindle are plagued with tool runout that limits the feature size and tolerance. A proposed concept is to replace the high-speed spindle with a piezoelectrically driven tool holder (for example, the UltraMill – see Section 10) that can move the diamond tool tip in an elliptical motion at frequencies up to 5000 Hz - the equivalent of 300,000 rpm. The two actuators are driven independently to create a tool path that can be changed from linear to elliptical to circular with the amplitude, frequency and phase of the excitation voltages.

The widespread use of this process would have a profound influence on fabrication techniques for micro-mechanical, micro-optical and micro-fluidic devices. Its key features are:

- Optical surface finish
- Sub-micrometer 3D feature size and position
- Extremely low cutting forces
- No burring at the edge of a cut
- Applicable to a wide range of materials – metals, plastics and ceramics

8.2 LITERATURE SEARCH

Existing research falls into several categories: microscale capability, pre- and post-processing, analysis and applications of general micromachining. Each of these will be addressed in the following sections.

8.2.1 MICROSCALE CAPABILITY

Schaller [2] illustrated the capability to mill small grooves with custom-made 35-120 μm tools. Figure 1 shows one of the tools. The tools were manufactured with diamond grinding wheels from tungsten carbide rods. With a non-CNC grinding machine, a tool break rate of up to 50% and tolerances of +/- 5 μm were reported during manufacture. Channel-cutting parameters of 19,000 rpm spindle speed and a feed rate of 35 μm/s were used. This resulted in a feed per tooth in the range of the cutting edge radii, 1 to 2 μm. A maximum depth of cut of 20 μm was tested. Run-out of the tool was minimized to 10 μm.

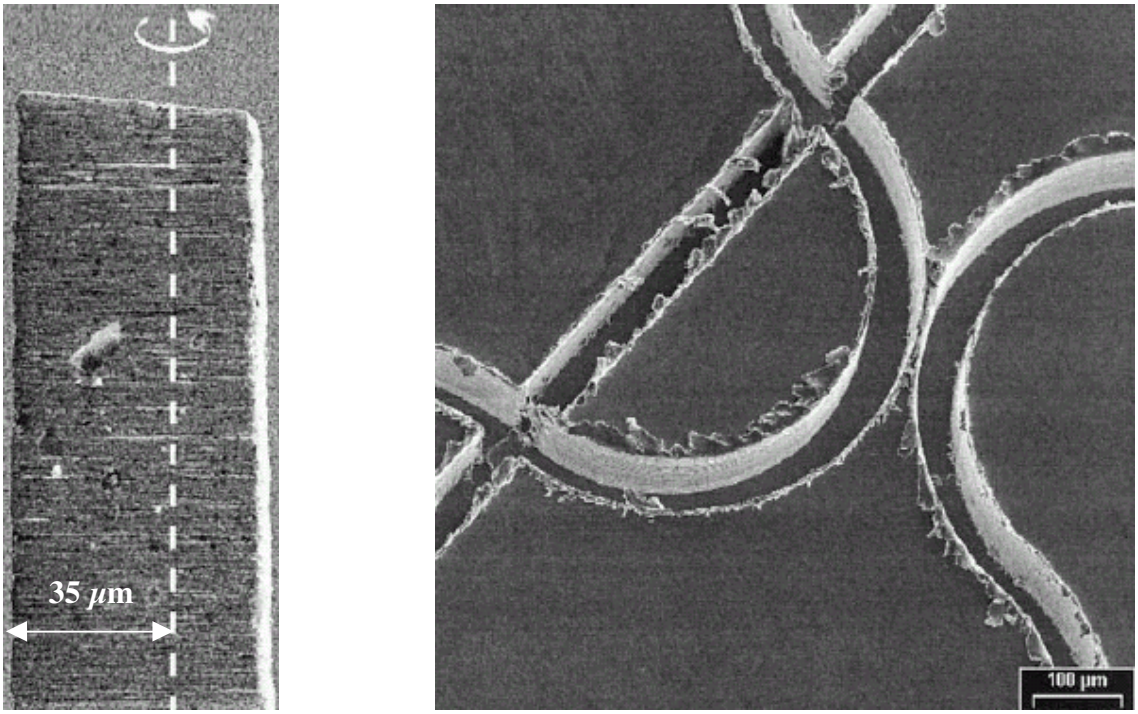

Figure 1. Custom-ground Carbide Tool and Grooves Machined in Brass (note burrs at edges of grooves) [2]

Burr creation occurred with both brass and steel workpieces when cutting with carbide tools. Figure 1 shows channels in brass with such burrs. Burrs were not seen when cutting brass with diamond tools. Diamond tools were not used for making channels due to the lack of very small-diameter sizes, but were valuable for deburring (milling the surface of the grooved part) after

channels were cut with carbide tools. Burr reduction and removal will be discussed, and the results shown, in Section 8.2.2 on pre- and post-processing.

Takeuchi [3] used a CNC 3-axis lathe with a spindle in place of the tool holder to confirm that ultra-precision sculptured metal workpieces could be made. Rough cuts were made with a 200 μm diameter tungsten carbide ball-endmill. Custom diamond pseudo-ball-endmills were used for finishing passes. The custom pseudo-mills had a single-crystal diamond edge of radius 100 μm offset from the axis of the tool by the same distance, as shown in Figure 2. A 3-mm diameter sculpture of a face similar to that in Figure 4 was made. Cutting parameters were 50,000 rpm, feed rate 50 mm/min, and depth of cut 1 μm (for finishing with the diamond tool). Tool path resolution was 2 μm x 5 μm, and the machining took 6 hours.

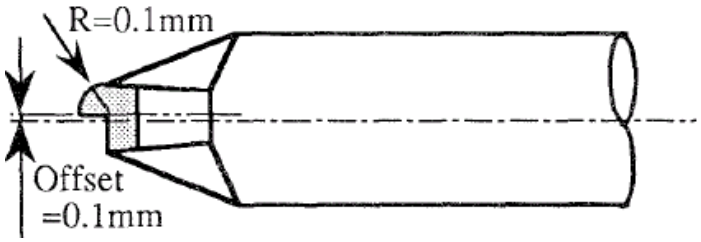

Figure 2. Pseudo Ball-end Diamond Mill [3]

Kawai [4] continued the research of Takeuchi [3]. Figure 3 shows (counter-clockwise from top left) high-density grooves milled in Ni-P plated steel, high aspect ratio trapezoidal grooves milled in brass, and a milled mold for a 25 μm pitch encoder disk.

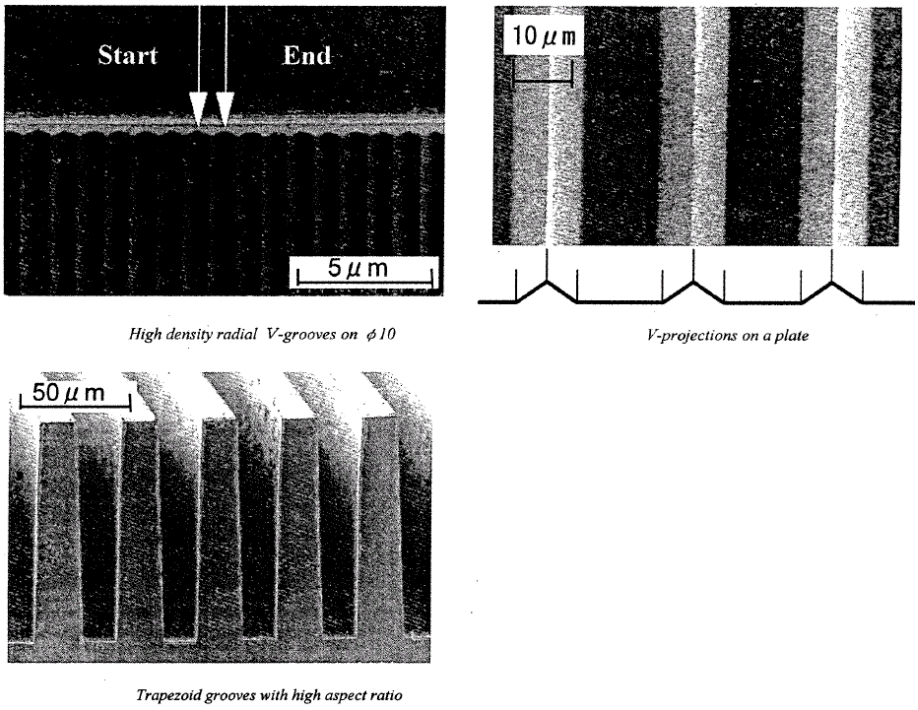

Figure 3. Diamond Milled Microstructures [4]

The array of lenses in Figure 4 was milled using tools that are approximately the same diameter as the lenses, about 230 μm. The wavy shape was milled by a single-crystal diamond endmill of radius 25 μm. The face in Figure 4 is smaller than that created in the previous study and was created with a diamond pseudo-ball-endmill of radius 30 μm. Kawai also machined a 25 μm square by 1 mm tall column from brass. The 40-to-1 aspect ratio of this structure was the highest found by the literature search.

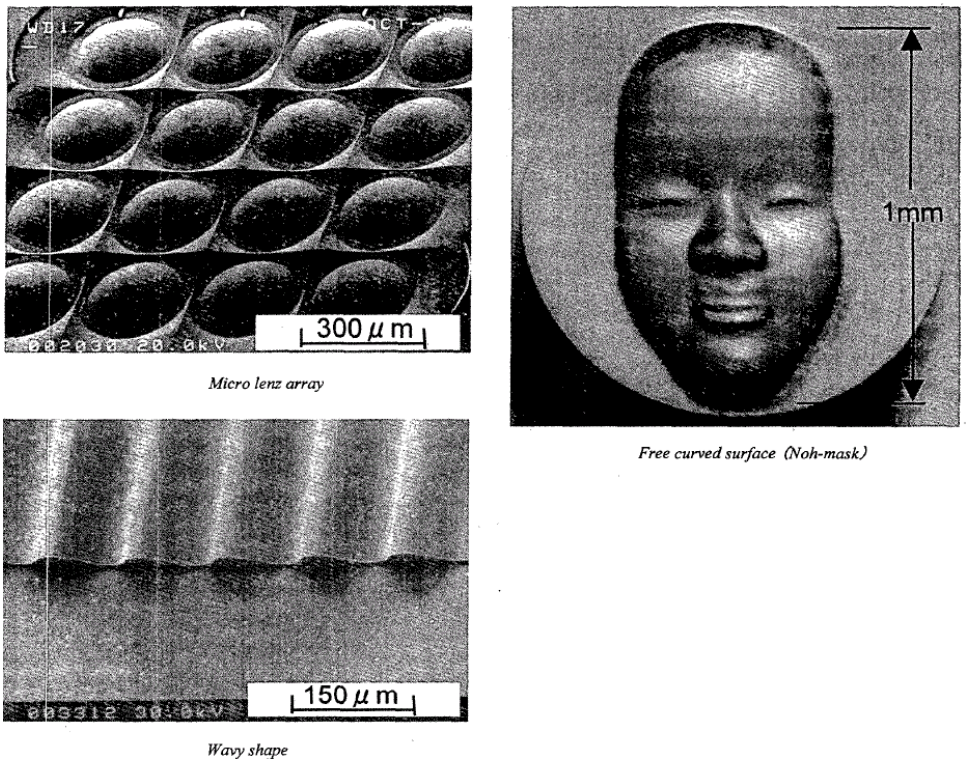

Figure 4. Diamond Milled Microstructures [4]

Friedrich [5] used custom milling tools (Figure 5), that were created using Focused Ion Beam (FIB) micromachining of steel or tungsten carbide blanks. The tool shown has an effective cutting diameter of 22 μm and a cutter length of 77 μm. Friedrich used these tools to manufacture the spiral pattern 1.5 mm in diameter, shown in Figure 6. The workpiece is PMMA, and the trench depth is 62 μm. Minimum wall thickness was investigated at the center of the pattern where the spirals converge. The radial trench allowed the investigation of

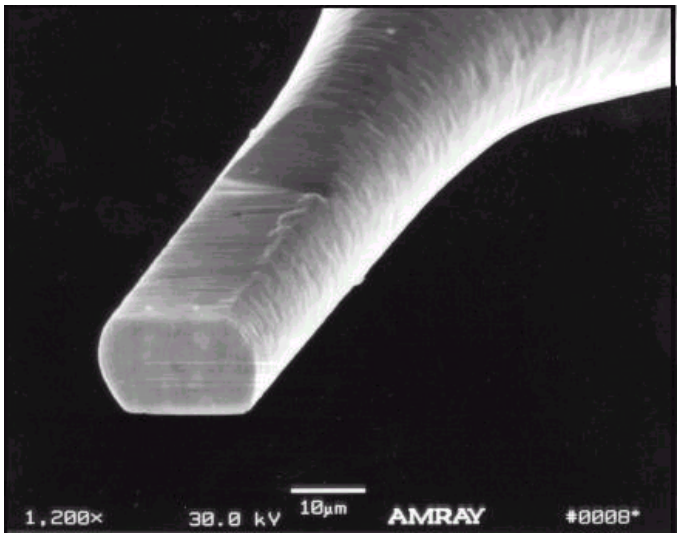

Figure 5. Rounded Cutting Tool [5]

rpm spindle speed and 35 μm per second feedrate. Depth of cut was 4 μm per pass for 15 passes and machining time was 3 hours.

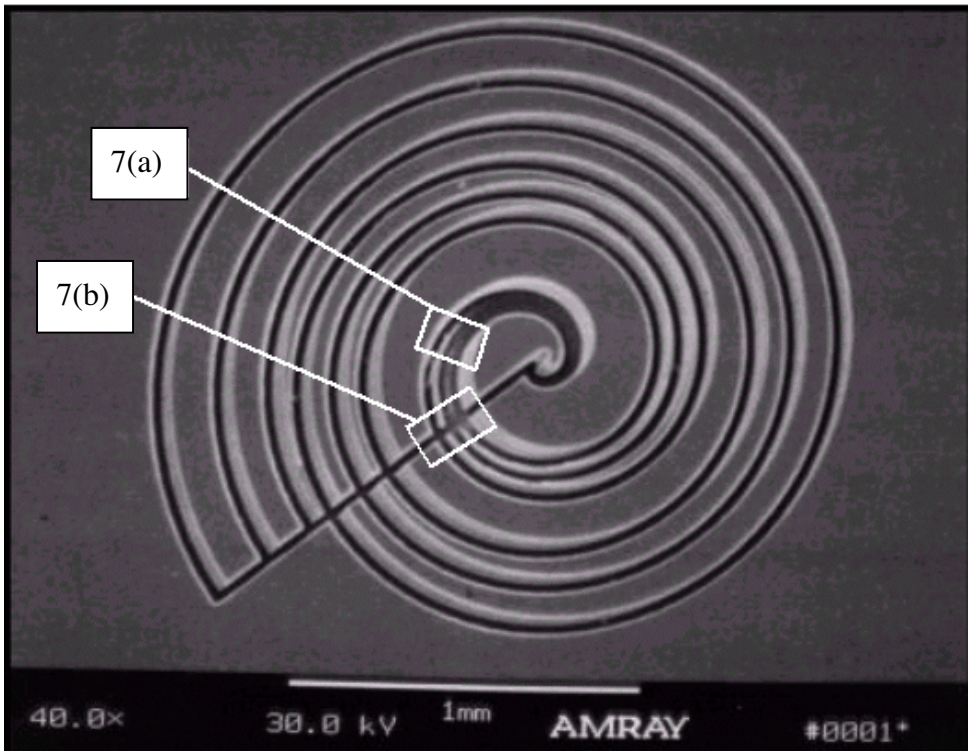

Figure 6. Micromilled Spiral Structure with details in Figure 7 [5]

Figure 7(a) shows a close-up of the intersection of the straight trench and spirals. The terraced structure of the walls resulted from a stepped tool movement of exponentially changing width.

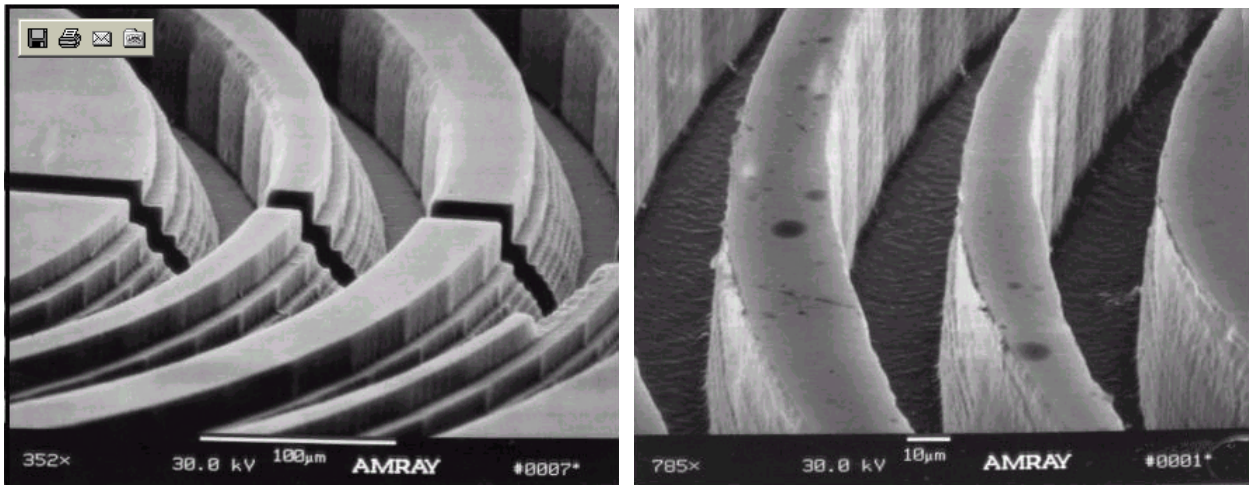

(a) Close-up of the intersections (b) Thin-wall channels

Figure 7. Intersection Detail of Spiral Structure [5]

The vertical facets are a result of the 5-degree polar resolution of the spiral shape. The minimum freestanding wall was 8 μm wide and 60 μm high, as shown in Figure 7(b). The aspect ratio of this wall is 7.5:1. The roughness of the trench bottom is 100 nm RMS. The walls are typically within 0.5 degrees of vertical.

Kawai [4] also performed scribing experiments. Scribing had the disadvantage of very slow cutting speed (on the order of 20 mm/min). The double-focused lens mold in Figure 9 was scribed in oxygen-free copper. The grooves are about 35 μm wide.

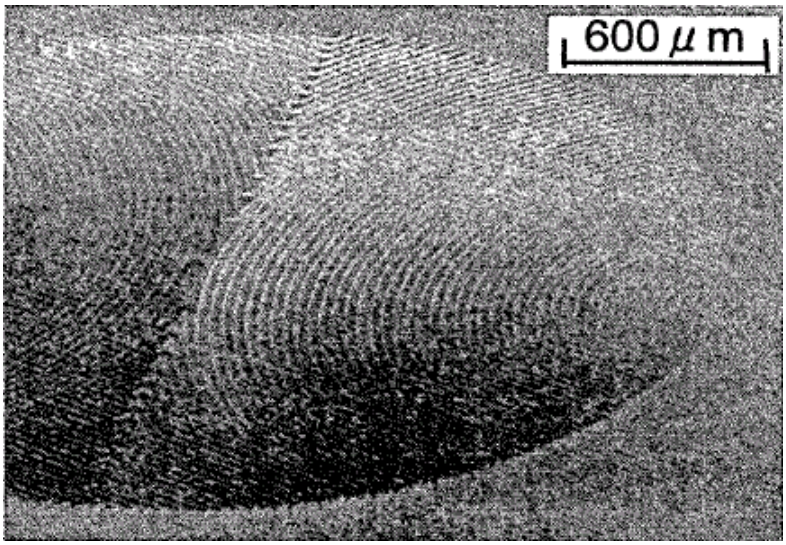

Figure 8. Scribed Double-focused Lens Mold [4]

8.2.2 PRE- AND POST-PROCESSING

Schiller's microchannel study [2] used pre- and post-processing to remove burrs. Brass workpieces were coated with a 10-μm layer of cyanoacrylate before milling. After grooves were cut with carbide tools, they were filled with the same coating. The coating above the un-milled surface of the workpiece was removed by diamond milling, and the coating within the milled structures removed by acetone in an ultrasonic bath. Burrs were removed with the coating. Figure 9 shows a brass microstructure both with and without the burr reduction procedure.

This approach did not work with stainless steel. Electrochemical polishing was needed to remove burrs from this material. Polishing time must be limited because structures begin to degrade soon after the point where burrs have been removed. Cleaning of the workpiece prior to polishing is also critical because non-uniform electrical fields surrounding foreign particles affect the polishing process.

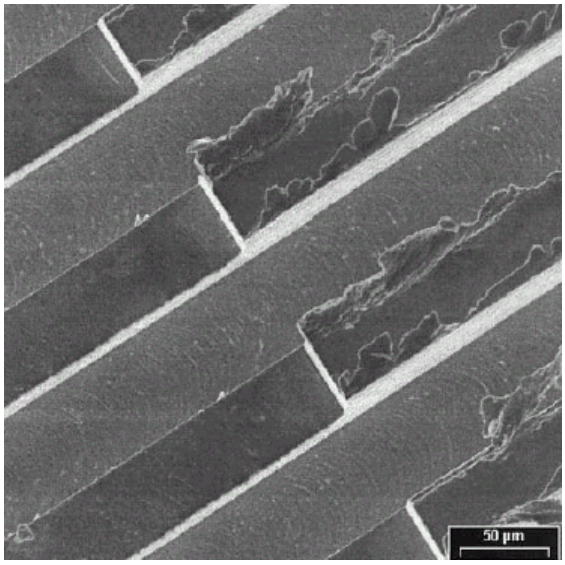

Figure 9. Microstructures in Brass With and Without Burr Reduction [2]

Park [6] studied the drilling and scribing of surfaces after reacting them with appropriate solutions. Silicon was reacted with potassium hydrate and aluminum with nitric acid prior to machining. The binding energy of the surfaces was reduced by these reactions. This reduced cutting forces to the depth of the reacted layer. The hardness of Si was reduced by about 20% due to the reaction. Drilling parameters for Si were 20,000 rpm and a 150 μm depth of cut. Crack formation was eliminated with chemical processing of the Si as compared to non-chemical machining. The thrust force for scribing nitric acid etched Al was reduced by about 50%, and burr formation was eliminated. Figure 10 shows scribed channels in Al.

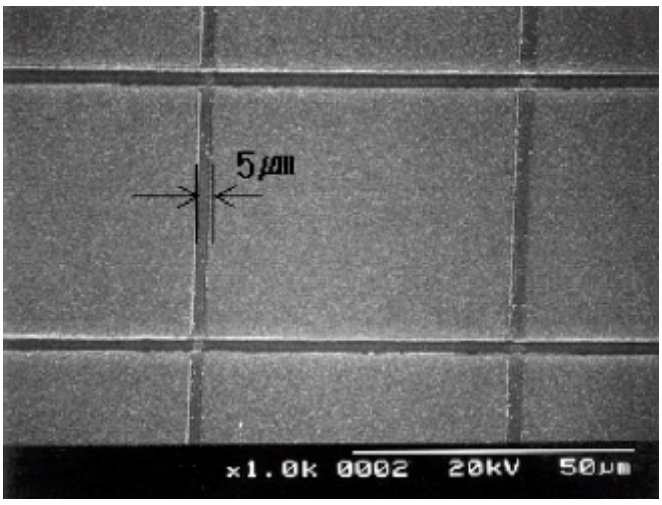

Figure 10. Chemical-mechanical Scribed Channels in Aluminum [6]

8.2.3 Analysis of the Machining Process

Modeling Cutting Force MEMO (micro-end-milling operations) differ from CEMO (conventional end-milling operations) in that the feed per tooth to tool radius ratio is much larger in MEMO for productivity reasons [7]. As a result, stress variation in the tool shaft is higher and tool life is shorter for MEMO. The proposed MEMO force model [7] proceeds from the Tlusty and Macniel [18] CEMO force model. The difference is in the method of chip thickness estimation. Tlusty [18] assumes that chip thickness is related only to feed per tooth and tool rotation angle. Bao [7] bases the estimation of chip thickness on the trajectory of the tool tip. Experimental verification of Bao's model showed good agreement with experimental data. Differences between predicted and measured forces averaged about 10%. Comparison between the MEMO [7] and CEMO [18] models shows that the feedrate per tooth to tool radius ratio is the determining factor in their respective errors. They are comparable when this ratio is less than 0.1. When it exceeds 0.1, the MEMO model is much more accurate.

Vogler's [8] model takes into account the fact that chip size approaches grain size in materials that are normally considered homogenous in macro-scale operations. One component of the model is a three-dimensional map of the various phases of the material. The workpieces used in the study were ductile iron, consisting of graphite, ferrite and pearlite. Different cutting coefficients are used to compute forces as tool flutes pass through the various phases. The forces during chip removal of pearlite were found to be larger than those for ferrite, even at a lower chip thickness. The model is validated by demonstrating the existence of high-frequency variations in ductile iron cutting force and the lack thereof in the cutting of single-phase ferrite and pearlite. It is also shown that smaller grain-size in the secondary phase reduces variation in the cutting forces, and that larger grain-size increases the variation. Scattergood [9] notes the approach of microscale feature-size to material grain-size and discusses research into the manufacture of nanocrystalline metals and alloys.

Modeling Tool Run-out In the second part of his paper [10], Bao adds the capability of predicting tool run-out from experimental cutting forces. Lee [11] collected average total run-out data for a variety of spindles and milling tool sizes. The data were used to create a model that predicts actual-versus-intended channel diameter. Milled channels were used to create ABS molded parts.

8.2.4 Applications

Applications of micro-machining include the manufacture of channels for microfluidic systems, masks for X-ray lithography, and micro-sized mechanical power systems. The current research in these applications is mostly concerned with semiconductor-type processes for manufacturing. Micro-machining should be capable of increasing the performance of parts through flexible

material selection and feature design. It will also reduce cost for small lot sizes and prototyping. For any of the applications listed above, micro-machining may be used to manufacture molds.

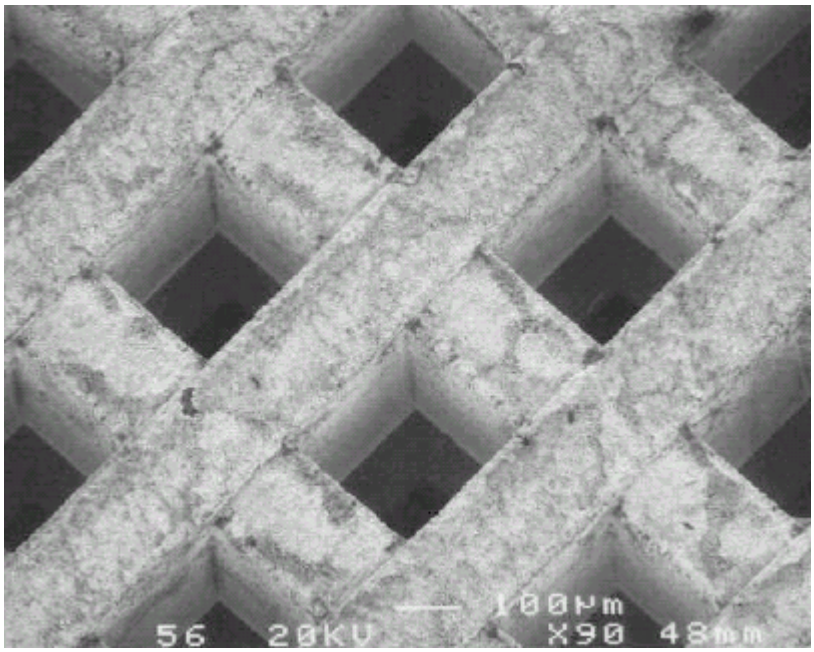

Figure 11. Injection-molded Microstructure [12]

Keppler [12] described the use of micro-machining for mold-making. Positive molds were cut from PMMA using 127 μm diameter end mills. Sputtering a conductive metal layer onto the positive mold created the negative substrate. This sputtered layer was electroplated with nickel to create a negative mold. After plating, an acetone bath was used to degrade the PMMA and leave a bare metal mold. The resulting molded structure is shown in Figure 11.

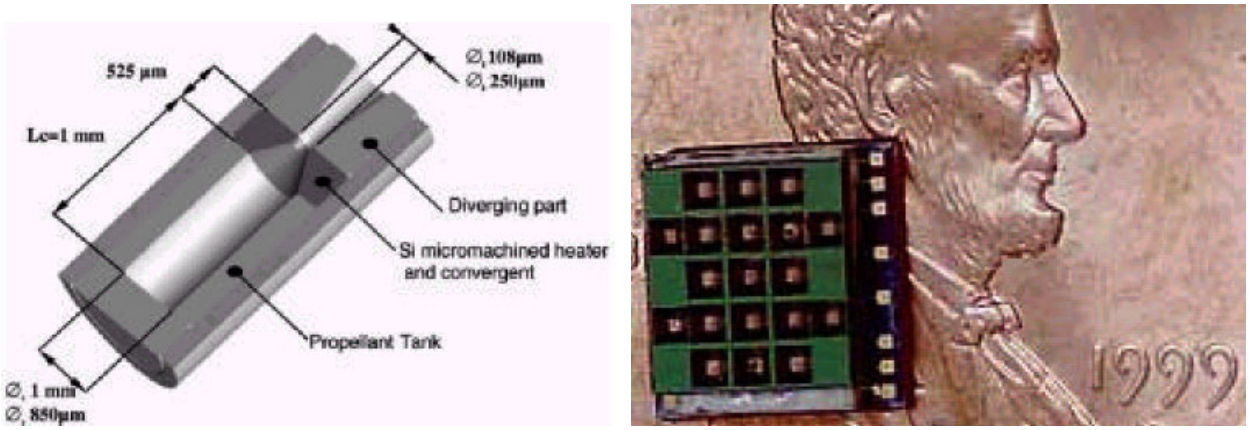

Figure 12. Micro-rocket Model [12]

An example of a microscale power system is the micro-rocket [12]. A 3D model of a combustion chamber is shown in Figure 12. Solid-fuel micro-rockets would not be reusable or restartable but could be in arrays such as that shown at right in Figure 12.

Another power system is the micro-sized expansion and/or combustion engine [14,15,16]. The energy density of compressed or combusting fuels is orders of magnitude higher than that of chemical batteries. Micro-machining of metals would be able to create high-strength engines capable of withstanding higher compression ratios than proposed etched engine designs. An example of an etched design is that of Jiang et al [14,15]. The proposed engine, shown in Figure 13 has 1.2 mm stroke, 1 mm square bore, and 6.3:1 compression ratio. It would operate at 1200 rpm and 7.3 mW in the combustion case. A prototype of the engine is shown in Figure 13.

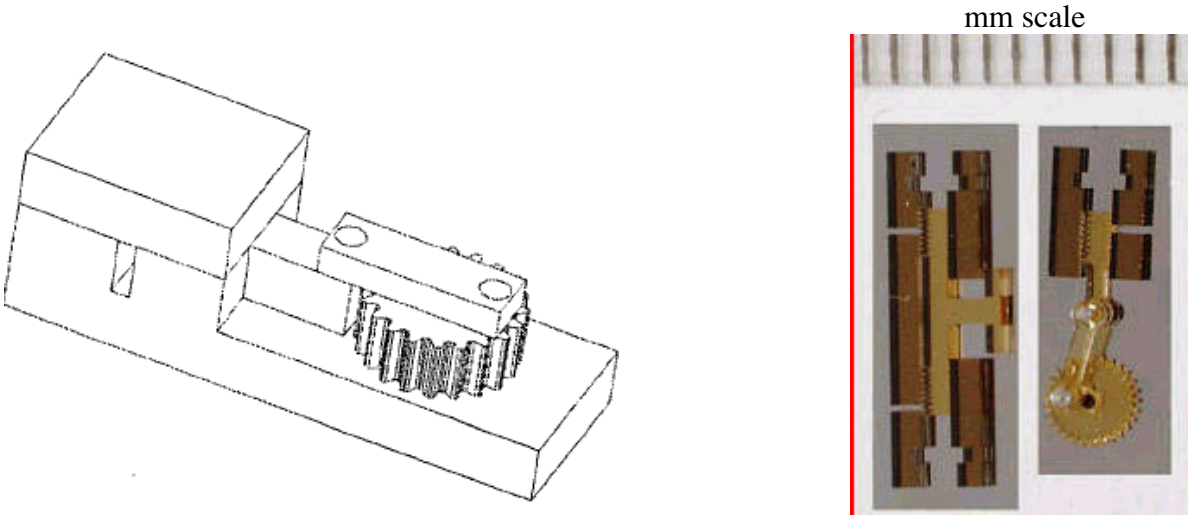

Figure 13. Micro-engine Model [14]

Sugiyama [13] designed a reciprocating engine to be built using semiconductor-type manufacturing. It may also lend itself to micro-machining.

REFERENCES

1. Benevides, G., "Meso-machining Capabilities", M⁴: Workshop on Micro/Meso-Mechanical Manufacturing, Evanston, IL, May 2000.
2. Shaller, Th. et al, *Microstructure grooves with a width less than 50 _m cut with ground hard metal micro end mills*. Precision Engineering, 23, pp 229, 1999.
3. Takeuchi, Yoshimi et al, *Computer Aided Ultra-Precision Micro-Machining of Metallic Materials*. IEEE International Conference on Robotics and Automation, pp 67, (1995).
4. Kawai, Tomohiko et al, *Ultra-Precision Micro Structuring by Means of Mechanical Machining*. IEEE, 2001.
5. Friedrich, Craig, Michigan Technical University. "MICROWEB". http://www.me.mtu.edu/~microweb/main.htm

6. Park, J.M. et al, *A Study on the Chemical Mechanical Micromachining (C3M) Process and its Application*. Journal of Materials Processing Technology, pp 130, 2001.
7. Bao, W.Y. and Tansel, I.N, *Modeling Micro-end-milling Operations. Part I: Analytical Cutting Force Model*. International Journal of Machine Tools and Manufacture, 40, pp 2155, 2000.
8. Vogler, Michael et al, *Microstructure-level Force Prediction for Micro-machining of Multi-phase Materials*. Proceedings of 2001 ASME International Mechanical Engineering Congress and Exposition November 11-16, New York, NY, 2001.
9. Scattergood, R.O. and Dow, T.A., *Mesoscale and Microscale Manufacturing Processes: Challenges for Materials, Fabrication, and Metrology*. Proceedings of the ASPE Winter Topical Meeting – Machines and Processes for Micro-scale and Meso-scale Fabrication, Metrology, and Assembly January 22-23, Gainesville, Florida, 2003.
10. Bao, W.Y. and Tansel, I.N, *Modeling Micro-end-milling Operations. Part II: tool run-out*. International Journal of Machine Tools and Manufacture, 40, pp 2175, 2000.
11. Keppler, Chrisian, *Micro-machining for Mold Fabrication,* Laboratory for Manufacturing Automation Precision Manufacturing Group, University of California, Berkeley, 2003.
12. Jiang, K.C. et al, *Design and Analysis of a Micro Reciprocating Engine for the Time Multiplexed Deep Etching Process*. School of Manufacturing and Mechanical Engineering, The University of Birmingham, UK, 2002.
13. Sugiyama, Susumu, and Toriyama, Toshiyuki, *Design of a Micro Engine for Power Generation*. Publishing data unknown.
14. Tlusty, J. and Macniel, P., *Dynamics of Cutting Force in End Milling*, Annals of the CIRP, Vol 24, No 1, 1975, pg 21-25.
15. "Micro Reciprocating Engine." The University of Birmingham. Birmingham, UK. http://www.micro-nano.bham.ac.uk/micro.htm
16. Sugiyama, Susumu, and Toriyama, Toshiyuki, *Design of a Micro Engine for Power Generation*. Publishing data unknown.
17. Fox, Daniel, *Micromachining – Function in a Small Package*. 14th Annual/USU Conference on Small Satellites, 2000.
18. Tlusty, J. and Macniel, P., *Dynamics of Cutting Force in End Milling*, Annals of the CIRP, Vol. 24, No 1, 1975, pp 21-25.

9 FIXTURING AND ALIGNMENT OF FREE-FORM OPTICS FOR DIAMOND TURNING

Alex Sohn
Ken Garrard
Precision Engineering Center Staff
Thomas A. Dow
Professor
Department of Mechanical and Aerospace Engineering

The fabrication of free-form optics presents unique challenges not only to the diamond turning process, but also to the process by which the whorkpiece is located with respect to the machine axes. While rotationally symmetric parts require alignment in at most three directions, free-form optics require alignment in up to six directions. Distinct from alignment in an optical system, fixture alignment for diamond turning requires a separate set of techniques to accommodate the forces encountered in machining. Some general principles, alignment techniques, and an application are discussed. While the techniques discussed focus on diamond turning, many of the considerations apply to other fabrication techniques as well.

9.1 BACKGROUND

Why is alignment important in fabrication? One important thing to remember about part alignment in diamond turning is that it has no effect on the figure error of the part. Figure alignment is mainly impacted by the geometric errors of the machine and tool alignment errors. Hence, it can be argued part placement has no impact on the final optical surface.

While in many cases part location is not critical to the precision of a diamond turned part, for many parts the location of the optical surface with respect to other part surfaces is critical. This is increasingly the case as optical assemblies become more complex and more difficult to align. Many systems now employ off-axis elements, aspheric surfaces and, increasingly, free-form surfaces. Their presence eliminates many of the characteristic optical signatures that were once used to dial in the correct location of spherical and flat surfaces. This is why fiducial surfaces and marks are now a requirement for many systems, reducing the effort needed to align them. In fact, optical alignment would be impossible without built-in alignment aides for some systems. When this is the case, the optical quality of a surface is irrelevant if it cannot be located properly within the optical system.

9.2 ADJUSTMENT MECHANISM

Alignment in an optical system is usually performed with a special fixture that allows adjustment via micrometer screws. Unfortunately, these fixtures are inherently compliant and therefore not

Figure 1. Optical alignment fixtures are not suitable for fixturing parts for fabrication.

Figure 2. The four degrees of freedom in positioning an optical part

suitable for ultraprecision machining operations. Kinematic or quasi-kinematic mounting are also commonly employed for optical mounts. Again, these mounts tend toward low stiffness due to the limited amount of contact with the workpiece, risking vibration and static deflection during machining.

The mainstay of optical workpiece fixturing in diamond turning is the vacuum chuck. Vacuum chucking allows rigid mounting of the workpiece without the need for fasteners that could distort the part. It also allows translation of the workpiece on a flat vacuum chuck and tip and tilt adjustment on a spherical vacuum chuck. The adjustment mechanism is usually a tapping device such as a small hammer. While this may seem crude in comparison to a micrometer screw, sub-μm adjustments can be made.

9.3 GEOMETRIC CONSIDERATIONS

While the techniques in optical alignment and diamond turning alignment are closely related in purpose, they differ somewhat in their geometric constraints (see Table 1). Oftentimes, rotationally symmetric parts require little or no fabrication alignment because their high level of symmetry makes the optical alignment less challenging. With free-form optics, however, optical alignment in six degrees of freedom quickly becomes a daunting, if not impossible, task without some built-in fiducials with a known relationship to the optical surface. This point becomes ever more true as the number of components in a given optical system increases.

Table 1. Critical degrees of freedom in aligning various surfaces for optical alignment and diamond turning

Surface	D.O.F. (optical)	D.O.F. (DT)
Flat	2 (Tip, Tilt)	1 (Z)
Sphere	3 (X, Y, Focus)	2 (Z, Runout)
Asphere	5 (Tip, Tilt, X, Y, Focus)	2 (Z, Runout)
Free-form	6 (Tip, Tilt, Rot., X, Y, Focus)	6 (Tip, Tilt, Rot., X, Y, Z)

The rotational nature of a diamond turning machine (DTM) can work to tremendous advantage when fabricating rotationally symmetric parts. In the case of diamond turning, alignment for fixturing rotationally symmetric parts as shown in Table 1 is generally limited to two directions: runout and depth. The rotational axis on which the part is mounted allows the consolidation of at least two and up to four degrees of alignment freedom. For depth, the fixture (commonly a vacuum chuck) is usually located with the diamond tool, providing a reference to the mounting surface of the part relative to the final optical surface.

Due to the lower level of symmetry inherent in free-form optical surfaces, accurate placement is more difficult than for conventional surfaces. For example, consider the case of placing a plane in an optical system versus aligning it on a DTM. The diamond turning machine normally has either a vacuum chuck or collet for mounting the workpiece. In the case of the vacuum chuck, the mounting surface has been produced by the machine axes during the facing operation. This provides a base reference for the mounting surface of the flat. The only optically significant degree of freedom is now the focus or axial translation of the flat. Translation in the radial direction, as well as rotation about the focal axis, have no optical impact, while pitch and yaw have been constrained by the vacuum chuck.

Moving to spheres and aspheres in Table 1, radial runout becomes critical as well. In the case of two-surface parts, relative alignment between surfaces is optically significant. While this adds a level of operation to fixturing, the most effective method for aligning dual surface optics, such as a biconvex lens, is to machine a contoured vacuum chuck. This will parlay the alignment problem into another runout alignment, in this case adding the axial direction.

Finally, free-form surfaces eliminate all the alignment advantages that the rotational symmetry of the DTM grants. The method of alignment for each direction will depend upon the accuracy requirements, the metrology methods available, and the physical constraints of the parts. Ideally, it is at this point that the fabricator is included in the design process, so that mechanical constraints encountered in fabrication can be considered in the optical system design. Usually, a combination of fiducial surfaces and marks will allow accurate location in six degrees of freedom.

9.4 BICONIC MIRROR FIXTURING AND ALIGNMENT

9.4.1 STATIC ALIGNMENT

IRMOS, the InfraRed MultiObject Spectrometer, incorporates several off-axis elements and one free-form surface [1,2]. This surface, called M4, is a biconic ellipsoid with no rotational axis of symmetry. M4 thus needed to be located accurately in six degrees of freedom to within ±25 μm for translation and 15 arcsec for rotation. To achieve this goal, two fiducial surfaces and eight crosshairs were machined into

Figure 3. Diamond flycut back surface of M4 showing the four alignment crosshairs and three part mounts

the part blank as shown in Figure 3. The two surfaces, one nominally parallel with the biconic surface, the other orthogonal, were diamond flycut into the Aluminum blank. The back surface would be mated to the vacuum chuck to account for three degrees of freedom: tip, tilt, and focus. The three quasi-kinematic mounts visible in Figure 3 could not be used since the thread locking system was only intended for a single use. These mounts were also too compliant to allow mounting the part off-axis. Accelerations at the machining speed of 120 rpm would have caused significant deflection. Translation in X and Y as well as rotation could be aligned using two of the fiducial crosshairs. These crosshairs were machined using a miniature ball endmill in a conventional CNC milling machine. The same fiducials used in aligning the parts for fabrication would later be used to align the parts in the optical system.

Figure 4. Alignment Fixture Showing Center Plug and two vacuum pedestals, with mirror blank mounted on left

While fabricating the fiducials presented somewhat of a challenge, the greater question was how they would be used to align parts on the machine. For mounting the parts in their proper off-axis location on the diamond turning machine, a special fixture somewhat reminiscent of a propeller was fabricated to mount two parts at one time (Figure 4). The fixture, which bolts directly to the DTM spindle, has an integrated vacuum chuck at its center for holding an alignment center plug. The off-axis location and tilt were necessary to minimize the excursion of the fast tool servo used to machine the non-rotationally symmetric component of the surface. Each mirror rested on an angled pedestal which had been diamond flycut on two surfaces to within 4 arcsec of the correct tilt angle. This pedestal was then mounted on a beam that had been faced off on the DTM, guaranteeing correct angular placement of the rear surface of the parts and forming the complete propeller-like structure. The beam had been designed with a large section to prevent significant bending during machining.

The crosshairs, now located against the vacuum chuck surface of the pedestals, were viewed through several holes bored through the rear of the chuck. As shown in Figure 5, a camera with a crosshair generator was placed on the DTM's X-axis to look at the crosshairs.

While relative alignment of the crosshairs to the camera could now be achieved, the camera view had to be related to the machine coordinates. Vertical alignment was made by looking at the top surface of the diamond tool, which, in turn, had been aligned to the spindle axis via a centering operation. The rotational position of the spindle, which the fast tool servo uses to contour the part in that direction, could now be related to the crosshairs on the back of the part. In this case,

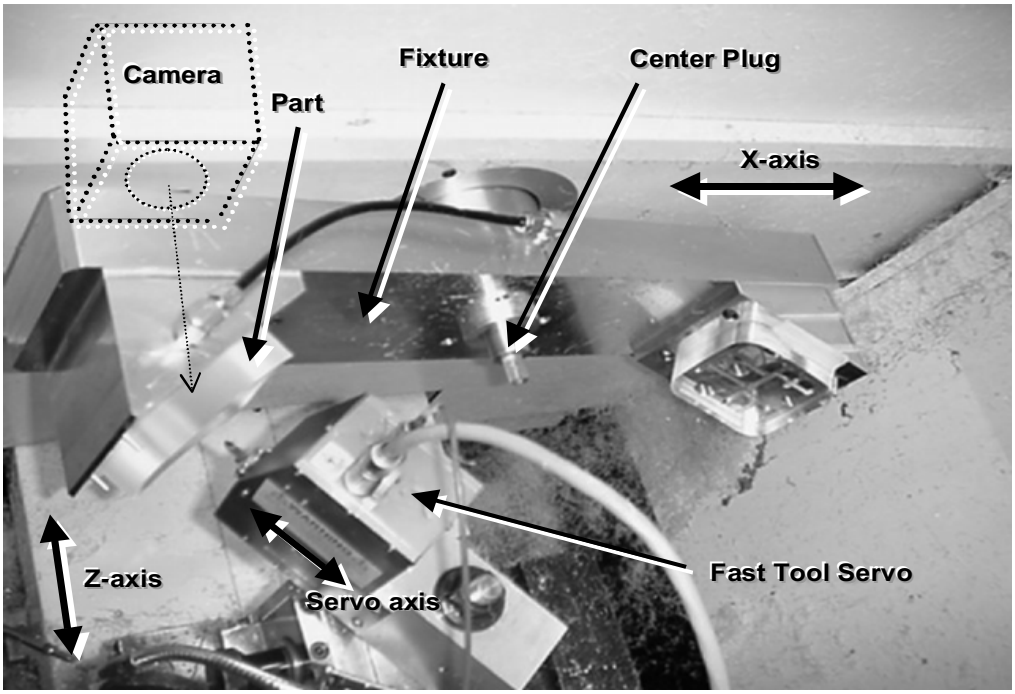

Figure 5. Machining setup showing acrylic test parts, camera arrangement, and centerplug.

an important limitation in positioning resolution was the spindle encoder resolution. With 10,000 counts per revolution, the positional resolution at the radial position of 270 mm was 160 µm. Fortunately, sub-count interpolation allowed a positional accuracy closer to the 25 µm goal, though this arrangement was hardly ideal. Interpolation was dependent on the operator's skill in manually rotating the fixture and noting the crosshair location when the encoder count occurred.

No such limitation existed for alignment in the radial direction. The radial position of the axis of rotation was determined during the tool centering operation as a function of the DTM's x-axis position. Unfortunately, the large nose radius of the tool does not provide a distinct feature on which to align the camera in the radial position, therefore a needle was mounted on the toolpost. The needle was then touched on the rotating center plug to produce a small circular scribe that could be measured in a microscope. The needle was then moved using the machine axes to the intended radial position of the crosshairs minus the radius of the circular scribe. With the camera crosshairs then aligned radially on the needle, the intended location of the part crosshairs was established.

9.4.2 DYNAMIC ALIGNMENT

The result of the machining operation revealed an important point to be considered in part alignment. While static alignment was successful and accurate within specifications, a dynamic

component arose in the rotational direction of the spindle that was missed. Early analysis deemed the spindle speed to be well within the dynamic limits of the fast tool servo. The excursions occurred at a rate of approximately 12 Hz, while the servo bandwidth is around 300 Hz. Unfortunately, even with a small phase shift of less than 1°, at a radial distance of 270 mm, a displacement error of more than 3 mm was encountered. This error was discovered during figure error measurements made after machining using a computer generated holographic mask in an interferometer. The fiducials used to align the part during machining were also used to align the part to the interferometer. When measurements were taken in the position determined by the fiducials, what appeared to be a large figure error was detected. When the part was subsequently translated by 3 mm, most of this figure error disappeared.

9.5 CONCLUSION

Alignment and fixturing for fabrication presents unique challenges distinct from optical alignment, particularly in the case of free-form optics. The example presented has brought to light a component that is usually not considered: The dynamics of the machining system. Also, while part alignment has no direct influence on figure error, misalignment can produce symptoms that behave like figure error. Consideration of all alignment issues, including dynamic components, is critical to the implementation of free-form optics.

REFERENCES

1. Garrard, K., A. Sohn, R. G. Ohl, R. Mink, V. J. Chambers. “Off-Axis Biconic Mirror Fabrication.” Proceedings from the EUSPEN 2002 Annual Meeting (2002).
2. Ohl, R.G., Werner Preuss, Alex Sohn, Shelly Conkey, Kenneth P. Garrard, John G. Hagopian, Joseph M. Howard, Jason E. Hylan, Sandra M. Irish, J. Eric Mentzell, Mechthild Schroeder, Leroy M. Sparr, Robert S. Winsor, S. Wahid Zewari, Mathew A. Greenhouse, and John W. MacKenty, “Design and fabrication of diamond machined, aspheric mirrors for ground-based, near-IR astronomy,” Proc. SPIE Vol. 4841, p. 677-688, Instrument Design and Performance for Optical/Infrared Ground-based Telescopes (2003)

10 ELLIPTICAL VIBRATION ASSISTED DIAMOND TURNING

Nobuhiko Negishi
Graduate Student
Thomas A. Dow
Professor, Mechanical and Aerospace Engineering

Over the past 3 years, a project to develop an Elliptical Vibration Assisted Machining (EVAM) system has been funded by Kodak. The goal was to create a device that could be used to study the influence of process variables on the material removal process; specifically the shape of the elliptical tool motion, the magnitude of the forces, tool wear and surface finish. Two different prototypes (called the UltraMill) were created: a slow-speed unit that was built with a standard diamond tool and a high-speed version using new actuators with a light-weight, hollow ceramic tool holder. The changes in the high-speed version resulted in an increase in operating speed from 500 Hz to over 4000 Hz. Enhancements included in this new version of the EVAM system are a closed loop temperature control system and a glued-in diamond tool. The performance of the UltraMill was impressive and a number of different materials were machined from plastic to aluminum to silicon carbide. The surface finish was nearly as good as diamond turning if the speed of the workpiece was low with respect to the oscillation speed of the elliptical motion and the peak cutting forces were reduced by 50%. The UltraMill can produce optical quality surfaces and tool wear is less than conventional diamond turning for difficult to machine materials such as steel and ceramics.

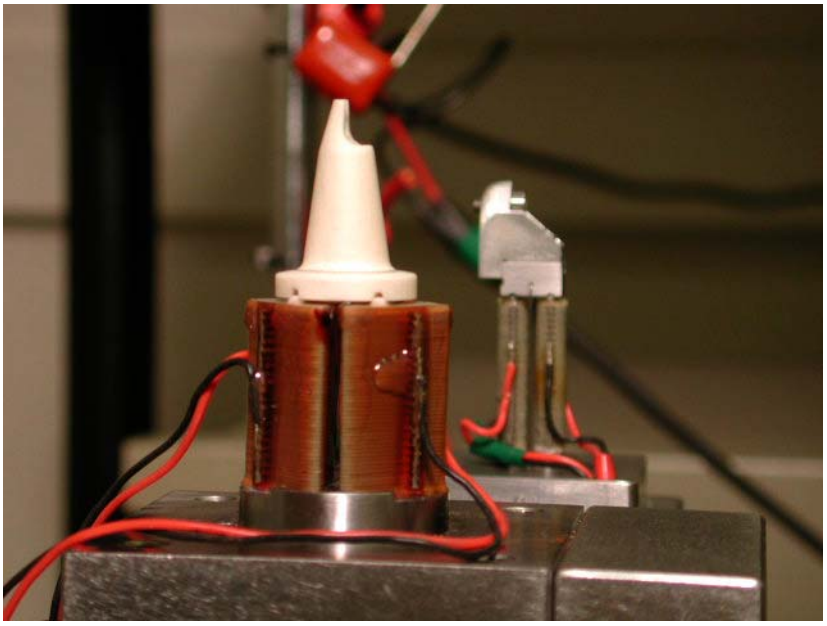

10.1 INTRODUCTION

Diamond turning has become a mainstay of optical fabrication. However, it is limited to certain workpiece materials [1] due to tool wear. To address this issue, a new class of machining was created. This technique involved independent, cyclic displacement of the cutting tool with respect to the workpiece and was referred to as vibration cutting. In early experiments, the tool was moved in a straight line along the cutting path at ultrasonic frequencies. It took nearly two decades of research before the technology began to show practical value. In the early 90's, research into vibration cutting at both low and high frequency produced results sufficient for industrial applications [2]. This mature class of machining is called Vibration Assisted Machining (VAM). Moriwaki has shown that when the tool was moved in an elliptical path rather than a straight line, lower cutting forces and longer tool life were achieved [3,4]. However the evidence presented was anecdotal. There were no specific measurements of force during ultrasonic operation or tool wear details.

The PEC has built an EVAM system known as the UltraMill [6] that combines a small elliptical tool path (40 µm horizontal by 6 µm vertical at 600 V excitation) to the linear motion of standard orthogonal cutting. Tool force and wear details using a low speed system were reported in 2001 [5]. The EVAM reduces cutting forces and tool wear by reducing chip thickness and keeping the tool tip out of contact with the workpiece for 75% of the time. These characteristics increase tool life and expand work piece material compatibility with single crystal diamond tools. This Section describes the Ultramill with details of the tool path, chip shape, forces and surface finish.

10.2 ULTRAMILL CONSTRUCTION AND TOOL MOTION

10.2.1 MECHANICAL STRUCTURE

A photograph of the two Ultramill designs developed at the PEC are shown in Figure 1: the new high speed version is in the foreground at left and the original low-speed version [5] is shown in the background at right. The basis for each design is a pair of piezoelectric actuators that support the tool and allow it to move with small displacements at high speed. The original version uses a pair of long, thin cylindrical actuators whereas the new design uses a pair of larger cross-section triangular actuators (base

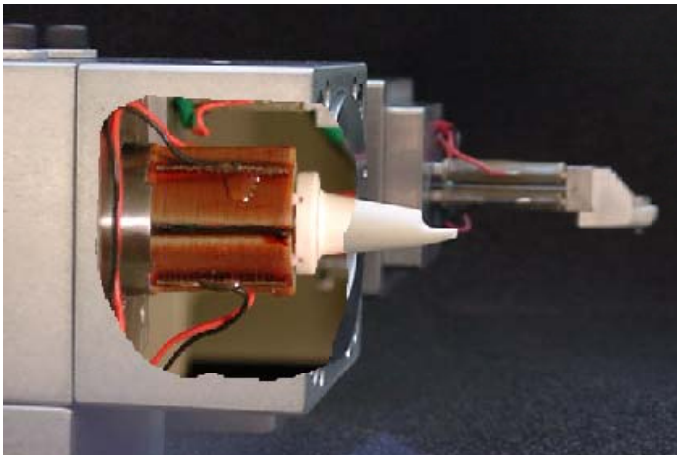

Figure 1. Photograph of the new high-speed design (left) and the original design (right)

30mm, height 13 mm, depth 22 mm). This shape was optimized for stiffness using a finite element model. The original tool head was fabricated from steel and aluminum with a standard diamond tool attached with a screw. The new design uses a hollow alumina head and a diamond tool attached with high-temperature epoxy. The shape of the head was optimized to keep the center-of-gravity near the center line of the stacks and to minimize the mass moment of inertia. The first natural frequency of the new design is 5000 Hz as compared to 500 Hz for the original design. Unfortunately the constraints on the shape and material of the head made it difficult to fabricate and therefore expensive.

The head rests on a pair of ceramic half-cylinders that allow it to displace and pivot as required for the desired motion. A thin titanium flexure pushes the head onto the actuators and seals the actuator cavity for cooling. High-voltage signals (up to 1000 V_{p-p} at 10 KHz) in the shape of a sine wave and cosine wave drive the two actuators. This excitation produces an elliptical motion of the diamond tool with the minor axis (up to 7 µm) and the major axis (up to 33 µm) determined by the stroke and phase of the actuators and the geometry of the head.

10.2.2 COOLING SYSTEM

The large piezoelectric actuators used to drive the tool at high frequencies generate a significant amount of heat and an active cooling system is required for sustained operation. The system, shown in Figure 2, consists of a thermoelectric cooler and pump to circulate a dielectric fluid (3M Flourinert 3283) over the stacks at a flow rate of about 1 liter/min. The system uses the chiller to modulate the temperature of the inlet to the actuator cavity such that the outlet temperature (as measured by the resistance thermometer – RTD - in the return line) is kept constant. The chiller has a capacity to remove 400 watts, sufficient to operate the system constantly at full voltage.

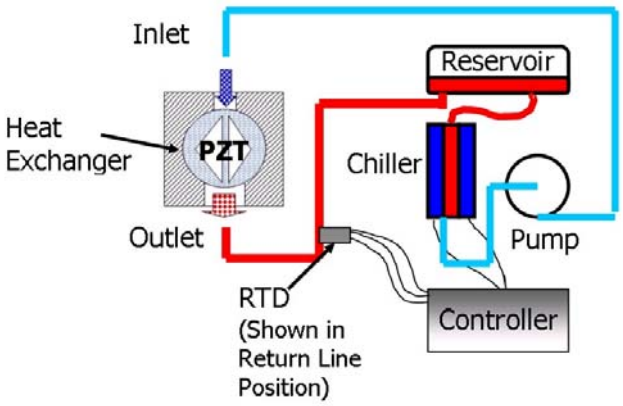

Figure 2. Active cooling system design for sustained high-speed operation of the actuator

10.2.3 TOOL MOTION

The desired tool motion for the Ultramill is generated in a different manner than other vibration assisted designs. In this case, the goal is to operate the system below its first natural frequency so that the motion can be changed in a controllable manner to study the details of the machining process. For elliptical cutting, the motion of the end of the tool is a combination of the elliptical motion from the actuator and the linear motion from the workpiece. Figure 3 shows the motion

of the tool (exaggerated in the vertical direction for clarity) and defines the important parameters. Only two cycles of the motion are shown but emphasis is on the second revolution (dotted line) that represents the steady-state motion during material removal.

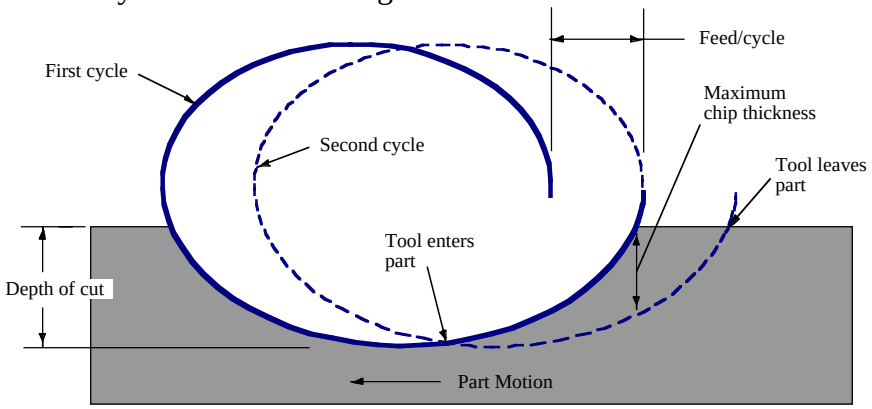

Figure 3. Tool motion and chip definitions at the center-line of the chip during elliptical cutting

10.2.4 CHIP GEOMETRY

Figure 3 also shows the chip geometry at the center of the cut as the tool moves through its elliptical path. The thickness of the chip is reduced as the tool frequency is increased or the part speed or depth of cut are reduced. SEM micrographs of non-overlapping groove cutting experiments in aluminum illustrate that chip geometry is directly related to cutting conditions. If the depth of cut is smaller than the minor axis of the tool motion, the chips are discontinuous (Figure 4), and if larger they are connected at the center (Figure 5). The discontinuous chips have a thickness related to the feed/cycle and are as wide as the cut. The continuous chips are longer because of the increased depth of cut but are discontinuous at each edge where the round nose tool leaves the flat workpiece. Notice that the chips appear transparent in the 1000x image of Figure 5, indicating a thickness less than 10 μm.

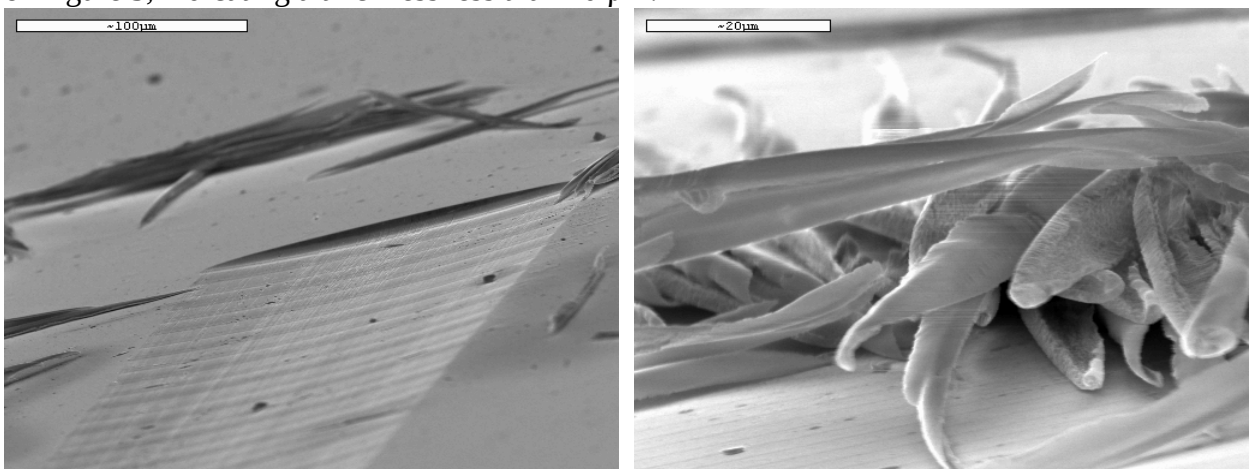

450x 1800x

Figure 4. SEM micrographs of discontinuous chip where depth of cut is 32% of the minor axis (depth = 1.4 μm and upfeed/cycle = 3.3, minor axis of elliptical motion =4.3 μm)

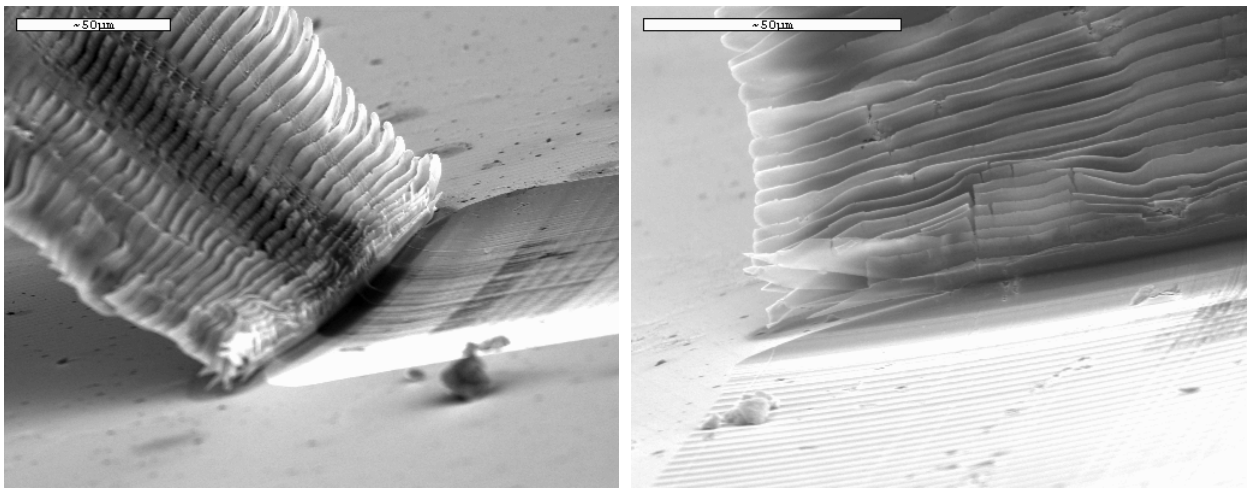

600x 1000x

Figure 5. SEM micrographs of continuous chip where the depth of cut is twice the minor axis (depth of cut = 8.9 µm and upfeed/cycle = 6.7 µm, minor axis of elliptical motion =4.3 µm)

10.2.5 TOOL FORCES

To measure the forces, a specimen was attached to a three-axis load cell mounted on the diamond turning machine. The oscillating tool was fed across the surface at a constant speed and depth of cut. The measured forces were acquired using a high-speed data acquisition system.

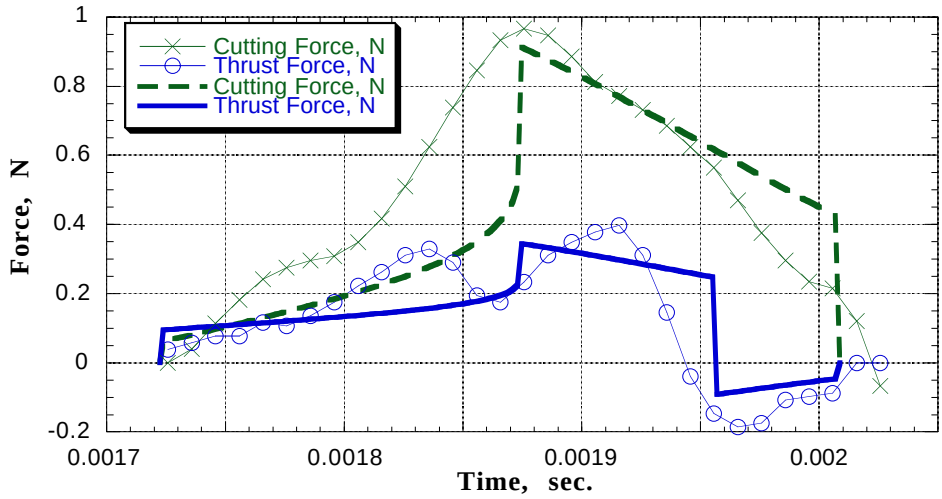

Figure 6. Theoretical and measured cutting and thrust forces during tool contact (material = 6061-T6 aluminum under same conditions as Figure 5)

The measured forces in the cutting and thrust directions as a function time are shown in Figure 6. The measurements are shown as a series of points connected by a line and the predicted forces are the solid and dotted lines. The workpiece was 6061 aluminum, the vibration frequency 1000 Hz, the depth of cut 8.9 µm and the upfeed/cycle 6.6 µm. Based on the geometry shown in

Figure 3, the maximum chip thickness for this condition is 7.7 µm. For these cutting conditions, the maximum force in Figure 6 is about 1 N and the tool is in contact for 0.3 ms out of a cycle time of 1 ms (at 1000 Hz operation) or a duty cycle of 30%. The predicted values were in agreement within 0.1 N of the magnitude of the measurements. However, secondary vibrations due to the load cell dynamics are apparent, especially in the thrust direction with a 12 kHz frequency (the natural frequency of the load cell with specimen).

10.2.6 SURFACE ROUGHNESS MEASUREMENTS

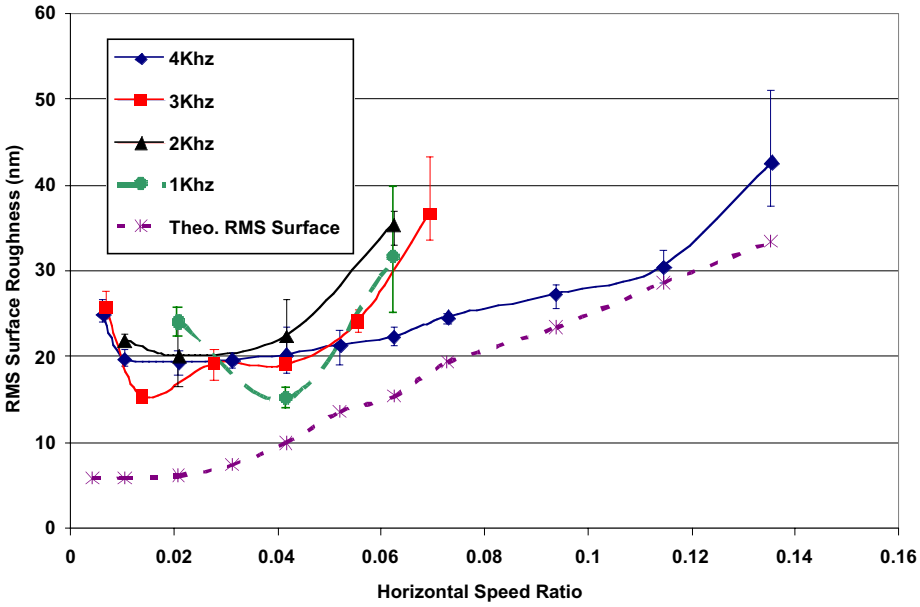

Figure 7. Surface Roughness as a Function of HSR on PMMA
(100 rpm Spindle Speed, 1.25 mm/min Cross Feed, 12.5 µm/rev)

The surface roughness of the EVAM machining experiments was compared to a theoretical prediction for grinding surface finish developed at the PEC by Storz [7]. This comparison is illustrated in Figure 7. Here the areal RMS roughness as measured on a Zygo New View is plotted as a function of the Horizontal Speed Ratio (HSR) for different EVAM frequencies. The HSR is the ratio of the maximum speed of the elliptical motion to the surface speed of the part and is proportional to the distance that the part moves for each elliptical cycle of the tool. The model tracks the experiments well above 7% HSR but below that value the experiments seem to reach a plateau of 20 nm while the predicted value drops to 5 nm. The speed of the EVAM motion (1-4 KHz) does not seem to affect the minimum roughness.

The 20 nm limit was the result of 60 Hz asynchronous surface features produced on the part. Since the **x** and **y** carriages of the Diamond Turning Machine (DTM) have a natural frequency of 60 Hz and 90 Hz respectively, these features were originally thought to be caused by machine

vibration introduced by the inertial forces of the UltraMill or by ancillary components such as the cooling system pump. Following a series of experiments designed to isolate the source of this vibration, the Kinetic Ceramics amplifiers were found to be defective; introducing noise spikes of 25 nm magnitude at a period of 16 msec (60 Hz) into the drive signal. Trek P1019 (PZD500) dual channel piezo drivers were loaned by Precitech for further experiments. These amplifiers were capable of producing a clean drive signal of 600 volts peak-to-peak but were limited to 1 KHz. The measured RMS surface roughness for an EVAM turned part is plotted in Figure 8 as a function of HSR.

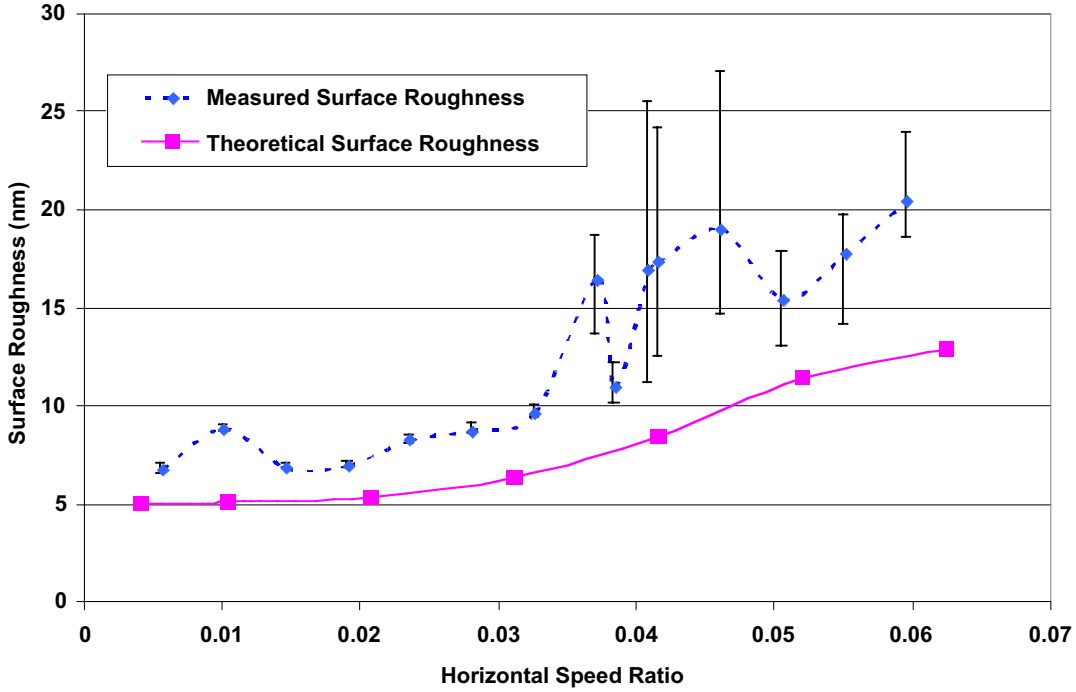

Figure 8. Measured and Theoretical Surface Roughness on PMMA
(1 Khz, 21.4 rpm, 0.25 mm/min, 12 µm/rev)

The minimum theoretical surface roughness values were calculated using the Storz's method [2] and the theoretical values are the smallest possible from the model. The general trend of the measured roughness curve follows the theoretical behavior. The 20 nm limit is no longer observed in these results where the minimum measured surface roughness is 6.5 nm RMS. The surface finish experiments showed that EVAM features could be predicted from the elliptical tool path and tangential workpiece velocity.

10.3 SIC MACHINING

The groove cutting experiment described in the 2002 Annual Report proved that the EVAM process could be used to machine SiC; however, creating an optical surface is a more challenging problem. To demonstrate the possibilities, the UltraMill was used to machine a surface with a 1

mm outer radius and a 0.5 mm inner radius. The fracture data from the groove cut experiment showed that damage free surfaces could be machined if the chip thickness is less than 20 nm. This value was used to determine the cutting conditions at the outer radius of the machined surface where the upfeed – and therefore the chip thickness – is the largest. The UltraMill was operated at 1 KHz and 600 volts peak-to-peak using the Trek amplifiers to create the 40 x 6 µm ellipse. The tool was fed across the part at 12 µm per revolution. The part rotated at 1 RPM and the maximum HSR, occurring at a radius of 1 mm, was 0.08%.

10.3.1 APPARATUS

The SiC specimen was vacuum mounted to the DTM spindle using a custom, diamond turned fixture. The workpiece velocity required for the desired maximum chip thickness at a 1 mm radius was determined to be 0.1 mm/s, or approximately 1 RPM. The motor for the DTM cannot operate at such a slow speed so the spindle was driven by a stepper motor through a flexible rubber belt. The SiC specimen was 25.4 mm square by 0.8 mm thick with a polished surface of less than 0.5 nm RMS over an area of 0.0156 mm^2. The surface of the unmounted specimen had a spherical shape with a P-V of 10 µm. Once supported on the vacuum chuck, the surface flatness was less than 600 nm over the area to be machined. Based on this runout, the desired nominal depth of cut was set at 600 nm.

The UltraMill was operated at 1 Khz for 40 minutes to allow the temperature to equilibrate. After the equilibration period, the tool was brought into contact with the rotating specimen at a radius of 0.4 mm. The tool tip was positioned to within several micrometers of the surface as observed with a telescope and moved in 100 nm increments until a chip was created. The oil jet was activated and the part program was run. The machining process required 44 minutes, during which the temperature of the UltraMill piezo stacks dropped by 0.4˚C. The goal for the touch off technique was to avoid depths of cut greater than 1.2 µm. The measured depth of cut for the surface ranged from 30 nm to 418 nm with an average depth of 300 nm.

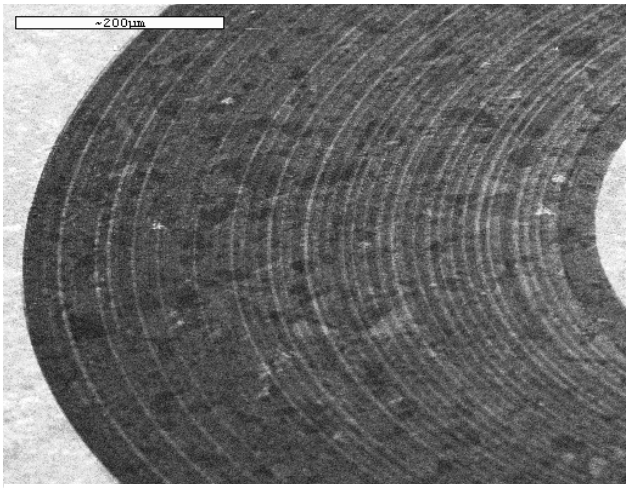

Figure 9. SEM Micrograph of SiC Surface

10.3.2 SURFACE MEASUREMENTS

Figure 9 is an SEM micrograph of the machined surface of the SiC. The nominal cutting distance was 196.25 mm and the volume removed was $7x10^{-4}$ mm^3 with a removal rate of 15,900 μm^3/min. The average of the tangential and radial profiles and surface measurements are plotted as a function of radial position in Figure 10. The machined SiC

surface has an average roughness of approximately 8 nm RMS. The theoretical RMS roughness of the machined surface is dominated by the cross feed and has a value of 5.5 nm. The theoretical roughness along the groove bottom is 1 angstrom. This value is much less than the spindle error motion and therefore is not visible. The value shown in Figure 4 is equal to the average spindle error.

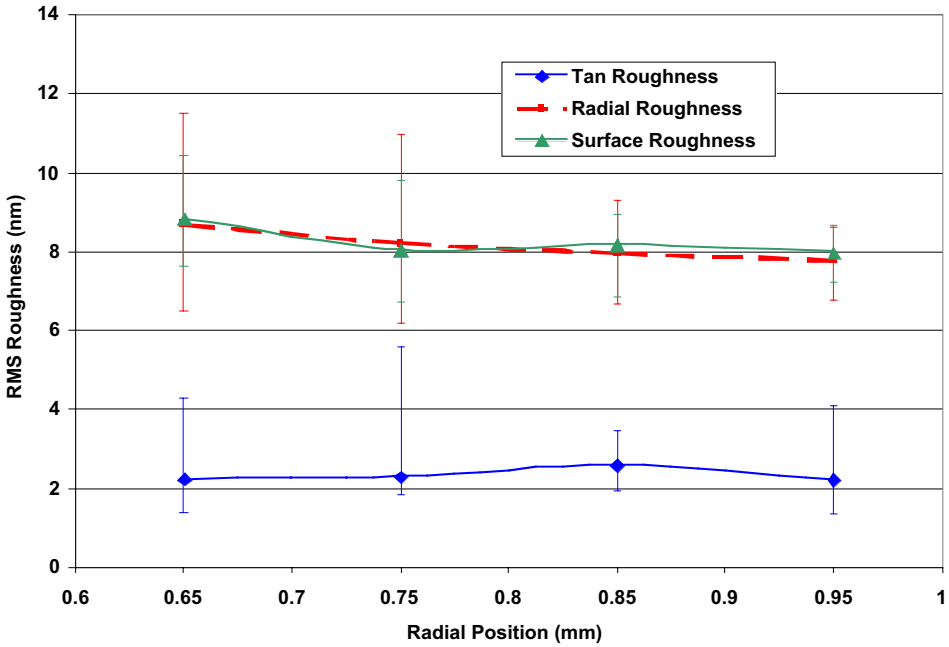

Figure 10. Surface Measurements of Machined SiC CVD
(1 rpm spindle speed, cross feed = 12 µm, upfeed = 40 nm, frequency = 1 Khz)

Figure 11 is a Zygo contour image of the machined surface at a radius of 0.85 mm. The cross feed marks can be clearly seen at 12 µm spacing. Normally these would be connected by vertical lines due to the upfeed motion created by the elliptical motion of the tool. However, for this experiment, the upfeed rate of 40 nm/cycle is beyond the resolution of the instrument. What are visible are lower frequency vibrations attributed to spindle and DTM slide motion. A trace along one of the grooves has amplitude of 2.5-5 nm at a frequency of 25 Hz. Surface roughness along the machined groove is 1.9 nm RMS. Some surface damage was noted and can be seen along the bottom of one of the up feed grooves.

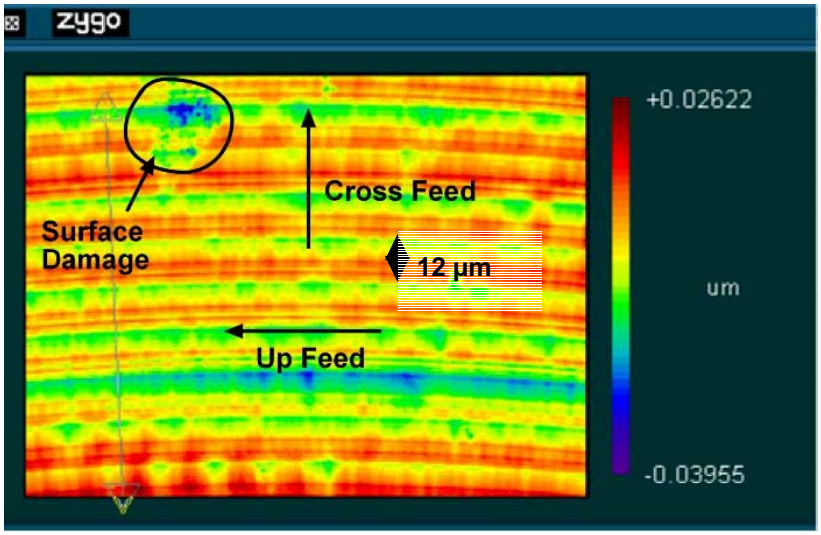

Figure 11. Contour Plot of EVAM Surface in SiC (HSR=0.08%)

A profile trace in the cross feed direction (Figure 12) provides another view of the surface. This scan reveals a cross feed period of approximately 11.9 µm and a local feature height of 16 µm. These values are similar to the theoretical 12 µm cross feed and 18 µm peak-to-valley feature height. The cross feed features have distinct, repeated characteristics which are believed to be the result of features on the tool edge being imprinted on the SiC surface during machining. These features appear to be small fractures or damage sites, less than 5 nm deep.

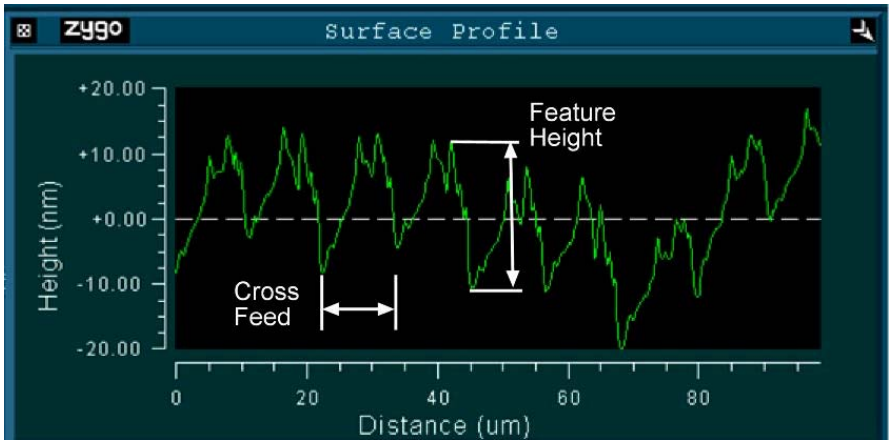

Figure 12. Radial Profile of SiC Surface (Cross Feed = 12 µm/ rev)

10.3.3 Tool Wear Machining SiC

SEM micrographs of the tool tip before and after the machining process reveal visible wear. The cutting edge was imaged with the SEM before machining the SiC and is shown on the left side of Figure 13. There appears to be no visible damage to the edge. After machining the SiC, the tool edge was again inspected with the SEM. No indication of tool wear could be found on the rake face; however, the flank face revealed features shown at the right of Figure 13. The width of the

worn area is the same as the theoretical contact length of 25 µm for a 1 mm radius tool at a depth of 300 nm. This correlation suggests that this wear area was created during the machining process.

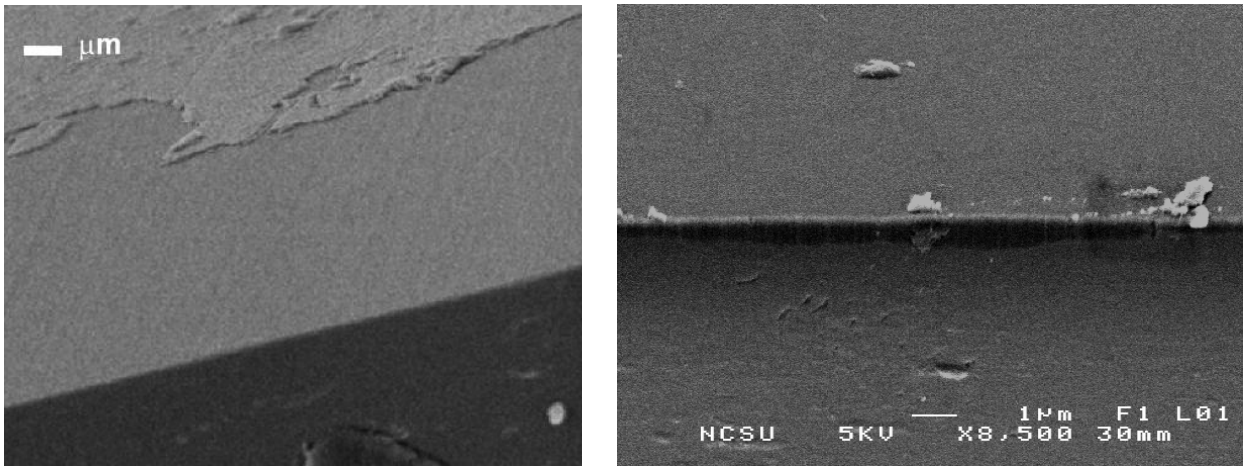

Figure 13. Worn and Unworn Tool Edge

A close up view of the flank wear region in Figure 14 shows wear patterns and striations in the upfeed direction as expected. The length of the wear land is approximately 400 nm. Given this wear land and a clearance angle of 10.4˚, a rake face recession of 74 nm is estimated. This calculation assumes a flat wear land, which may not be the case for the EVAM process. The radial and surface measurements are similar in magnitude, 8 nm RMS, suggesting that the overall surface roughness is mostly a result of cross feed features. This was expected based on the selected machining conditions.

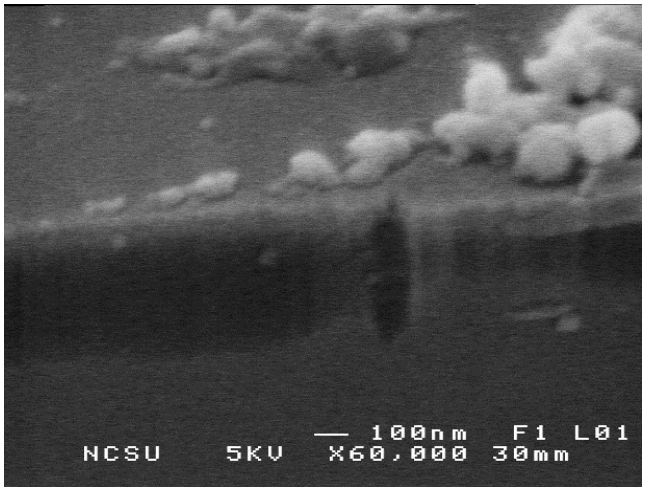

Figure 14. Worn Edge on Diamond Tool

10.4 CONCLUSIONS

The UltraMill is a rugged, reliable design for creating surfaces using elliptical vibration assisted machining. It has two major advantages over previous designs; first, the elliptical motion has a significant vertical component that can be used to control the thickness of the chip; and second, motion of the tool is below the first natural frequency so the speed is easily adjustable from 1-5 KHz. This device has been used to machine a variety of materials, from aluminum to plastics to

SiC. It can produce optical quality surfaces and the accompanying tool wear for difficult to machine materials – steel and ceramics – is less than conventional diamond turning.

REFERENCES

1. Evans, C., Paul, E., Mangameli, A., McGlaufin, M., "Chemical Aspects of Tool Wear in Single Point Diamond Turning", Precision Engineering, Vol 18, 1996, pg 4-19.
2. Moriwaki, T., "Machinability of CBN Tools in Precision Engineering of Stainless Steel", Proc. 5th International Conf. on Mfg. Engineering, Wollongong, pg. 129-133, 1990.
3. Moriwaki, T. and Shamoto, E., "Ultra-precision Diamond Turnign of Stainless Steel by applying Ultrasonic Vibration", Annals of the CIRP, Vol. 40, Pg. 559-562, 1991.
4. Moriwaki, T and Shamoto, E., "Ultra-precision Diamond Cutting of hardened Steel by applying Elliptical Vibration Cutting", Annals of the CIRP, Vol. 48, Pg. 441-444, 1999.
5. Dow, Cerniway, Sohn and Negishi, "Vibration assisted diamond turning using elliptical tool motion", Proceedings 2001 ASPE Annual Meeting, Vol 25, 2001, pg 92-97.
6. Negishi, N., "Elliptical Vibration Assisted Machining with Single Point Diamond Tools" MS Thesis, NC State University, 2003.
7. Storz, G. E. II, "Theoretical Modeling of Precision Contour Grinding Operations" MS Thesis, NC State University, 1994.

11 ERROR COMPENSATION USING INVERSE ACTUATOR DYNAMICS

Witoon Panusittikorn
Graduate Student
Kenneth Garrard
Precision Engineering Center Staff
Thomas A. Dow
Professor
Department of Mechanical and Aerospace Engineering

All actuators exhibit varying amplitude and phase response to varying or multiple frequency input command signals. This makes it difficult to utilize their full small-signal bandwidth. Two adaptive, open-loop schemes that compensate actuator motion errors using an inverse dynamics, or deconvolution, approach have been developed. A significant issue that must be addressed by a practical implementation of any command signal modification technique is the interdependence of the parametric (i.e., time-based) commands for the multiple axes of a machining system. The short-time Fourier transform and an equivalent inverse dynamics filter have been developed for operation in a such machining environment where parameters such as spindle speed may change. Two hardware issues related to the use of these techniques to correct the motion errors of a Variform fast tool servo (FTS) are also discussed. First, the operating range where the actuator performs as a linear system is investigated. Second, the dynamic response of an actuator's internal displacement sensor may mask the actual tool motion. These hidden dynamics can be compensated using the proposed corrective algorithm. An off-axis spherical surface feature has been selected for machining tests of these algorithms. The spherical profile is easily measured interferometrically and the machining parameters can be adjusted to obtain a wide range of frequencies and amplitudes in the FTS command signal. The final phase of this project is to develop an actuator independent software package implementing the inverse dynamics algorithm for arbitrary, rotationally variant surfaces.

11.1 INTRODUCTION

The dynamic response of a mechatronic system is a function of the frequency and amplitude of its input signal. An open-loop control approach using an inverse dynamics algorithm, or deconvolution of a desired motion path can compensate for attenuation and phase yielding a significant reduction in steady-state tracking errors [1]. The performance is significantly improved, especially for high frequency motion.

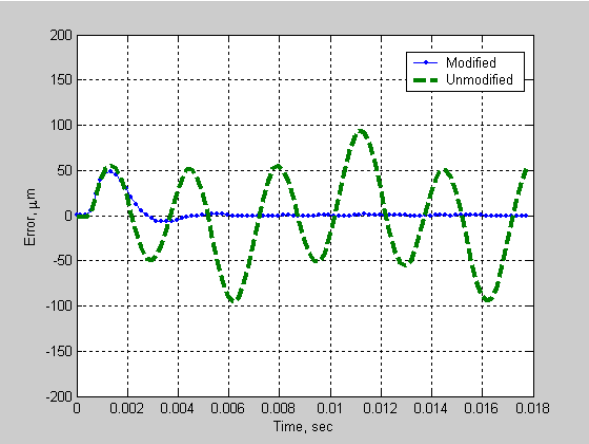

Figure 1. Path difference associated with modified and unmodified input.

Figure 1 shows a comparison of the following error for a Variform fast tool servo with and without motion path deconvolution. The dashed line represents the following error for an input signal whose frequency approaches the bandwidth of the actuator. The dotted line shows the actuator following error to a *deconvolved* version of the same input command. The response of the modified signal shows significantly less attenuation and delay from the desired signal after a startup interval lasting approximately 4 ms.

Several interesting hardware issues have been encountered during the implementation of this control approach that will be discussed in subsequent sections. First, the modified input drives the FTS to precisely follow a desired motion path at low amplitudes and high frequencies. However, the acceleration and hence the maximum attainable velocity of the Variform is limited. As a result, for large amplitude and high frequency command signals, the actuator motion will exhibit large path differences with respect to the desired excursions. To assure that the FTS performance is within its physical capability, its operating range (frequency, amplitude combination) must be determined.

Second, the dynamics of the Variform's internal displacement sensor (a Linear Variable Differential Transformer or LVDT) shadows the true tool motion undermining the signal modification algorithm. An additional sensor, a capacitance gage, was used to determine the transfer function of the LVDT. The dynamics of the LVDT can be convolved with the previously measured actuator dynamics to derive the true actuator frequency response.

Third, the desired path of the FTS is usually expressed as a parametric function of spindle speed and the axis cross-feed rate of a diamond turning machine (DTM). As either velocity changes, the time period of the desired path is also altered. Since deconvolution over the entire command signal is only valid for non-varying machining parameters, a more robust approach would be to perform the deconvolution in *real-time*. Adaptive schemes such as the short-time Fourier

transform (STFT) and an equivalent inverse dynamics filter have been developed to use the most recent parameters known during machining. The maximum rate at which this adaption can be performed is same as the impulse response decay rate; that is, the time that it takes for the actuator motion to decay to zero following an impulse input.

Both deconvolution techniques are being validated by machining a small, concave off-axis sphere into a flat surface. To determine the form error contributed by the FTS for both an unmodified and deconvolved command signal, a comparison will be made with identical spheres machined on-axis. Finally, a software package that implements the validated deconvolution algorithm will be constructed. A generic, text format will be used to describe both the desired tool path and the actuator dynamics.

11.2 DETAILS OF THE PROJECT

11.2.1 VELOCITY SATURATION AND OPERATING RANGE

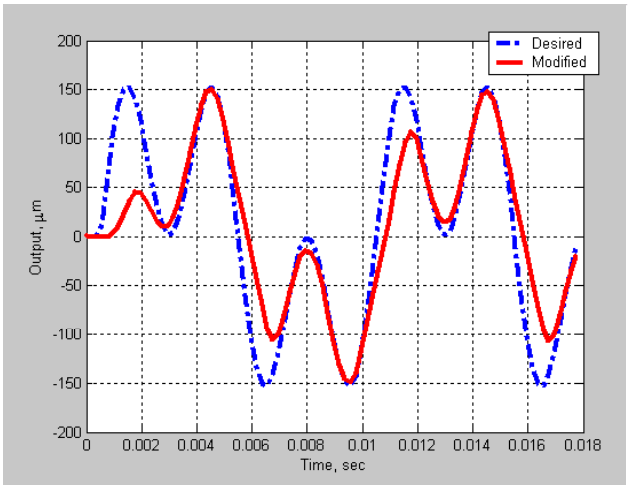

Figure 2. FTS response with respect to high frequencies and large amplitudes input signal.

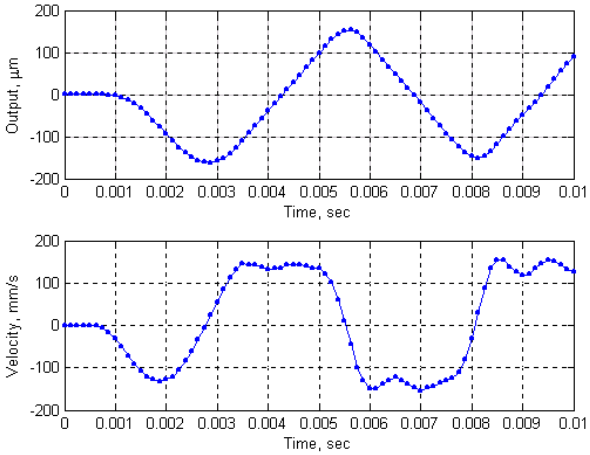

Figure 3. FTS response associated with 200 Hz, 7.5 volts P-P input signal and its velocity.

Limitations of the deconvolution technique appear with the combination of high frequencies and large amplitudes. In general, an actuator can be considered as a linear spring-mass-damper system whose dynamic response is expressed as a function of frequencies of the applied signals. Though the response results in an attenuated and delayed motion, the output of a linear system contains only the frequencies of the input signals. Since the velocity of the Variform FTS is constrained due to physical limitations, as a large amplitude and high frequency input signal is applied the output profile is reshaped. In other words, the Variform behaves non-linearly. Figure 2 shows that the Variform response (a solid line) cannot follow the desired excursion (a dashed dotted line) when the velocity exceeds the maximum. The velocity saturation reshapes the response associated with a sinusoidal input to a triangle-like signal with the maximum

velocity of 140 mm/sec as shown in Figure 3. The effects of the distortion on the operating range of the Variform as well as the measured impulse response employed in the deconvolution technique can be thoroughly investigated using a frequency spectrum analyzer.

In Figure 4(a), the deformed shape (a line with dots) of the FTS response as measured by the internal LVDT sensor is compared with the shape of the desired excursion (a line with diamond marks). The lower plot illustrates the frequency spectrum of the output profile. The distorted response comprises not only the base frequency component of 200 Hz, but also the 3rd (600 Hz) and 5th (1000 Hz) harmonics. Figure 4(b) shows the frequency components with respect to the Variform response. While the constituent sinusoid associated with the base frequency is in-phase with the desired signal, the 3rd harmonic is out-of-phase, leading to a triangle-like output response. Note that the amplitude of the constituent sinusoid is smaller than the amplitude of the distorted output excursion.

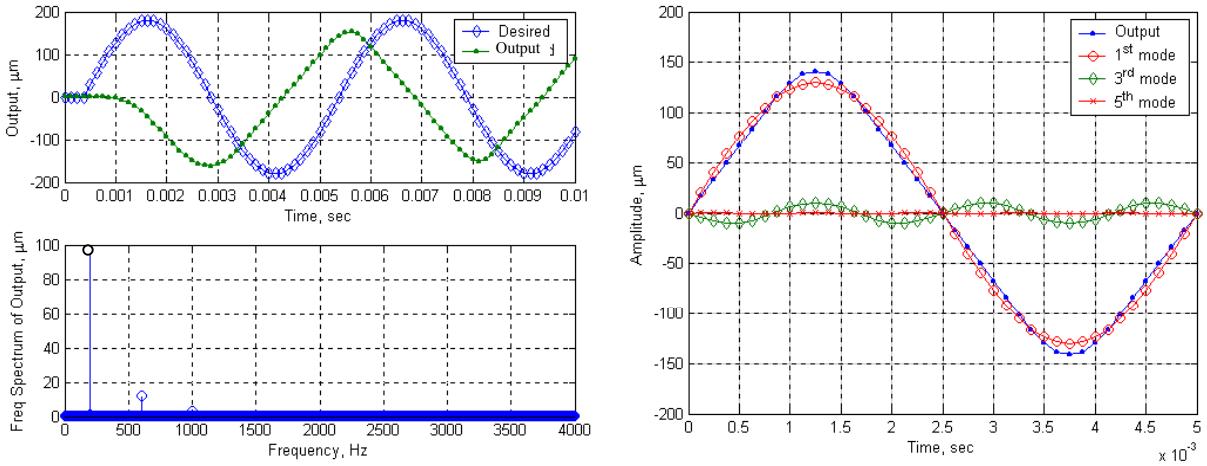

a) b)

Figure 4. a) Shape of the FTS response and its frequency spectrum, b) Assembly of the frequency components with respect to the FTS output.

This amplitude difference has a large effect on the accuracy of the impulse response measurement using a spectrum analyzer (Stanford SR780). The analyzer generates a varying frequency input with fixed amplitude (i.e. a swept sine wave) to the FTS, and determines attenuation and phase of the tool motion captured by an internal LVDT at each input frequency. If the output path signal is velocity-saturated, its frequency component associated with the input frequency has, in effect, smaller amplitude than the actual output signal. As a result, the frequency response of the Variform shows significant attenuation. Figure 5 depicts the attenuation of the Variform as a function of the frequency and amplitude of the command signal. The frequency response illustrates a large amplitude drop where the input signal contains large amplitudes with high frequencies. This implies that the operating range of the Variform is

limited to combinations of amplitude and frequency where the velocity is below the constraint of 140 mm/sec as shown in Figure 6.

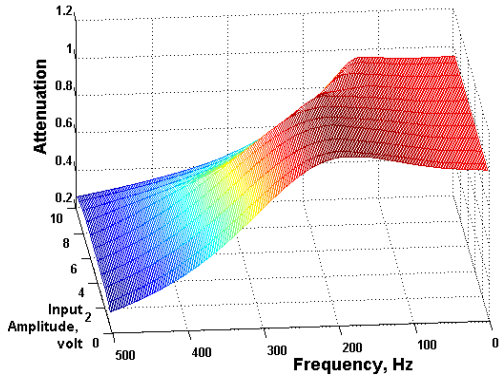

Figure 5. 3D frequency response as a function of input amplitudes.

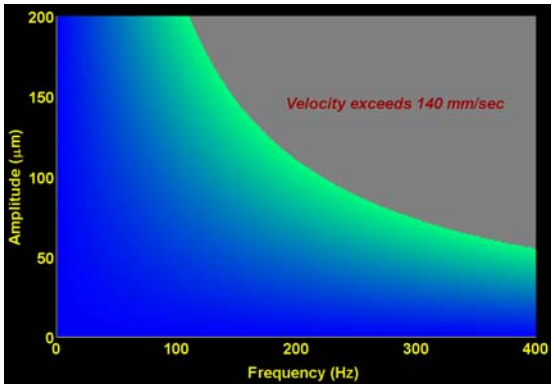

Figure 6. Operating range of the Variform.

11.2.2 DYNAMICS OF THE VARIFORM POSITION SENSOR

The Variform employs an internal LVDT to measure the displacement of the tool. This contact displacement measuring system has its own dynamic response that *filters* the position measurement as shown in Figure 7. Actual tool motion was measured with an external capacitance gage placed in front of the tool holder. The capacitance gage signal is inverted in the scope plot shown in the figure. The actual phase is 21° with respect to a 100 Hz sine wave input signal, but the LVDT is 39° out of phase with the input command. Figure 8 illustrates the transfer function between the capacitance gage and the LVDT that was determined using the same measurement technique as the actuator dynamic response. Note that the phase response starts at 180° because the two sensors are measuring in opposite directions and the LVDT signal leads the non-inverted capacitance gage signal by 18° at 100 Hz. As with the inverse dynamic

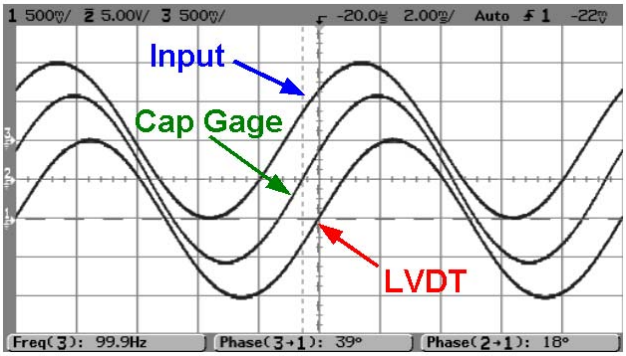

Figure 7. Phase of the tool motion measured by the LVDT and a capacitance gage (inverted) with respect to a 100 Hz input signal.

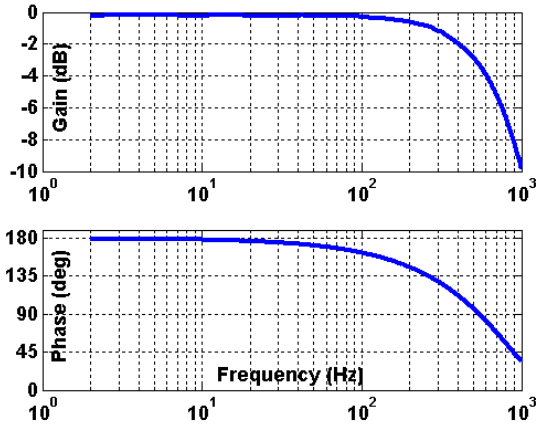

Figure 8. Dynamic response measured by the LVDT with respect to the capacitance gage.

response of the mechatronic system, the deconvolution algorithm can also compensate for the feedback sensor's dynamic response. Another note is that the gain at high frequencies descends about 40 dB over ten increments of the LVDT natural frequency range (500 – 5000 Hz). This implies that a 2nd order internal filter is implemented in the Variform's displacement sensor.

11.2.3 DECONVOLUTION IN REAL-TIME

The inverse dynamic technique can be performed once for a given set of machining parameters (e.g., spindle speed, cross-feed). However, if the spindle speed changes, the time period of the desired path is also altered. Deconvolution over the entire tool excursion requires immutable parameters. However, the initial machining parameters may drift over a long machining time. One solution is to run the deconvolution in *real-time* and update the command signal by monitoring the machining parameters. Consequently, deconvolution over a long desired excursion must be segmented so that the short pieces are individually modified using the deconvolution technique. While the Variform follows the current input command, the next piece of the desired tool path will be modified using the most recent parameters.

Short-time Fourier transform

The *real-time* deconvolution can be achieved by using a window function[1] applied to a long path signal. Figure 9 demonstrates how the rectangular window (Equation (1)) and the triangular window functions draw a short piece ($x_s[n]$) out of a long sinusoidal signal ($x[n]$). The short signals are the product of the applied signal and the window function as shown in Equation (2).

$$w[n] = \begin{cases} 1 & a \le n \le b \\ 0 & \text{otherwise} \end{cases} \tag{1}$$

$$x_s[n] = x[n] \times w[n] \tag{2}$$

The reverse process, an overlap-add method is used to reconnect the short pieces together. Each individual piece combines with the overlaps of the adjacent pieces as shown in Figure 10. Note that the reconstructed signal is distorted at both ends as a result of the window characteristics, but is a copy of the input signal where the overlap is complete. Finally, the entire combined signal is scaled to correct its amplitude.

The short-time Fourier transform utilizes a window function and transforms the short pieces to the frequency domain [2] where the operation of inverse dynamics occurs [3-4]. The window function is applied again in a reconnecting process as shown in Figure 11. In practice, the length

[1] A window function is a vector of weight coefficients, which are zero everywhere but within a certain length.

of the window must be short to be sensitive to high frequency components as well as variations of the signal. Figure 12 illustrates the synthesis process for windowed signals. The series of modified signals in Figure 12(a) reconnect at the appropriate time to the adjacent pieces to reconstruct the entire modified signal as shown in Figure 12(b).

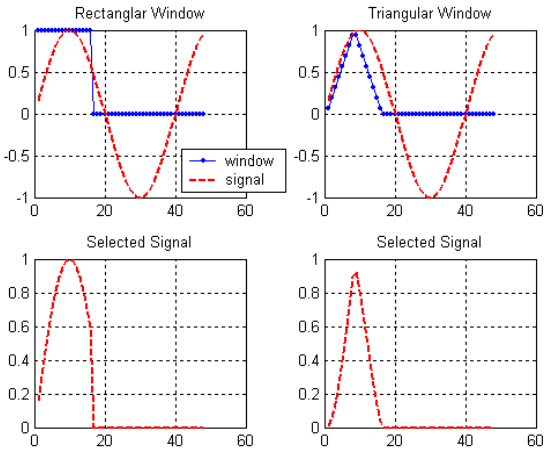

Figure 9. Rectangular and triangular window functions draw out a short piece of a long signal.

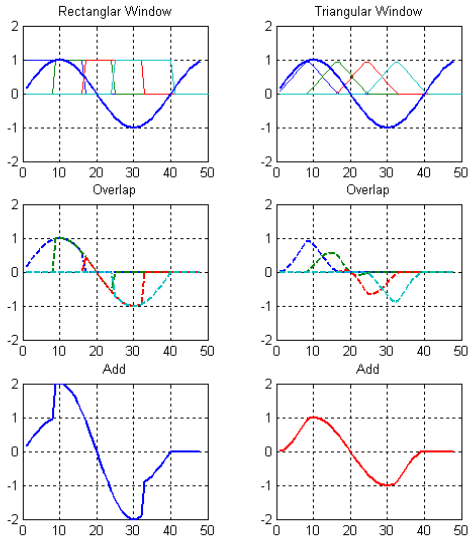

Figure 10. Overlap-add method reconstructs the original signal from small pieces.

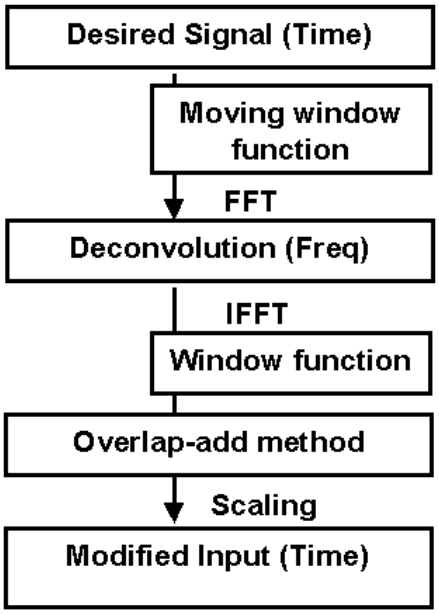

Figure 11. Schematic of the short-time Fourier transform.

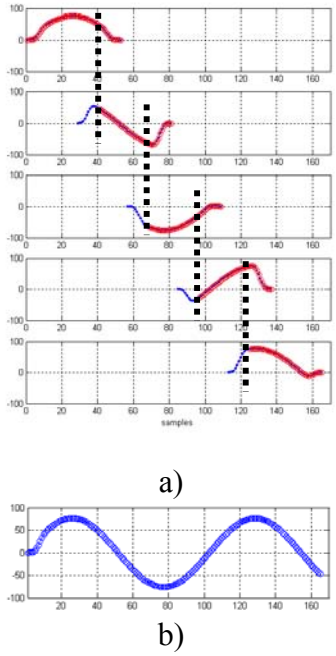

a)

b)

Figure 12. a) Series of windowed signals after individual deconvolution, b) The entire of the modified signal.

Equivalent inverse dynamics filter

Another approach to *real-time* deconvolution development is to build an equivalent inverse dynamics filter which yields a more efficient implementation. Conceptually, the modified input command $x[n]$ is obtained when the desired tool path $y[n]$ is transformed to the frequency domain where the deconvolution (or division operation with the frequency response $H[\omega]$ of the system) occurs. Equation (3) expresses the deconvolution operation following the method of the previous section with a single rectangular window applied to the entire command signal.

$$x[n] = IFFT\left(\frac{FFT(y[n])}{H[\omega]}\right) \tag{3}$$

where

FFT, IFFT	fast Fourier transform algorithm and its inverse
n	discrete time
ω	frequency

The filter approach eliminates the division operation in the frequency domain by creating an equivalent inverse dynamics filter as written in Equation (4). Consequently, the deconvolution in Equation (3) can be expressed as a convolution of this inverse filter with the desired motion path as shown by Equation (5). Figure 13 depicts the inverse of the FTS's frequency response. The filter gain is amplified and the phase is adjusted to compensate for the dynamic response of the actuator.

$$h^{-1}[n] = IFFT\left(\frac{1}{H[\omega]}\right) \tag{4}$$

$$x[n] = y[n] * h^{-1}[n] \tag{5}$$

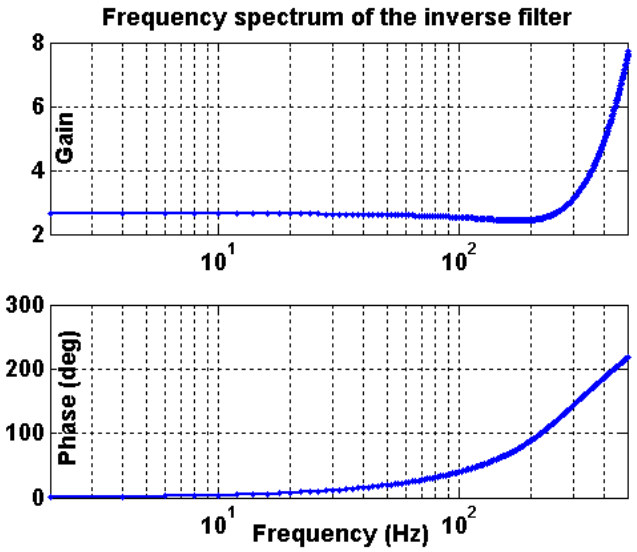

Figure 13. Frequency spectrum of the equivalent inverse dynamic filter.

Under varying machining conditions, this approach can be implemented using the overlap-add and overlap-save methods. These two algorithms implement block convolution; that is, a segmented convolution of a long parametric desired tool path $y[n]$ and the inverse dynamic filter $h^{-1}[n]$. The exact convolution can be retrieved as segmented convolution blocks are reconnected.

Overlap-Add Method Using Equation (6), this method implements a linear convolution of the short desired signal $y[n]$, of length L, to the M+1 point inverse impulse response $h^{-1}[n]$.

$$x[n] = \sum_{k=-\infty}^{\infty} y[k]h^{-1}[n-k] \tag{6}$$

The operation results in an L+M point modified signal $x[n]$. The first L points of this modified command are correct. However, the last M points must overlap and add with the next modified piece to obtain the correct linear convolution. The overlap-add technique can be implemented efficiently with the FFT algorithm. The procedure is to:

1. Pad zeros to the inverse impulse response and all of the short desired signals so that all have the signal length L+M.
2. Perform the convolution operation using an FFT as illustrated in Equation (7) yielding the signal $x[n]$ of length L+M.
$$x[n] = IFFT\left(FFT\left(y[n]\right) \times FFT\left(h^{-1}[n]\right)\right). \tag{7}$$
3. Overlap the last M-points of the modified signal $x_i[n]$ with the first M points of the next modified signal $x_{i+1}[n]$ as shown in Figure 14.
4. Add the overlapping segments.

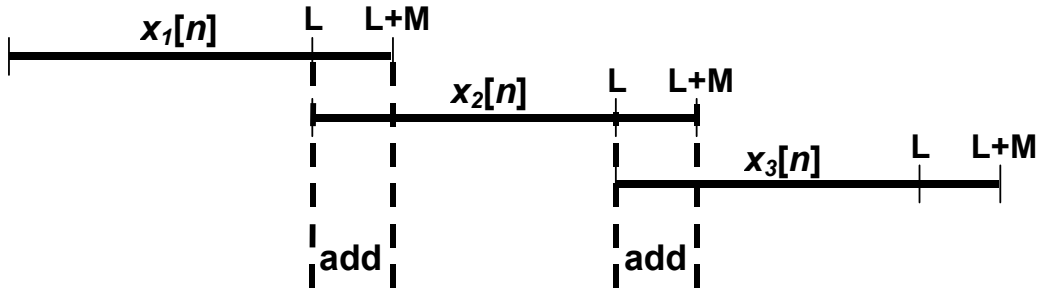

Figure 14. Block convolution using the overlap-add method.

Overlap-Save Method Using Equation (8), this method implements an L+M point circular convolution of the M+1 point inverse impulse response $h^{-1}[n]$ with an L+M point segment from the desired path $y[n]$.

$$x[n] = \sum_{m=0}^{N-1} y[m]h[n-m]_N \qquad 0 \le n \le N-1 \tag{8}$$

The first M points of the resulting output are incorrect, while the remaining points are identical to those obtained by linear convolution. The algorithm proceeds by dividing the desired path

$y[n]$ into sections of length L+M and overlapping these pieces with the last M points of the preceding section as shown in Figure 15. Note the first section is padded at the beginning with M zeros.

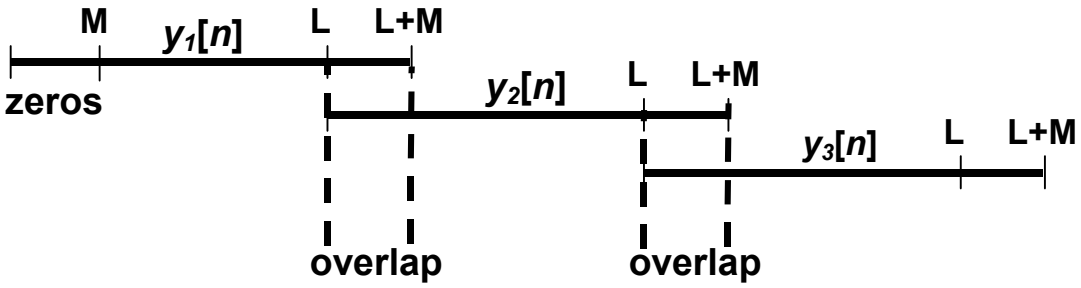

Figure 15. Block convolution using the overlap-save method.

After performing a convolution for each section using the FFT, the first M points of all resulting outputs are discarded. The output segments are patched together to complete the convolution of the inverse dynamic filter $h^{-1}[n]$ and the long desired tool path $y[n]$.

The two block convolution methods described above have advantages over the approach using the short-time Fourier transform. First, division operations are only performed during the construction of the inverse dynamics filter instead of during the deconvolution of each windowed piece of the command signal. This makes it much easier to deal with zeros (and near zeros) in the response function and results in a more efficient implementation. Second, block convolution is an exact operation, yielding the same answer as a single convolution over the unsegmented signal. The STFT algorithm gives different results depending on the characteristics of the chosen windowing function. And finally, the reconnecting process for each block convolution method is very simple compared to the STFT.

11.2.4 OFF-AXIS SPHERE

A spherical optical surface has been chosen to demonstrate the inverse dynamics error compensation technique. An off-axis sphere will be machined into a flat surface as shown in Figure 16. This geometry has been selected because the command trajectory is not periodic and its frequency content can be modified by changing the off-axis distance and/or spindle speed. Most important though is that the *f-number* of the spherical surface can be selected

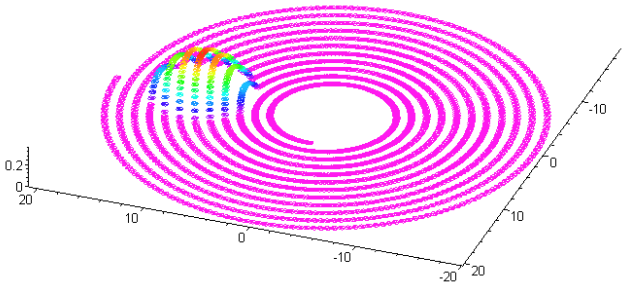

Figure 16. An off-axis sphere selected for technique validation experiments.

so that the results are easily characterized with an interferometer. While the machine axes follow a spiral pattern overlaid on the machined surface, the FTS moves as a parametric function of r and θ expressed in Equation (10). The spherical surface can be expressed as Equation (9),

$$(x-a)^2 + (y-b)^2 + (z-c)^2 = R^2 \tag{9}$$

where the x and y axes motions are described as,

$$x = r\cos\theta$$
$$y = r\sin\theta$$

Then, z (or tool position) of the FTS to form an off-axis sphere can be written as

$$z = c + \sqrt{R^2 + 2r\,a\cos\theta - a^2 + 2r\,b\sin\theta - b^2 - r^2}\ . \tag{10}$$

Equation (10) can be expressed as a parametric function of time by writing r and θ as functions of axis cross-feed and spindle speed, respectively. Then, the FTS command signal required to generate the entire surface can be easily generated as a time-based vector at any desired resolution.

The sagittal component of the tool path that generates this surface is a set of nearly circular trajectories with different widths and depths depending on the radial position of the tool. An example of one unique pass of the tool is shown in Figure 17. This picture shows the tool path beginning at a particular height above the surface then plunging into the part and finally returning to that height. The deviation from a circular trajectory is a result of the shape of the intersection of the sphere with the spiraling radial tool position and the correction needed for the nose radius of the tool. Because the depth of the sphere is too large to create in a single pass across the part, the surface will be created by a series of passes following the same trajectory but with increased depth on each pass.

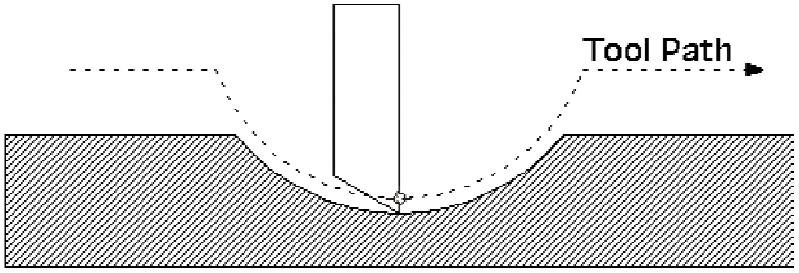

Figure 17. Tool cutting motion along spiral path to create a concave sphere.

11.3 EXPERIMENTAL CORROBORATION OF DECONVOLUTION

11.3.1 EXPERIMENTAL SETUP FOR THE SHORT-TIME FOURIER TRANSFORM

An experiment was performed using a dSPACE (RS1104) data acquisition board to invert the dynamic response of the actuator. Dynamics of the LVDT were not compensated in this experiment. In Figure 18, any desired tool path and machining parameters are uploaded to the dSPACE processor and the *real-time* deconvolution algorithm is performed. The tool excursion was windowed, transformed to the frequency domain, modified by the inverse dynamics algorithm [5], synthesized, and conveyed to the FTS as a modified input command. Note that, at the time of writing, the algorithm that acquires the varying parameters was still being formulated. The deconvolution was exercised using fixed machining parameters.

To implement the overlap method with the *real-time* deconvolution, the model employed an input buffer block to store arrays of the desired signal. The *Hanning* window function was selected for the Short-Time Fourier Transform (STFTsim block).

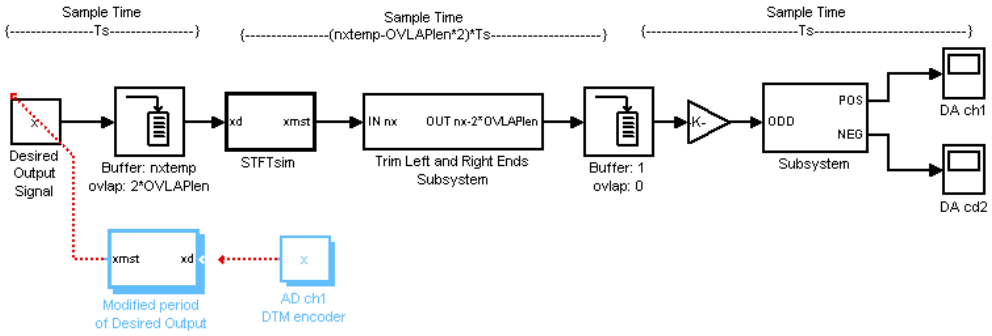

Figure 18. Model of *real-time* deconvolution.

Analytical approach

In Figure 19(a), the modified input of the Variform is calculated using the *real-time* deconvolution and the frequency response of the system. The buffer block takes about 55 ms to collect the input signal resulting in an initial delay before the deconvolution operator delivers the modified input command. Note that the modified input signal does not jump at the start to correct the phase as the modified input obtained from a normal deconvolution since the weight coefficients of the *Hanning* window function eliminate this discontinuity.

As with the reconstructed signal in Figure 10, the path associated with the modified signal experiences distortion at the initial state due to the weight coefficients of the window function. The tool path evolves to the desired excursion in less than 80 ms. Path difference with respect to the desired path is less than 1 μm (P-V) at the steady state as shown in Figure 19(b).

Experimental results

The modified input signal as displayed in Figure 19(a) was sent to the Variform FTS resulting in an output tool motion in which the attenuation and phase is corrected. Figure 20(a) illustrates the Variform response (dash line) with respect to the desired profile (solid line). The output excursion measured by the LVDT was essentially in-phase with the desired tool path; however, the gain was slightly mismatched. The path difference at the steady state is about 8 μm (P-V) as depicted in Figure 20(b). The difference is larger than that of the model. This may be caused by drift of the PZT stacks after they warm up. More work is needed to draw a conclusion.

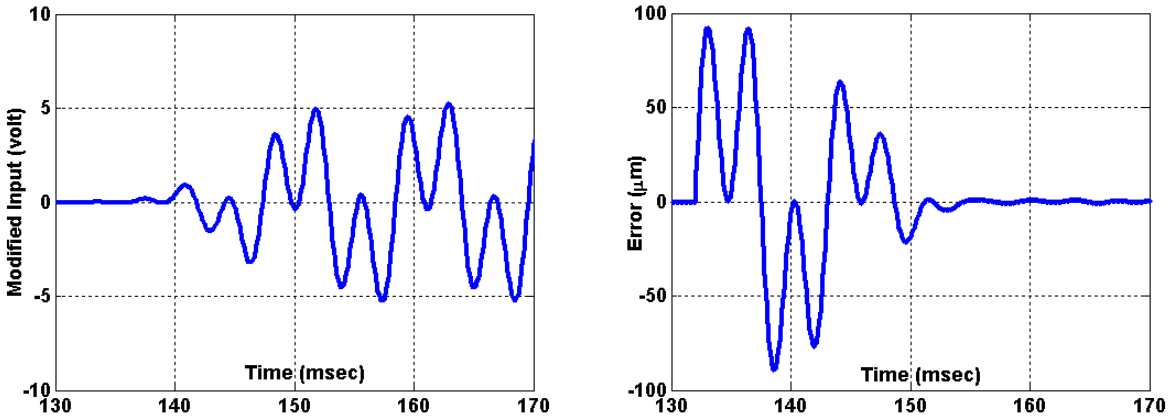

a) b)

Figure 19. a) Modified input associated with the real time deconvolution, b) Path difference with respect to the desired excursion.

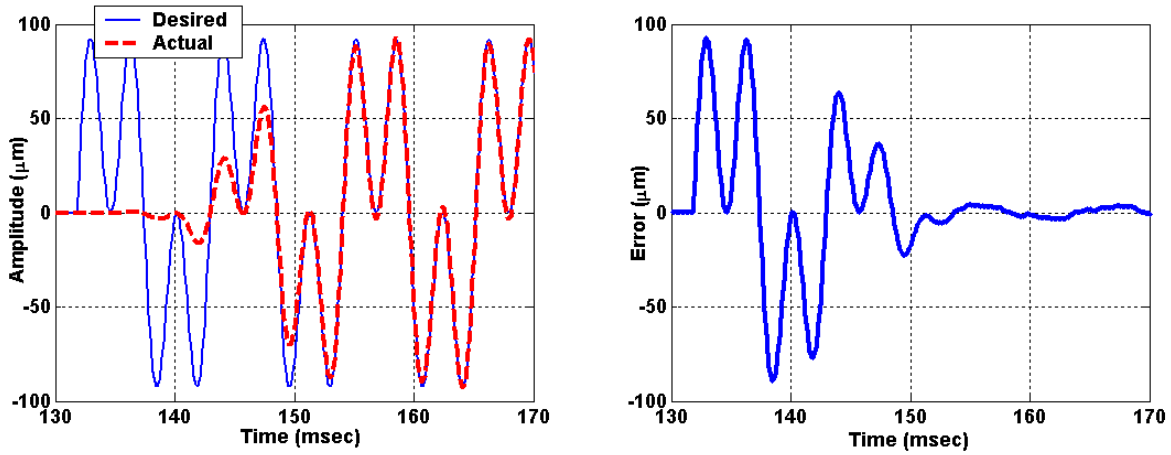

a) b)

Figure 20. a) Desired tool path of 90 μm P-P, 90 and 270 Hz and the Variform response, b) Path difference with respect to the desired excursion.

11.3.2 MACHINING EXPERIMENTS

An on-axis concave sphere with dimension equal to the off-axis sphere described in section 11.2.4 was machined. Three samples are shown in Figure 21. Since the surface was machined on center, the form error and surface finish reflect the best possible on the ASG-2500. The form error (rms) using a diamond tool with a nose radius of 1.512 mm was 12.5 nm as shown in Figure 22 and the surface roughness (rms) was 3.5 nm as depicted in Figure 23. Since the surface error is a result of the vibration of the machine axes and the features of the tool, the same tool will be used to machine the off-axis sphere.

Figure 21. On-axis sphere diamond turned on copper-plated blocks.

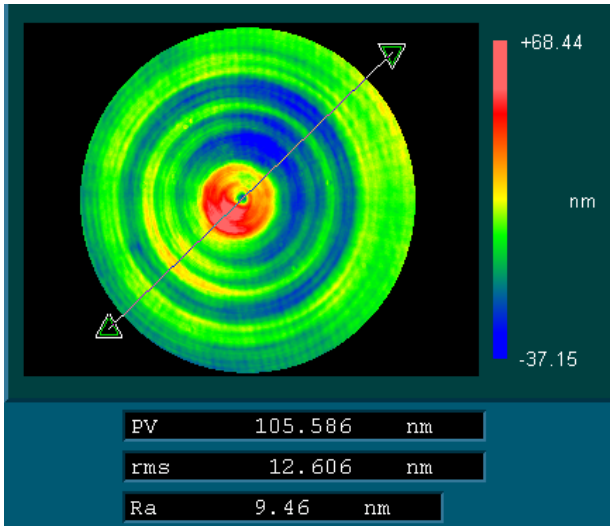

Figure 22. Interferometer shows the form error of 12.6 nm.

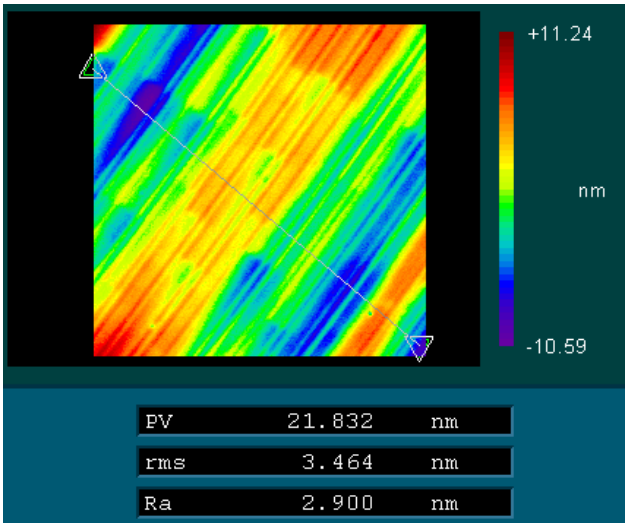

Figure 23. The roughness of the on-axis sphere is 3.5 nm.

11.4 SOFTWARE DEVELOPMENT

The final task of this project is to build a software package that modifies the motion path of a high bandwidth actuator to significantly reduce phase and attenuation errors in the resulting non-rotationally symmetric component of a three dimensional part geometry. The 3D surface has been decomposed into a 2D cross-section that is swept out by the Cartesian axes of a diamond turning machine to produce a *best-fit* or *mean* surface of revolution. High frequency, low

amplitude deviations from this path produce a non-rotationally symmetric (NRS) surface. These deviations are programmed as the motion of a fast tool servo (FTS) axis that is mounted on one of the machine axes although not necessarily orthogonal or parallel to the direction of motion of that axis.

11.4.1 DATA FORMATS

A free-form 3D optical surface that has been decomposed into a surface of revolution and a non-rotationally symmetric perturbation is the primary input to the software. This predetermined decomposition is contained in an input text file that describes a surface in terms of a series of meridional curves, each of which is divided into a number of zones which join linear and circular sections. Figure 24 shows a low resolution view of this web-like structure. Each zone specifies the curvature along a segment of a line from the pole (or center) to the equator (or edge). A series of these zones defines the curvature along the meridian. A meridian thus represents one-half of a cross section of a rotationally symmetric solid. Multiple meridians are used to specify a non-rotationally symmetric solid as the umbra of the surfaces of revolution swept out by the constituent meridians. That is, the resulting surface is defined by the top or highest point in the union of this collection of surfaces of revolution. A single input file can contain multiple *paths*, each of which specifies a machining operation on the same workpiece. The ordered sequence of these machining steps produces the final part surface.

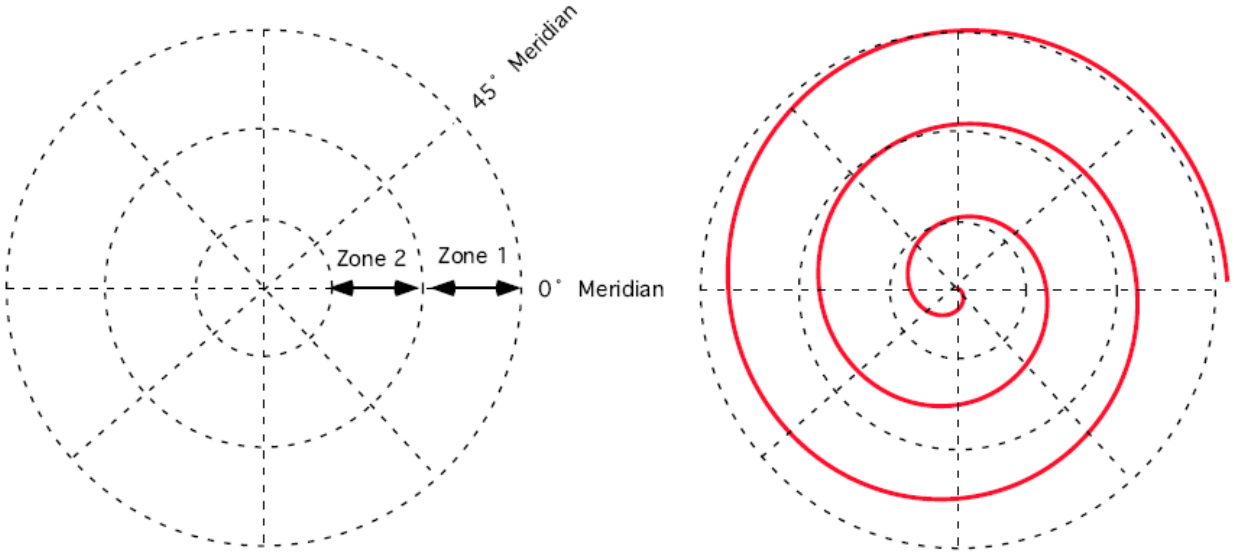

Figure 24. Spiral overlay of tool path on surface description web.

The deconvolution process can be applied to any selected NRS path in the input file and the remainder of the input file will be ignored and copied to the output file. The start and end of each path description will be delimited with simple mnemonic text strings. Similarly, the data

needed to specify tool locations along a meridian (i.e, the curvature of the surface along a line of longitude) will be delimited with text strings. For each of these zones, the input file must contain the starting and ending coordinates as well as a radius and direction of curvature. For a linear section a special case of zero radius is recognized. The intent is to provide a flexible, free-form input format that is unambiguous and configurable by the user. For example, all delimiting text strings will be stored in a preference file. The format of output file will be identical to the input, except that the data within the selected path will be modified and the *start-of-path* text line will contain additional information to indicate that this path has been processed.

The impulse response of the actuator will also be an input to the software. The format of this data is a matrix of actuator displacements stored in a text file. Each column of the file is a time sampled response to an impulse of specific amplitude and each row is the response to a specific frequency. The information needed is the same as that shown graphically in Figure 5.

11.4.2 ANALYSIS

Analysis of a surface description with respect to the dynamics of an axis requires a representation of the surface in terms of the independent, synchronized motions of the axes with respect to time. In this way the motions of each axis are decoupled and expressed as functions of a common parameter, time (t). This parametric transformation is accomplished for a NRS surface by overlaying a spiral tool path on the meridional web structure as depicted in Figure 24. This spiral is defined by angular and radial velocities (i.e., spindle speed and cross-feed). This spiral path can then be sampled at any frequency greater than the inverse of the product of the angular velocity and the number of meridians to obtain the desired tool path, $y_d[n]$. Equations (3) or (5) can then be applied to generate a modified tool path.

11.4.3 INTERPOLATION

As can be seen from Figure 24, points on the spiral path do not always intersect the web structure and must be interpolated. The accuracy of the unmodified tool path (i.e., its fidelity to the desired 3D surface) is limited by factors such as the number of meridians, the number of zones, the radius of the workpiece and the meridional and cross-meridional interpolation algorithms. Interpolation of the surface profile along a meridian is specified unambiguously for any given step length or cross feed velocity. That is, it can be performed to any desired numerical accuracy. Interpolation between points on adjacent meridians will utilize a spline smoothing algorithm that passes exactly through the longitudinal curves. Various techniques (e.g., cubic spline, B-spline) and relaxation orders (e.g., spline stiffness) will be evaluated. To convert the modified tool path from a spiral back into a web the interpolation process is reversed. As a result of the deconvolution process both the number of meridians and the number of zones within a meridian may be increased and the zone boundaries and curvatures will be adjusted.

11.4.4 ANTICIPATED RESULTS

Software

Software will be developed to implement the deconvolution of a desired motion path with the dynamic response of an actuator to produce a modified tool path that effectively cancels the actuator dynamics. The results are a dramatic improvement in tracking response and an increase in usable bandwidth. The user interface will run on a PC under the Windows™ operating system and process ASCII text files containing,

1. Actuator impulse response data,
2. Surface description data,
3. Configuration parameters and user preferences.

User Interface

The user interface, data handling and analysis functions of the code will be contained in separate modules. Additional parameters needed by the program at run time (spindle speed, cross-feed, etc.) will be provided by the user via the usual mechanisms of tool bar icons, check boxes, radio buttons, menus and numeric data fields typical of Windows-based software.

Error Checking

Error checking of all user selections will be performed and appropriate error messages displayed. Input files containing NRS paths with large amplitude and/or high velocity will be compared with the known range, velocity and acceleration limits of the actuator. In some cases it may be possible to determine a modification of the parameter set (e.g., slowing down the spindle) that does not violate actuator constraints and allows the deconvolution to produce a useful modified signal.

Output Display

In addition to a text output file containing the modified command signals, three types of contour plots will be available for display,

1. actuator amplitude,
2. actuator velocity,
3. actuator acceleration.

Each plot can be applied to an input surface description or the deconvolved surface description.

11.5 CONCLUSIONS

Inverse dynamics algorithms in *real-time* were developed to adapt to varying machining conditions using the most recent parameters. The optimal machining condition is assured when the Variform FTS functions within its operating range in which the velocity is less than its constraint of 140 mm/sec. Out of this range, the Variform FTS loses its driving acceleration and distorts a sinusoid command signal to a triangle-like output motion. Frequency spectrum analysis showed that the frequency response measurement became less accurate. The measured response contained significant attenuation with respect to the actual tool excursion.

The LVDT implements a 2^{nd} order internal filter on the position measurement resulting in a lag behind the actual tool motion. This hidden response can be measured by a capacitance gage and compensated using the proposed inverse dynamics algorithm.

Real-time deconvolution was formulated in two approaches. First, the short-time Fourier transform applied to a sliding window function over a desired excursion and deconvolved with the dynamic response in the frequency domain. Simulation of the corrective scheme under a fixed machining condition indicated that the steady-state form errors associated with a modified input command were significantly reduced after an approximately 75 ms startup interval. Experiments without a *real-time* machining parameter feedback made use of a Real-Time Workshop and a dSPACE (RS1104) data acquisition board showing similar results to the model. However, the path error was greater than that of the simulation. The causes are still under investigation.

The second approach is to construct an equivalent inverse dynamics filter. Complication of the deconvolution operation is now implemented as a convolution operation (or multiplication in the frequency domain). Block convolution using overlap-add and overlap-save methods was introduced to develop the inverse dynamics algorithm in *real-time*. This approach yields a simpler as well as faster implementation than the STFT method.

An off-axis sphere was selected as a surface-machining test of both deconvolution schemes. Form error measured with spheres machined on-axis illustrate the best features obtainable using the ASG-2500 diamond turning machine. The form error (rms) was 12.5 nm and the surface roughness was 3.5 nm. The off-axis sphere will be machined in the near future both with and without applying the deconvolution techniques and the results compared with the on-axis spheres.

REFERENCES

1. Panusittikorn, W., and K. Garrard, *Surface Decompositon for Diamond Turning Machine.* Precision Engineering Center Annual Report, 20, pp 117, (2002).
2. Oppenheim, A.V., and R.W. Schafer, *Discrete-Time Signal Processing.* Prentice Hall, pp 541, (1998).
3. Lim, J.S., and A.V. Oppenheim, *Advanced Topics in Signal Processing.* Prentice Hall, pp 289, (1987).
4. Quatieri, T.F., *Discrete-Time Speech Signal Processing.* Prentice Hall, pp 309, (2001).
5. Writing S-functions for Real-Time Workshop, http://www.mathworks.com.

FACULTY, STAFF, AND STUDENTS OF THE PRECISION ENGINEERING CENTER

Standing (L to R): W. Panusittikorn, N. Buescher, T. Randall, J. Eischen, R. Scattergood, K. Freitag, G. Buckner and T. Dow

Sitting: (L to R): Y. Yin, P. Ro, K. Garrard, L. Bodenhamer, A. Sohn and K. Folkert

Students Not Pictured: S. Clayton, D. Hood, R. Huth, P Morrissey, N. Negishi, R. Staton, A Wong and T. Wu

Faculty Not Pictured: P. Russell and D. Youden

Staff Not Pictured: L. Underhill

FACULTY

THOMAS A. DOW

Director, Precision Engineering Center
Professor, Department of Mechanical and Aerospace Engineering

BS, Mechanical Engineering, Virginia Polytechnical Institute, 1966
MS, Engineering Design, Case Institute of Technology, 1968
PhD, Mechanical Engineering, Northwestern University, 1972

After receiving his PhD degree from Northwestern University in 1972, Dr. Dow joined the Tribology Section of Battelle Columbus Laboratories and worked there for ten years. His research interests were in the areas of friction and wear and included studies on a wide variety of topics from lubrication of cold-rolling mills using oil-in-water emulsions to wet braking effectiveness of bicycle brakes to elastohydrodynamic lubricant film generation in ball and roller bearings. He developed experimental apparatuses, established analytical models, and corroborated those analyses with experimental measurements. Dr. Dow joined the faculty at North Carolina State University in 1982 and was instrumental in developing the academic and research program in precision engineering. His current research interests include the design of precision machining systems, real-time control, and metrology. He was one of the founders of the American Society for Precision Engineering and currently acts as the Executive Director.

GREGORY D. BUCKNER

Assistant Professor, Department of Mechanical and Aerospace Engineering

BS, Mechanical Engineering, Louisiana State University, 1986
MS, Mechanical Engineering, Virginia Polytechnic Institute, 1987
PhD, Mechanical Engineering, University of Texas at Austin, 1996

After receiving his PhD degree from the University of Texas at Austin in 1996, Dr. Buckner joined the University of Texas Center for Electromechanics (UT-CEM), where he served as a research engineer until 1999. His research at UT-CEM focused on the design and implementation of advanced controllers for electromechanical systems. Applications included self-learning control systems for active vehicle suspensions, magnetic bearings for flywheel systems, and manufacturing processes. Dr. Buckner joined the faculty at North Carolina State University in 1999 as an Assistant Professor of Mechanical and Aerospace Engineering. Dr. Buckner's research and teaching interests focus on the design and control of electromechanical systems, with an emphasis on self-learning algorithms. Current research topics include electromechanical actuators for system identification of milling processes, and magnetic bearings for flywheel and milling applications.

JEFFREY W. EISCHEN

Associate Professor
Department of Mechanical and Aerospace Engineering

BS, Mechanical Engineering, UCLA, 1978
MS, Mechanical Engineering, Stanford University, 1981
PhD, Mechanical Engineering, Stanford University, 1986

Dr. Eischen has been with N.C. State since 1986 and his research areas of interest include computational solid mechanics, elasticity, fracture mechanics and structural dynamics. Dr. Eischen worked with Failure Analysis Associates from June 1978 - June 1986 as a Mechanical Engineer. His primary responsibilities included analysis and prevention of industrial equipment failures.

PAUL I. RO

Associate Professor
Mechanical and Aerospace Engineering Department

BS, Mechanical Engineering, University of Minnesota, 1982
MS, Mechanical Engineering, Massachusetts Institute of Technology, 1985
PhD, Mechanical Engineering, Massachusetts Institute of Technology, 1989

Dr. Ro joined the faculty of North Carolina State University in January 1989, as an Assistant Professor in the Mechanical & Aerospace Engineering Department. He became an Associate Professor in July 1994. Dr. Ro has developed two graduate courses in the department (multivariable Control and Robotics) and has taught undergraduate Automatic Control and Dynamics courses. His research covers a wide range of controls and various applications of control theories in the following three areas: Precision Engineering, Robotics and Intelligent Vehicle Control.

In precision engineering, Dr. Ro's research concentrates on the characterization and control of microdynamic behaviors of precision slide systems (ball-screw, traction drive, piezo-electric drive, electrostatic drives and magnetic servo levitated drive) to enhance their nano-motion capabilities, development of advanced control schemes and experimental verifications to improve diamond turning process using force and position sensory feedbacks, design of a long-range fast tool servo system using magnetic servo levitated actuators, and active control of precision slide vibration using piezo-electric drives. In robotics, some of the on-going projects include design and implementation of free-floating non-holonomic space robot and a planar passive-joint robot for fuel consumption minimization, neural-fuzzy hybrid scheme for mobile robot path planning, and two-arm coordinated motion control for fixtureless assembly. In intelligent vehicle control, on-going projects include nonlinear tire model identification by Artificial Neural Network, hybrid neural-sliding mode control of 4 Wheel steering for robust handling, semi-active suspension control using
energy based Fuzzy Logic scheme, and others.

PHILLIP E. RUSSELL

Professor
Department of Materials Science and Engineering

BS, Physics, Appalachian State University, 1975
MS, Physics, West Virginia University, 1977
PhD, Materials Science and Engineering, University of Florida, 1982

After graduate work at the University of Florida, Dr. Russell joined the Solar Energy Research Institute (a DOE lab) in Golden Co. in 1980. There he developed a photovoltic materials and device characterization laboratory with emphasis on electron and ion beam analytical instrumentation. After three years at SERI, Dr. Russell joined JEOL, Inc. in Boston, Massachusetts, an electron optical instrumentation company where he led the technical and application groups. One of his major projects was the development of an electron beam based integrated circuit metrology system. He was also involved in the development and application of focused ion beam systems and electron beam lithography systems, as well as numerous analytical instrumentation projects.

On joining North Carolina State University, Dr. Russell took on the role of Director of the Analytical Instrumentation Facility and has established graduate level courses in electron optics and electron optical instrumentation techniques. He was awarded the NSF Presidential Young Investigator Award in 1987. His research at NCSU and the Precision Engineering Center are in the areas of Scanned Probe Microscopy, Focused Ion Beam Technology, Scanning Electron Microscopy, Lithography metrology and beam testing of integrated circuits.

RONALD O. SCATTERGOOD

Professor
Materials Science and Engineering Department

BS, Metallurgical Engineering, Lehigh University, 1961
MS, Metallurgy, Massachusetts Institute of Technology, 1963
PhD, Metallurgy, Massachusetts Institute of Technology, 1968

R.O. Scattergood is a Professor in the Department of Materials Science and Engineering. He received BS degrees in Mining Engineering and Metallurgical Engineering from Lehigh University. His MS and PhD degrees were obtained in Metallurgy from M.I.T. In 1968 he became a member of the basic research staff in the Materials Science Division at the Argonne National Laboratory. In 1981, he joined the faculty as a Professor of Materials Engineering at North Carolina State University.

Professor Scattergood's major research interests have been focused on the mechanical behavior of solids. He has worked in the areas of strengthening mechanisms in solids, continuum theory of defects, radiation effects, wear and fracture processes in ceramics, and precision engineering with emphasis on machining processes. He has expertise in both analytical and computer modeling as well as in mechanical testing methods and microscopy. He has published over 140 technical papers, books and reports.

DAVID YOUDEN

Technical Associate, Eastman Kodak Company
Adjunct Lecturer, Department of Mechanical and Aerospace Engineering

ASME, Central New England College, Worcester, MA, 1965

Prior to joining Eastman Kodak's Manufacturing Systems Technology Division in 1997, Mr. Youden was Research and Development Manager at Rank Pneumo, a division of Rank Taylor Hobson Inc. for ten years. Before that, he was Director of Engineering at the Cone Blanchard Machine Company. He has also worked at Ocean Systems, Inc. of Reston, Virginia and the Heald Machine Company, a division of Cincinnati Milacron. During his professional career, Mr. Youden has been granted numerous patents in the field of machine tools, and he has published and presented technical papers on the design and testing of ultra-precision machine tools in the US, Japan, and Germany.

Mr. Youden graduated from Central New England College and attended Worcester Polytechnic Institute and Clark University. He is a charter member of the American Society for Precision Engineering.

STAFF

LARA BODENHAMER

Administrative Assistant
Precision Engineering Center

BA, Religious Studies, College of Charleston, 2000
MPA Candidate, North Carolina State University

Miss Bodenhamer became a member of the PEC Staff in August 2003. Previously she served as public policy intern at North Carolina Center *for* Nonprofits in Raleigh, NC, and as an event planner at Capital City Club in Raleigh, NC. Miss Bodenhamer brings to the Center her knowledge of nonprofit management and public policy. Miss Bodenhamer provides the overall administrative support for the Center.

KENNETH P. GARRARD

Research Assistant
Precision Engineering Center

BS, Computer Science, North Carolina State University, 1979
MS, Computer Studies, North Carolina State University, 1983

As a full-time research assistant, Mr. Garrard is studying the design of systems software that supports the development of high-speed real-time applications for special purpose multiprocessor computer systems. He has several years experience in academia and industry designing and implementing real-time systems. As a Precision Engineering Center staff member, Mr. Garrard's current activities include the design and implementation of software for Diamond Turning Machine and Fast Tool Servo controller projects.

ALEXANDER SOHN

Research Assistant/Lecturer
Precision Engineering Center

B.S., Physics, University of Texas at Arlington, 1992
M.S., Physics, University of Texas at Arlington, 1994

Mr. Sohn joined the Precision Engineering Center in August, 1997 as a member of the technical staff. His current research interests range from machine design and metrology to the design and fabrication of nonimaging optics. Mr. Sohn's varied research activities began in microwave optics and atomic physics as a student at the University of Texas at Arlington and later progressed to precision machine design, design and fabrication of plastic optics as well as automation and machine vision at Fresnel Technologies, Inc. in Fort Worth, Texas.

LAURA UNDERHILL

Administrative Assistant, 2001-2003
Precision Engineering Center

BA, Education, University of North Florida, 1994

Ms. Underhill became a member of the PEC Staff in August 2001. Previously she was an administrative assistant at North Florida Shipyards in Jacksonville, FL, and Computer Source in Jacksonville, FL. Ms. Underhill brought to the Center many years of administrative experience and provided the overall administrative support for the Center until August 2003.

GRADUATE STUDENTS DURING 2003

BRETT BROCATO interned at Fort James Paper and TRW Vehicle Safety Systems prior to graduating from the University of Alabama in 1999 with his bachelor's degree is in Mechanical Engineering with a minor in the Computer Based Honors Program. Before enrolling in the NC State master's program, he worked for Bell Helicopter and Corning Optical Fiber.

NATHAN BUESCHER was born and raised in Raleigh, NC. He received his BS in Mechanical Engineering as well as a Minor in Mathematics from NC State University in May 2003. He began work with the PEC in August 2003. Some of his prior work experience includes Stantec Consulting, Inc. and Joel Wittkamp Design.

STUART CLAYTON received his BS degree in Mechanical Engineering from NC State University in May 2001. After taking a summer off from school, Stuart enrolled in graduate school at the PEC. While pursuing a Master's of Science degree in Mechanical Engineering, Stuart's research involved an investigation of deflections of high-speed miniature milling tools and the ability to compensate for tool deflections using magnetic bearing spindles. Stuart graduated in May 2003.

KARALYN FOLKERT is originally from Zeeland, MI. She received her BS in Mechanical Engineering from Western Michigan University. While completing her undergraduate workk, she participated in Tribology research and was published. Her senior design project involved the design of a range interlock system for a heavy-duty, 10-speed transmission. She began her work at the PEC in the fall of 2003.

KARL FREITAG graduated from Clarkson University in 1995 with a BS in Mechanical Engineering. After graduation he went to work in the automotive industry for New Venture Gear's Transfer Case Division in Syracse, NY. At NVG, he worked as a product engineer and worked on the transfer case design for the 1998 Dodge Durango. After NVG, Karl has been working for the past 7 years as a Senior Engineer in Optical Fiber Manufacturing for Corning, Inc. in Wilmington, NC. Upon completion of his master's degree in spring 2004, Karl plans to continue on in pursuit of a PhD in Mechanical Engineering.

DAVID HOOD received his BS degree in mechanical engineering from NC State University in 2001. The next semester he enrolled at NC State to pursue his MS degree in Mechanical Engineering. His research involved active magnetic bearings and compensation for high-speed miniature milling tools and the ability to compensate for tool deflections. David graduated in May 2003.

PATRICK MORRISSEY received his BS degree from NC State University in December 2000. During his undergraduate studies he worked at Guilford Mills in Greensboro, NC for two summers where he focused on improving the heating system used to dry dyed fabrics. Patrick joined the PEC in August 2001 where he focused on the fabrication, distortion, and metrology of shrink fit electrical connections. He also worked on a project with Los Alamos National Laboratories that involved the design of thin composite cylinders. Patrick received his MS degree in Mechanical Engineering in May 2003.

NOBUHIKO NEGISHI received his BS degree in Mechanical Engineering from NC State University in May of 2001. The next semester he enrolled at NC State and received his MS degree in Mechanical Engineering in August 2003. His research involved elliptical vibration assisted machining with single point diamond tools.

WITOON PANUSITTIKORN began his graduate study at NCSU in Industrial Engineering and earned his MIE in 1998. Before graduating with his MSME in May 2001, Witoon developed a nonlinear control algorithm to manipulate a magnetic-free material handling system, using ultrasonic vibration. He applied his knowledge of the nonlinear controller on a magnetic hysteresis in a magnetostrictive transducer and completed this project in the first year of his tenure as a Ph.D. student in Mechanical Engineering. Currently, he is developing an open-loop control algorithm for precision manufacturing at he PEC. The technique uses digital signal processing to correct amplitude and phase response of a fast tool servo. Witoon plans to complete his Ph.D. in 2004.

TRAVIS RANDALL received his BS in Ceramic Engineering from Alfred University in May 2002. Originally from Ann Arbor, MI, Travis spent most of his life in upstate New York. He started working with the PEC and NC State in August 2002. Prior to arriving at NC State, he worked for NYS Department of Transportation and Alcoa Chemical. His research at the PEC entails the study of scribing mechanics in single crystal silicon.

TAO WU received her BS and MS degree in Electrical Engineering from Northwestern Polytechnic University, China in 1993 and 1996. Prior to coming to NCSU in August 2000, She also received her Ph.D. degree in Electrical Engineering in Shanghai Jiaotong University, China in 1999 and studied at University of Virginia for one year. As a Ph.D. student in Mechanical and Aerospace Engineering, Tao's research focused on Modeling and Design of a Novel Cooling Device for Microelectronics Using Piezoelectric Resonating Beams. Tao gave birth to a seven pound 13 ounce baby boy, Evan Wu Zhang, on July 31, 2003 and passed her final defense on December 8, 2003.

UNDERGRADUATE STUDENTS DURING 2003

RYAN HUTH lived in Wilmington, NC for the majority of his life. He began his career at NC State during fall 2000 and is currently pursuing an undergraduate degree in Mechanical Engineering. Ryan's work at the PEC involved helping to develop a closed loop technique to compensate for deflection in miniature ball end mills.

RYAN STATON is from Concord, NC. He began his undergraduate education at NCSU majoring in Electrical Engineering in fall 2000. After the spring 2002 semester, Ryan changed his major to Mechanical Engineering. He expects to graduate in Spring 2005.

ANTHONY WONG was raised in Virginia Beach, VA. He first came to NC State in fall 2001 to begin his undergraduate study of Mechanical Engineering. Before working as a Research Assistant at the PEC, Anthony previously did research in structural health monitoring and structure of CuA1C14.

GRADUATES OF THE PRECISION ENGINEERING CENTER

Student	Degree	Date	Company/Location
Jeffrey Abler	PhD	December 1994	ETEC Systems, Inc. Tucson, AZ
William Allen	PhD	December 1994	North Carolina State Univ. Raleigh, NC
Kelly Allred	MS	June 1988	
Christopher Arcona	PhD	May 1993	Norton Worcester, MA
Bradford Austin	MS	June 2000	IBM Corporation Fishkill, NY
Markus Bauer	PhD	December 2001	SCYNEXIS Chemistry & Automation, Inc. Research Triangle Park, NC
Tom Bifano	PhD	June 1988	Boston University Boston, MA
Scott Blackley	MS	May 1990	Motorola Austin, TX
Peter Blake	PhD	December 1988	NASA Goddard Greenbelt, MD
Mark Cagle	MS	June 1986	NASA-Langley Norfolk, VA
John Carroll	PhD	January 1986	Cummins Engine Co. Columbus, IN
Matthew Cerniway	MS	October 2001	Naval Surface Warfare Ctr West Bethesda, MD
Damon Christenbury	MS	June 1985	Michelin Tire Co. Spartanburg, SC
Stuart Clayton	MS	May 2003	Naval Depot Cherry Point
James Cuttino	PhD	December 1994	UNC – Charlotte Charlotte, NC
Bob Day	PhD	July 1998	Los Alamos National Lab Los Alamos, NM

Joseph Drescher	PhD	May 1992	Pratt & Whitney East Hartford, CT
William Enloe	MS	December 1988	ITT Roanoke, VA
Karl Falter	MS	December 1989	Eastman Kodak Company Raleigh, NC
Peter Falter	PhD	May 1990	Lockheed-Martin Orlando, Florida
John Fasick	MS	May 1998	Kodak Rochester, NY
Steven Fawcett	PhD	June 1991	MicroE Natick, MA
Andre Fredette	PhD	May 1993	IBM Research Triangle Park, NC
David Gill	PhD	August 2002	Sandia National Laboratories Albuquerque, NM
Jim Gleeson	MS	June 1986	Battelle Columbus Labs Columbus, OH
Mary Smith Golding	MS	May 1990	Harris Corporation Melbourne, FL
David Grigg	PhD	August 1992	Zygo Corporation Middlefield, CT
Hector Gutierrez	PhD	October 1997	Florida Inst. Of Tech. Melbourne, FL.
Christian Haeuber	MS	December 1996	Harris Corporation Melbourne, FL
Matias Heinrich	MS	July 2001	Vistakon Jacksonville, FL
Gary Hiatt	PhD	May 1992	Caterpiller Zebulon, NC
David Hood	MS	May 2003	
Peter Hubbel	MS	December 1991	Delco Electronics Kokomo, IN

Konrad Jarausch	PhD	December 1999	Intel Corporation San Jose, CA
Bradley Jared	PhD	December 1999	3M Cincinnati, OH
David Kametz	MS	August 2002	Naval Air Warfare Center Aircraft Division Patuxent River, MD
Jerry Kannel	PhD	June 1986	Battelle Columbus Labs Columbus, OH
Byron Knight	MS	May 1990	Harris Corporation Melbourne, FL
Mark Landy	MS	June 1986	Battelle Columbus Labs Columbus, OH
Mike Loewenthal	MS	December 1988	SVG Norwalk, CT
Michael Long	PhD	June 2000	Eastman Kodak Rochester, NY
Bryan Love	MS	May 2001	Virginia Tech
Michael Hung-Tai Luh	MS	June 1989	Proctor and Gamble Cincinnati, OH
Dan Luttrell	MS	1987	Luttrell, Inc. New Boston, NH
Edward Marino	MS	September 1999	Pratt Whitney Hartford, CT
Edward Miller	MS	December 2000	General Electric Greenville, SC
Michele Miller	PhD	December 1994	Michigan Tech. University Houghton, MI
Paul Minor	MS	September 1998	Hartford, CT
Gary Mitchum	MS	June 1987	Harris Corporation Melbourne, FL
Charles Mooney	MS	December 1994	JEOL Peabody, MA
Patrick Morrissey	MS	May 2003	

Larry Mosley	PhD	June 1987	Intel Corporation Chandler, AZ
Patrick Moyer	PhD	May 1993	UNC-Charlotte Charlotte, NC
Nobuhiko Negishi	MS	August 2003	
Ayodele Oyewole	MS	October 1997	Pratt & Whitney East Hartford, CT
Hakan Ozisik	PhD	December 1989	
John Pellerin	MS	May 1990	Sematech Austin, TX
Ganesh Rao	MS	December 1994	Oak Ridge National Lab Oak Ridge, TN
John Richards	MS	September 1997	Intel Corporation San Jose, CA
Walter Rosenberger	MS	May 1993	The East Group Kinston, NC
Alex Ruxton	MS	December 1996	Pratt &Whitney Palm Beach, Florida
Anthony Santavy	MS	August 1996	Ford Dearborn, MI
Keith Sharp	PhD	May 1998	Morgan Crucible Dunn, NC
Gordon Shedd	PhD	March 1991	
Wonbo Shim	PhD	May 2000	Seagate Inc. Oklahoma City, OK
Robert Skolnick	MS	September 1997	San Diego, CA
Denise Skroch	MS	May 1989	IBM Corporation Raleigh, NC
Elizabeth Smith	MS	April 1989	
Stanley Smith	PhD	May 1993	
Ronald Sparks	PhD	May 1991	Alcoa Corporation Pittsburg, PA

Brent Stancil	MS	December 1996	Harris Corporation Melbourne, FL
Gene Storz	MS	May 1994	
Anand Tanikella	PhD	August 1996	Norton Industrial Ceramics Northboro, MA
Donna Thaus	MS	May 1996	Northern Telecom Research Triangle Park, NC
John Thornton	MS	December 1993	Digital Instruments Santa Barbara, CA
Michael Tidwell	MS	December 1991	
John Tyner	MS	June 1995	Naval Depot Cherry Point
Tao Wu	PhD	December 2003	Gave birth to Evan Wu Zhang July 31, 2003.

ACADEMIC PROGRAM

Problems and limitations associated with precision manufacturing can originate in the machine, the process, or the material. In fact, most problems will probably be caused by a combination of these factors. Therefore, improvement of current processes and development of new manufacturing methods will require knowledge of a multi-disciplinary array of subjects. The educational goal of the Precision Engineering Center is to develop an academic program which will educate scientists and engineers in metrology, control, materials, and the manufacturing methods of precision engineering.

The graduate students involved in the Precision Engineering Center have an annual stipend as research assistants. They can take up to 3 classes each semester while spending about 20 hours per week on their research projects. These students also work in the Center full-time during the summer months.

The Precision Engineering Center began in 1982 with an emphasis on the mechanical engineering problems associated with precision engineering. As a result, the original academic program proposed was biased toward courses related to mechanical design and analysis. However, as the research program has developed, the need for complementary research in sensors, materials, and computers has become obvious. A graduate student capable of making valuable contributions in the computer area, for example, will require a significantly different academic program than in mechanical engineering. For this reason, the Center faculty have set a core curriculum and each student in the program is required to take at least 3 of these core courses. The remainder of the courses for the MS or the PhD degree are determined by the university or department requirements and the faculty committee of the student.

The required courses are:

- MAE 545 Metrology in Precision Manufacturing
- PY 516 Physical Optics
- MAT 700 Modern Concepts in Materials Science
- CSC (ECE) 714 Real Time Computer Systems

PhD DEGREE PROGRAM

The PhD program in Precision Engineering has been set up as a multi-disciplinary program, drawing upon courses throughout the University to provide background and expertise for the students. It should contain required courses to insure solid grounding in the fundamentals plus electives to prepare the student in his area of specialization. Because Precision Engineering is concerned with an integrated manufacturing process, students interested in computer control, materials, machine structure, and measurement and actuation systems are involved in the program. Student research projects include the wide variety of topics addressed in this report. Each student's thesis should have an experimental component because Precision Engineering is basically a hands-on technology.

MS DEGREE PROGRAM

The Master of Science degree will have a higher percentage of application courses than the PhD degree. The emphasis will be to develop the foundation for involvement in precision engineering research and development. A total of 30 credits including 6 credits for the MS thesis is required. The thesis, while less comprehensive than the PhD dissertation, will be directed at important problems in Precision Engineering. Typically the MS program will take four semesters plus one summer.

UNDERGRADUATE PROGRAM

The undergraduate degree broadly prepares an engineering student for industrial activities ranging from product design and engineering sales to production implementation. Because a large share of engineers only have the BS degree, these will be the people who must implement the new technology developed in research programs like the Precision Engineering Center. Therefore, a way must be found to acquaint engineers at the BS level with the techniques, problems, and potential of precision manufacturing.

In most undergraduate degree programs only limited time is available for technical electives. However, these electives offer the student the opportunity to expand his knowledge in many different directions. Beginning graduate courses (such as metrology) can be used as undergraduate electives.

Undergraduate projects and summer employment have also been utilized to include undergraduate students into the research program of the Center. During the 1998-1999 academic year, four undergraduate students in Mechanical Engineering were involved various projects at the PEC.

STUDY PLANS

Study plans for several example students are given below both for the MS and the PhD degree. Because of the breadth of the field and the wide range of thesis topics, few if any study plans will be exactly the same. The plan will depend upon the student's background, his interests, his thesis topic, the department, and the chairman and members of his committee.

PhD PROGRAM IN MECHANICAL ENGINEERING

Major Courses:

- MAE 740 Advanced Machine Design I
- MAE 741 Advanced Machine Design II
- MAE 706 Heat Transfer Theory & Applications
- MAE 713 Principles of Structural Vibration
- MAE 760 Computational Fluid Mechanics and Heat Transfer
- MAE 545 Metrology in Precision Manufacturing
- MAE 715 Nonlinear Vibrations
- MAE 716 Random Vibration
- MAE 714 Analytical Methods in Structural Vibration
- MAE 742 Mechanical Design for Automated Assembly
- MAE 895 Doctoral Dissertation Research

Minor Courses:

- MA 511 Advanced Calculus I
- MA 775 Mathematical Methods in the Physical Sciences I
- CSC 780 Numerical Analysis II
- PY 516 Physical Optics
- ECE 716 System Control Engineering
- MAT 700 Modern Concepts in Materials Science
- ECE 726 Advanced Feedback Control
- ECE 764 Digital Image Processing

PhD PROGRAM IN MATERIALS ENGINEERING

Major Courses:

- MAT 710 Elements of Crystallography and Diffraction
- MAT 700 Modern Concepts in Materials Science
- MAT 556 Composite Materials
- MAT 715 Transmission Electron Microscopy
- MAT 795 Defect Analysis/Advanced Materials Experiments
- MAT 753 Advanced Mechanical Properties of Materials
- MAT 712 Scanning Electron Microscopy
- MAT 895 Doctoral Dissertation Research

Minor Courses:

- PY 414 Electromagnetism I
- ST 502 Experimental Statistics for Engineers I
- MAE 740 Advanced Machine Design I
- MAE 741 Advanced Machine Design II
- MAE 545 Metrology in Precision Manufacturing
- PY 516 Physical Optics
- MA 401 Applied Differential Equations II

PhD PROGRAM IN ME (FOR STUDENT WITH MS DEGREE)

- ECE 716 System Control Engineering
- ECE 791 Gate Array Design
- MAT 700 Modern Concepts in Materials Science
- PY 516 Physical Optics
- MA 502 Advanced Mathematics for Engineers and Scientists II
- MA 775 Mathematical Methods in the Physical Sciences I
- MA 780 Numerical Analysis II
- MAE 732 Fundamentals of Metal Machining Theory
- MAE 740 Advanced Machine Design I
- MAE 741 Advanced Machine Design II
- MAE 545 Metrology in Precision Manufacturing
- MAE 716 Random Vibration

MS PROGRAM FOR ME STUDENT

- MAE 713 Principles of Structural Vibration
- MAE 740 Advanced Machine Design I
- MAE 545 Metrology in Precision Manufacturing
- MAT 700 Modern Concepts in Materials Science
- PY 516 Physical Optics
- MA 501 Advanced Math for Engineers and Scientists I
- MA 502 Advanced Math for Engineers and Scientists II
- MAE 695 Master's Thesis Research

MS PROGRAM FOR COMPUTER SCIENCE STUDENT

- CSC 501 Operating Systems Principles
- CSC 506 Architecture of Parallel Computers
- CSC 512 Compiler Construction
- ECE 521 Computer Design and Technology
- CSC 715 Concurrent Software Systems
- MAE 545 Metrology for Precision Manufacturing
- MAE 789 Digital Control Systems
- ECE 764 Digital Image Processing

MS PROGRAM FOR MATERIALS SCIENCE STUDENT

- MAT 700 Modern Concepts in Material Science
- MAT 710 Elements of Crystallography and Diffraction
- MAT 715 Transmission Electron Microscopy
- MAT 712 Scanning Electron Microscopy
- MAT 722 Advanced Scanning Electron Microscopy and Surface Analysis
- MAE 545 Metrology for Precision Manufacturing
- PY 516 Physical Optics
- ECE 738 IC Technology and Fabrication
- MAT 695 Master's Thesis Research

MS PROGRAM FOR PHYSICS STUDENT

- PY 516 Physical Optics
- PY 552 Introduction to Structure of Solids I
- PY 753 Introduction to Structure of Solids II
- PY 781 Quantum Mechanics I
- PY 782 Quantum Mechanics II
- PY 783 Advanced Classical Mechanics
- PY 785 Advanced Electricity and Magnetism I
- PY 786 Advanced Electricity and Magnetism II
- MAT 700 Modern Concepts in Material Science
- MAE 545 Metrology for Precision Manufacturing
- PY 695 Master's Thesis Research

SHORT COURSES AND TV COURSES

Six graduate level courses: Scanning Electron Microscopy (MAT 712), Advanced SEM Surface Analysis (MAT 722), Modern Concepts in Material Science (MAT 700), Mechanical Properties of Materials (MAT 705), and Metrology (MAE 545) have been offered as video courses nationwide via National Technological University. In a typical year, approximately 120 students from industry and national laboratories participate in these courses. Future plans call for a MS program in Precision Engineering to be offered via the television network.

TECHNICAL REPORTS

Volume 1 - 1983	December 1983	136 pages
Volume 2 - 1984	January 1985	168 pages
Volume 3 - 1985	January 1986	294 pages
Volume 4 - 1986	January 1987	255 pages
Volume 5 - 1987	December 1987	336 pages
Volume 6 - 1988	December 1988	362 pages
Volume 7 - 1989	March 1990	357 pages
Volume 8 - 1990	March 1991	385 pages
Volume 9 - 1991	March 1992	382 pages
Volume 10 - 1992	March 1993	289 pages
Volume 11 - 1993	March 1994	316 pages
Volume 12 - 1994	March 1995	268 pages
Volume 13 - 1995	January 1996	251 pages
Volume 14 - 1996	January 1997	232 pages
Volume 15 - 1997	January 1998	298 pages

Volume 16 – 1998	January 1999	258 pages
Volume 17 – 1999	January 2000	232 pages
Volume 18 – 2000	January 2001	274 pages
Volume 19 – 2001	January 2002	201 pages
Volume 20 – 2002	January 2003	328 pages
Volume 21 - 2003	January 2004	208 pages

PUBLICATIONS

PAPERS PUBLISHED

1. Bakkal, M., C. T. Liu, T. R. Watkins, R. O. Scattergood and A. J. Shih, "Oxidation and Crystallization of Zr-based Bulk Metallic Glass due to Machining", *Intermetallics*, vol.12, 195, 2004.

2. Bakkal, M., A. J. Shih, R. O. Scattergood and C. T. Liu, "Machining of a Zr-Ti-Al-Cu-Ni Metallic Glass, *Scripta Mater*., vol. 50, 583, 2003.

3. Clayton, S., "Closed Loop Control of Tool Deflection", *Proceedings of the ASPE 2003 Annual Meeting*, Vol 30, pg 459-462, October, 2003.

4. Craft, M.J. and G.D. Buckner, "Fuzzy logic control algorithms for Magneshock semi-active vehicle shock absorbers: design and experimental evaluations", *SPIE's 10th Annual International Symposium on Smart Structures and Materials*, San Diego, CA, March 2003.

5. Dow, T.A., Miller, E. and Garrard, K., "Tool Force And Deflection Compensation For Small Milling Tools", *Precision Engineering- Journal of the International Societies for Precision Engineering and Nanotechnology*, Vol 28, No 1, pg 31-45, January 2004.

6. Dow, T. A. and R. O. Scattergood, "Mesoscale,and Microscale Processes: Challenges for Materials, Fabrication and Metrology", *Proceedings of the ASPE Winter Topical Meeting*, January 2003, ASPE, 14, 2003.

7. Esterling, D., F.D. Caulfield, A.J. Kiefer, G.D. Buckner, and P. Jaju, "Non-contact Device for Measuring Frequency Response Functions of CNC Machine Tools", *Proceedings of the International Mechanical Engineering Congress* (IMECE2003), Washington, D.C., November 15–21, 2003.

8. Garrel, M. G., A. J. Shih, E. Lara-Curzio, R. O. Scattergood, "Finite-Element Analysis of Stress-Concentration in ASTM D638 Tensile Test Specimens", *Journal of Testing and Evaluation 2002*, vol. 31, 52, 2003.

9. Garrel, M. G., A. J. Shih, B. M. Ma, E. Lara-Curzio, R. O. Scattergood, "Mechanical Properties of Nylon Bonded Nd-Fe-B Permanent Magnets", *Journal of Magnetism and Magnetic Materials*, vol. 257, 32, 2003.

10. Gibson, N.S., H. Choi, and G.D. Buckner, "H_∞ Control of Active Magnetic Bearings Using Artificial Neural Network Identification of Uncertainty", *Proceedings of the 2003 IEEE International Conference on Systems, Man and Cybernetics*, vol. 2, pp. 1449-1456, 2003.

11. Hood, D. Buckner, G. and Dow, T., “Force Feedback Control of Tool Deflection in Miniature Ball End Milling”, *Proceedings of the ASPE 2003 Annual Meeting,* Vol 30, pg 155-158, October, 2003.

12. Kuniholm, J., G. Buckner, J. Stevens, W. Nifong, M. Orrico, P. Douglas, and R. Nering, “An automated knot tying device for minimally invasive, robot assisted (MIRA) cardiac surgery”, *Proceedings of the International Society of Cardio-Thoracic Surgeons 13th World Congress*, November 2-5, 2003, San Diego, CA (will also be published in the Journal of Cardiothoracic Surgery).

13. Kong, J., M. Bakkal, S. F. Miller, R. O. Scattergood, and A. J. Shih (2003) "Temperature Measurement in Ceramic Grinding, Machining of Bulk Metallic Glass, and Electrical Discharge Machining," *NSF Workshop on Research Needs in Thermal Aspects of Material Removal Processes*, Stillwater, Okalahoma, June 2003.

14. Kong, J., A. J. Shih, R. O. Scattergood, T. M. Yonushonis, D. J. Gust, M. B. Grant, and S. B. McSpadden (2003) "Cost-Effective Form Grinding of Zirconia using Silicon Carbide Wheels and Ceramic Grinding Temperature Measurement," *2003 NSF Design, Service and Manufacturing Grantees and Research Conference*, Birmingham, Alabama, Jan. 6-9, 2003.

15. Qu, J., L. Reister, A. J. Shih, R. O. Scattergood, E. Lara-Curzio, "Nanoindentation Characterization of Surface Layers of Electrical Discharge Machined WC-Co", *Materials Science and Engineering: A*, vol. A344, 125, 2003.

16. Panusittikorn W., K.P. Garrard and T.A. Dow, "Error Compensation Using Inverse Actuator Dynamics", *Proceedings of the ASPE 2003 Annual Meeting*, pp. 107-110.

17. Randall, T., P.I. Ro and R. Scattergood, “Characterizing Residual Stress in Scribes on Silicon using Deflection Measurements”, *Proceedings of the ASPE 2003 Annual Meeting*, vol. 30, pp 71-74, October 2003.

18. Saadat, S.A., G.D. Buckner, T. Furukawa, and M.N. Noori, “An Intelligent Parameter Varying (IPV) Approach for Non-linear System Identification of Base Excited Structures”, *International Journal of Non-Linear Mechanics*, vol. 39, no. 6, pp. 993-1004, 2004.

19. Saadat, S.A., G.D. Buckner, T. Furukawa, and M.N. Noori, “An Intelligent Parameter Varying (IPV) Approach for Non-linear System Identification of Base Excited Structures”, *SPIE’s 10th Annual International Symposium on Smart Structures and Materials*, San Diego, CA, March 2003.

20. Saadat, S.A., G.D. Buckner, and M.N. Noori, “An Intelligent Parameter Varying Approach For Structural Health Monitoring and Damage Detection”, *Proceedings of the Ninth International Conference on Applications of Statistics and Probability in Civil Engineering* (ICASP9), San Francisco, CA, July 6-9, 2003.

21. Shih, A. J., A. C. Curry, R. O. Scattergood, T. M. Yonushonis, D. J. Gust, M. B. Grant, S. B. McSpadden, "Grinding of Zirconia using the Dense Vitreous Bond Silicon Carbide Wheel", *Journal of Manufacturing Science and Engineering*, vol. 125, 297, 2003.

22. Sohn A., and K.P. Garrard, "Tip Waviness Compensation in a Polar Profilometer," *Proceedings from the ASPE 2003 Annual Meeting*, VOL. 30, pp 355-358, October 2003.

23. Stevens, J.M. and G.D. Buckner, "Intelligent control of a micro-manipulator actuated with shape memory alloy tendons", *SPIE's 10th Annual International Symposium on Smart Structures and Materials*, San Diego, CA, March 2003.

24. Stevens, J., G. Buckner, J. Kuniholm, W. Nifong, M. Orrico, P. Douglas, and R. Nering, "An endoscopic atrial retractor for robotic mitral valve repair", *Proceedings of the International Society of Cardio-Thoracic Surgeons 13th World Congress*, November 2-5, 2003, San Diego, CA (will also be published in the Journal of Cardiothoracic Surgery).

REPORTS PUBLISHED

1. Clayton, S. and. T.A. Dow, "Closed Loop Control of Tool Deflection", *2003 Precision Engineering Center Interim Report*, pp. 42-52, October 2003.

2. Freitag, K., R. Huth, and T.A. Dow "Force Feedback Deflection Compensation of Miniature Ball End Mills", 2003 *Precision Engineering Center Interim Report*, pp. 53-58, October 2003.

3. Hood, D. and G. Buckner, "Force Feedback Control of Tool Deflection in Miniature Ball End Milling", *Precision Engineering Center Interim Report*, pp. 34-42, October 2003.

4. Huth, R., "Force Sensing Calibration on Milling Spindle", *REU Summer Final Report*, Precision Engineering Center, August, 2003.

5. Morrissey P. and J. Eischen, "Fabrication, Distortion, and Metrology of Shrink Fit Electrical Connections", *Precision Engineering Center Interim Report*, pp. 1-6, October 2003.

6. Negishi, N. and T.A. Dow, "Elliptical Vibration Assisted Diamond Turning", *Precision Engineering Center Interim Report*, pp. 65-71, October 2003.

7. Panusittikorn W., K.P. Garrard and T.A. Dow, "Surface Deconvolution for Diamond Turning", *2003 Precision Engineering Center Interim Report*, pp. 59-64, October 2003.

8. Randall, T. and R. Scattergood, "Characterizing Residual Stress in Scribes on Silicon Using Deflection Measurements", *Precision Engineering Center Interim Report*, pp. 7-14, October 2003.

9. Sohn, A., K. Garrard, and T.A. Dow, “Ultraform 2D”, *Precision Engineering Center Interim Report*, pp. 19-28, October 2003.

10. Wong, A., K. Folkert, and T.A. Dow, “Metrology Artifact Development”, *Precision Engineering Center Interim Report*, pp. 13-18, October 2003.

11. Wu, T. and P.I. Ro, “Experimental Study on Cooling Effects Generated by Piezoelectric Bimorph Structures”, *Precision Engineering Center Interim Report*, pp. 29-34, October 2003.

PAPERS SUBMITTED OR ACCEPTED FOR PUBLICATION AND PRESENTATIONS

1. Balkey, M.M., R.D. Day, S.H. Batha, N.E. Elliot, T. Pierce, D.L. Sandoval, K.P. Garrard and A. Sohn, “Production and Metrology of Cylindrical Inertial Confinement Fusion Targets with Sinusoidal Perturbations.” *Fusion Science and Technology*, March 2004.

2. Buckner, G.D., H. Choi, and N.S. Gibson, "Estimating Model Uncertainty using Confidence Interval Networks: Applications to Robust Control", submitted for review October 2003, *ASME Journal of Dynamic Systems, Measurement, and Control*.

3. Dixit, R.K. and G.D. Buckner, “Sliding Mode Control and Observation for Semiactive Vehicle Suspensions”, to appear February 2004, Vehicle System Dynamics

4. Gibson, N.S., H. Choi, and G.D. Buckner, “Estimating Model Uncertainty using Confidence Interval Networks: Applications to Robust Control of a Flexible Rotor Supported on Active Magnetic Bearings”, *Ninth International Symposium on Magnetic Bearings*, University of Kentucky, Lexington, Kentucky, August 3-6, 2004.

5. Kuniholm, J., G. Buckner, W. Nifong, and M. Orrico, “Automated Knot Tying for Fixation in Minimally Invasive, Robot Assisted Cardiac Surgery”, submitted for review August 2003, *Journal of Engineering in Medicine*.

6. Lawrence, B., G. Buckner, and G. Mirka, "Intelligent System Identification Applied to the Biomechanical Response of the Human Trunk during Sudden Loading Part I: Modeling Approach", submitted for review September 2003, *Journal of Biomechanics*.

7. Lawrence, B., G. Mirka, and G. Buckner, "Intelligent System Identification Applied to the Biomechanical Response of the Human Trunk during Sudden Loading Part II: Application in Ergonomics", submitted for review September 2003, *Journal of Biomechanics*.

8. Lawrence, B.M., G.A. Mirka, and G.D. Buckner, “System Identification Applied to the Biomechanical Response of Sudden Loading”, *Proceedings of the IIE Annual Conference*, Houston, Texas, May 15-19, 2004.

9. Panusittikorn W., P.I. Ro, "Modeling and Control of a Magnetostrictive Transducer", submitted, *ASME Journal of Dynamic Systems, Measurement and Control*.

10. Panusittikorn W., M.C. Lee and P.I. Ro, "Modeling and Sliding Mode Control of The Object Transport Using Two-Mode Ultrasonic Excitation", accepted, *IEEE Transaction on Industrial Electronics.*

11. Saadat, S.A., M.N. Noori, and G.D. Buckner, "Health Monitoring and Damage Detection for Base Excited Structures Using An Intelligent Parameter Varying (IPV) Approach", submitted for review June 2003, *International Journal of Non-Linear Mechanics*.

12. Saddat, S., G. D. Buckner, M. N. Noori, and T. Furukawa, "Structural Health Monitoring and Damage Detection Using the Intelligent Parameter Varying (IPV) Approach", *Fifth Korea-Japan Workshop on System Identification and Structural Health Monitoring*, Seoul, Korea, January 30-31, 2004.

13. Stevens, J.M. and G.D. Buckner, "Actuation and Control Strategies for Miniature Robotic Surgical Systems", submitted for review December 2002, *ASME Journal of Dynamic Systems*, Measurement, and Control.

PENDING PATENTS

1. Sohn, A., K.P. Garrard, and T.A. Dow, "Polar Coordinate-Based Profilometer and Methods", November 2002.

THESES AND DISSERTATIONS

1. Clayton, Stuart, *Force Modeling and Deflection Compensation of Miniature Ball End Mills*, MS Thesis, North Carolina State University, July 2003.

2. Hood, David, *Force Feedback Control of Tool Deflection in Miniature Ball End Milling*, MS Thesis, North Carolina State University, June 2003.

3. Morrissey, Patrick, *Fabrication, Distortion, and Metrology of Shrink Fit Electrical Connections*, MS Thesis, North Carolina State University, June 2003.

4. Negishi, Nobuhiko, *Elliptical Vibration Assisted Machining with Single Point Diamond Tools*, MS Thesis, North Carolina State University, October 2003.

5. Wu, Tao, *Modeling and Design of a Novel Cooling Device for Microelectronics Using Piezoelectric Resonating Beams*, Ph.D. Dissertation, North Carolina State University, December 2003.